

UNIVERSITY OF TRENTO

Department of Physics



Master Degree in Physics

**Gravitational wave searches for
transient signals: classification of
candidates consistent with binary
black hole mergers**

Rapporteur:
Giovanni Andrea Prodi

Co-Rapporteur:
Marco Drago

Student:
Serena Vinciguerra

Academic Year 2012 - 2013

To all the people near me... Thanks!!!

Contents

Preambolo	i
Abstract	v
1 Introduction to Gravitational Waves	1
1.1 Gravitational Waves: Theory	2
1.1.1 Geodesics	2
1.1.2 Newtonian limit	4
1.1.3 Riemann, Ricci and Einstein tensors	5
1.1.4 Field equations	7
1.2 Gravitational waves	8
1.2.1 Harmonic coordinates	8
1.2.2 Linearized field equations	10
1.2.3 Plane gravitational waves	11
1.2.4 GW radiation	12
1.2.5 GW effects on free bodies	13
2 Astrophysical sources	15
2.1 Core collapse supernovae	16
2.1.1 Origin	16
2.1.2 Rate	17
2.1.3 GW characteristics	17
2.2 Compact binary coalescence (CBCs)	18
2.2.1 Signal and phenomenon description	18
2.2.2 Rate	21
2.2.3 Simulations	23
3 LIGO-VIRGO detectors	27
3.1 Gravitational wave detectors	28
3.1.1 The basic principle of interferometry	31
3.2 Virgo	41
3.2.1 Virgo noise	42
3.3 Detector directional sensitivity	48
3.4 Advanced detectors	51

3.4.1	Advanced Virgo detector	51
4	cWB analysis	53
4.1	Data Quality Flags	56
4.2	Likelihood method	57
4.2.1	Single detector	57
4.2.2	Detector network	59
4.2.3	Regulators	67
4.2.4	Energy disbalance	68
4.2.5	Polarization constrains	69
4.3	Production stage	70
4.3.1	Data conditioning	72
4.3.2	TF data representation	72
4.3.3	Enhancement of BKG statistics	78
4.3.4	Waveform parameter reconstruction	80
4.4	Post-Production stage	81
4.4.1	Network correlation coefficient	82
4.4.2	Effective Correlated SNR	83
4.4.3	Post Production effects	84
5	Artificial Neural Networks	85
5.1	Machine learning techniques and GW detection	86
5.1.1	Machine Learning	87
5.2	Artificial Neural Network	91
5.2.1	Biological neural networks vs artificial neural networks	92
5.2.2	Learning procedures	94
5.2.3	Applications	95
5.3	Multilayer perceptron	96
5.3.1	Perceptron	97
5.3.2	Multilayer perceptron	101
5.3.3	Back propagation	107
5.3.4	Learning methods and conjugate gradients	109
6	Implementation and results	117
6.1	Matrix implementation	118
6.2	Train and Test ANNs varying the parameters	120
6.2.1	Architecture	122
6.2.2	Learning method	125
6.3	Graph explanation	136
6.4	Results for injections on gaussian noise	136
6.4.1	Tested events	136
6.4.2	Results	141
6.5	Results for recolored data	147
6.5.1	Tested events	147

6.5.2	ANNs trained with waveforms injected on gaussian noise	150
6.5.3	ANNs trained with recolored data	153
7	Developements and comparisons	157
7.1	Input matrix developements	157
7.2	Comparison between performances of different ANNs	159
7.3	Averaging over more ANN outputs	161
7.4	Fitting procedure	165
7.4.1	Chirp mass	166
7.4.2	Our implementation of the fitting procedure	167
7.5	Fisher Discriminant	171
8	Conclusions and future ideas	177

Preambolo

“Già! D’après Sophocle, dice il manifestino. Sarà l’Elettra. Ora senta un po’ che bizzarria mi viene in mente! Se nel momento culminante, proprio quando la marionetta che rappresenta Oreste è per vendicare la morte del padre sopra Egisto e la madre, si facesse uno strappo nel cielo di carta del teatrino, che avverrebbe? Dica lei. ””

“Ma è facilissimo, signor Meis! Oreste sentirebbe ancora gl’impulsi della vendetta, vorrebbe seguirli con smaniosa passione, ma gli occhi, sul punto, gli andrebbero lì, a quello strappo, donde ora ogni sorta di mali influssi penetrerebbero nella scena, e si sentirebbe cadere le braccia. Oreste, insomma diventerebbe Amleto. Tutta la differenza, signor Meis, fra la tragedia antica e la moderna consiste in ciò, creda pure: in un buco nel cielo di carta. ””

Tratto da *“Il fu Mattia Pascal”* di Luigi Pirandello.

“ Dove sono e quali sono gli aspetti affascinanti della fisica? ”

Spesso la gente associa la scienza a qualcosa di freddo, lontano dalla personalità umana. Niente può essere più lontano dal vero. Al contrario in essa riponiamo la nostra essenza, il nostro pensiero. La scienza è la proiezione della realtà sui nostri sensi e sulla nostra personalità. Proprio per questo motivo anche nell’ambito scientifico è fondamentale la comunicazione tra persone di differenti culture. La diversità nel concepire il mondo mette in luce idee nuove che ci possono aiutare a svelare qualche caratteristica della nostra realtà che fin’ora c’è sfuggita.

Quindi non solo la scienza ci permette di comprendere meglio il pensiero e l’animo umano in ogni suo tempo, ma, aspetto ben più significativo, essa ci consente di evolverlo, di migliorare la "proiezione del mondo" in cui viviamo e quindi apprezzare e interiorizzare nuove, fantastiche idee.

Pensiamo, per esempio, a come la scienza ci ha permesso di evolvere il nostro giudizio su noi stessi. All’inizio della nostra storia i nostri sensi “primitivi” ci hanno posto al centro del mondo, o per meglio dire, al centro dell’universo. Nei secoli, però, grazie alla nostra curiosità, al nostro

porci continuamente nuove domande e alla nostra tenacia nel tentare di darvi risposta, il nostro pensiero e la concezione della realtà che ci circonda si sono evoluti. Tanto che, nel 1543 con la pubblicazione del "De revolutionibus orbium celestium", Niccolò Copernico diede inizio ad una nuova fisica ponendo al centro dell'universo non più la Terra, bensì il Sole. Con quest'idea rivoluzionaria cominciò una nuova era, non solo per quanto riguarda l'astronomia, ma anche per il pensiero umano. Infatti, con le prove scientifiche fornite in seguito da Galileo, l'uomo ha dovuto fare i conti con una nuova realtà, nella quale gli è stato negato il ruolo privilegiato di cui aveva precedentemente goduto. Il senso di smarrimento che consegue questa nuova consapevolezza spiazza l'animo umano che si sente costretto ad una revisione delle proprie certezze. È geniale Pirandello che riesce ad esprimere questo sentimento in un'immagine tanto semplice quanto efficace: lo strappo nel cielo di carta.

Un tempo anche noi, come le marionette dell'Elettra, vivevamo impavidi, sicuri delle nostre azioni in quanto guidate dalle nostre certezze. Ma Copernico ha strappato le nostre convinzioni, rappresentate da Pirandello come un cielo di cartapesta, obbligandoci a constatare la falsità delle nostre precedenti idee. Anche questo sentimento di sconforto e sconcerto ha portato, però, i suoi frutti partecipando alla nostra crescita.

Ogni scoperta porta con sé qualcosa di nuovo: abbiamo cominciato costruendo castelli di sabbia e, quando li abbiamo visti distruggersi sotto l'azione della pioggia o del mare, ne abbiamo sofferto, ma il giorno dopo abbiamo concepito un nuovo progetto, più bello e solido del precedente. Così quando la realtà porrà in luce nuovi difetti distruggendo il nostro lavoro, non tutto sarà perduto. Al contrario ci arricchiremo di nuove conoscenze migliorando sempre più la nostra creazione che così rispecchierà la nostra crescita.

Sebbene quindi l'uomo rimanga spiazzato di fronte alla rivelazione copernicana, condividendo perfettamente il sentimento di confusione e di disorientamento che caratterizza il personaggio shakespeariano di Amleto, essa gli pone una fantastica occasione. Gli permette di arricchirsi di una nuova consapevolezza, non più fragile sul mondo ma bensì salda, basata invece sulla forza dell'animo umano.

Ecco, in questo trovo affascinante la fisica, e la scienza in generale, nella consapevolezza che essa è l'interpretazione del mondo esterno ad immagine del mondo interiore dell'uomo. Per questo la fisica, per me, è fantastica! Immagino però, caro lettore, che non ti sia capitato spesso di pensare all'ambito scientifico come qualcosa di "fantastico" (bada bene che in tale aggettivo intendo comprendere, non solo il senso di meraviglia, ma anche quella sfumatura di fantasia che in esso si cela). In mia opinione, però, esistono poche parole più calzanti di questa per descriverlo.

In che altro modo lo descriveresti, tu, un mondo dove vige la relatività del trascorrere del tempo, dove le particelle hanno una "doppia personalità" (che, come per esempio i fotoni, ci mostrano di essere particelle ma di "ri-

cordarsi" di essere pure parte di un'onda elettromagnetica), dove un gatto in una scatola è contemporaneamente sia vivo che morto e dove è possibile la contrazione e dilatazione, non solo degli oggetti, ma proprio dello spazio!?

Abstract

Gravitational Waves are the key prediction of General Relativity. They are space-time perturbation coming from gravitational sources with some specific characteristics (chapter 1). In the following we are going to consider signal coming from coalescence compact binaries (chapter 2).

At the moment the only Gravitational waves detectors are on Earth. We are interesting on VIRGO and LIGO interferometric detectors (chapter 3), which are the most sensitive instruments devoted to gravitational waves detections.

The analysis of the data coming from the LIGO-VIRGO detectors are differently analyzed depending on the interested search. We are going to use the cWB-2G pipeline for the data analysis, which concerns are specific for burst waves (chapter 4). The aim of the notes is the pattern recognition of signals coming from coalescence compact binaries. The first analysis concerns the use of Artificial Neural Networks (chapter 5). By this procedure hopeful results are obtained (chapter 6). Another different approach is the use of the fit techniques, which anyway presents some statistical difficulties (chapter 7). The future ideas mainly concern improvements and deeper studies on the performed analysis to finally reach a more general signal classification (chapter 8).

Chapter 1

Introduction to Gravitational Waves

[1] [2] [3] Every night nature offers us the possibility to admire its power, its fantasy, its masterpiece, simply looking at the sky. Without any instrument, besides our eyes, we can see several of shiny stars coloring the deep blue of the night, we can see the past of other worlds and an incredibly small taste of the Universe immensity. But what other surprising astrophysical objects are hidden in the Universe?

In this field a special role is played by Gravity which drives the larger scale processes present in the Universe. The gravitational interaction makes the aggregation of matter possible, forming planets, stars and galaxies. It drives the motion objects and part of their evolutions. Therefore thanks to gravity stars are born, evolve and die enriching the interstellar medium and making possible incredible things, like life. Can the gravitational interaction make more? Of course it can. Not only it rules the Universe and the Earth as we know them, but also it allows us to discover part of the mysteries which are around us. Indeed different phenomena have origin in gravity, like gravitational lensing and Gravitational Waves (GW). The latter can be a very useful tool non only to discover systems of different nature but also to better understand all the celestial entities. Indeed, differently from the electromagnetic radiation, GWs weakly interact with matter carrying more genuine information about their sources. Gravitational Waves are a key prediction, not yet directly seen, of General Relativity (GR) formulated by Albert Einstein in 1916. GR gives a new and very important role to the space-time, which before was consider only as a passive frame.

In the first section of this chapter (Section 1.1) we will briefly see where the Einstein's GR equations come from and then we will focus on one of their key prediction and solution: the Gravitational Waves (GW)(Section 1.2).

1.1 Gravitational Waves: Theory

To understand the GW origin we have to start with an introduction to GR. This theory describes gravitational phenomena starting from a new consideration of the correspondence between gravitational and inertial masses. While for Newtonian theory it is treated as a mere coincidence, in GR this equivalence is a fundamental assumption called **weak equivalence principle**. The Einstein lift experiment underlines the real importance of this consideration, which allows the equivalence between the lift in absence of gravity and the one in free fall. This idea is the base of GR and is extended to the so called **strong equivalence principle**. It states that: *in every point of the space-time and in presence of any gravitational field, it's always possible to choose a reference frame where nature, with all its laws, behaves like in absence of gravity.*

With GR Einstein extends the space-time studies conducted in Special relativity to a more general contest, characterized by the presence of a gravitational field. In Special Relativity the inertial reference frames play a preferential role, which is now justified and contextualized by GR. Indeed the effect of the gravitational field introduction is a distortion of the Minkowski space-time and consequently the break up of the inertial reference frame, typical of Special Relativity, into infinite locally inertial reference frames.

1.1.1 Geodesics

In GR the geometry of the space-time is strictly connected to the physical phenomena. An important example of this connection is represented by geodesics. In geometry a Geodesic is the shortest line which links two points on any mathematically defined surface. In Riemann space, which is the typical GR environment, this definition is equivalent to the generalization of the straight line. A straight line is the curve whose tangent vector remains parallel when transported along it.

The connection between physics and space-time structure is so strong that we can think to trajectories as straight lines which links different events. Therefore we can find the geodesic equation analyzing the motion of a free particle in a gravitational field. The equivalence principle allows us to start considering the locally inertial reference frame, where the particle motion is the one described by Special Relativity. Suppose X^μ are the coordinates of the considered particle in this reference frame, than the equation of motions is:

$$\frac{d^2 X^\mu}{ds^2} = 0$$

where $ds^2 = -c^2 d\tau^2 = \eta_{\mu\nu} dX^\mu dX^\nu$ with $\mu, \nu = 0, 1, 2, 3$. Here ds is the *invariant interval*, $d\tau$ the *proper time* and $\eta_{\mu\nu}$ the *Minkowski metric*, for which we adopt the signature convention $(-, +, +, +)$. Now using a "smooth" func-

tion (continuous, differentiable, invertible ecc..) we can define the coordinates of an arbitrary reference frame: $x^j = x^j(X^\mu)$ where $j = 0, 1, 2, 3$.

Therefore we can introduce

$$a_\mu^j(X) = \frac{\partial x^j(X)}{\partial X^\mu}$$

and its inverse

$$A_j^\mu(x) = \frac{\partial X^\mu(x)}{\partial x^j}$$

so that $A_\mu^k a_i^\mu = \delta_k^i$ and $A_\mu^j a_j^\nu = \delta_\mu^\nu$. By definition the interval ds is invariant and therefore has the same value in all the reference frames:

$$ds^2 = \eta_{\mu\nu} dX^\mu dX^\nu = g_{ij} dx^i dx^j$$

from which we can write the *metric tensor* of an arbitrary reference frame $g_{ij}(x)$ as:

$$g_{ij} = \eta_{\mu\nu} A_i^\mu A_j^\nu$$

which equals the Minkowski metric only in inertial reference frames. In view of these considerations the equation of motion is

$$0 = \frac{d^2 X^\mu}{ds^2} = \frac{d}{ds} \left(A_j^\mu(x) \frac{dx^j}{ds} \right) = A_j^\mu(x) \frac{d^2 x^j}{ds^2} + \frac{\partial A_k^\mu(x)}{\partial x^j} \frac{dx^j}{ds} \frac{dx^k}{ds}$$

Now, multiplying the previous equation by the A-inverse matrix a_μ^i we obtain the **geodesic equation**

$$\frac{d^2 x^i}{ds^2} + \Gamma_{jk}^i \frac{dx^j}{ds} \frac{dx^k}{ds} = 0 \quad (1.1)$$

which describes also the particle trajectory. In the last equation we have introduced the *Christoffel symbols* or *Levi-Civita connections* Γ_{jk}^i , which therefore are defined as:

$$\Gamma_{jk}^i = \Gamma_{kj}^i = a_\nu^i \frac{\partial A_j^\nu}{\partial x^k} = -A_j^\nu \frac{\partial a_\nu^i}{\partial X^k} = \frac{\partial x^i}{\partial X^\nu} \frac{\partial^2 X^\nu}{\partial x^j \partial x^k} \quad (1.2)$$

The equation (1.1) shows that the formal difference between GR and Special Relativity is represented by the *Christoffel symbols*. Therefore these quantities are strictly connected the gravitational interaction.

Christoffel symbols are completely defined by the metric tensor g , indeed we have $g_{ij}(x) = \eta_{\mu\nu} A_i^\mu A_j^\nu$ and therefore:

$$\frac{\partial g_{ij}}{\partial x^k} = \eta_{\mu\nu} \left(A_i^\mu \frac{\partial A_j^\nu}{\partial x^k} + A_j^\nu \frac{\partial A_i^\mu}{\partial x^k} \right)$$

and since $\eta_{\mu\nu} A_i^\nu = g_{ij} a_\mu^j$ we obtain:

$$\frac{\partial g_{ij}}{\partial x^k} = \Gamma_{ki}^\alpha g_{\alpha j} - \Gamma_{kj}^\beta g_{\beta i}$$

Then circularly permutating the index we find

$$\frac{\partial g_{jk}}{\partial x^i} = \Gamma_{ij}^\alpha g_{\alpha k} - \Gamma_{ik}^\beta g_{\beta j}$$

$$\frac{\partial g_{ki}}{\partial x^j} = \Gamma_{jk}^\alpha g_{\alpha i} - \Gamma_{ji}^\beta g_{\beta k}$$

Finally, through these expressions and considering the Γ symmetries we obtain:

$$\Gamma_{ik}^\lambda = \frac{1}{2} g^{j\lambda} \left(\frac{\partial g_{ij}}{\partial x^k} + \frac{\partial g_{jk}}{\partial x^i} - \frac{\partial g_{ki}}{\partial x^j} \right) \quad (1.3)$$

We can see that in Minkowski space, where the metric tensor is constant in space and therefore $\Gamma = 0$, the previous equation (1.1) becomes linear.

A very nice example of this space-time distortion is represented by the Earth motion around the Sun. Despite the ellipticity of this orbit we can say that, in this case, the space-time distortion is minimal. This seems strange because we are used to think in the 3-dimensional space, instead of in the 4-dimensional space-time. Anyway if we take into account the time dimension we will easily find that the Earth trajectory around the Sun describes a very extended helix. Therefore in this case the Minkowski space well approximates the geometry of the space-time perturbed by the analyzed system.[2]

1.1.2 Newtonian limit

In order to better understand the relationship between space curvature and gravity we start considering the newtonian limit. In case of weak gravity we can make the following approximations:

a. linear approximation:

$$g_{\mu\nu}(x) \approx \eta_{\mu\nu} + h_{\mu\nu} + O(|h_{\mu\nu}^2|)$$

where $|h_{\mu\nu}| \ll 1$ and thus we neglect higher order terms of the perturbation-matrix h ;

b. static gravitational field: $\frac{\partial h_{\mu\nu}}{\partial x^0} = 0$;

c. non-relativistic velocities v , i.e. $\left| \frac{dx^a}{ds} \right| \ll \left| \frac{dx^0}{ds} \right|$, where $a = 1, 2, 3$.

In view of these considerations the geodesic equation becomes:

$$0 \approx \frac{d^2 x^k}{ds^2} + \Gamma_{00}^k \left(\frac{dx^0}{ds} \right)^2 \quad (1.4)$$

To obtain the last formula we consider the **c.** approximation neglecting the derivatives of the spatial coordinates. Moreover the **a.** point allows us to write the remaining Christoffel coefficients as:

$$\Gamma_{00}^k \approx -\frac{1}{2}g^{k\alpha}\frac{\partial g_{00}}{\partial x_\alpha} \approx -\frac{1}{2}\eta^{k\alpha}\frac{\partial h_{00}}{\partial x_\alpha}$$

For this reason using the **b.** consideration we find $\Gamma_{00}^0 \approx 0$ and consequently also $\frac{d^2x^0}{ds^2} \approx 0$. Instead for spatial coordinates we obtain

$$\frac{d^2x^a}{ds^2} \approx -\Gamma_{00}^a \left(\frac{dx^0}{ds}\right)^2 = \frac{1}{2}\eta^{a\alpha}\frac{\partial h_{00}}{\partial x^\alpha} \left(\frac{dx^0}{ds}\right)^2$$

where $a = 1, 2, 3$ concerns to the space-coordinates. This last equation can be set in the form:

$$\frac{1}{c^2} \frac{d^2\vec{x}}{dt^2} = \frac{1}{2} \vec{\nabla} h_{00}$$

where we have considered $c \cdot d\tau \approx c \cdot dt$, valid in Newtonian limit. In the analyzed situation the body satisfies also the Newtonian equation which describes the motion of a particle in a static gravitational field, i.e.

$$\frac{d^2\vec{x}}{dt^2} = -\vec{\nabla} \phi$$

In light of this consideration we have

$$h_{00} = -\frac{2\phi}{c^2}$$

and therefore

$$g_{00} = -1 - \frac{2\phi}{c^2}$$

In conclusion, under the Newtonian limit approximations, the tensorial gravitational field, has only a term significantly different from zero and therefore here it can be considered a scalar field. Only in relativistic conditions the terms different from g_{00} become relevant.

1.1.3 Riemann, Ricci and Einstein tensors

The previous considerations allow the introduction of the **Riemann tensor** \mathbf{R} defined by the formula as:

$$R_{\mu\nu\gamma}^\sigma = -\frac{\partial\Gamma_{\mu\nu}^\sigma}{\partial x^\gamma} + \frac{\partial\Gamma_{\mu\gamma}^\sigma}{\partial x^\nu} + \left(\Gamma_{\gamma\mu}^\lambda\Gamma_{\lambda\nu}^\sigma - \Gamma_{\mu\nu}^\lambda\Gamma_{\lambda\gamma}^\sigma\right) \quad (1.5)$$

By definition the Riemann tensor has 256 components, but only few of these are independent. The reason is the presence of many symmetries, for example it's easy to see that $R_{\mu\nu\gamma}^\sigma = R_{\mu\gamma\nu}^\sigma$, and that $R_{\mu\nu\gamma}^\sigma + R_{\gamma\mu\nu}^\sigma + R_{\nu\gamma\mu}^\sigma = 0$. Other

symmetries can be found lowering the σ index and so defining the tensor $R_{\tau\mu\nu\gamma} = g_{\tau\sigma}R_{\mu\nu\gamma}^{\sigma}$. Thanks to the tensor transformation law it can be add that verify a tensor's symmetry in a reference frame means that it is everywhere satisfied. Considering the Γ definition we can also verify that

$$R_{\tau\mu\nu\gamma} = \frac{1}{2} \left(\frac{\partial^2 g_{\tau\gamma}}{\partial x^\mu \partial x^\nu} - \frac{\partial^2 g_{\gamma\mu}}{\partial x^\tau \partial x^\nu} - \frac{\partial^2 g_{\tau\nu}}{\partial x^\mu \partial x^\gamma} + \frac{\partial^2 g_{\mu\nu}}{\partial x^\gamma \partial x^\tau} \right) \quad (1.6)$$

Two of the most evident symmetries of this object are:

$$R_{\tau\mu\nu\gamma} = -R_{\mu\tau\gamma\nu} \text{ and } R_{\tau\mu\nu\gamma} = R_{\nu\gamma\tau\mu}.$$

Therefore taking into account all these symmetries it can be proven that the Riemann tensor in a n-dimensional manifold has $\frac{n^2(n^2-1)}{12}$ independent components. New symmetries and physical tensors can be found contracting two Riemann tensor's indeces. In particular we obtain the following relations:

1. contracting the first and the second indeces: $R_{\sigma\mu\nu}^{\sigma} = 0$ because $R_{\sigma\mu\nu}^{\sigma} = g^{\sigma\tau} R_{\tau\sigma\mu\nu} = -g^{\sigma\tau} R_{\sigma\tau\mu\nu} = -R_{\tau\mu\nu}^{\tau}$;
2. contracting the first and the third indeces: $R_{\gamma\nu} \equiv R_{\gamma\mu\nu}^{\mu} = g^{\mu\sigma} R_{\sigma\gamma\mu\nu} = g^{\mu\sigma} R_{\mu\nu\sigma\gamma} = R_{\nu\sigma\gamma}^{\sigma} = R_{\nu\gamma}$.
3. contracting the first and the fourth indeces we obtain the same relation found in the previous point. In particular, thanks to the antisymmetry between the third and four Riemann tensor's indeces, the resulting contracted tensor is it's opposite.

The found property, 2. in the previous list, defines a new symmetric tensor of rank 2 called **Ricci tensor**. For better understand it's meaning we can develop this tensor in terms of Christoffel symbols:

$$R_{\mu\nu} = \frac{\partial \Gamma_{\mu\gamma}^{\gamma}}{\partial x^{\nu}} - \frac{\partial \Gamma_{\mu\nu}^{\gamma}}{\partial x^{\gamma}} + \Gamma_{\mu\gamma}^{\sigma} \Gamma_{\nu\sigma}^{\gamma} - \Gamma_{\mu\nu}^{\sigma} \Gamma_{\sigma\gamma}^{\gamma} \quad (1.7)$$

Thinking of Ricci tensor as a 4x4 matrix we can calculate it's trace $R = g^{\nu\mu} R_{\nu\mu} = R_{\nu}^{\nu}$ and therefore define the so called **scalar curvature**. Using this scalar quantity we can define the tensor family $G_{\mu\nu}^{(l)} = R_{\mu\nu} + l g_{\mu\nu} R$, where l is a real number. The most important element of this family is the **Einstein tensor** for which $l = -\frac{1}{2}$. This tensor has the interesting property to be a covariant constant, i.e.

$$D_{\mu} G_{\nu}^{\mu} = \frac{\partial G_{\nu}^{\mu}}{\partial x^{\mu}} + \Gamma_{\mu\lambda}^{\mu} G_{\nu}^{\lambda} - \Gamma_{\mu\nu}^{\lambda} G_{\lambda}^{\mu} = 0$$

where we have define the covariant derivative D_{μ} . To prove this formula we have to contract the Bianchi identity ¹, obtaining $D_{\alpha} R_{\tau\mu} - D_{\mu} R_{\tau\alpha} + D_{\beta} R_{\tau\mu\alpha}^{\beta} = 0$ and than multiply this relation by $g^{\mu\tau}$.

¹ $D_{\alpha} R_{\beta\sigma\tau}^{\alpha} + D_{\sigma} R_{\beta\tau\alpha}^{\alpha} + D_{\tau} R_{\beta\alpha\sigma}^{\alpha} = 0$

1.1.4 Field equations

The Newtonian limit of the paragraph (1.1.2) shows a strong relation between metric tensor g and gravitational potential ϕ :

$$\phi \approx -\frac{c^2 (g_{00} + 1)}{2}$$

In this limit, characterized by small velocities and weak gravitational field, the gravitational potential is defined by the Poisson equation:

$$\nabla^2 \phi = 4\pi G \mu_0 \quad (1.8)$$

where $\mu_0(x)$ is the matter density, G the universal gravitational constant and whose solution is $\phi = -\frac{MG}{r^2}$.

Moreover we note that the matter density can be written as

$$\mu_0 \approx \frac{T_{00}}{c^2}$$

where the T is the energy-momentum tensor. Now we are looking for more general equations to define the gravitational potential. In light of the above, these equations have to satisfy the following constraints:

- be tensorial equations;
- be second-order differential equations in the metric tensor g ;
- be 10, as the independent components of the metric tensor;
- coincide to the Poisson's equation in the classical limit;
- link the metric tensor g to the matter distribution.

Starting from the Newtonian limit we can rewrite the Poisson equation (1.8) in a different form:

$$\nabla^2 g_{00} \approx -\frac{8\pi G}{c^4} T_{00} \quad (1.9)$$

To generalize the right-hand side of this formula we can use the full energy-momentum tensor², while the left-hand side needs some considerations. We are looking for a tensor $W_{\mu\nu}$ which contains the second derivatives of the metric g . The only tensor's family which satisfies all the requirements is $G_{\mu\nu}^{(l)}$ ³. The possible l factors are reduced by the continuity equation, which must be satisfied by the energy-momentum tensor:

$$D_\mu T_\nu^\mu = 0$$

²The constant can be formally found using the Newtonian limit.

³To be precise the most general tensor which satisfies the requirements is a linear combination of $R_{\mu\nu}$, $Rg_{\mu\nu}$ and $\Lambda g_{\mu\nu}$, where Λ is the *cosmological constant*. Different theories were and are developed about the generalization of the left-hand side of the (1.9). In these notes we assume the easier hypothesis, which takes into account a linear combination of only the first two tensors.

Indeed also the left-hand side of (1.9) has to satisfy the same equation and this limits the choice to $l = \frac{1}{2}$. In view of these considerations we have $W_{\mu\nu} = G_{\mu\nu}$ and therefore we find:

$$G_{\mu\nu} = R_{\mu\nu} - \frac{1}{2}Rg_{\mu\nu} = \frac{8\pi G}{c^4}T_{\mu\nu} \quad (1.10)$$

which are called the **Einstein equations** or **field equations**. The aim of GR is therefore to find general solutions of these equations and compare them to the astrophysical sources as Black Holes, neutron stars etc.. The most problematic difficulty is the non linearity of the equations and the consequent invalidity of the superposition principle. This is due to the relation which links mass and energy. The solutions of (1.10) are known in some particular cases:

- in presence of spherical symmetry (Schwarzschild solution);
- for the cosmologic case (Friedmann Lemaitre solutions);
- in presence of weak gravitational fields (linear approximation) in harmonic coordinates, also in presence of non-static gravitational fields (as GW).

1.2 Gravitational waves

Gravitational waves are key predictions of the Einstein field equations (1.10). They represent ripples in the space-time metric which propagate at the speed of light, in this context better called *speed of gravity*.

The strong non-linearity of the Einstein equations makes them hard to solve exactly in presence of strong fields. Nevertheless in absence of analytical solutions, numerical methods are often developed to describe the GWs emitted.

However it is always possible to analyze the space-time geometry far away from the sources. Indeed these situations are characterized by weak gravitational fields, which allow us to treat them with a perturbative approach. In this case it consists in the application of the *linear approximation* (the same introduced in the Newtonian limit):

$$g_{\mu\nu}(x) \approx \eta_{\mu\nu} + h_{\mu\nu} + O(|h_{\mu\nu}^2|) \quad (1.11)$$

where we neglect higher order terms of $|h_{\mu\nu}| \ll 1$.

To simplify the expression we are going to consider harmonic coordinates.

1.2.1 Harmonic coordinates

In a Riemannian manifold a coordinate system is called **harmonic** if its coordinates satisfy $\square x^\mu = 0$, where \square is Laplace-Beltrami operator. This

operator consists in

$$\square = g^{\mu\nu} \left(\frac{\partial}{\partial x^\mu} \frac{\partial}{\partial x^\nu} - \Gamma_{\mu\nu}^\sigma \frac{\partial}{\partial x^\sigma} \right) \quad (1.12)$$

In Minkowski space it becomes

$$\square = -\frac{\partial^2}{c^2 \partial t^2} + \nabla^2$$

Therefore $\square x^\mu = 0$ means

$$g^{\mu\nu} \Gamma_{\mu\nu}^\sigma = 0 \quad (1.13)$$

In the linear approximation (i.e when $g_{\mu\nu} = \eta_{\mu\nu} + h_{\mu\nu}$) this coordinate property provides a useful relation between the second derivatives of the perturbation-matrix elements:

$$\frac{\partial^2 h}{\partial x^\nu \partial x^\mu} = 2 \frac{\partial^2 h_\mu^\beta}{\partial x^\nu \partial x^\beta} \quad (1.14)$$

To prove this equation we start approximating the Cristoffel coefficients :

$$\begin{aligned} \Gamma_{\alpha\beta}^\sigma &= \frac{1}{2} g^{\mu\sigma} \left(\frac{\partial g_{\mu\alpha}}{\partial x^\beta} + \frac{\partial g_{\beta\mu}}{\partial x^\alpha} - \frac{\partial g_{\alpha\beta}}{\partial x^\mu} \right) \\ &\approx \frac{1}{2} \eta^{\mu\sigma} \left(\frac{\partial h_{\mu\alpha}}{\partial x^\beta} + \frac{\partial h_{\beta\mu}}{\partial x^\alpha} - \frac{\partial h_{\alpha\beta}}{\partial x^\mu} \right) \end{aligned} \quad (1.15)$$

Thus the harmonic condition (1.13) becomes

$$\frac{1}{2} \eta^{\alpha\beta} \eta^{\sigma\mu} \left(\frac{\partial h_{\mu\alpha}}{\partial x^\beta} + \frac{\partial h_{\beta\mu}}{\partial x^\alpha} - \frac{\partial h_{\alpha\beta}}{\partial x^\mu} \right) = 0 \quad (1.16)$$

which means

$$\eta^{\alpha\beta} \left(\frac{\partial h_{\mu\alpha}}{\partial x^\beta} + \frac{\partial h_{\beta\mu}}{\partial x^\alpha} - \frac{\partial h_{\alpha\beta}}{\partial x^\mu} \right) = 0 \quad (1.17)$$

Developing this expression we obtain the relation:

$$\frac{\partial h}{\partial x^\mu} = 2 \frac{\partial h_\mu^\beta}{\partial x^\beta} \quad (1.18)$$

Finally, deriving this equation in terms of x^ν , we find the desired formula (1.14).

1.2.2 Linearized field equations

In this section we are going to derive the linearized form of the field equations (1.10). To provide these relations we start writing the approximations of the Ricci-tensor and of the scalar curvature in the weak field limit:

$$R_{\mu\nu} = -\frac{1}{2} \left(\square h_{\mu\nu} + \frac{\partial^2 h}{\partial x^\mu \partial x^\nu} - \frac{\partial^2 h_\nu^\beta}{\partial x^\mu \partial x^\beta} - \frac{\partial^2 h_\mu^\beta}{\partial x^\nu \partial x^\beta} \right) \quad (1.19)$$

$$R = -\square h + \frac{\partial^2 h^{\nu\beta}}{\partial x^\nu \partial x^\beta} \quad (1.20)$$

In light of the relation (1.14), the (1.19) formula becomes:

$$R_{\mu\nu} = -\frac{1}{2} \left(\square h_{\mu\nu} + \frac{\partial^2 h}{\partial x^\mu \partial x^\nu} - \frac{1}{2} \frac{\partial^2 h}{\partial x^\mu \partial x^\nu} - \frac{1}{2} \frac{\partial^2 h}{\partial x^\nu \partial x^\mu} \right) = -\frac{1}{2} \square h_{\mu\nu} \quad (1.21)$$

Now multiplying the (1.14) equation by the tensor $\eta^{\mu\nu}$ we obtain:

$$\eta^{\mu\nu} \frac{\partial^2 h}{\partial x^\mu \partial x^\nu} := \square h = 2\eta^{\mu\nu} \frac{\partial^2 h_\mu^\beta}{\partial x^\nu \partial x^\beta} \quad (1.22)$$

from which we have $\frac{\partial^2 h^{\beta\nu}}{\partial x^\nu \partial x^\beta} = \frac{1}{2} \square h$ and thus

$$R = -\frac{1}{2} \square h \quad (1.23)$$

Finally these relationships allow us to write the *linearized field equations* in the form:

$$-\frac{1}{2} \square \left(h_{\mu\nu} - \frac{1}{2} \eta_{\mu\nu} h \right) = \frac{8\pi G}{c^4} T_{\mu\nu} \quad (1.24)$$

Therefore defining

$$h'_{\mu\nu} = h_{\mu\nu} - \frac{1}{2} \eta_{\mu\nu} h \quad (1.25)$$

in harmonic coordinates, we have

$$G_{\mu\nu} = -\frac{1}{2} \square h'_{\mu\nu} \quad (1.26)$$

Moreover the calculation is performed in *Lorentz gauge*:

$$\frac{\partial h'_{\mu\nu}}{\partial x^\nu} = 0 \quad (1.27)$$

Summarizing the description of the GWs, emitted by a source characterized by an energy-momentum tensor $T_{\mu\nu}$, is performed by the following equations:

$$\begin{cases} \square h'_{\mu\nu} = -\frac{16\pi G}{c^4} T_{\mu\nu} \\ \frac{\partial h'_{\mu\nu}}{\partial x^\nu} = 0 \end{cases} \quad (1.28)$$

Instead the propagation of GWs in vacuum ($T_{\mu\nu} = 0$) is represented by

$$\begin{cases} \square h'_{\mu\nu} = 0 \\ \frac{\partial h'_{\mu\nu}}{\partial x^\nu} = 0 \end{cases} \quad (1.29)$$

which confirms GWs travel with velocity c .

1.2.3 Plane gravitational waves

The general solution of the equations (1.29) is a linear combination of plane waves:

$$h'_{\mu\nu} = \text{Re} \int A_{\mu\nu}(\mathbf{k}) e^{i(\mathbf{k}\cdot\mathbf{x} - \omega t)} d^3k \quad (1.30)$$

Here k is the wave 4-vector $k_\mu = (\frac{\omega}{c}, -\mathbf{k})$ and $A_{\mu\nu}$ is the *polarization tensor* which only depends on the wave 4-vector k .

The Lorentz Gauge assures the transverse property of the wave $k^\mu A_{\mu\nu} = 0$, while the equation $\square h'_{\mu\nu} = 0$ implies $k_\mu k^\mu = 0$ and thus the GW propagation at the speed of light.

Being symmetric the *polarization tensor* has 10 independent components, which are further reduced to 6 by the transverse property. Anyway we have to consider that the harmonicity of the system does not univocally define the coordinates. Indeed any transformation characterized by

$$\bar{h}_{\mu\nu} = h_{\mu\nu} - \frac{\partial \zeta_\mu}{\partial x^\nu} - \frac{\partial \zeta_\nu}{\partial x^\mu} \quad (1.31)$$

gives a relation between the perturbation-matrix elements different from (1.18) only for the presence of $\square \zeta_\mu$ which is zero (i.e. $\square \zeta_\mu = 0$) if we choose ζ_μ with a plane-wave behaviour. All these considerations show the tensor $h'_{\mu\nu}$ has only two independent terms (h_+ and h_\times), therefore we can choose a reference frame in which $h_{\mu\nu}$ has null time components and null trace. This coordinate frame is called **Transver-Traceless Gauge** (TT). Considering the wave-propagation on the z -axis, we find the only non-trivial components are h_{xx} , h_{xy} , h_{yx} and h_{yy} where x , y and z refers to the space directions. However these h terms are linked together by the metric tensor symmetry, $h_{xy} = h_{yx} \equiv h_\times$, and by the traceless property, $h_{xx} = -h_{yy} \equiv h_+$. The two defined quantities, h_+ and h_\times , are the amplitudes of the two **wave polarizations** “plus” and “cross”.

Thus we can describe this situation by a wave 4-vector

$$k = (k_0, 0, 0, k_z) \quad (1.32)$$

Here $k_0 := \frac{\omega}{c} = c\sqrt{(k_x)^2 + (k_y)^2 + (k_z)^2}$. Therefore in the *TT gauge* the perturbation-tensor can be written as:

$$h_{\mu\nu}^{TT} = \begin{bmatrix} 0 & 0 & 0 & 0 \\ 0 & h_{0+} & h_{0\times} & 0 \\ 0 & h_{0\times} & -h_{0+} & 0 \\ 0 & 0 & 0 & 0 \end{bmatrix} e^{-i\omega(t-z/c)} = \begin{bmatrix} 0 & 0 & 0 & 0 \\ 0 & h_+ & h_\times & 0 \\ 0 & h_\times & -h_+ & 0 \\ 0 & 0 & 0 & 0 \end{bmatrix} \quad (1.33)$$

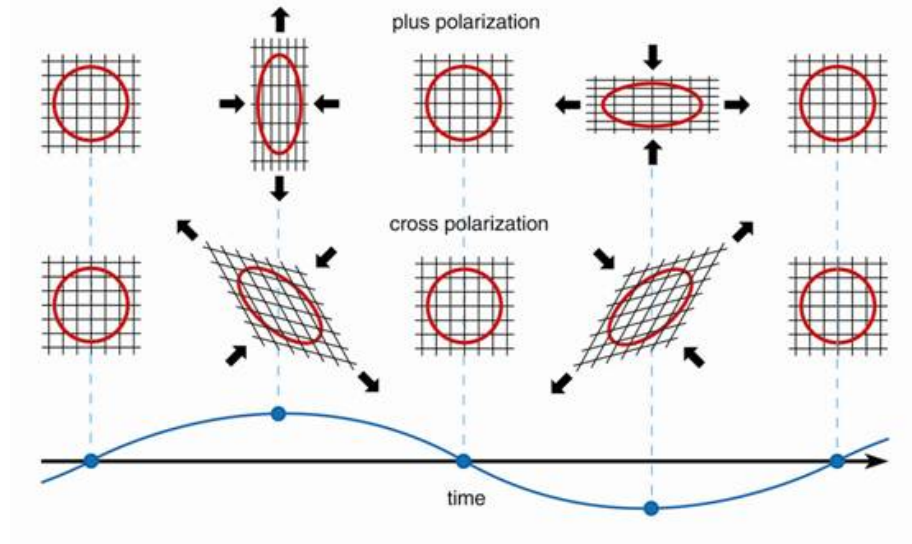


Figure 1.1: The picture represents the behaviour of a circle-mass in presence of a gravitational wave. On the top and bottom graphs are shown the evolutions produced respectively by the plus h_+ and cross polarization h_\times

1.2.4 GW radiation

In this section we will briefly see an estimate of some physical quantities involved in the GW detection. Inside GW sources the stress-energy tensor is different from zero and the field equations are reported in the formula (1.28). They are inhomogeneous differential equations which can be solved introducing the Green function. When the motions inside the source are not relativistic, the calculations show the components of the polarization tensor can be approximated by the **quadrupole formula**[6]

$$h_{ij}(t, r) = \frac{2G}{c^4} \frac{1}{r} \frac{\partial^2 I_{ij}}{\partial t^2} \left(t - \frac{r}{c} \right) \quad (1.34)$$

where r is the source distance and

$$I_{ij} = \int d^3x \mu(t, \mathbf{x}) \left(x^i x^j - \frac{1}{3} r^2 \delta^{ij} \right)$$

is the mass quadrupole moment tensor of the source ($\mu(t, \mathbf{x})$ is the source mass density). In this last equation the δ^{ij} is the Kronecker delta and the integral is calculated inside the source.

The equation (1.34) shows GWs are emitted by mass distributions of quadrupolar order which vary with time. Moreover the formula (1.34) reveals that the

GW amplitude is proportional to the quantity $G/c^4 \approx 5.6 \times 10^{-42} s^2 \cdot kg^{-1} \cdot m^{-1} \approx 2.8 \times 10^{-12} s^2 \cdot M_\odot \cdot m^{-1}$, this implies that only very massive bodies radiate non negligible GWs.

It is also possible to obtain an expression for power P radiated by a GW source

$$P = \frac{G}{5c^5} \left\langle \frac{\partial^3 I_{\mu\nu}}{\partial t^3} \frac{\partial^3 I^{\mu\nu}}{\partial t^3} \right\rangle \quad (1.35)$$

The impossibility to produce visible Gravitational waves in laboratories is therefore due to the factor $G/5c^5$, whose value is $\sim 10^{-53} W^{-1}$.

To better understand the involved quantities as example we can consider a rotating object with an asymmetry on the mass-distribution [5]. Assuming that its energy lost by GW emission is $E_{GW} \approx M_\odot \cdot c^2$ and that its distance is $r \approx 15 Mpc$ we obtain

$$h \approx 10^{-21}$$

According to what we will see in the following the resulting distance variation on a length of $L \approx 10^3 m$ is

$$\Delta L \approx \frac{1}{2} \tilde{h} L \approx 10^{-18} m$$

Finally considering the quantities involved we can provide also an estimate of the maximum frequency expected by a GW. Indeed the minimum radius permitted is the Shwarzshild one $R_S = 2GM/c^2$ and the maximum velocity is the speed of light. Considering orbiting celestial objects we have that the superior limit on the GW frequency is reached under these conditions and it is equal to

$$f_{max} = \frac{c}{2\pi R_S} = \frac{c^3}{4\pi GM} \approx 10^4 \frac{M_\odot}{M} Hz \quad (1.36)$$

1.2.5 GW effects on free bodies

The goal of this section is to describe the variation on the metric tensor in presence of a GW. In order to reach this aim we need to analyze its trajectory with respect to another body, indeed from the point of view of the coordinates it remains at rest. This is the reason why in this sections we are going to describe how the distance between two particles changes in presence of a GW.

Suppose to have two particles A and B moving on two near geodesics. The two bodies are characterized by their proper times τ and $\tau + d\tau$ and by an initial distance of δx_0^μ . To analyze the evolution of their distance δx^μ , the chosen local reference frame is related to the A mass, thus $\delta x^\mu(t) = x_B^\mu(t)$, where x_B^μ are the spatial coordinates of the B body. The distance evolution $\delta x^\mu(t) = \delta x_0^\mu + \delta x_1^\mu(t)$ is described by the *deviation geodesic equation* [4]

$$\frac{d^2 \delta x^\alpha}{d\tau^2} = R_{\beta\nu\mu}^\alpha \frac{dx^\beta}{d\tau} \frac{dx^\nu}{d\tau} \delta x^\mu \quad (1.37)$$

This relationship shows the relative acceleration between the two particles depends on the Riemann tensor. Therefore to acquire some information about the gravitational field this link can be very useful. Indeed the curvature tensor is strictly correlated to the second derivatives of the metric tensor and therefore, for weak gravitational field, of the perturbation-matrix. In the chosen reference frame the geodesic deviation in first approximation becomes:

$$\frac{d^2 \delta x_1^\mu}{d\tau^2} = \frac{1}{2c^2} \frac{\partial^2 h_k^{\mu(TT)}}{\partial t^2} \delta x_0^k \quad (1.38)$$

which has the following solution

$$\delta x^\mu(\tau) = \delta x_0^\mu + \frac{1}{2} h_k^{\mu(TT)} \delta x_0^k \quad (1.39)$$

For example if the GW propagates on the z-axis in the TT gauge we find the waveform described by the equation (1.33). The only non-zero components are $h_{11}^{TT} = -h_{22}^{TT} = h_+$ and $h_{12}^{TT} = h_{21}^{TT} = h_\times$. Thus at time t the coordinates of the B particle, seen by A, follow the formulas

$$\begin{cases} \delta x^0 = \delta x_0^0 + h_k^0 \delta x_0^k / 2 = \delta x_0^0 \\ \delta x^1 = \delta x_0^1 + h_k^1 \delta x_0^k / 2 = \delta x_0^1 + (h_1^1 \delta x_0^1 + h_2^1 \delta x_0^2) / 2 \\ \delta x^2 = \delta x_0^2 + h_k^2 \delta x_0^k / 2 = \delta x_0^2 + (h_2^1 \delta x_0^1 + h_2^2 \delta x_0^2) / 2 \\ \delta x^3 = \delta x_0^3 + h_k^3 \delta x_0^k / 2 = \delta x_0^3 \end{cases} \quad (1.40)$$

where with respect to the situation described by the formula (1.33) the perturbation matrix elements are $h_\nu^\mu = \eta^{\mu\sigma} h_{\sigma\nu}$. Therefore the equation (1.33) shows the oscillating behaviour of these distance. Finally an adimensional parameter can be used to measure the geodesic deviation expressed by the relation (1.39):

$$\tilde{h} = 2 \frac{\Delta L}{L_0} \quad (1.41)$$

where $\Delta L := \delta x^\mu - \delta x_0^\mu$ and $L_0 := \delta x_0^\mu$.

Chapter 2

Astrophysical sources

There are many theoretical predictions about GW emissions. The frequency range of these phenomena can vary a lot, owing to the different nature of the possible sources. Considering the temporal evolution of the signals, GWs can be divided in 3 main groups:

- **transient signals:** these signals are generally emitted during very violent events happening in the universe. The main feature of this kind of GWs is their short life-time, typical from few *ms* to some *s*. Their principal progenitors are *supernovae explosions* and *compact binary coalescences*;
- **periodic signals:** these GWs are characterized by a constant frequency, the main sources are the *neutron stars*, *the pulsars* and *the binary systems*;
- **stochastic signal:** this signal is created by the emissions of a large number of undefined sources. It represents a stochastic background of GWs and detect it can be useful for cosmological knowledges.

We are particularly interested in transient emissions characterized by a frequency range of few $10^2 - 10^3 \text{ Hz}$. In the following are described the main features of the principal topics of this category.

In the previous chapter we have seen the equations which characterize GWs and their propagations in vacuum. Now we are looking for possible GW sources; in particular here we will focus on core collapse supernovae (Section 2.1) and especially on compact binary coalescences (Section 2.2).

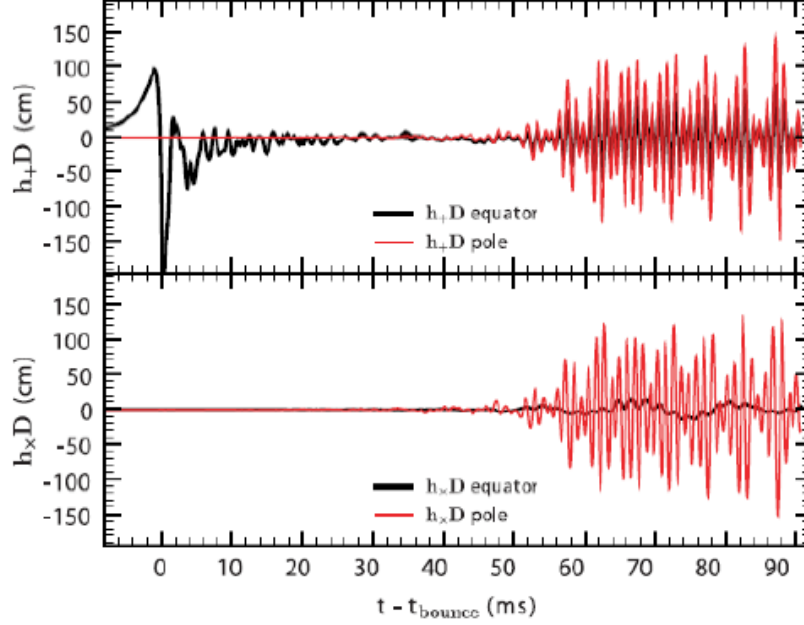


Figure 2.1: h_+ (top) and h_\times (bottom) multiplied by distance D as seen by observers along the equator (black) and along the pole (red) of the source for the model S20A2B4 from [20Marco]. Note that the GW burst signal from core bounce is purely axisymmetric, since an axisymmetric system has vanishing h_\times and vanishing GW emission along the axis of symmetry.

2.1 Core collapse supernovae

2.1.1 Origin

The **core collapse supernova** or **type II supernova** is a process which occurs in the final stage of a massive star. The star is characterized by different layers, some of which are still burning and therefore growing the core mass. Owing to this mass accretion the core reaches the Chandrasekar limit, becoming gravitationally unstable [7]. The core contracts, increasing its density and temperature. This process feeds the photodisintegration and the electron-capture so that even less electrons contrast the gravity action, causing a further contraction. The collapse is suddenly stopped thanks to neutrino reactions, creating a shock wave, which propagates outward the core throwing the external layers out. Therefore the shock blows up the star and a type II supernovae explosion happens. The resulting compact structure can be a neutron star or a black hole depending on the stellar mass.

2.1.2 Rate

Galacting type II supernovae are known to be rare; the estimates supported by indirect evidence (abundance of ^{26}Al whose main source are supernovae explosions) shows less than 1 event per two decades in Milky Way. Nevertheless recent review [8] recalls there may be ~ 1 supernova event per year between 3-5Mpc from Earth.

2.1.3 GW characteristics

The iron core collapse is one of the most energetic astrophysical processes known. It is calculated that $\sim 10^{53}\text{erg}$ is emitted during this event, but only $\sim 1\%$ becomes visible in the electromagnetic spectrum. The estimates of the energy emitted on GW form was recently reduced from an initial optimistic value of $\sim 10^{52}\text{erg}$ to a more realistic $\leq 10^{36}\text{erg}$ [9]. Its entity depends also on the mechanism which takes place during the collapse. Three main mechanisms are currently under studies: neutrino mechanism [10], magneto-rotational mechanism [11] and acoustic mechanism [12]. Anyway in terms of GW emission the most promising processes are the rotating collapse and bounce, non asymmetric rotational instabilities and proto neutron star pulsation. However several processes can contribute to the overall GW signature: anisotropic neutrino emission, global precollapse asymmetries in the iron core and surrounding burning shells, aspherical mass ejection, magnetic stresses and the late-time formation of black hole. Moreover the GWs emitted by core collapse supernova are characterized by a frequency range above 1kHz. The shape of the GWs obtained by such processes are not well defined. Even if complex simulations allow the extence of some moldels, they are characterized by a large uncertainty. For this reason, as generally happens for impulsive events of unknown shape, the GW strenght is expressed in term of “root sum squared”(rss) amplitude h_{rss}

$$h_{rss}(t) = \sqrt{\int |h(t)|^2 dt} \quad (2.1)$$

where $h(t)$ is a linear combination of the two wave-polarizations (we will see a better explanation later). Sometimes it's possible to convert this quantity in terms of energy depending on the adopted models. For core collapse supernova we can use this formula:

$$E_{GW} = \frac{r^2 c^2}{4\pi} (2\pi f_0)^2 h_{rss}^2 \quad (2.2)$$

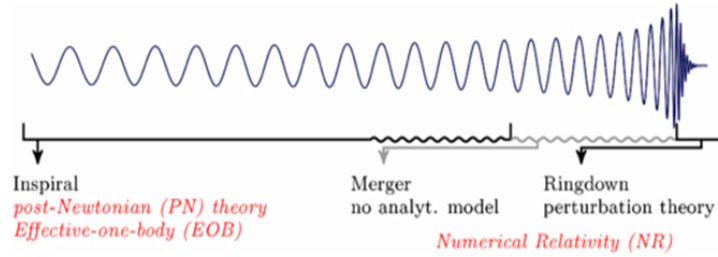


Figure 2.2: Typical strain behaviour in time for signal emitted by a compact binary coalescence.

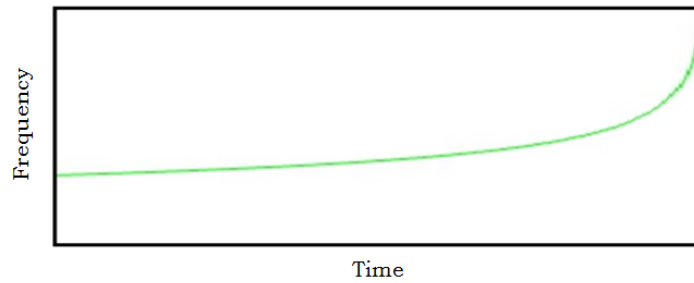


Figure 2.3: Typical frequency behaviour in time for signal emitted by a compact binary coalescence.

2.2 Compact binary coalescence (CBCs)

One of the most promising sources of impulsive GWs are coalescing compact binaries, whose recognition represents the main goal of this study.

2.2.1 Signal and phenomenon description

We are interested in the coalescence of three types of binary systems:

- systems formed by two neutron stars (**NS-NS**);
- systems formed by two black holes (**BH-BH**);
- mixed systems formed by a neutron star and a black hole (**NS-BH**)

NS-NS binaries are the only systems observationally tested [Faber, J.A. and Rasio, F.A., *Living Rev.Relat.* **15** (2012)], but the existence of the other two classes are supported by good arguments.

Mergers of a binary systems are generally related to the *short Gamma Ray Bursts (GRBs)*, which are powerful flashes of soft ($\sim MeV$) γ -rays. Since this type of rays are principally generated by the coalescence of a neutron star with another compact object (like a NS or a BH), they are considered a

signature of the GW emission. Not only they represent the electromagnetic counterpart of most promising sources of GWs, but they mark also different phenomena linked to GW radiation.

The binary systems are characterized by several physical properties, the main of which are:

$$M_{tot} = (m_1 + m_2), \quad \mu = \frac{m_1 m_2}{m_1 + m_2}, \quad q = \frac{m_2}{m_1} \leq 1, \quad (2.3)$$

$$M_{chirp} = \mu^{3/5} M_{tot}^{2/5} = \frac{(m_1 m_2)^{3/5}}{(m_1 + m_2)^{1/5}} \quad (2.4)$$

The coalescence of these compact objects can be divided in three different phases ¹:

- **the inspiral:** at the beginning the distance of the two bodies is much larger than their dimension. In this phase the system is in a non-relativistic regime. Even though the most general orbit is elliptical the losses of energy and angular momentum, due to GW emission, circularize it [13]. This process causes the two binary components get closer and the consequently beginning of the early-relativistic regime. This phase is well described by Post-Newtonian (PN) methods [14]. To the lowest PN order in the amplitude evolution, the emitted gravitational radiation can be written as [15]:

$$h_+(t) = - \frac{GM_{chirp}}{c^2 r} \left(\frac{t_c - t}{5GM_{chirp}/c^3} \right)^{-1/4} \times \left(\frac{1 + \cos(\iota)}{2} \right) \cos [2\phi_c + 2\phi(t - t_c; M_{tot}; \mu)] \quad (2.5)$$

$$h_\times(t) = - \frac{GM_{chirp}}{c^2 r} \left(\frac{t_c - t}{5GM_{chirp}/c^3} \right)^{-1/4} \times \cos(\iota) \cos [2\phi_c + 2\phi(t - t_c; M_{tot}; \mu)] \quad (2.6)$$

where r is the source distance, ι is the angle between the the normal to the orbit and the line-of-sight, $\phi(t - t_c; M_{tot}, \mu)$ is the orbital phase of the binary and finally t_c and ϕ_c are respectively the coalescence time and phase. The equations (2.5) and (2.6) show the signal amplitudes increasing with bigger values of M_{tot} and with the orbit decay. Moreover these formulas offer us the possibility to find circularly and linearly polarized GWs. The first case consists in the equivalence of the two polarization amplitudes $h_+(t) = h_\times(t)$, which occurs when $\iota = 0$. Instead linearized polarization happens when $\iota = \frac{\pi}{2}$ and h_\times vanishes. Other physically interesting properties of the binary motion

¹The following discussion concerns non-spinning binary components.

concerns the “innermost stable circular orbit”(ISCO), which limits the end of the inspiral phase and the beginning of the merger. The radius is approximately

$$R_{ISCO} = 3R_S = \frac{6GM_{tot}}{c^2} \quad (2.7)$$

where R_S is the Schwarzschild radius associated to the binary total mass. Considering the rough approximation given by the assumption of the Kepler-laws validity, from the equivalence between centripetal and gravitational forces we find

$$f_c^2 = \frac{GM_{tot}}{4\pi^2 R^3} \quad (2.8)$$

and thus for the ISCO orbit

$$f_{c|ISCO} = \frac{1}{2\sqrt{6}\pi} \frac{c^3}{GM_{tot}} \quad (2.9)$$

This equation shows the $f_{c|ISCO}$ increasing for smaller value of the total binary mass M_{tot} . The direct consequence is a longer duration of this signal phase above a given frequency. The typical “chirping”behaviour, which consists in the frequency and amplitude increasing with the orbit decay.

- **the merger:** When the binary reaches the ISCO orbit the merger begins. It happens under a fully-relativistic regime, where the velocities are comparable to the one of light c and the distance between the two components becomes similar to their dimensions. Under these conditions the PN methods fail and the best reconstruction of this stage is made by numerical solutions of the full field equations (1.10) in a highly dynamical strong field regime [16].
- **the ringdown:** This phase describes the relaxation of the resulting object toward a stable orbit. This process happens emitting a characteristic GW given by a superposition of damped sinusoids (quasi-normal modes QNM) [17]. The modes are defined by complex angular frequencies ω_{lm} , whose imaginary part represents the inverse of the damping-time and the real one the oscillating frequency. The most determinant mode for the signal waveform characterization is the fundamental mode, defined by $l = m = 2$. When the resulting object is a black hole all its properties are defined by its mass and spin, due to the **no hair theorem** [18]. The validity of this consideration concerns also the GWs, whose amplitude evolution can be written as:

$$h(t) = A \frac{GM}{c^2 r} e^{-\pi f_0 t / Q} \cos(2\pi f_0 t) \quad (2.10)$$

In this equation A is the amplitude of the mode, $f_0 = Re(\omega_{22})/2\pi$ is the oscillation frequency and $Q = \pi f_0 / Im(\omega_{22})$ is the quality factor.

Another interesting property of these systems is the relation between the orbital frequency ω and time t , which gives the attribute of “chirping” to these signals.

$$\omega(t) = \omega(t_0) \left[1 - \frac{256G^{5/3}\mu M^{2/3}t_c}{5c^5\omega(t_0)^{-8/3}} \right]^{-3/8} \quad (2.11)$$

To find this equation the Kepler law validity was assumed. Considering the initial time $t_0 = 0$, this formula shows the breakdown of the used approximation after a time:

$$t_c = \frac{5c^5}{256G^{5/3}\mu M^{2/3}\omega(t_0)^{8/3}} \quad (2.12)$$

which is the *coalescence time*. This expression of t_c can be rewritten in terms of GWs frequency ν_0 (twice the orbital frequency) which the wave has at $t = 0$:

$$t_c = \frac{5}{256} \frac{c^5}{G^{5/3}} \frac{(\pi\nu_0)^{-8/3}}{M_{chirp}^{5/3}} \quad (2.13)$$

Due to the equation (2.11) we can estimate the inspiral duration in a fixed frequency range $[f_l, f_u]$:

$$t_u - t_l = t_c(\nu_0) \left[\left(\frac{f_l}{\nu_0} \right)^{-8/3} - \left(\frac{f_u}{\nu_0} \right)^{-8/3} \right] \quad (2.14)$$

2.2.2 Rate

Because of the different evolution end born probability of the celestial objects which differ in masses, we have to distinguish the rate of the three classes of systems: NS-NS, NS-BH and BH-BH binaries. To be quantitative we have to introduce the instrument context. The first generation of interferometer-detectors has stopped the data acquisition in 2010. Now they are under developments which would, once reached the optimal operating condition, considerably improve the sensitivity curves. Moreover other detectors are instead under construction. All these instruments will become newly operative, starting from 2015 and they will constitute the *Advanced* or second generation **2G** of detectors(see chapter 2).

- **NS-NS binaries:** to obtain this quantity two different approaches can be applied; the *theoretical* one and the *empirical* one. The first is based on models of binary star formation and evolution. The rate found with the theoretical method can vary also of orders of magnitude, depending on the way they are calibrated. Considering star formation assumptions, low rates are estimated, while the evaluation on supernova events

in Milky Way gets higher rates. Differently the empirical method is based on the observations of binary systems which are thought to collide. These objects are visible only if at least a component is a pulsar. Therefore a factor corrects the result obtained by the direct observations, reaching a rate value of $Rate_{emp} \in 3 - 190 Myr^{-1} \times MWE G^{-1}$ where MWE G means Milky Way Equivalent Galaxy. The realistic NS-NS rate value is expected to be $Rate_{re} \approx 100 Myr^{-1} MWE G^{-1}$, but, owing to the large model uncertainties, we have to be careful with this estimate.

Concerning the rate of detectable coalescences for binary systems composed by two neutron stars, we can reduce its evaluation to the following relation

$$\rho = V_{BNS} \times \mathcal{R}_{MW} \times \rho_{gal} \quad (2.15)$$

where \mathcal{R}_{MW} is the merger rate in the ‘‘Milky Way equivalent galaxies’’, ρ_{gal} is the density of ‘‘Milky Way equivalent galaxies’’ and finally V_{BNS} is the observable volume. The latter quantity is calculated taking into account the maximum distance at fixed SNR (Signal to Noise Ratio) from which a GW source can emit a detectable signal. Anyway we have to underline that this distance depends on the GW radiation mechanism involved and consequently on the source physical properties.

Some studies [9] suggest for the network of the new generation of detectors, AdV and aLIGO, a realistic rate of NS-NS detectable coalescences of about 40 events/year which has to be compared with the 2 events/century of the first generation of interferometries.

- **NS-BH binaries:** any direct proof of the existence of NS-BH systems was discovered. Anyway following the current evolution theory this is probably due to practical difficulties for the identification of such systems. Even for these source class the rate can be calculated in two different ways; theoretically or empirically. To infer the NS-BH population through the first approach the same models applied to BNS (Binary Neutron Star) systems can be used. This method strongly depends on the assumption about the systems evolution. The obtained values for galactic mergers are: $Rate_p \in [0.06 - 0.11] Myr^{-1}$ and $Rate_o \in [3.2 - 4.8] Myr^{-1}$. Here we report respectively the most pessimistic and the most optimistic results.

The empirical approach is instead based on few observations of binaries with very massive components. They suggest that these systems are actually formed and that they are detectable by the second generation instruments. Anyway the predictions about the detection rates of these events can vary a lot, depending on the chosen strategy to perform the calculation. For what concerns the first generation interferometries the estimated number of events per year vary from few in

a thousand year to a more optimistic evaluation of one event every few years. Instead the Advanced GW detectors allow much more favorable predictions: $\sim 10 \text{ yr}^{-1}$ NS-BH mergers, which in the most optimistic case becomes $\sim 300 \text{ yr}^{-1}$.

- **BH-BH binaries:** also for this kind of objects does not exist any direct proof, anyway they are supported by the majority of the theories. Therefore to infer the population of these systems theoretical assumptions are needed. Also in this case the predictions are made starting from the observations or considering pure theoretical models. The first approach is based on the data concerning the NS-BH populations, through which the BH-BH binaries rate is inferred. For the same reason explained for the NS-BH systems the estimates coming from this procedure gives rise to large uncertainty. Even if also for the theoretical predictions the rate values can be very different, due to the various assumptions, we report two of these estimations about galactic events: $Rate_p \in [0.02 - 0.03] \text{ Myr}^{-1}$ and $Rate_o \in [7.7 - 11] \text{ Myr}^{-1}$ which represent respectively the most pessimistic and the most optimistic predictions.

The expected rate for the **2G** instruments is $\sim 20 \text{ yr}^{-1}$ BH-BH coalescences, but the most optimistic estimation allows $\sim 1000 \text{ yr}^{-1}$ detections.

[9] Estimations of the expectation rates obtained for the second generation of instruments are thus summarized in the following table (Tab. 2.1). [35]

System	Masses (M_{sun})	Range (Mpc)	expected detection rate for aLIGO		
			low (yr^{-1})	realistic (yr^{-1})	high (yr^{-1})
NS-NS	1.4/1.4	200	0.4	40	400
NS-BH	1.4/10	410	0.2	10	300
BH-BH	10/10	970	0.4	20	1000

Table 2.1: Predicted detection rates for aLIGO interferometers.

2.2.3 Simulations

As we said, the main purpose of these notes is the coalescence compact binaries recognition. To reach this goal we need simulations which mimic the expected GW signals coming from these sources. In the last years several models have been developed to describe the gravitational emission of the three stages which characterize these phenomena; they are called **IMR waveforms** (Inspirational Merger Ringdown). In this study we will consider the EOBNRv2 family [19]. The (EOBNR) is an acronym of “Effective One Body Numerical Relativity”, which introduces the assumptions used to model and test these waveforms. Binary systems are described by a generalization to

General Relativity of the center-of-mass frame provided by the Effective One Body (EOB) approach. These models are based on the description of the system dynamics through a particular external space-time metric. Here the binary can be treated as a test particle, whose motion information can be reconducted to the PN expansion. However here the information carried by this approach is resummed differently from the usual power expansion of v/c [20].

This approach for waveform reconstruction is based on the assumption of a negligible merger duration. Therefore the simulations consists in the inspiral and ringdown stages. However the EOB formalism exhibits accurate approximations of the both the waveforms. In view of the above, the gravitational waves emitted by coalescence binary systems are modelled in the following way:

$$h_{EOBNR}(t) = \theta(t_m - t)h_{i,p}(t) + \theta(t - t_m)h_r \quad (2.16)$$

where $\theta(t)$ is the Heaviside function, t_m the matching time and $h_{i,p}$, h_r are respectively the reconstructed amplitude evolutions of the inspiral-plus-plunge and of the ringdown phases. The EOBNR waveform family can be used to describe the emitted gravitational radiation by non-spinning binary components and its validity is tested by numerical-relativity (NR) simulations. In the following we are going to use subgroup of this family, called EOBNRv2. Here another approximation is applied. Indeed these waveform reconstruction includes for the ringdown phase only the fundamental mode, where $m = 2$ and $l = 2$.

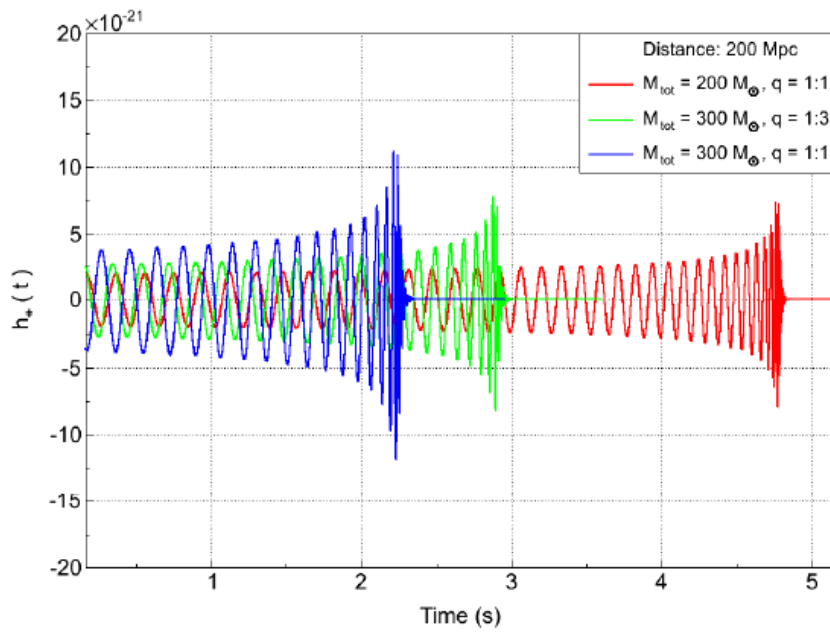


Figure 2.4: Plus polarization evolution in time $h_+(t)$ during the three main phases typical of the compact binary coalescence signals. Three curves are reported relative to three different combinations of the main simulation parameters: M the total mass and q the ratio between the two single components.

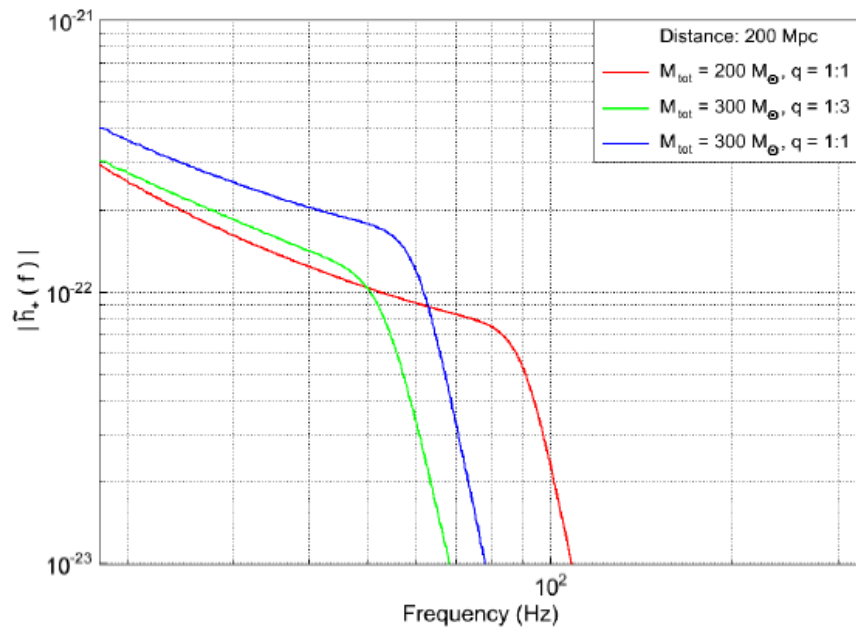


Figure 2.5: Plus polarization evolution in frequency $h_+(f)$ during the three main phases typical of the compact binary coalescence signals. Three curves are reported relative to three different combinations of the main simulation parameters: M the total mass and q the ratio between the two single components.

Chapter 3

LIGO-VIRGO detectors

Gravitational waves detection

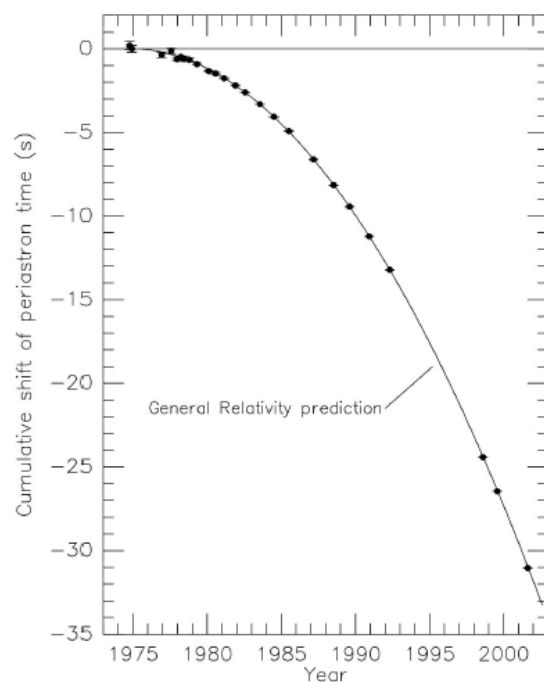


Figure 3.1: Timing results for the Hulse-Taylor binary pulsar PSR1913+16. The image shows the periastron shift caused by the decay of the orbit via emission of gravitational radiation

No direct evidence of GWs has been measured. Nevertheless an indirect proof of their existence was given in 1993 by R. Hulse and J. Taylor. In 1974 the two physicists discovered the binary system PSR1913+16 composed by two pulsars orbiting around each other. For about 20-years they

have studied the main properties of the pulsar binary and in particular they have measured its orbital period. Analyzing this quantity they realized that its reduction was in in good agreement with the GW emission, as predicted by GR. Indeed the experimental value of the time-revolution decrease is

$$-\frac{dP(s)}{dt} = (2.4211 \pm 0.0014) \cdot 10^{-12} s \cdot s^{-1} \quad (3.1)$$

while the GR predicts

$$-\frac{dP(s)}{dt} = (2.402531 \pm 0.000014) \cdot 10^{-12} s \cdot s^{-1} \quad (3.2)$$

[21] For this important contribution to the GR knowledges R. Hulse and J. Taylor earned the Nobel Prize in 1993 .

Nevertheless direct evidences of the GW properties are needed to confirm and test the general relativity and other alternative branches of the gravity theory. However a GW detection can bring even more interesting consequences indeed, since due to their very low cross-section with ordinary matter, they can carry information about the internal structure and physics of celestial bodies.

In this chapter we will illustate the principal GW detectors (Section 3.1), paying particular attention to the main detection principle of interferometry (Section 3.1.1). Thus we will focus on Virgo detector (Section 3.2) and its characteristic sensitivity (Section 3.2.1). Then we will breafly analyse the interferometer response (Section 3.3) and finally we will give a short overview on the second generation instruments (Section 3.4), specifically on the Virgo improvements (Section 3.4.1).

3.1 Gravitational wave detectors

In 1957 Joseph Weber began the attempts of a GW direct measurement, developing the first acoustic detector.

Nowadays two different classes of based-ground GW detectors are operating:

- resonant antennas;
- interferometers.

[22] [1] In 2015-2016, a new generation of advanced interferometers will start observations with unprecedented sensitivities. Experimental demonstrations of the feasibility of the space-based interferometer eLISA will be completed in the same time scale by the LISA Pathfinder mission. However, the time scale for the first observations by a space based gravitational wave detector is shifted beyond 2028.

DETECTORS	f(Hz)	TARGET SOURCES
Criogenic resonant bars (es. AURIGA, NAUTILUS)	$\approx 10^3$	Neutron stars; Supernovae;
Terrestrial interferometers (es. LIGO, VIRGO)	$\approx 30 - 5 \cdot 10^3$	Compact binary coalescences up to $10^3 M_{sun}$; Neutron stars; Supernovae; Gamma Ray Bursts;
Space interferometer eLISA/NGO	$\approx 10^{-4} - 10^{-1}$	Binary systems; Hypermassive black holes;

Table 3.1: Frequency-range and the main target sources of existing and planned of detectors.

Resonant antennas

These instruments are based on the acoustic oscillations induced in a cylindrical bar by the interaction with a gravitational wave. The motion is then measured and converted in electronic signals by a transducer mounted on the bar. Focusing on the fundamental longitudinal mode of the bar, it can be modeled as an equivalent oscillator made by two masses linked together by a spring. The presence of a GW opposes the internal elastic force. Considering the TT gauge and a GW with plus polarization along the bar axis with respect to the plus one, the system can be described by the equation:

$$\ddot{\xi}(t) + \omega_0^2 \frac{\xi(t)}{2Q} + \omega_0 \xi(t) = \frac{1}{2} l \cdot \ddot{h}_+(t) \quad (3.3)$$

Here $\xi(t)$ is the displacement of ω_0 is the bar natural frequency, and $Q = \tau\omega_0$ is the Q-factor. For a continuous wave with amplitude $h_+(t)$ frequency equal to the natural one this equation has an oscillating solution with amplitude $\xi_0 = \frac{Qh_+}{2}$, where $l = 4L/\pi^2$ and L is the bar length.

The dominating noise source close to the resonant frequency is Brownian or thermal noise, whose Power Spectral Density scales as $T/(MQ)$. This sets requirements on the operating temperatures, mass and quality factor of the oscillator. Best resonant detectors in operation are cooled to liquid Helium temperatures, have $Q \sim 10^6$ and masses $\sim 10^3 kg$. The detector has to be isolated from seismic environmental disturbances by means of mechanical suspensions.

At present the best acoustic detector performances are given by AURIGA located at Legnaro (Italy) [23] (see Fig. 3.2).

Its peak sensitivity, square root of the noise power spectral density, reaches about $\sim 1.5 \cdot 10^{-21} Hz^{-1/2}$ while its operative frequency range is approxi-

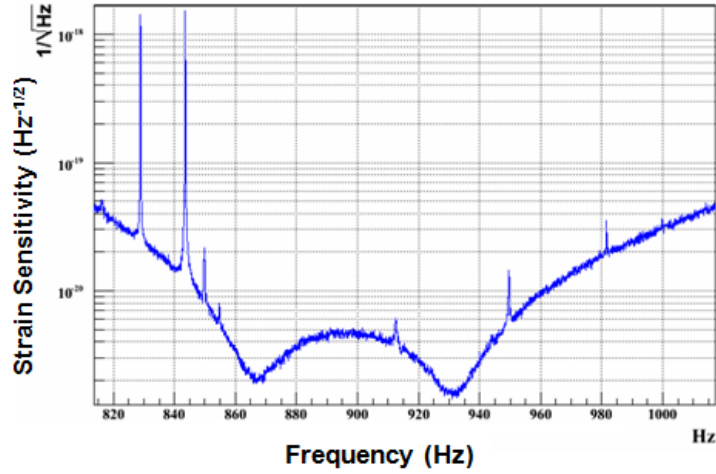


Figure 3.2: Auriga sensitivity 2006-2008 [24]

mately $(850 - 950) Hz$ where the sensitivity is under $6 \cdot 10^{-21} Hz^{-1/2}$. These characteristics limit the detectability to GWs emitted by very strong galactic sources which are expected to be rare ($\leq 1/century$). Despite the several efforts, the acoustic detectors are characterized by a limited sensitivity and a narrow frequency band in comparison with their successors.

Intereferometric detectors

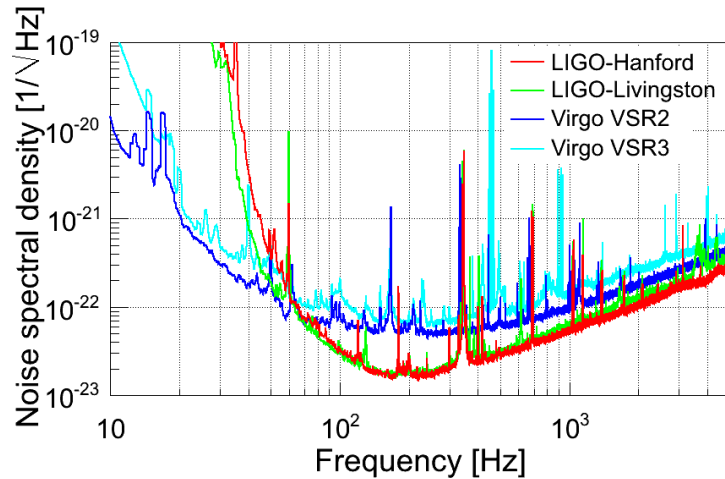


Figure 3.3: Ligo and Virgo sensitivity curves in the S6 run.

The second class of GW detectors are inspired by Michelson Morley in-

terferometer. A laser beam is splitted in two perpendicular optical paths, of approximately equal lengths L , defined by suspended mirrors acting as free-falling masses in the audio-frequency range ($\sim (30 - 5 \cdot 10^3)Hz$). A GW incoming perpendicularly to the detector plane with plarization axis along one arm causes opposite change in the arm lenght $\Delta L \approx \pm h_+ L$. Therefore the presence of a signal shifts the interference figure. The target signal amplitudes are very small $\frac{\Delta L}{L}$ smaller or at least $\approx 10^{-21}$, for this reason the arm lenght is as long as possible and this characteristic is determinant for the achieved sensitivity.

Past observations resulted in many upper limits on GW emission processes,

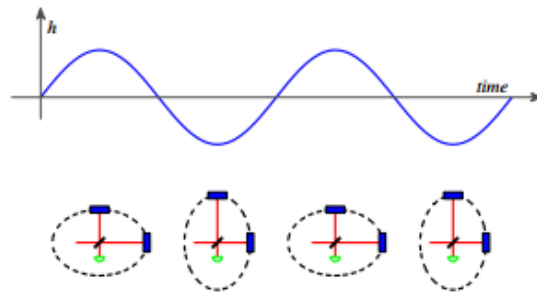


Figure 3.4: A GW traveling perpendicular to the plane of the diagram is characterized by a strain amplitude h . The wave distorts a ring of test particles into an ellipse, elongated in one direction in one half-cycle of the wave, and elongated in the orthogonal direction in the next half-cycle. This oscillating distortion can be measured with a Michelson interferometer oriented as shown. The length oscillations modulate the phase shifts accrued by the light in each arm, which are in turn observed as light intensity modulations at the photodetector (green semi-circle). This depicts one of the linear polarization modes of the GW.

and expectations are that the upcoming observation of the second generation of LIGO and Virgo detectors (so-called Advanced detectors) will eventually detect the first GWs in the next few years [25]. Virgo **V1** is a instrument placed in Cascina (Italy) and characterized by a arm lenght of $\sim 3Km$. LIGO, whose name is an acronym of Laser Interferometric Gravitational-waves Observatory, is now composed by 2 detectors with arm lenght $\sim 4Km$, one located at Livingstone (Lousiana) **L1**, the other at Hanford (Washington State) **H1**.

3.1.1 The basic principle of interferometry

[26]The paragraph (1.2.5) shows the necessity of a non local measurements to obtain information on the gravitational field. In interferometer detectors the test masses are the two mirrors at the end of each arm. A simple scheme

of an interferometer is represented in the picture (Fig. 3.5). The principal

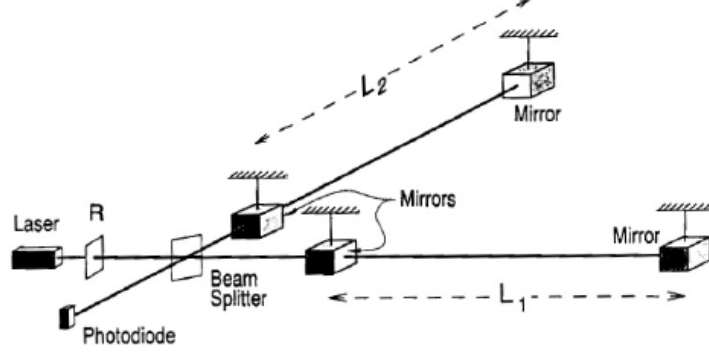


Figure 3.5: Schematic diagram of a laser interferometer GW detector

operating idea can be summarized in the following steps:

- **light injection and splitting:** a laser emits a beam divided in two perpendicular rays by a *beam splitter*;
- **light storage:** each ray is reflected by the mirrors at the end of the two arms, which also have the role of *test masses*;
- **light recombination and detection:** any displacement between the two test masses are acquired by a *photodetector*, which connects the interference figure with the different length traveled by the two rays.

Operating principle: absence of signal

We are going to discuss the behaviour of the light in a simplified Michelson-Morley interferometer whose scheme is represented in the following figure (Fig. 3.6). For simplicity we will analyze only the electric part of the electromagnetic radiation. For this simple analysis we consider the beam emitted by the laser as plane waves travelling in l_2 -direction

$$E_{in}(t, x) = E_0 e^{i(k_L x - \omega_L t)} e^{i\phi_{in}} \quad (3.4)$$

characterized by an angular frequency ω_L , by wavelength λ_L , by a wave vector $k_L = \frac{2\pi}{\lambda_L}$, by an initial phase ϕ_{in} and by an amplitude E_0 .

The beam splitter divides this beam in two orthogonal rays, whose amplitudes are proportional to its *amplitude transmissivity* t_{BS} ,

$$E_1(t, y) = t_{BS} E_{in}$$

or to its *amplitude reflectivity* r_{BS} ,

$$E_2(t, x) = i r_{BS} E_{in}$$

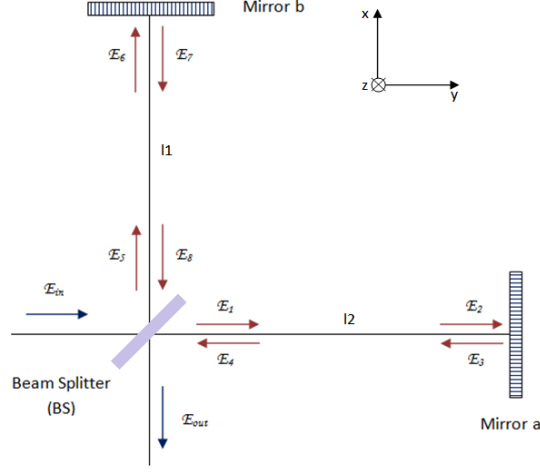


Figure 3.6: Schematic representation of the beams involved in the analysis.

depending on their direction (respectively l_2 and l_1). At the end of the arms both of them have acquired a phase proportional to the respective optical path i.e.

$$\begin{aligned} E_2(t, y) &= e^{ik_L l_2} E_1(t, y) \\ E_6(t, x) &= e^{ik_L l_1} E_5(t, x) \end{aligned} \quad (3.5)$$

Then the rays are partially reflected by the two mirrors a and b becoming

$$\begin{aligned} E_3(t, y) &= ir_a E_2(t, y) \\ E_7(t, x) &= ir_b E_6(t, x) \end{aligned} \quad (3.6)$$

Finally the resulting beams

$$\begin{aligned} E_4(t, y) &= e^{ik_L l_2} E_3(t, y) \\ E_8(t, x) &= e^{ik_L l_1} E_7(t, x) \end{aligned} \quad (3.7)$$

again in presence of the beam splitter, generate the detected light

$$E_{out}(t, x) = ir_{BS} E_4(t, x) + t_{BS} E_8(t, x) \quad (3.8)$$

In view of these considerations it is possible to calculate the power of the detected signal

$$P_{out} = P_{in} r_{BS}^2 t_{BS}^2 (r_a^2 + r_b^2) (1 + C \cdot \cos(2k_L \Delta l)) \quad (3.9)$$

Here P_{in} is the power of the incident beam E_{in} while $\Delta l = l_1 - l_2$ is the difference between the lengths of the two arms, which also corresponds to the

difference between the optical paths. Finally the constant C is the *contrast* of the interference figure, defined as

$$C = \frac{2r_a r_b}{r_a^2 + r_b^2} \quad (3.10)$$

As the useful light part for the detection is the output one E_{out} , we desire the mirror reflection coefficients r_a and r_b as possible near to one, to reduce the power losses. Therefore the closer C gets to 1, the better performances are reached by the interferometer.

Taking into account the formula (3.9) we can see that the phase which makes the detection possible is

$$\Delta\phi_{L_{noS}} = 2k_L \Delta l = 2\frac{2\pi}{\lambda_L} \Delta l \quad (3.11)$$

The working points of the LIGO-Virgo interferometers are set to *the dark fringe condition* i.e. the two beams interfere destructively. This configuration, which assures the maximum Signal to Noise Ratio, is reached when $\cos(\Delta\phi_{L_{noS}}) = -1$ which means:

$$\Delta\phi_{L_{noS}} = (2n + 1)\pi \quad (3.12)$$

Operating principle: presence of a signal with $\lambda_{GW} \gg \bar{l}$

This section concerns the effects produced on a interferometer by a GW. For this demonstrative exposition we consider the simplest case: a monochromatic plane wave, characterized by an angular frequency ω_{GW} and by a wave vector $k_{GW} = \frac{2\pi}{\lambda_{GW}}$, travelling orthogonally (z-direction) with respect to the interferometer plane. l_1 and l_2 are the arm lengths respectively in x and y direction. To visualize this system look at the picture (Fig. 3.6). We assume also that the GW has only the plus-polarization, therefore the interested waves can be described by the equation:

$$h_+(t, z) = h_{+0} e^{i(k_{GW}z - \omega_{GW}t)} = h_0(z) e^{-i\omega_{GW}t} \quad (3.13)$$

As described in the previous chapter, we are applying the linear approximation which substantially consist in the consideration of $g_{\mu\nu} = \eta_{\mu\nu} + h_{\mu\nu}$. Therefore the space-time interval fulfills the equation

$$\begin{aligned} ds^2 &= g_{\mu\nu} dx^\mu dx^\nu \\ &= [\eta_{\mu\nu} + h_{\mu\nu}(t)] dx^\mu dx^\nu \\ &= -c^2 dt^2 + (1 + h_+(t, z)) dx^2 + (1 - h_+(t, z)) dy^2 \end{aligned} \quad (3.14)$$

Considering two light-rays travelling respectively along the x -direction and the y -direction we obtain:

$$\begin{aligned} ds^2 &= -c^2 dt^2 + (1 + h_{+0} e^{i(k_{GW}z - \omega_{GW}t)}) dx^2 = 0 \\ ds^2 &= -c^2 dt^2 + (1 - h_{+0} e^{i(k_{GW}z - \omega_{GW}t)}) dy^2 = 0 \end{aligned} \quad (3.15)$$

In the following we will analyze in details the beam moving along the x-axis. In view of the previous equations we can calculate the time $\Delta\tau_x$ used by the light to complete its optical path, which consist in arrive at the mirror b and come back to the beam splitter.

$$\begin{aligned}\Delta\tau_x &= \tau_1 + \tau_2 \\ &= \int_0^{\tau_1} dt + \int_0^{\tau_2} dt \\ &= \frac{1}{c} \int_0^{l_1} \sqrt{1+h(z,t)} dt - \frac{1}{c} \int_{l_1}^0 \sqrt{1+h(z,t)} dt\end{aligned}\quad (3.16)$$

Considering weak fields $h(t, z) \ll 1$ the integrals can be approximated taking into account only the first two terms of Taylor expansion:

$$\Delta\tau_x \approx \frac{1}{c} \int_0^{l_1} \left(1 + \frac{1}{2}h(z,t)\right) dt - \frac{1}{c} \int_{l_1}^0 \left(1 + \frac{1}{2}h(z,t)\right) dt \quad (3.17)$$

Now we focus on GWs characterized by wavelenghts far greater than the arm lenghts, which consequently have a period much longer than the time needed to travel the arms. Under this condition the wave amplitude can be approximized as constant, therefore we consider $h(t, z) = h_+$. In view of this assumptions solving the integrals we find:

$$\begin{aligned}\Delta\tau_x &\approx \frac{2}{c} \left(l_1 + \frac{1}{2}h_+l_1\right) \\ &\approx \frac{2l_1}{c} + \frac{h_+l_1}{c}\end{aligned}\quad (3.18)$$

Similarly for the ray travelling along the arm in the *y-direction* we obtain

$$\begin{aligned}\Delta\tau_y &\approx \frac{2}{c} \left(l_2 - \frac{1}{2}h_+l_2\right) \\ &\approx \frac{2l_2}{c} - \frac{h_+l_2}{c}\end{aligned}\quad (3.19)$$

where the minus sign underlines that if in the *x-direction* (*y-direction*)the GW increases the arm lenght, in the orthogonal *y-direction* (*x-direction*) it is decreased. In light of these results the phase shift between the two perpendicular rays can be calculated. In order to obtain this quantity we have to find the temporal shift between the two beams when they come back to the beam splitter.

$$\begin{aligned}\Delta\tau &= \Delta\tau_x - \Delta\tau_y \\ &= \frac{2}{c} (l_1 - l_2) + \frac{1}{c} (l_1 + l_2) h_+\end{aligned}\quad (3.20)$$

From this equation we obtain the total difference between the two optical paths (concerning the round-trip of both the beams):

$$\begin{aligned}\Delta l_{tot(r-t)} &= c \cdot \Delta\tau \\ &= 2(l_1 - l_2) + (l_1 + l_2)h_+\end{aligned}\quad (3.21)$$

Therefore the resulting phase shift, from which depend the detected power, is

$$\begin{aligned}\Delta\phi_{LS} &= \omega_L \cdot \Delta\tau \\ &= k_L \cdot \Delta l_{tot(r-t)} \\ &= \frac{2\pi}{\lambda_L} [2(l_1 - l_2) + (l_1 + l_2)h_+]\end{aligned}\quad (3.22)$$

Referring to the formula (3.11) we can note that the presence of a GW adds to the original $\Delta l = l_1 - l_2$ an equivalence distance of

$$\Delta l_{GW} = \frac{1}{2} (l_1 + l_2) h_+ \quad (3.23)$$

indeed

$$\begin{aligned}\Delta\phi_{LS} &= \frac{4\pi}{\lambda_L} \left[l_1 - l_2 + \frac{1}{2} (l_1 + l_2) h_+ \right] \\ &= \frac{4\pi}{\lambda_L} (\Delta l + \Delta l_{GW}) \\ &= \Delta\phi_{L_{noS}} + 2k_L h_+ \bar{l}\end{aligned}\quad (3.24)$$

where we have introduced the arm length average $\bar{l} = \frac{l_1 + l_2}{2}$. This equation clearly shows that longer arms cause greater phase shifts. These considerations allow us to calculate the expected power detected by the photodiode in presence of gravitational signals

$$\begin{aligned}P_{out} &= a [1 + C \cdot \cos(\Delta\phi_{L_{noS}} + 2k_L h_+ \bar{l})] \\ &= a \{1 + C [\cos(\Delta\phi_{L_{noS}}) \cos(2k_L h_+ \bar{l}) + \sin(\Delta\phi_{L_{noS}}) \sin(2k_L h_+ \bar{l})]\} \\ &\approx a [1 + C \cdot \cos(\Delta\phi_{L_{noS}}) + C \cdot 2k_L h_+ \bar{l} \sin(\Delta\phi_{L_{noS}})]\end{aligned}\quad (3.25)$$

Here we have introduced the constant $a = P_{in} r_{BS}^2 t_{BS}^2 (r_a^2 + r_b^2)$.

The last relationship arises from the Taylor expansion of $\sin(\alpha) \sim \alpha$ and $\cos(\alpha) \sim 1$ in the limit of $\alpha \rightarrow 0$. Indeed we have considered the case of $h_+ \ll 1$, such that $2k_L h_+ \bar{l} \ll 1$.

Operating principle: presence of a general signal

In this section we will find the interferometer behaviour in function of the frequency through the description of a general gravitational signal, i.e. without making any assumption on its feature. To analyze this situation we have

to consider the GW shape dependence on the x and y coordinates. Before the two rays reflect at the mirrors a b , the GW phase is determined by the times:

$$\begin{aligned} t(x) &= \frac{x}{c} + t_0 \\ t(y) &= \frac{y}{c} + t_0 \end{aligned} \quad (3.26)$$

where t_x and t_y are the time used by the beams to reach the respective mirror, while t_0 is the time at the beginning of the measurements. Instead during the each travel from the respective mirror to the beam splitter, the GW phase is determined by the times:

$$\begin{aligned} t(x) &= \frac{l_1 - x}{c} + \frac{l_1}{c} + t_0 \\ &= \frac{2l_1 - x}{c} + t_0 \end{aligned} \quad (3.27)$$

$$\begin{aligned} t(y) &= \frac{l_2 - y}{c} + \frac{l_2}{c} + t_0 \\ &= \frac{2l_2 - y}{c} + t_0 \end{aligned} \quad (3.28)$$

Thus the time necessary for the two beams to follow their respective optical paths until their composition at the beam splitter are:

$$\Delta\tau_x = \frac{1}{c} \int_0^{l_1} \left(1 + \frac{1}{2} h_0 e^{-i\omega_{GW}t(x)} \right) dx - \frac{1}{c} \int_{l_1}^0 \left(1 + \frac{1}{2} h_0 e^{-i\omega_{GW}t(x)} \right) dx \quad (3.29)$$

$$\Delta\tau_y = \frac{1}{c} \int_0^{l_2} \left(1 - \frac{1}{2} h_0 e^{-i\omega_{GW}t(y)} \right) dy - \frac{1}{c} \int_{l_2}^0 \left(1 - \frac{1}{2} h_0 e^{-i\omega_{GW}t(y)} \right) dy \quad (3.30)$$

In view of the previous relations (3.26), (3.27) and (3.28) the integrals become

$$\Delta\tau_x = \frac{1}{c} \int_0^{l_1} \left(1 + \frac{1}{2} h_0 e^{-i\omega_{GW}\left(\frac{x}{c}+t_0\right)} \right) dx - \frac{1}{c} \int_{l_1}^0 \left(1 + \frac{1}{2} h_0 e^{-i\omega_{GW}\left(\frac{2l_1-x}{c}+t_0\right)} \right) dx \quad (3.31)$$

$$\Delta\tau_y = \frac{1}{c} \int_0^{l_2} \left(1 + \frac{1}{2} h_0 e^{-i\omega_{GW}\left(\frac{y}{c}+t_0\right)} \right) dy - \frac{1}{c} \int_{l_2}^0 \left(1 + \frac{1}{2} h_0 e^{-i\omega_{GW}\left(\frac{2l_2-y}{c}+t_0\right)} \right) dy \quad (3.32)$$

Therefore, solving the integrals, we obtain

$$\Delta\tau_x = \frac{2l_1}{c} + \frac{1}{2} \frac{h_0}{i\omega_{GW}} e^{-i\omega_{GW}t_0} \left(1 - e^{-i\omega_{GW}\frac{2l_1}{c}} \right) \quad (3.33)$$

$$\Delta\tau_y = \frac{2l_2}{c} + \frac{1}{2} \frac{h_0}{i\omega_{GW}} e^{-i\omega_{GW}t_0} \left(1 - e^{-i\omega_{GW}\frac{2l_2}{c}} \right) \quad (3.34)$$

Thus the temporal shift between the two rays is

$$\begin{aligned}\Delta\tau &= \Delta\tau_x - \Delta\tau_y \\ &= \frac{2}{c}(l_1 - l_2) + \frac{1}{2} \frac{h_0}{i\omega_{GW}} e^{-i\omega_{GW}t_0} \left(2 - e^{-i\omega_{GW}\frac{2l_1}{c}} - e^{-i\omega_{GW}\frac{2l_2}{c}} \right)\end{aligned}\quad (3.35)$$

From this equation we can calculate the total difference in the optical paths of the two beams

$$\begin{aligned}\Delta l_{tot(r-t)} &= c \cdot \Delta\tau \\ &= 2\Delta l + \frac{1}{2} \frac{h_0 c}{i\omega_{GW}} \left(2 - e^{-i\omega_{GW}\frac{2l_1}{c}} - e^{-i\omega_{GW}\frac{2l_2}{c}} \right)\end{aligned}\quad (3.36)$$

Assuming now the initial equality between the two arm lengths $l_2 = l_1 = l_0$ the previous equation becomes:

$$\begin{aligned}\Delta l_{tot(r-t)} &= \frac{h_0 c}{i\omega_{GW}} e^{-i\omega_{GW}t_0} \left(1 - e^{-i\omega_{GW}\frac{2l_0}{c}} \right) \\ &= 2 \frac{h_0 c}{\omega_{GW}} e^{-i\omega_{GW}\left(t_0 + \frac{l_0}{c}\right)} \sin\left(\frac{\omega_{GW}l_0}{c}\right)\end{aligned}\quad (3.37)$$

From which we can easily obtain the total phase shift in presence of a general signal

$$\begin{aligned}\Delta\phi_{LS} &= k_L \cdot \Delta l_{tot(r-t)} \\ &= \frac{4\pi}{\lambda_L} h_0 l_0 e^{-i\omega_{GW}\left(t_0 + \frac{l_0}{c}\right)} \frac{\sin\left(\frac{\omega_{GW}l_0}{c}\right)}{\frac{\omega_{GW}l_0}{c}}\end{aligned}\quad (3.38)$$

Finally under this assumption of equality between the two arm lengths we find the power detected at the output of the interferometer

$$P_{out} = a \left[1 + C \cdot \cos\left(2k_L h_0 l_0 e^{-i\omega_{GW}\left(t_0 + \frac{l_0}{c}\right)} \frac{\sin\left(\frac{\omega_{GW}l_0}{c}\right)}{\frac{\omega_{GW}l_0}{c}} \right) \right]\quad (3.39)$$

Taking into account this last relation we can understand that the instrument response depends on the signal frequency. Indeed there exist a cutoff frequency, given by the equation

$$\omega_{cutoff} = \frac{2\pi c}{l_0}\quad (3.40)$$

As shown by the relation (3.40) this critical frequency correspond to the time needed by the light to follow each arm. Signals with frequency greater than this value provoke an attenuate instrument response. Moreover from (3.38) we can also note that the interferometer is blind for signals which are characterized by an angular frequency multiple to this cutoff value, due to the null phase shift. This behaviour is well shown by the picture (Fig. 3.7).

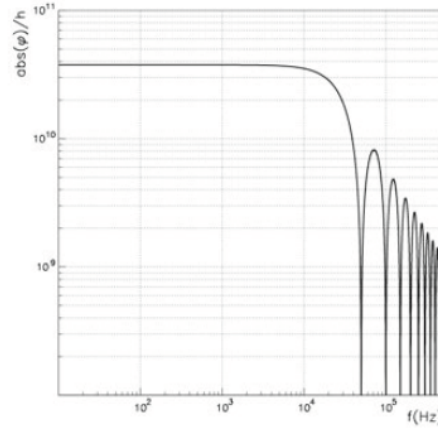


Figure 3.7: Frequency response of an interferometer characterized by arm lengths of 3 km and by a laser wavelength of $\lambda_L = 1064 \text{ nm}$

Necessary improvements

The simple configuration explained in this paragraph is very different with respect to the real one. Several external devices are introduced to improve the performances and reduce the noises. In particular all the most performing interferometric detectors have:

- **Fabry-Perot cavities**

As showed in the previous paragraphs, a GW provokes a displacement between the two test masses dependent on their initial distance. This is the reason why the physical arms of these detectors are as long as possible. Anyway the arm lengths are limited by physical constrains, like the Earth curvature, (nature, human activity and so on). Therefore to increase the optical path between the two test masses, and thus to improve the instrument sensitivity, Fabry-Perot cavities are introduced.

A Fabry-Perot cavity is composed by two mirrors set at l_0 distance and characterized by reflecting coefficients r_1 and r_2 . Through the introduction of this device the effective length of the arms are amplified by a factor $\frac{2\mathcal{F}}{\pi}$, i.e.

$$l_{eff} = \frac{2\mathcal{F}}{\pi} l_0 \quad (3.41)$$

where

$$\mathcal{F} \approx \pi \left(\frac{\sqrt{r_1 r_2}}{1 - r_1 r_2} \right) \quad (3.42)$$

is the *Finesse* of the Fabry-Perot cavity. Consequently also the ratio between the phase shift produced by the interferometer with and without the Fabry-Perot cavities is equal to $\frac{2\mathcal{F}}{\pi}$. For the Virgo case

$r_1 \sim 0.88$ and $r_2 \sim 0.99$ therefore, for the equation (3.42), the finesse is equal to $\mathcal{F} \sim 140$ and the increasing sensitivity factor is $\frac{2\mathcal{F}}{\pi} \sim 90$. Considering an initial distance between each of the test masses and the beam splitter of 3 km the resulting effective length of each arm is $l_{eff} \sim 270 \text{ km}$.

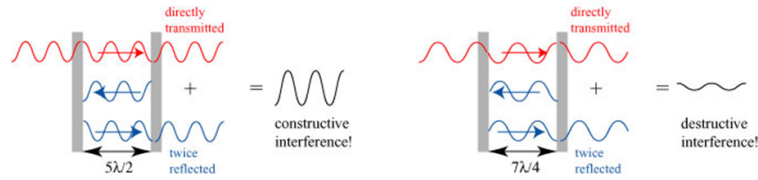


Figure 3.8: Light in a Fabry Perot cavity

- **Power Recycling mirror**

As we will see the optimal incident power is greater than the one of the interferometer. To mitigate the consequences of this choice (also imposed by practical limits) a recycling cavity is used in order to amplify the incident power. Indeed set the destructive interference as working point provokes a big lost in terms of light, due to its almost totally reflection to the laser. This expedient consists in the introduction of a semireflective mirror, the *power recycling mirror*, between the laser and the beam splitter. In this way the incident power is increased by a gain G_{PR}

$$G_{PR} \approx \frac{t_{rm}^2}{(1 - r_{rm}r_{int})^2} \quad (3.43)$$

This equation shows the dependence of the gain on the optical characteristics reflectivity and transmissivity, of the recycling mirror r_{rm} and t_{rm} and of the total inereferometer r_{int} . Obviously additional limits on the gain value are due to the optical losses, anyway if they are less than 2% the resulting gain is $G_{PR} \approx 50$ [27].

- **Super attenuator**

Another important noise source is the the seismic noise produced by geology and human activity. To reduce the movements of the test masses provoked by these phenomena is introduced the *super attenuator*. It is composed by 5 mechanic *standard filters* (see the paragraph 3.2.1) and its aim is to lessen the test masses vertical, horizontal and torsional movements of the test masses due to the soil motion. The filters consist on steel cilindrs linked together by different cables, special springs and systems of antisprings. In this way the vibrations are weakened by a chain of oscillators. The superattenuator is hung on a

system composed by three bars and is called *inverted pendulum*

3.2 Virgo

Virgo is a project designed and developed by an Italian-French collaboration and its name is inspired by the nearest rich galaxy cluster. Indeed the Virgo Cluster is about $\sim 15 \text{ Mpc}$ from the Earth and is composed by $\sim (1.5-2) \cdot 10^3$ galaxies. Taking into account the probably best known GW source, the coalescence of neutron star binary system, we desire to have a sensitivity of about $10^{-21} \text{ Hz}^{-1/2}$ to detect these kind of signals coming from the Virgo Cluster. Indeed they would have a strain of the order $h \approx (10^{-21} - 10^{-22}) \text{ Hz}^{-1/2}$ in a range of about $30 - 5 \cdot 10^3 \text{ kHz}$, which is exactly the interested range of frequency of the interferometric detectors.

Virgo detector

The main components of the three detectors are previously described in the paragraph (3.1.1). Here we focus on the main properties and working principle of the Virgo interferometry.

The laser light is shifted in frequency by modulation-demodulation tech-

λ_L (nm)	P_{in} (W)	l_0 (Km)	G_{PR}	p_{arms} (mbar)
~ 1064	~ 20	~ 3	~ 50	$\sim 10^{-10}$

Table 3.2: Main property of Virgo interferometry: λ_L is the laser wavelength, P_{in} is the light power, l_0 is the arm length, G_{PR} is the Power Recycling gain and finally p_{arms} is the vacuum preseny in the arms.

niques at 6 MHz and 14 MHz . Then the beam enters in the arm cavities, where the pressure is lowered to $\sim 10^{-10} \text{ mbar}$, forming the largest vacuum chamber in Europe [29]. Before the light is transmitted and reflected by the Beam Splitter its fundamental mode is selected by a *mode cleaner*. After these stabilization techniques, the light passes through the Power Recycling mirror and finally through the Beam splitter. This element splits the light in two perpendicular rays which follows the interferometer West and North arms. Here they enter in the Fabry Perot cavities which extend both the optical paths, increasing the sensitivity. The expedients adopted provide a circulating power in the instrument of few tens of kW .

This operating principle, with the main devices, is summarized by the picture Fig. 3.9.

To maintain the Virgo detector in the *dark fringe* working point, it is necessary to precisely control the test masses and the interferometer motion.

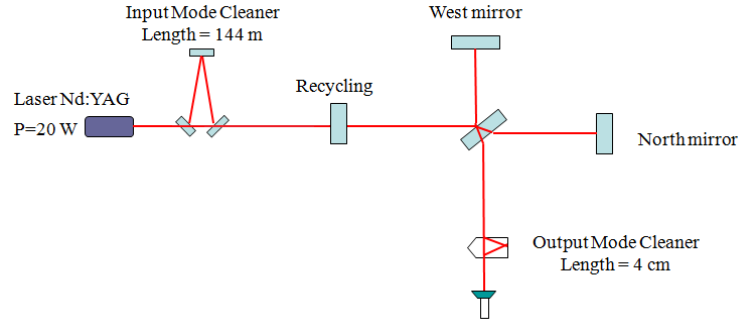


Figure 3.9: Virgo optical scheme

To reach this supervision and to consequently regulate the devices position a dumping active procedure is used. Some accelerators are located on the superattenuator system and on the ring which collect the three legs of the inverted pendulum. These devices measure the test masses horizontal, vertical and torsional acceleration. This information is used to move the suspension point with a low frequency movements, applying a small force on the joints. Finally with the superattenuator system a last suspension step is introduced to reduce the seismic noise and mainly to command the mirror position. The main component of this phase is the *marionetta* which is connected to the attenuator system by a steel cable. It is composed by a central body and four arms endowed with magnets and with coils. This system allows the mirror movements and alignment.

3.2.1 Virgo noise

In the following we describe the noise sources of the Virgo detector, which limit the GWs detection.

In an interferometer any noise can be described as real or apparent displacements of the mirror, which causes a non-null signal to the photodetector. In this section we treat the noise as a stationary and gaussian stochastic process. These assumptions allow us to describe the involved processes with low order approximations (gaussianity) and using the frequency domain (stationary). Therefore the noise phenomena can be usefully studied through their spectral density. Indeed this representation underlines their roles in the interferometer sensitivity.

Considering $h(t)$ the temporal series provided by the detector, we can define the following quantity

$$A(f) = \lim_{T \rightarrow \infty} \left| \frac{1}{T} \int_{-T/2}^{T/2} h(t) e^{-i2\pi ft} dt \right| \quad (3.44)$$

Therefore the resulting one-sided power spectral density can be written as

$$S_h(f) = |A(f)|^2 + |A(-f)|^2 = 2|A(f)|^2 \quad (3.45)$$

Therefore we can call amplitude spectral density $h(f)$ the square root of this quantity (Fig. 3.3):

$$h(f) = \sqrt{S_h(f)} \quad (3.46)$$

[28]

Seismic noise

At low frequency the data capture is perturbed by several noise sources due to human activities and to natural phenomena. In the range $\approx (1-10)$ Hz the main measurements perturbations are related to traffic, train passage, winds ecc.. [30]. These processes can be represented in the seismic noise spectrum as a decreasing power law, describing the frequency range $\approx (1-10)$ Hz. Anyway the main picks are produced by the ocean wave period (12s-24s). In Virgo the seismic noise behaviour, at the very low frequency, can be described through the plot displacements $x_{seis}(f)$:

$$|x_{seis}(f)| \left[m/\sqrt{Hz} \right] = \begin{cases} 10^{-10} f^{-3}, & \text{if } f < 0.05 \text{ Hz} \\ 10^{-6}, & \text{if } 0.05 \text{ Hz} < f < 0.3 \text{ Hz} \\ 10^{-7} f^{-2}, & \text{if } f > 0.3 \text{ Hz} \end{cases} \quad (3.47)$$

This value would correspond to an equivalent amplitude spectral density of

$$h_{seis}(f) = \frac{10^{-9}}{f^2} Hz^{-1/2} \quad (3.48)$$

However this noisy effect is lowered by the superattenuator introduction. Indeed the impact of seismic vibrations on the measurements can be drastically decrease hanging the test mass to a pendulum by a steel cable l_c long. Considering the superattenuator transfer function $H(f)$, the sensitivity can be described by the following relation

$$h_{seis}(f) = \frac{2}{l_0} H(f) \sigma |x_{seis}(f)| \quad (3.49)$$

where σ is the coupling constant between the horizontal and vertical notions of the superattenuator, whose value is around $\sim 10^{-2}$. This formula shows that $h_{seis}(f)$ strongly depends on the superattenuator transfer function, which in the frequency range $f \gg f_0$ can be approximated by

$$H(f) \approx \left(\frac{f_0}{f} \right)^{2N} \quad (3.50)$$

where N is the number of filters and $f_0 = \frac{1}{2\pi} \sqrt{\frac{g}{l_c}}$ is the resonance frequency. It was decided $N = 5$ to reach the desired sensitivity $h(f) = 10^{-21} Hz^{-1/2}$ at a frequency of $f = 10 Hz$ starting from an initial value (in absence of the superfilter) of $h(f = 10 Hz) \approx 10^{-11} Hz^{-1/2}$ (in agreement with the formula (3.48)).

Thermal noise

The thermal noise is the main limit for the GWs detection in the frequency interval $\approx (5 - 300) Hz$. This is due to the operating conditions of the interferometer components, which indeed work at the environmental temperature. The consequently fluctuation properties of the system are strictly linked to its dissipative processes. Under the assumptions of the system linearity and of its thermodynamic equilibrium this relation is described by the *Fluctuation and dissipation theorem*. Thanks to this theorem we are able to describe the macroscopic thermal noise without analyzing any microscopic processes involved in the dissipation, but simply describing it through a macroscopic impedance $Z(f)$.

Indeed the fluctuation-dissipation theorem states that the power spectrum of a force $F_{therm}^2(f)$ is

$$F_{therm}^2(f) = 4K_B T Re(Z(f)) \quad (3.51)$$

Here K_B is the Boltzmann constant, T the environmental temperature and $Re(Z(f))$ the real part of the system impedance.

Adopting an adequate model, this theorem permits to find a relationship between the mirror movements and the amplitude spectral density due to the thermal noise [32]

$$h_{therm}(f) = \frac{1}{l_0} \sqrt{x_p(f)^2 + x_m(f)^2 + x_{vm}(f)^2} \quad (3.52)$$

where the terms $x(f)$ are power spectral density related to the mirror displacement, whose main causes are:

x_p : thermal pendulum motion;

x_m : normal modes provoked by the thermal noise of the mirrors;

x_{vm} : violin mode, associated to the vibrational modes of the suspension wires which link the marionetta to the mirror.

Shot noise

The GWs detection is realized measuring the power variations at the photodiode provoked by the optical path difference along the North and the West

arms. For this reason any phenomenon which influences the light power can increase the noise on the data. Therefore to optimize the instrument sensitivity we have to minimize the power variations caused by processes different from the GW transit.

The power measured in a temporal interval τ at the interferometer output can be described in terms of average energy \bar{E} carried by the photons and therefore as function of the laser physical properties

$$P_{out} = \frac{\bar{E}}{\tau} \eta = \frac{\bar{N} \hbar \omega_L}{\tau} \eta \quad (3.53)$$

where \bar{N} is the average of the photon number detected by the photodiode and η its quantum efficiency.

Because of the Poisson distribution of the photon number, the standard deviation of this quantity can be written as:

$$\Delta N_{shot} = \sigma_N = \sqrt{\bar{N}} = \sqrt{\frac{P_{out} \tau}{\hbar \omega_L \eta}} \quad (3.54)$$

where the last equation arises from the formula (3.53). In view of the above (3.53) and (3.54), the power fluctuation results

$$\Delta P_{shot} := \left| \frac{\partial P_{out}}{\partial \bar{N}} \right| = \sqrt{\frac{P_{out} \hbar \omega_L}{\tau} \eta} \quad (3.55)$$

Assuming an interferometer characterized by a beam splitter with $r_{BS} = t_{BS} = 1/\sqrt{2}$, and by mirrors with $r_1 = r_2 = 1$ we find

$$P_{out} = \frac{P_{in}}{2} (1 + \cos \Delta \phi_{noS}) \quad (3.56)$$

Under these conditions a GW produces a change in the detected power of

$$\begin{aligned} P_{out} (\Delta \phi_{noS} + \Delta \phi_S) &= P (\Delta \phi_{noS}) + \frac{\partial P_{out}}{\partial \Delta \phi_{noS}} \Delta \phi_S \\ &= P (\Delta \phi_{noS}) - \frac{P_{in}}{2} \sin(\Delta \phi_{noS}) \Delta \phi_S \\ &= P (\Delta \phi_{noS}) + \Delta P_{GW} \end{aligned} \quad (3.57)$$

Therefore considering the best instrument configuration, given by the dark-fringe condition ($\Delta \phi_{noS} = \pi$), the value at which the signal matches the noise (SNR=1):

$$\left| \frac{\Delta P_{GW}}{\Delta P_{shot}} \right| = \frac{\frac{P_{in}}{2}}{\sqrt{\frac{P_{in}}{2} \frac{\hbar \omega_L}{\tau} \eta}} \frac{\sin(\Delta \phi_{noS})}{\sqrt{1 + \cos(\Delta \phi_{noS})}} \Delta \phi_S = 1 \quad (3.58)$$

From this equation we can infer that the phase shift for SNR equal to one is

$$\begin{aligned}\Delta\phi_S (\Delta\phi_{noS} = \pi) &= \Delta\phi_{Smin} \\ &= \sqrt{\frac{2\hbar\omega_L}{P_{in}\tau}} \eta \frac{1}{\sqrt{2}} \\ &= \sqrt{\frac{\hbar\omega_L}{P_{in}\tau}} \eta\end{aligned}\quad (3.59)$$

Indeed the phase shift between two orthogonal light beams is a key physical quantity in an interferometric GW detector. Moreover it offers the possibility to make a comparison between this result and the limit imposed by the Heisenberg indetermination principle

$$\Delta\phi\Delta N \leq \frac{1}{2} \quad (3.60)$$

where N is the number of photons detected by the photodiode. Now using the previous equations (3.54) and assumption (3.56) we obtain the indetermination on the $\Delta\phi$

$$\Delta\phi > \frac{1}{2} \sqrt{\frac{2\hbar\omega_L}{P_{in}\tau (1 + \cos(\Delta\phi_{noS}))}} \eta = \frac{1}{2} \sqrt{\frac{\hbar\omega_L}{P_{in}\tau}} \eta := \phi_H \quad (3.61)$$

Therefore

$$\Delta\phi_{Smin} \sim 2\phi_H \quad (3.62)$$

This equation shows that the phase shift, at SNR equal to one, is just twice the limit phase shift imposed by the Heisenberg indetermination principle. The previous analysis can be used to find the amplitude spectral density due to the shot noise. Indeed a GW produces a phase shift of

$$\Delta\phi_S = \frac{4\pi}{\lambda_L} \Delta l_{GW} \quad (3.63)$$

with $\Delta l_{GW} = hl_0$. In view of these considerations we have

$$\Delta\phi_{Smin} = \frac{4\pi}{\lambda_L} \frac{h_{shot}}{\sqrt{\tau}} l_0 \quad (3.64)$$

and finally

$$h_{shot} [Hz^{-1/2}] = \frac{\lambda_L}{l_0 4\pi} \sqrt{\frac{\hbar\omega_L}{P_{in}}} \eta \quad (3.65)$$

This relation reveals an indirect proportionality between the h_{shot} and the product $l_0\sqrt{P_{in}}$, thus increasing this latter quantity the shot noise can be reduced.

Radiation Pressure Noise

Also the Radiation Pressure noise has origin in the photon statistical fluctuations. Indeed when the laser light hits a mirror, it produces a force which moves the test mass in a new position. Anyway the main source of noise coming from this mechanism remains the fluctuations, because they can not be easily opposed. Considering an incident power P_{in} and a mirror with mass m , the spectrum of the test mass displacement is given by the formula

$$x_{rad}(\omega) = \frac{2}{\omega^2 m} \sqrt{\frac{2\pi\hbar P_{in}}{c\lambda_L \tau}} \eta \quad (3.66)$$

Thus the amplitude spectral density becomes:

$$h_{rad}(\omega) = \frac{2}{\omega^2 m l_0} \sqrt{\frac{2\pi\hbar P_{in}}{c\lambda_L}} \eta \quad (3.67)$$

Therefore also in this case the noise can be reduced increasing the arm length l_0 , but in opposite to the shot noise behaviour an improvement on the instrument sensitivity can be obtained lowering the input power.

Quantum noise limit

The last two paragraphs illustrate the different dependence on the input power of the noises originated by photon fluctuations. Therefore an optimal power value has to be provided. This would represent a compromise between the two involved processes, and therefore can be found equaling the two amplitude spectral density (3.65) and (3.67). The result obtained is:

$$P_{opt} = \frac{\pi c \lambda_L m f^2}{2} \quad (3.68)$$

Substituting this equation in one of the previous relationships (3.65) or (3.67) we obtain the correspondent sensitivity:

$$h_{ql} = \frac{1}{2\pi f l_0} \sqrt{\frac{\hbar}{m}} \eta \quad (3.69)$$

When this condition is satisfied the, so called, *quantum limit* is reached. In Virgo case $\lambda_L \approx 1\mu m$, therefore the optimal value of the laser power is

$$P_{opt}(f) \approx 10^4 f^2 W \quad (3.70)$$

This relation shows that the optimal power can not be reached in determined frequency ranges, indeed $P_{opt}(f = 10Hz) \approx 1 MW$.

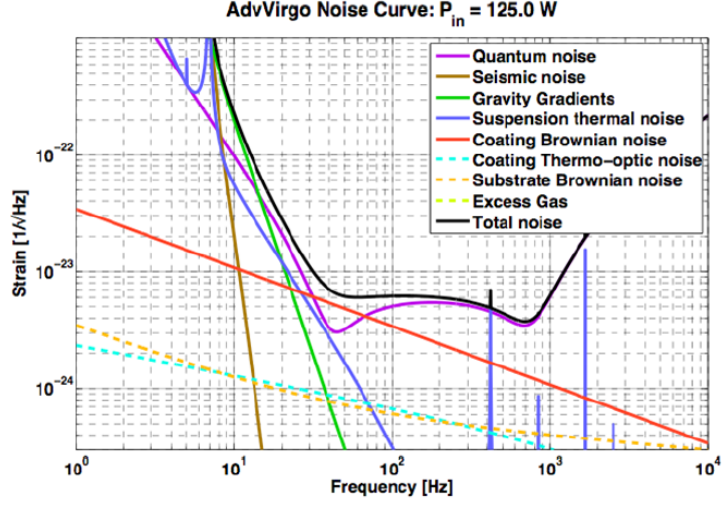


Figure 3.10: Different noise impacts predicted for AdvVirgo.

3.3 Detector directional sensitivity

In presence of a GW the response of an interferometer $X(t)$ is composed by the noise $n(t)$ and the signal $\xi(t)$ contributes:

$$X(t) = \xi(t) + n(t) \quad (3.71)$$

Assuming the equality between the arm lengths of the detector l_0 , the instrument response produced by the GW transit can be written in terms of the test mass displacements δl_x and δl_y as:

$$\xi(t) = \frac{(\delta l_x - \delta l_y)}{l_0} \quad (3.72)$$

The relation which links this quantity to the GW tensor $h_{\mu\nu}(t)$ is obtained with the introduction of the *detector tensor* $D^{\mu\nu}$

$$\xi(t) = D^{\mu\nu} h_{\mu\nu}(t) \quad (3.73)$$

We can simplify this equation adopting the TT gauge, where the GW tensor is reduce to have only two independent components $h_+(t)$ and $h_\times(t)$. Indeed this choice permits to obtain a reduced formulation of the previous equation

$$\xi(t) = F_+ h_+(t) + F_\times h_\times(t) \quad (3.74)$$

Here we have introduced the **Antenna Pattern functions** F_+ and F_\times for the two polarizations, which are linear combinations of some detector tensor components. These quantities depend only on the source direction with

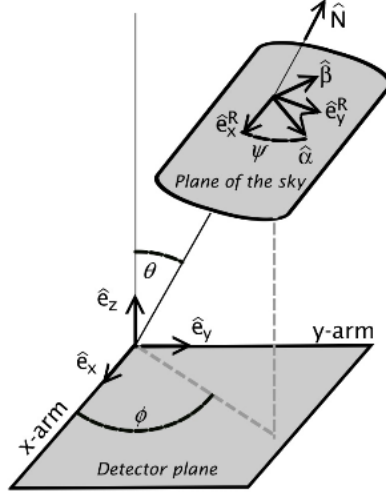


Figure 3.11: Relationship between TT wave frame and detector frame. For an interferometer, the arms are located at the x, y-axis. The angle (θ, ϕ, ψ) are the Euler Angle of the transformation between detector frame and wave frame.

respect to the interferometer orientation. Considering the system visualized by the picture (Fig. 3.11), the antenna pattern are functions of the Euler Angles (θ, ϕ, ψ) . The interferometer plane is represented by the two arms which determine the unit vectors (\hat{e}_x, \hat{e}_y) ; the GW direction is defined by the spherical coordinates θ and ϕ relative to the detector axes, while the two GW polatization components are along the x-y directions in the plane of the sky, rotated by the angle ψ with respect the interferometer plane. In these coordinate systems the antenna pattern functions are [33]

$$\begin{cases} F_+(\theta, \phi, \psi) = [(1 + \cos^2\theta) \cos 2\phi \cos 2\psi] / 2 - \cos\theta \sin 2\phi \sin 2\psi \\ F_\times(\theta, \phi, \psi) = [(1 + \cos^2\theta) \cos 2\phi \sin 2\psi] / 2 + \cos\theta \sin 2\phi \cos 2\psi \end{cases} \quad (3.75)$$

As shown by these last equations the sensitivity of each detector to the different signal directions depends on its arm orientation. In particular the best GW detections happen when the signal direction of propagation is orthogonal to the detector plane ($\cos\theta = 1$), whereas the interferometer is blind for directions whose component on the detector plane is one of its bisectors ($\cos 2\phi = 0$, $\phi = n\pi/4$ with n odd). In the picture (Fig 3.12) is shown how the antenna pattern functions change their value in relation with the sky location from which the GW source emits. Specifically the graphs represent, for each interferometer of the interested network (**Virgo**, **L1**, **H1**), the quantity $\sqrt{F_+^2 + F_\times^2}$ on varying the direction angles θ and ϕ .

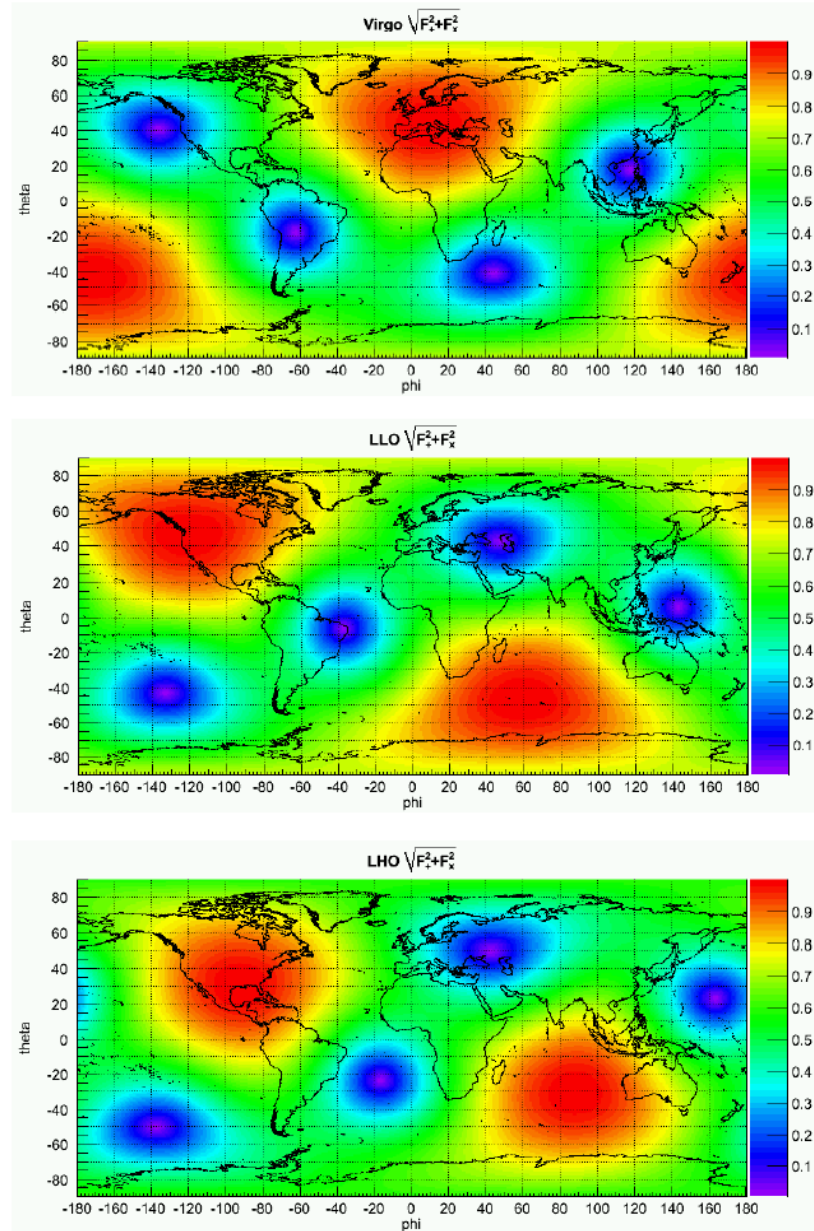


Figure 3.12: Variation of $\sqrt{F_+^2 + F_x^2}$ quantity following earth coordinate. On x-axis is reported the longitude, and on y-axis the latitude. Coloured axis reports value of antenna patterns. From top to bottom the detectors are: V1, L1, H1.

3.4 Advanced detectors

In 2011 the first generation of interferometric GW detectors completed the data acquisition. The observing time lasted some years during which the interferometry networks achieved the design sensitivity and surpassed the scientific goals, despite the many difficulties. Indeed, even if the several noises described in the previous section had afflicted the instrument measure, in a wide range of frequencies the mirror position had been located with a precision better than 10^{-18} m. Although no signal was detected, the sensitivity reached allowed the setting of upper limits on many possible GW sources and the achievement of the necessary requirements for the detection of a neutron star binary coalescence at about ~ 20 Mpc with a noise to ratio of 8.

From 2015 the second instrument generation (**2G**) will progressively start the new *science runs*. Improvements on the Virgo and LIGO detectors are currently under development, whereas the new KAGRA interferometer is now under construction. With respect to the other, the latter will present two main dissimilarities: its location will be underground, to reduce the seismic noise, and the its principal optics will be cooled down to ~ 20 K, to decrease the thermal effects on the measurements.

The major goal of the new generation instruments will be an improvement by a factor ~ 10 over a large frequency range. This means an increasing on the observable volume by a factor ~ 1000 . Consequently a the chances of detections are expected to drastically increasing: by a factor ~ 100 for continuous signals and cosmological stochastic background; by a factor ~ 1000 for the impulsive events. [9]

3.4.1 Advanced Virgo detector

Virgo is one of the best performing GW detector whose infrastructure is now under development. The planned improvements are:

- introduce a new mirror between the beam splitter and the detection bench, in order to improve the sensitivity at specific frequency bands [34] (**signal recycling**);
- increase the laser power, which will reach ~ 250 W, to reduce the shot noise;
- double the mirror weight (~ 42 Kg), to mitigate the growing effects of the radiation pressure produced by the increased input power;

- improve the *Thermal Compensation System*, which is used to mitigate the problems caused by the mirror absorption of the light power (*thermal lensing*);
- the new finesse will reach the value of 450 so that the optical path will increase to an effective length of 860 *km*.

These changes are expected to improve sensitivity by an order of magnitude in the frequency width $\sim (10 - 1000)$ *Hz*. Once this goal will be achieved, the coalescence of a neutron star binary system would be detected by Virgo from a source distance of ~ 155 *Mpc* [9], to compare with the ~ 11 *Mpc* reached by the previous configuration.

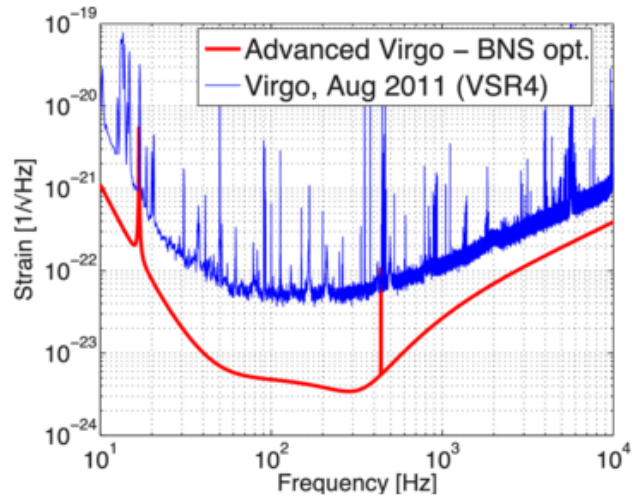


Figure 3.13: Comparison between Virgo sensitivity during the *science run VSR4* and the design sensitivity of Advanced Virgo.

Chapter 4

Coherent Waveburst Analysis

For the development of this project I became a member of the LIGO-Virgo collaboration. The real data utilized were collected during the last operating period by the GW observatory network: Virgo (**V1**), LIGO-Hanford (**H1**) and LIGO-Livingston (**L1**). To reach the main topic of the thesis I focus on data-analysis which starts from the time-frequency representation of candidates provided by the **coherent Waveburst** pipeline.

Burst GWs are signals characterized by a short time duration. This general definition permits the inclusion on this class of a large variety of gravitational emissions. The best known expected waveforms arise from Supernova explosions and from compact binary coalescences. There are two main approaches for the detection of these kind of signals: the Template-based methods and the unmodelled searches.

★ The **template-based methods** are set up starting from the recognition of GW classes theoretically well modelled. The aim of this kind of analysis is the identification of determinate waveforms. This approach is advantageous when the interested signals have well known properties, which noises mimic with difficulty.

★ The **unmodelled searches** instead are based on the individuation of energy excesses. Therefore, to discriminate the noise events, more efforts are needed. On the other hand the resulting algorithm is extremely more robust with respect to the signal shapes. This characteristic increase the possibility of the detection of GWs with unknown waveforms. The lack of detected signals makes this robustness a really important quality.

The **coherent Waveburst (cWB)** pipeline is based on the unmodelled searches, anyway some polarization constrains on the interested signals can easily be introduced. The analysis applied to the data does not consider any prior about the signal (no assumption on waveform, arriving time, source direction ecc...). Anyway this algorithm is equipped by the possibility to choose a partially different analysis in presence of external triggers, generally

constituted by knowledge of the sky location and of the event time. Usually the signal information are provided by different astrophysical searches, but also the GW observatories will have the possibility to broadcast notices on celestial sources. Indeed in the last years joint collaboration between different detector types (neutrinos, gamma rays, ecc...) have been started.

The collaboration internal the gravitational-wave community is ruled by several formal agreements to improve the information flowing between the different GW observatories. Indeed a signal detection would probably happen in a very noisy environment, thus, in order to reduce the impact of these measurement perturbations, coincidence studies are performed. Indeed if a real emission is detected it will appear in each of the operative instruments equipped with the necessary sensitivity. Two main approaches are developed to take into account the detector networks and their data correlation in GW presence(sets):

incoherent analysis : the candidates of each detector which survive at all the decision rules are selected for the composition of a trigger list related to the considered instrument. Then all the lists belonging to the interested detector set are compared and analyzed to find the network events. The individuation of the emission direction is implemented with an angular accuracy (typically of few degrees) which depends on the source position with respect to the detector arm orientation. At the moment this strategy is applied for data analysis based on templates. [36]

coherent analysis : a direct unique list of triggers is performed by the network adopting different selection rules. This method permits to connect the data acquired by the different detectors with more incisive relations, which allow better confidence in the detection and better performances in source localizations and waveform reconstructions with respect to the incoherent analysis.

The Waveburst pipeline, first based on incoherent approach, is now developed adopting a coherent analysis and therefore it needs data streams provided by a set of detectors. The basic idea of this algorithm consists on the identification of the most energetic data and the main problem is the rejection of the noisy events. For this reason the joined analysis of the information provided by different instruments represents a basilar tools for this kind of unmodelled searches. Anyway estimating the coincidence of a candidate is not an easy task. Indeed the inteferometers must detect the same GW during different times, due to their various locations on the Earth. Take into account these temporal displacements is even complicated by the dependence of their value on the source direction. Finally also the amplitude of the possible signal has to be different in the involved detectors, because of their

antenna pattern function. However consider several instrument outputs not only help in the discrimination process but it also allow a the source location [37] (more involved detectors means more precision) in the sky and a better coverage of the possible emission directions. Anyway a large statistic permits the occurrence of events with the signal expected characteristics but generated by noisy processes.

The cWB algorithm analyzes candidates classifying them as background events or as signals.

Applying this procedure two kinds of errors are possible: the **false dis-**

	Signal presence	Signal absence
Hypothesis of presence	True Alarm	False Alarm
Hypothesis of absence	False Dismissal	True Dismissal

Table 4.1: Possible cases derived by decision rules.

missals and the **false alarms**. The former represents the fraction of simulated waveforms wrongly evaluated, whereas the latter refers to the exchanged noisy events (*glitches*) with signals. The other two quantities written in the table Tab. 4.1 are associated to the correct classified events, the **false dismissal** refers the glitches and the **true alarm** to the signal. Anyway the most used parameters for evaluate the analysis performances are the efficiency and the false alarm. The former is a quantification of the signal identified and it is associated to true alarms. Sometimes this information is summarized in the Receiver Operating Characteristic (ROC) curves. These graphs usually have on ordinate the efficiency rate and on the x-axis the false alarm rate (with *rate* we indicate the ratio between the event number and the live-time in which they occur).

Because of the signal lack the efficiency is predicted considering injected waveforms, which follow different models depending on what we are interested in. The target signals for Waveburst algorithm are bursts whose maximum duration lasts few seconds. Generally to evaluate the pipeline performances generic signal are used, such as Gaussian and Sine-Gaussian bursts which can easily test all the available frequency range. A key quantity which describes the injected waveforms is their h_{rss} (rss: root square sum)

$$h_{rss} [Hz^{-1/2}] = \sqrt{\int_{-\infty}^{+\infty} h(t)^2 dt} \quad (4.1)$$

This signal property is the root mean square of the GW energy and, how shown by it unit of measurement, it can be directly compared to the sensitivity of the instruments.

A new version of the cWB pipeline, called cWB 2G, was recently implemented and improvements on its algorithm are currently under developing.

In this chapter are briefly shown the 2 main sections of the Waveburst analysis: the production and the postproduction stages.

In this chapter we will see how data are selected according to their quality (Section 4.1), the likelihood method which is on the basis of the cWB analysis (Section 4.2), the main steps included in the pipeline (Section 4.3) and then how the data are finally rated (Section 4.4).

4.1 Data Quality Flags

For Waveburst algorithm one of the most important goal is to perform an efficient glitch rejection. In the previous chapter (Sec. 3.2.1) we have seen some of the noisy processes which generate these disturbing triggers. To reduce their impact on the analysis the quality of the data are tagged through data-quality-flags (**DQFs**) [38]. Indeed there are strong correlation between gravitational channel and the enviromental disturbances recorded by the auxiliary channels, which allow the identification of some glitches. Therefore we can discard some of the data segments considered not reliabile. The DQFs are assigned to the temporal series by different analysis from the Waveburst one. The data quality flags can be divided in three main classes:

- **Category 1 (CAT1)**: the analysis of the data tagged by this DQF is substantially unfeasible. This category also includes periods during which the interferometer does not collect data or the noise sources cause important corruption on them.
- **Category 2 (CAT2)**: this category define data influenced by detector multifunctions which are well understood. Thus the events reconstructed in periods belonging to this data-quality class probably arise from these disturbances, and so usually disregarded. This kind of DQFs are applied or data surviving the CAT1 and typically last few seconds.
- **Category 3 (CAT3)**: the purpose of this category is to limited the data acquired when the instruments have reached its optimal operating regime. To reach this aim this category defines aquirements weakly related to the present noises. Therefore a GW candidate, found in data classified as CAT3, has to be evaluated carefully. Only data passing CAT1 and CAT2 DQFs are subject to CAT3 evaluation. The discard of all the periods tagged by this class of DQFs means a lost of about $\sim 20\%$ of the observing time. For this reason Waveburst algorithm usually does not apply this category of DQFs.

Another veto class is applied for the rejection of glitches: the **HVETO flags** [39]. This kind of tag is given to the triggers which present an excess of coincidence between the GW channel and the interferometric and environmental

auxiliary channels. This correlation means that probably the same source have produced the tagged event in both the lists and therefore that it is caused by a noisy process. In view of the above and because the time lost with the application of this vetos is negligible, the labeled data are normally disregarded.

4.2 Likelihood method

The likelihood function is a powerful tool used to statistically test two different models. For the implementation of this method all the available information about the involved processes are collected: both from the observed data and from the probability mechanism of the phenomenon. The general idea is to compare two different hypotheses, characterized by two distinct parameter spaces, and to decide by the ratio between the respective likelihood functions which best interpret the available observations.

Likelihood function [40]: Given a statistical model $(X^I, f_I(x_I; \theta), \theta \in \Theta)$ for a random sample X_I of I observations, the *likelihood function* associated to x is the function

$$\mathcal{L}_{x_o}(\theta) = f_I(x_o; \theta) = \prod_{i=1}^I f_X(x_o[i], \theta) \quad (4.2)$$

where $x_o = (x_o[1], x_o[2], \dots, x_o[I])$ represents the achieved data.

The implementation of the test consist in considering the ratio of the likelihood functions related to two different hypotheses, θ' and θ'' , to infer which model more likily describes the data. Therefore ths method consists in evaluating the function

$$\Lambda(x_o) = \frac{\mathcal{L}_{x_o}(\theta')}{\mathcal{L}_{x_o}(\theta'')} \quad (4.3)$$

Find $\Lambda(x_o) > 1$ means θ' is more reliable than θ'' .

The cWB pipeline adopts a coherent method to analyze the data stream of detector network based on a **Constrained Likelihood** process.

4.2.1 Single detector

To better understand the Likelihood method we start analyzing the data provided by a sigle detector. For the development of the procedure we use the notation expressed in the following.

Complex notation

Considering the detector response to a GW $\xi(t)$

$$\xi(t) = F_+ h_+(t) + F_\times h_\times(t) \quad (4.4)$$

we can simplify the formalism introducing a complex representation (i imaginary unit) for the antenna pattern functions and for the waveforms

$$\zeta(t) = h_+(t) + ih_\times(t) \quad (4.5)$$

$$A = \frac{1}{2}(F_+ + iF_\times) \quad (4.6)$$

Calling z^* the complex conjugate of the quantity z , the previous notation allows a new formulation of the detector response

$$\xi(t) = \zeta(t) \cdot A^* + \zeta^* \cdot A \quad (4.7)$$

In this coordinate frame a system rotation in agreement with the wave plane is performed by the transformation

$$A' = A \cdot e^{2i\psi} \quad (4.8)$$

$$\zeta' = \zeta \cdot e^{2i\psi} \quad (4.9)$$

The last formula shows that a change of the coordinate frame has no effect on the detector response.

Likelihood analysis

The analysis aims to recognize GW signal from the noisy glitches present in the interferometer data stream $x_o = x_o[1], x_o[2], \dots, x_o[I]$. To achieve this result a *decision rule* is needed and it is performed by the Likelihood test. It explores the two mutually exclusive hypotheses of **presence** (H_1 , *alternative*) or **absence** (H_0 , *null*) of signals. The variable x is characterized by the probability densities $f(x|H_1)$ and $f(x|H_0)$ which differs in the parameter spaces used for the definition of the statistical model. The collected data can be represented as the sum of the noise $n(t)$ and the detector response to an eventual gravitational signal $\xi(t)$, i.e.

$$x(t) = n(t) + \xi(t) \quad (4.10)$$

Assuming the disturbances as Gaussian white noise with 0-mean we can define the two likelihood functions, in agreement with the definition (4.2):

$$\mathcal{L}_{x_o|H_0} = f(x_o|H_0) = \prod_{i=1}^I \frac{1}{\sqrt{2\pi}\sigma} \exp\left(-\frac{x_o^2[i]}{2\sigma^2}\right) \quad (4.11)$$

$$\mathcal{L}_{x_o|H_1} = f(x_o|H_1) = \prod_{i=1}^I \frac{1}{\sqrt{2\pi}\sigma} \exp\left(-\frac{(x_o[i] - \xi[i])^2}{2\sigma^2}\right) \quad (4.12)$$

where σ is the noise standard deviation. Through these functions it is possible to choose the desired false alarm probability and thus define the decision

rule. The selection happens applying a threshold (correspondent to a specific false alarm probability) on the *Likelihood ratio*, which is defined as followed

$$\Lambda(x_o) := \frac{\mathcal{L}_{x_o|H_1}}{\mathcal{L}_{x_o|H_0}} = \frac{\mathcal{L}_{x_o}(\vec{\xi} \neq 0)}{\mathcal{L}_{x_o}(\vec{\xi} = 0)} = \frac{f_I(x_o|H_1)}{f_I(x_o|H_0)} \quad (4.13)$$

where $x_o = (x_o[1], x_o[2], \dots, x_o[I])$ are the observed data, $\vec{\xi} = (\xi[1], \xi[2], \dots, \xi[I])$ and $\mathcal{L}_{x_o|H_1(0)}$ is the likelihood function for the hypothesis of presence (absence) of signal. The *Neymann-Pearson criterion* assures that the optimal decision rule can be found fixing the false alarm probability and lowering the false dismissal to find its minimum value. Anyway this approach is effective when H_1 is a simple hypothesis.

To simplify the formulation of the likelihood ratio in function of the data (noise and signal) parameters we can introduce *likelihood functional* (or simply likelihood), i.e. the logarithm of the likelihood ratio:

$$L = \ln(\Lambda(x_o)) = \sum_{i=1}^I \frac{1}{\sigma^2} \left(x_o[i]\xi[i] - \frac{1}{2}\xi^2[i] \right) \quad (4.14)$$

where we used the equations (4.11) and (4.12). For the analysis both the likelihood ratio and the likelihood functional can be used almost independently because of the monotonicity of the logarithmic function.

4.2.2 Detector network

The treatment of the likelihood functions in presence of more instruments has not been developed through criterions similar to the Neyman-Pearson one. Anyway the cWB algorithm starts its analysis from the likelihood method, whose formalism is extended by the single detector case to a set of N interferometers.

Notation

To describe the relevant quantities we define an N -dimensional space, in which each dimension refers to a specific detector k :

$$\begin{aligned} \sigma &= (\sigma_1, \sigma_2, \dots, \sigma_k, \dots, \sigma_N) \\ \zeta &= (\zeta_1, \zeta_2, \dots, \zeta_k, \dots, \zeta_N) \\ A &= (A_1, A_2, \dots, A_k, \dots, A_N) \\ F_+ &= (F_{1+}, F_{2+}, \dots, F_{k+}, \dots, F_{N+}) \\ F_\times &= (F_{1\times}, F_{2\times}, \dots, F_{k\times}, \dots, F_{N\times}) \end{aligned} \quad (4.15)$$

where we have extended the relation introduced in the previous section to any k instrument

$$\xi_k = \zeta_k \cdot A_k^* + \zeta_k^* \cdot A_k \quad (4.16)$$

Also normalized vectors can be defined in the N-detector space

$$\begin{aligned}
X &= (x_{o1}/\sigma_1, x_{o2}/\sigma_2, \dots, x_{ok}/\sigma_k, \dots, x_{oN}/\sigma_N) \\
\xi_\sigma &= (\xi_1/\sigma_1, \xi_2/\sigma_2, \dots, \xi_k/\sigma_k, \dots, \xi_N/\sigma_N) \\
f_+ &= (F_{1+}/\sigma_1, F_{2+}/\sigma_2, \dots, F_{k+}/\sigma_k, \dots, F_{N+}/\sigma_N) \\
f_\times &= (F_{1+}/\sigma_1, F_{2+}/\sigma_2, \dots, F_{k+}/\sigma_k, \dots, F_{N+}/\sigma_N)
\end{aligned} \tag{4.17}$$

and finally

$$\begin{aligned}
A_\sigma &= (A_1/\sigma_1, A_2/\sigma_2, \dots, A_k/\sigma_k, \dots, A_N/\sigma_N) \\
&= \frac{1}{2} (f_{1+} + if_{1\times}, f_{2+} + if_{2\times}, \dots, f_{k+} + if_{k\times}, \dots, f_{N+} + if_{N\times})
\end{aligned} \tag{4.18}$$

Normalized Antenna Patterns

To develop the analysis we can introduce the real g_r and the complex g_c network antenna patterns

$$g_r = A_\sigma A_\sigma^* = \sum_{k=1}^N \frac{A_k \cdot A_k^*}{\sigma_k^2} = \frac{1}{4} \sum_{k=1}^N (f_{k+}^2 + f_{k\times}^2) \tag{4.19}$$

$$g_c = A_\sigma^2 = \sum_{k=1}^N \frac{A_k^2}{\sigma_k^2} = \frac{1}{4} \sum_{k=1}^N (f_{k+}^2 + 2if_{k+}f_{k\times} - f_{k\times}^2) \tag{4.20}$$

To simplify some expressions we compute a coordinate transformation. We focus on the transformation to which correspond a null imaginary part of the complex network antenna pattern $g'_c = |g_c| e^{-2i\gamma}$. Therefore $A'_k = A_k e^{-i\gamma} = (F'_{k+} + iF'_{k\times})/2$, which means

$$\begin{aligned}
F'_{k+} &= F_{k+} \cos\gamma + F_{k\times} \sin\gamma \\
F'_{k\times} &= -F_{k+} \sin\gamma + F_{k\times} \cos\gamma
\end{aligned} \tag{4.21}$$

in analogy we find for the normalized vectors $A'_{\sigma k} = A_{\sigma k} e^{i\gamma}$ and consequently

$$\begin{aligned}
f'_{k+} &= f_{k+} \cos\gamma + f_{k\times} \sin\gamma \\
f'_{k\times} &= -f_{k+} \sin\gamma + f_{k\times} \cos\gamma
\end{aligned} \tag{4.22}$$

In this new frame the complex antenna pattern becomes

$$\begin{aligned}
A'^2_\sigma &= \frac{1}{2} (f'_+ + if'_\times) \cdot \frac{1}{2} (f'_+ + if'_\times) \\
&= \frac{1}{4} (f'^2_+ - f'^2_\times) + \frac{i(f'_+ \cdot f'_\times)}{2}
\end{aligned} \tag{4.23}$$

The last equation shows that the requirement of a null g'_c imaginary part is equivalent to the orthogonality between the normalized antenna pattern

vectors f'_+ and f'_\times . The satisfaction of this property, $f'_+ \cdot f'_\times = 0$, defines the **Dominant Polarization Frame (DPF)**.

Developing the previous considerations we can find the relation which transforms any frame (f_+, f_\times) to the DPF frame (f'_+, f'_\times) . The only parameter of the transformation $A'_k = A_k e^{-i\gamma}$ is the angle γ , therefore we are looking for a relationship which links γ to the normalized antenna patterns of the starting frame.

Considering the inverse transformation $A_k = A'_k e^{i\gamma}$ we find

$$\begin{aligned} \frac{1}{4} (f_+^2 - f_\times^2) + \frac{i(f_+ \cdot f_\times)}{2} &= A_\sigma^2 = (A'_\sigma e^{i\gamma})^2 = |A'_\sigma|^2 e^{2i\gamma} \\ &= |A'_\sigma|^2 (\cos 2\gamma + i \sin 2\gamma) \end{aligned} \quad (4.24)$$

where we have considered the equality $|A'_\sigma|^2 = |A_\sigma^2|$. Elaborating these equations we obtain

$$\begin{aligned} |A'_\sigma|^2 \cos 2\gamma &= (f_+^2 - f_\times^2) / 4 \\ |A'_\sigma|^2 \sin 2\gamma &= (f_+ \cdot f_\times) / 2 \end{aligned} \quad (4.25)$$

from which we can easily calculate the γ angle

$$\gamma = \frac{1}{2} \arctan \left(\frac{f_+^2 - f_\times^2}{2f_+ \cdot f_\times} \right) \quad (4.26)$$

Now to test the transformation and verify it leads to the DPF frame, we can check the orthogonality between the two vectors f_+ and f_\times

$$\begin{aligned} f'_+ \cdot f'_\times &= (f_+ \cos \gamma + f_\times \sin \gamma) \cdot (-f_+ \sin \gamma + f_\times \cos \gamma) \\ &= -(f_+^2 - f_\times^2) \cos \gamma \sin \gamma + (f_+ \cdot f_\times) (\cos^2 \gamma - \sin^2 \gamma) \\ &= -\sin 2\gamma (f_+^2 - f_\times^2) / 2 + (f_+ \cdot f_\times) \cos 2\gamma \\ &= 0 \end{aligned} \quad (4.27)$$

Moreover it is useful to discover the relation which connects the normalized antenna patterns of the DPF frame to the ones defined in a generic frame

$$\begin{aligned}
|f'_+|^2 &= |f_+ \cos \gamma + f_\times \sin \gamma|^2 \\
&= f_+^2 \cos^2 \gamma + f_\times^2 \sin^2 \gamma + 2(f_+ \cdot f_\times) \cos \gamma \sin \gamma \\
&= f_+^2 \frac{1 + \cos 2\gamma}{2} + f_\times^2 \frac{1 - \cos 2\gamma}{2} + (f_+ \cdot f_\times) \sin 2\gamma \\
&= \frac{1}{2}(f_+^2 + f_\times^2) + 2 \cdot \left(\frac{1}{4} \cos 2\gamma (f_+^2 - f_\times^2) + \frac{1}{2} \sin 2\gamma (f_+ \cdot f_\times) \right) \\
&= \frac{1}{2}(f_+^2 + f_\times^2) + 2(|A_\sigma^2| \cos^2 2\gamma + |A_\sigma^2| \sin^2 2\gamma) \\
&= 2 \left(\frac{1}{4}(f_+^2 + f_\times^2) + |A_\sigma^2| \right) \\
&= 2(|A_\sigma|^2 + |A_\sigma^2|) \\
&= 2(g_r + |g_c|)
\end{aligned} \tag{4.28}$$

in analogy we obtain for $|f'_\times|$

$$|f'_\times| = 2(|A_\sigma|^2 - |A_\sigma^2|) = 2(g_r - |g_c|) \tag{4.29}$$

Through these equation we discover an important property of the normalized antenna patterns in the DPF frame

$$|f'_+|^2 \geq |f'_\times|^2 \tag{4.30}$$

Two interesting cases can be studied by these equations:

1. $|\mathbf{f}'_+| = |\mathbf{f}'_\times|$

When this condition is satisfied we find $|A_\sigma^2| = 0$ and thus by the equations (4.28) and (4.29) we obtain for any general frame

$$\begin{aligned}
f_+^2 &= f_\times^2 \\
f_\times \cdot f_+ &= 0
\end{aligned} \tag{4.31}$$

because to verify $|A_\sigma^2| = 0$ both the real and the complex part have to be null. The relation (4.31) reveals that under the condition $|\mathbf{f}'_+| = |\mathbf{f}'_\times|$ the normalized antenna patterns in a generic frame have the same value and are othogonal.

2. $|\mathbf{f}'_\times| = \mathbf{0}$

This assumption requires

$$\begin{aligned}
f_{k+} &= f'_{k+} \cos \gamma \\
f_{k\times} &= f'_{k+} \sin \gamma
\end{aligned} \tag{4.32}$$

due to the equation (4.23). These relations shows that in this case each detector of the network gives the same response to a GW, indeed the ratio between the two normalized antenna patterns is equal for all the instruments. Therefore all the interferometers of the set have parallel arms.

The property $|f'_+| \geq |f'_\times|$ is well illustrated by the image (Fig. 4.1) where is represented the quantity $|f'_\times| / |f'_+|$ related to the full network V1L1H1. We note that it always satisfies the inequality of the relation (4.30) and that in a big region of the sky the cross component is almost negligible with respect the plus one (blue color).

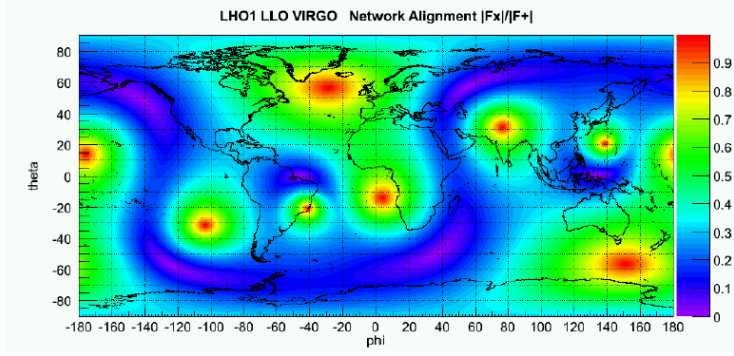


Figure 4.1: Variation of L1H1V1 network antenna pattern $|f'_\times| / |f'_+|$ in the DPF following earth coordinates. On x-axis is reported the longitude, and on y-axis the latitude. Coloured axis reports valued of the plus componet of antenna pattern.

For this thesis we analyze the data stream collected by the detectors network V1, L1, H1. We are interested in the advantageous carried by the instrument set in comparison with a unique interferometer. In the picture (Fig. 4.2) are represented the plus components of the antenna pattern for the interferometer couples H1L1, H1V1, L1V1. Finally the same quantity is shown by the image (Fig. 4.3) for the complete network V1L1H1. We focus on the plus polarization because of the discovered relation between the two antenna pattern components $|f'_+| \geq |f'_\times|$ (Fig. 4.1).

Likelihood analysis

In presence of data collected by a network of N detectors, coherently with the adopted notation, we can write the total likelihood

$$L = \sum_{k=1}^N \sum_{i=1}^I \frac{1}{\sigma_k^2} \left(x_{ok}[i] \xi_k[i] - \frac{1}{2} \xi_k^2[i] \right) \quad (4.33)$$

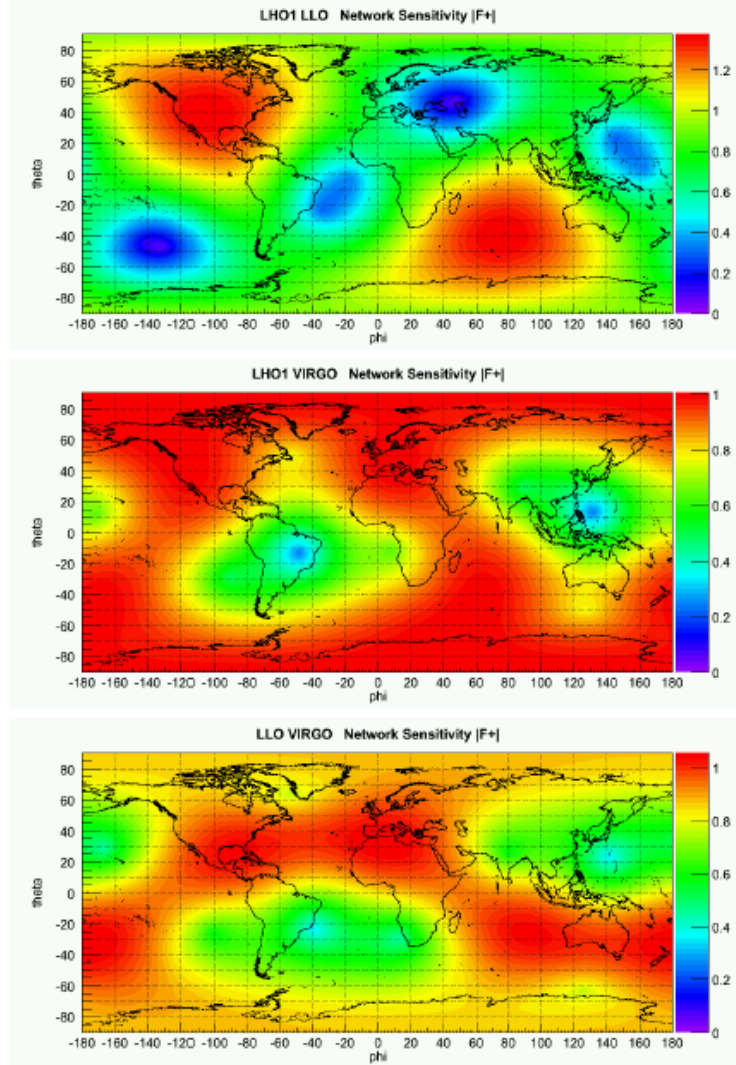


Figure 4.2: Variation of plus component of antenna patterns following earth coordinate for a network of two detectors. On x-axis is reported the longitude, and on y-axis the latitude. Coloured axis reports value of antenna patterns. From top to bottom the networks are: H1L1, H1V1, L1V1.

To simplify the notation we omit the sum over the I data acquired and use the vector notation

$$\begin{aligned}
 L &= \left(X \cdot \xi_\sigma - \frac{1}{2} \xi_\sigma \cdot \xi_\sigma \right) \\
 &= \left[X \cdot (f'_+ h_+ + f'_\times h_\times) - \frac{1}{2} (f'_+ h_+ + f'_\times h_\times) \cdot (f'_+ h_+ + f'_\times h_\times) \right] \quad (4.34) \\
 &= \left[X \cdot f'_+ h_+ + X \cdot f'_\times h_\times - \frac{1}{2} (f'^2_+ h^2_+ + f'^2_\times h^2_\times) \right]
 \end{aligned}$$

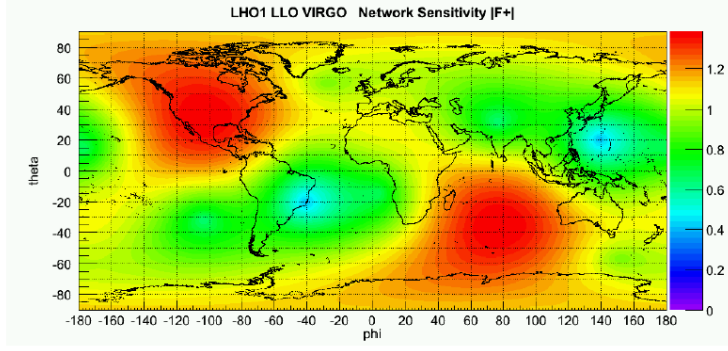


Figure 4.3: Variation of L1H1V1 network antenna pattern $|f'_+|$ in the DPF following earth coordinates. On x-axis is reported the longitude, and on y-axis the latitude. Coloured axis reports values of the plus component of antenna pattern.

where the last equality we have assumed $f'_\times \cdot f'_+ = 0$ which is verified only in the DPF.

To find the most likely estimates of the plus and cross GW polarizations we maximize the likelihood functional with respect to these unknown variables

$$\frac{\delta L}{\delta h_+} = X \cdot f'_+ - |f'_+|^2 h_+ = 0 \quad (4.35)$$

$$\frac{\delta L}{\delta h_\times} = X \cdot f'_\times - |f'_\times|^2 h_\times = 0 \quad (4.36)$$

whose solutions are

$$h_+ = \frac{X \cdot f'_+}{|f'_+|^2} \quad (4.37)$$

$$h_\times = \frac{X \cdot f'_\times}{|f'_\times|^2} \quad (4.38)$$

The maximum reached by the Likelihood functional is therefore obtained by inserting these two values into the equation (4.34). The result of this operation is

$$\begin{aligned} L_{max} &= \left[X \cdot f'_+ h_+ + X \cdot f'_\times h_\times - \frac{1}{2} (f'^2_+ h^2_+ + f'^2_\times h^2_\times) \right] \\ &= \left[X \cdot f'_+ \frac{X \cdot f'_+}{|f'_+|^2} + X \cdot f'_\times \frac{X \cdot f'_\times}{|f'_\times|^2} - \frac{1}{2} \left(f'^2_+ \frac{(X \cdot f'_+)^2}{|f'_+|^4} + f'^2_\times \frac{(X \cdot f'_\times)^2}{|f'_\times|^4} \right) \right] \\ &= \frac{1}{2} \left(\frac{(X \cdot f'_+)^2}{|f'_+|^2} + \frac{(X \cdot f'_\times)^2}{|f'_\times|^2} \right) \end{aligned} \quad (4.39)$$

The GW polarizations obtained by the likelihood maximization procedure can be used to find what would be the factorail detector response in presence of such signal

$$\begin{aligned}
 \xi_\sigma &= h_+ f'_+ + h_\times f'_\times \\
 &= \frac{X \cdot f'_+}{|f'_+|^2} f'_+ + \frac{X \cdot f'_\times}{|f'_\times|^2} f'_\times \\
 &= \frac{X \cdot f'_+}{|f'_+|} e'_+ + \frac{X \cdot f'_\times}{|f'_\times|} e'_\times
 \end{aligned} \tag{4.40}$$

where we have introduced the unitary vectors $e'_+ = f'_+/|f'_+|$ and $e'_\times = f'_\times/|f'_\times|$. The above relation proves that the detector response is the projection of the data vector on the DPF antenna pattern plane (e'_+, e'_\times) , as the picture (4.4) illustrates, and that the maximum likelihood is the square of its module

$$L_{max} = \frac{(X \cdot \xi_\sigma)^2}{|\xi_\sigma|^2} \tag{4.41}$$

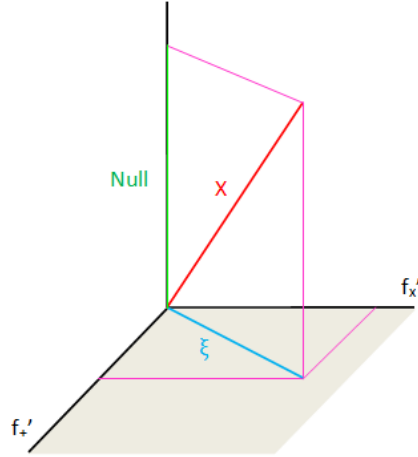


Figure 4.4: Dominant Polarization Frame

Maximum Likelihood and SNR

The *Null* vector is defined in the DPF by the relation $Null = X - \xi$, where all the involved quantities are N-dimensional vectors. For an interferometer k characterized by a detector response ξ_k and in presence of white Gaussian noise, whose standard deviation is σ_k , an appropriate Signal Noise Ratio SNR_k can be defined by the formula

$$SNR_k^2 = \xi_k^2 / \sigma_k^2 \tag{4.42}$$

For a networks of N detector and adopting the notation previously explained we find

$$\sum_{k=1}^N SNR_k^2 = \sum_{k=1}^N \frac{\xi_k^2}{\sigma_k^2} = \sum_{k=1}^N \xi_{\sigma k}^2 = \xi_{\sigma} \cdot \xi_{\sigma} \quad (4.43)$$

We can refer to this quantity as to the maximum Likelihood. Indeed the data vector X is related to the normalized detector response ξ_{σ} by

$$X = \xi_{\sigma} + n \quad (4.44)$$

Here n represents the noisy part of the data. In the DPF (where $Null = n$) this relation allow us to obtain the following equation

$$X \cdot \xi_{\sigma} = \xi_{\sigma} \cdot \xi_{\sigma} + n \cdot \xi_{\sigma} = \xi_{\sigma} \cdot \xi_{\sigma} \quad (4.45)$$

To perform this result we have considered the othogonality between the detector response ξ_{σ} and the Null stream n , shown by the picture (Fig. 4.4). Using the last relationship we can easily prove the equality between the likelihood and the sum of the SNR_k^2

$$\sum_{k=1}^N SNR_k^2 = \xi_{\sigma} \cdot \xi_{\sigma} = \frac{(\xi_{\sigma} \cdot \xi_{\sigma})^2}{|\xi_{\sigma}|^2} = \frac{(X \cdot \xi_{\sigma})^2}{|\xi_{\sigma}|^2} = 2L_{max} = \hat{L} \quad (4.46)$$

Here we have introduced the quantity \hat{L} , double of the maximum likelihood.

4.2.3 Regulators

To find the maximum likelihood we started from the assumption of the orthogonality between the detector response and the noise. In reality this is not properly true; the noise could partially be in the plane defined by the normalized antenna patterns of the DPF (f'_+ , f'_\times).

To mitigate this problem new tools are introduced: the **Regulators**. The data analysis depends on the chosen regulator, whose mechanism is based on assumptions concerning the instrument response. To be aware on the introduced procedures we can test the detector responses simulating a uniform distribution in the polarization angle of GW sources.

The results is non uniform distribution in the angle between the projection of the intrument response in the axes of the normalized antenna pattern plane. In particular in the DPF the detector response is preferably near the f'_+ axis. This is due to the antenna pattern influence on the detection. Indeed even if signals can assume indifferently any location in the sky in the collected data they are weighted by the antenna pattern functions. This is clearly shown in the following image (Fig. 4.5), where is simulated a GW with circular polarization. Here is reported an example: given an angle of $\pi/4$, the circularly polarized wave projections have both the same module h_+ and h_\times ,

while the corresponding antenna patterns are unbalanced in favor of the plus component.

Therefore the basic idea of regulators is to introduce different treatments

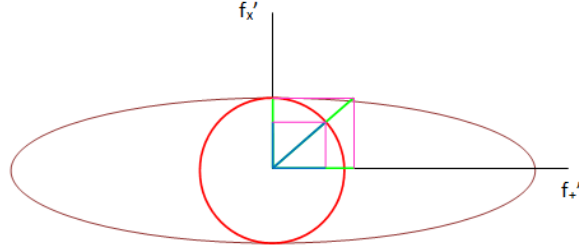


Figure 4.5: Visualization of a circularly polarized signal (red) and of the related detector response (brown) in the Dominant Polarization Frame. Plus component is greater because of the definition of DPF.

of the cross polarization: consider it normally (*weak*), consider it softly (*soft* or *mild*) or neglect it (*hard*). Unfortunately a compromise between the efficiency and the glitches rejection is always present. Normally the weak regulator better reconstruct and recognize the injected waveforms, but, for the same reason, it collects more noisy events. Instead the hard regulator is characterized by more selective constrains. Therefore its glitches detection is lower, but on the other hand also the efficiency decreases.

Moreover the performances of the chosen regulator strongly depends on the GW direction in the sky. Indeed the regions characterize by a negligible f'_+ do not suffer the application of the hard regulator, as instead happens for locations where the two antenna pattern components have almost the same value. Thus the most suitable regulator is selected principally depending on the sky direction, but also considering the kind of analysis desired.

Anyway a particular case exist: when the network is composed by only two detectors. In this situation the *Null* space does not exit and the most effective way to treat the data is to impose the *hard* regulator.

4.2.4 Energy disbalance

The Coherent Waveburst pipeline starts from a combined analysis of data stream through a constrained likelihood approach. The regulators are one of the constrains added to the standard application of the likelihood method. A further implemented quantity which can be used in cWB to reduce the glitch detection is the *Energy disbalance*. To perform its definition we start from the introduction of the *k-detector energy disbalance*

$$\Delta_k := X_k \xi_{\sigma k} - \xi_{\sigma k}^2 \quad (4.47)$$

This quantity appears developing the squared null stream

$$n_k^2 = (X_k - \xi_{\sigma k})^2 = X_k^2 - \xi_k^2 - 2(X_k \xi_{\sigma k} - \xi_{\sigma k}^2) \quad (4.48)$$

A useful property of the detector energy disbalance can be discovered taking into account the maximum likelihood. Indeed ideally we have

$$\hat{L} = \sum_{k=1}^N X_k \xi_{\sigma k} = \sum_{k=1}^N \xi_{\sigma k}^2 \quad (4.49)$$

from which

$$\sum_{k=1}^N X_k \xi_{\sigma k} - \xi_{\sigma k}^2 = \sum_{k=1}^N \Delta_k = (X - \xi_{\sigma}) \cdot \xi_{\sigma} = n \cdot \xi_{\sigma} = 0 \quad (4.50)$$

This result is due to the likelihood maximization which imposes the null stream minimization. Anyway this relation concerns the sum over the N-instruments of the detector energy disbalance. So this does not imply that for the single interferometer the equation $\Delta_k = 0$ holds. For this reason we can help the correct glitch individuation evaluating these quantities: $\Delta_k \ll 0$ is an unphysical solution.

The explained idea is practically applied minimizing the quantity

$$\sum_{k=1}^N (X_k \xi_{\sigma k} - \xi_{\sigma k}^2)^2 = \sum_{k=1}^N \Delta_k^2 \quad (4.51)$$

To perform this calculation the key quantity is in effect the *energy disbalance*, which in the DPF is defined by the relation

$$q_k = \frac{X_k \xi_{\sigma k}}{|\xi_{\sigma k}|} = X_k u_k - u_k^2 |\xi_{\sigma k}| \quad (4.52)$$

where u_k is the direction chosen by the regulator applied.

Substantially this procedure, based on the energy disbalance evaluation, has the goal to find the best direction for the likelihood analysis in the plane of the normalized antenna patterns (usually the DPF). This means find the unit vector which minimizes the energy disbalance. Compute this analysis step seems to be an efficient approach to reduce the impact of the noises.

4.2.5 Polarization constrains

The Waveburst algorithm allow the possibility to introduce signal assumption in the maximum likelihood procedure. In particular some constrains on the polarization can be add to the analysis. Indeed the search can be focused on signals with random, elliptical, circular or linear polarizations, here

expressed with increasing limits. The introduction of these particular waveform properties makes the algorithm more selective (how much depends on the chosen constrain), lowering the surviving glitches but losing generality on the targeted signals.

In the algorithm the decision of the target signals happens selecting on of the following labels, to which correspond a specific constrain on the GW polarization. This table shows the addition of the mark i , a further restriction on

Polarization	label
unmodelled	r
elliptical	e
circular	g, c
linear	l
fixed chirality (all sky search)	i

Table 4.2: Principal constrains used in Choerent Waveburst and their relative label. g refers searches of inspirals, c of generic circularly polarized signals. A further kind of constrain is introduced: a fixed chirality, i .

the 2G pipeline which fixes the chirality. It represents an interesting physical constrain used for the analyses presented in the following chapters. The idea can be easier explained focusing on signals with circular or elliptical polarization, from which also emission compatible with compact binary coalescences (target signal of the thesis) belongs. The main idea of this search restriction consists in the consideration that a GW during its time evolution maintains the same chirality, property aquired by its astrophysical source. Two different values of chirality are defined relatively to the clockwise or anticlockwise manner of two polarization evolution. In the DPF this property can be represented as shown by the picture (Fig. 4.6).

The chirality, so defined, is thus an important characteristic of physical GWs which can help to distinguish them from the glitches. Indeed the events produced by noises do not have any physical reason to obey at the same kind of time evolution, therefore the pixels, through which they are described, probably show an angle between the two polarization which randomly varies in time. All these constrains are applied at the end of the *Production Stage* (see Sec. 4.3).

4.3 Production stage

The cWB pipeline analyzes periods of detection limited in time. Thus the data provided by the detector network are divided in **segments** whose duration is normally between the 300 s and 600 s. The constrains on their minimum and maximum lengths are respectively due to the approximation procedures applied on the data, which become dangerous for short time pe-

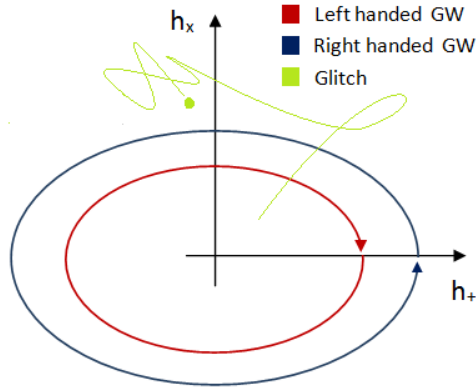


Figure 4.6: Chirality as discriminant parameter (the independence of the two polarizations are represented by orthogonal axes). The red and blu lines concern signals elliptically polarized with respectively anticlockwise (right-handed)/clockwise (left-handed) chirality. For both the GWs the chirality value remains constant in time. The green line refers to a glitch and describes its random behaviour. Note: in real signals, different features would appear on this schematic polarization evolutions.

riods, and to the computational demanding. Indeed the implementation of the likelihood method, on which is based the *cWB* analysis (Sec. 4.2), needs a wide memory usage and high computational load. Moreover some approximations are introduced for the same reason and thus to speed the analysis. The time necessary to process the data is further reduced by the possibility to run simultaneously several **jobs**, i.e. to apply the pipeline on different segments making use of various machines. The first version of the pipeline (**cWB1G**) was focused on signal duration of ~ 1 s, while now we are interested in events which can also last an order of magnitude more. For this reason in the future the segments will probably include longer periods.

The new pipeline structure is divided in two parts:

- the first consists in a closed analysis, performed for any tests, and which contains a preliminary event selection based on the likelihood evaluation;
- whereas the second concerns a more flexible structure, which can be partially modified by **Plugins** in consideration of the analysis aim.

The implementation of the *cWB* algorithm exploits ROOT, an informatic program and library written in C++ and developed for the particle physics data analysis by CERN. The results of the Waveburst search is reported, for each job, in a ROOT output file, which can be collected with the others in unique merge file.

In the following are reported the main steps of the production stage in the cWB analysis: the data conditioning (Sec. 4.3.1), the time-frequency data representation (Sec. 4.3.2), the enhancement of background statistics (Sec. 4.3.3) and finally the waveform parameter reconstruction (Sec. 4.3.4).

4.3.1 Data conditioning

The cWB pipeline is performed to achieve the best results in presence of data previously treated by a data-conditioning stage. In cWB this procedure includes the implementation of three main processes:

Linear prediction error (LPE) filter : the main effect of this filter application is the suppression of the lines produced by stationary noises, which are recognized by controls on the GW channel. The LPE filter is applied on each level of the time frequency decomposition (Sec. 4.3.2) and thus the time serie cleaned by these disturbances can be obtained performing the inverse transformation.

Regression : in the new version of the pipeline (**cWB2G**) is implemented the regression stage. This consists on the recognition of noisy lines through the analysis of the data collected by the auxiliary channels. Actually this tool is not applied by default, tests on it are in progress.

Whitening : this process is applied to take into account the detector behaviour in frequency and to consequently normalize the energy of the collected data. Indeed, even if the previous stages mitigate the influence of some known noisy components on the time series, the data still follow the sensitivity curve, whose value varies in frequency. To perform the whitening process, taking into account the non stationarity of the interferometer noises, PSD estimates are evaluating every ~ 20 s.

4.3.2 TF data representation

Unmodelled searches are normally equipped by the data representation on the time-frequency plane (**TF**) to make the analysis more effective. This transformation allows the use of the most reliable collected information about the signal: its time duration and its frequency extension. Indeed the strength measurement is often ruined by the noise presence. Anyway the efficacy of this strategy depends on the signal reconstructed properties: more limited is its representation on the TF plane more effective is the application of this approach.

One of the main improvements on the cWB2G pipeline concern the data transformation on the TF plane.

1G The previous version computes this process using the **Wavelet Transform** [41], which completely characterizes the signal in time and frequency.

The resolutions of the two components define the considered level of the decomposition, anyway the two quantities are connected: improving one means worsen the other. Then the 1G analysis performs the likelihood on the level which better describes the event, called the **optimal level**. This procedure is still available in the 2G analysis, because it seems better recognize some particular waveforms. The new version of the pipeline make use of the **Wilson-Daubechies-Meyer (WDM) TF transformation**. This new decomposition lowers the computational demanding and better represents the signal in the TF plane: its energy is more confined in the TF plane. Also in this case the representation can happens in different levels, which completely and independently describe the event and are characterized by different time and frequency resolution liked by a fixed relation. The WDM TF transformation also introduces two complete representations of the event. Differently from the 1G analysis the likelihood is applied on the best representation of the data, which can include components of different levels. This approach is particularly effective to describe signals compatible with compact binary mergers, which are on of the most promising GW sources.

For both the versions the likelihood methods is applied on pixels resulting by the data decomposition on the TF plane. This process is particularly complex and computing demanding thus this step, with the data conditioning, requires the majority of the analysis time $\sim 90\%$.

Wilson-Daubechies-Meyer TF transformation

[42] To perform the data representation in the TF plane a new tool is introduced in the 2G pipeline version: **Fast Wilson-Daubechies-Meyer transform (WDM)**.

The WDM transform consists in the application of a set of band-pass filters, similarly to the wavelet case. Considering a data serie $x[k]$ collected with a sample rate r_s a TF representation of the signal can be obtained introducing the discrete Wilson-Daubechies-Meyer filters $f_{nm}[k]$

$$w_{nm} = \sum_k f_{nm}[k]x[k] \quad (4.53)$$

In the Fourier domain the functions which describe the WDM basis are

$$\begin{aligned} \tilde{g}_{n0}(\omega) &= e^{in\omega T} \tilde{\phi}(\omega) \\ \tilde{g}_{nm}(\omega) &= \frac{1}{\sqrt{2}} e^{-in\omega T/2} \tilde{\psi}_{nm}(\omega) \end{aligned} \quad (4.54)$$

where T defines the resolution in time, $\tilde{\phi}$ is the generalized Meyer scaling function and $\tilde{\psi}$ is a linear combination of $\tilde{\phi}$. The explicit formulations of

these functions are

$$\tilde{\phi}(\omega) = \begin{cases} 1/\sqrt{\Delta\Omega}, & |\omega| < A \\ \cos[\nu_n(|\omega| - A)\pi/(2B)]/\sqrt{\Delta\Omega}, & A \leq |\omega| < A + B \end{cases} \quad (4.55)$$

$$\tilde{\psi}(\omega) = C_{m+n}^* \tilde{\phi}(\omega + m\Delta\Omega) + C_{m+n} \tilde{\phi}(\omega - m\Delta\Omega), \quad m > 0 \quad (4.56)$$

Here we have introduced the following quantities:

- the coefficients: $C_{2k} = 1$, $C_{2k+1} = i$ (i : *imaginary unit*);
- the nominal band width: $\Delta\Omega = 2A + B$ where A and B are two positive parameters (Fig. 4.7);
- the monotonically increasing function ν_n :

$$\nu_n = \frac{B(x; n, n)}{B(1; n, n)}, \quad B(x, a, b) = \int_0^x t^{a-1}(1-t)^{b-1} dt \quad (4.57)$$

where $B(x, a, b)$ is the Beta function and the n parameter determines the shape of the scaling function.

r_s	sampling rate
$\Delta\Omega$	nominal band width
T	time resolution
Ω	maximum angular frequency detected
L	level number
ΔF	$\Delta\Omega/(2\pi)$
Δf	frequency resolution $\Delta F/2$

Table 4.3: Adopted notation.

The basis functions useful for the data transformation on the TF plane are characterized by frequency-bands included in the frequency interval $[-\Omega, \Omega]$. Here $\Omega = \pi r_s$ and, due to the Sampling theorem, is the maximum angular frequency of the signal that can be represented by the data. Thus defining the parameter

$$M = \frac{\Omega}{\Delta\Omega} = \frac{T}{2\tau} = \frac{Tr_s}{2} \quad (4.58)$$

we can redefine the functions \tilde{g}_{nM} as

$$\tilde{g}_{nM} = e^{-iM\omega\tau(2n+q)} \left[\tilde{\phi}(\omega + \Omega) + \tilde{\phi}(\omega - \Omega) \right], \quad |\omega| < \Omega \quad (4.59)$$

where $q = 0$ if M is even, $q = 1$ otherwise.

Through these new \tilde{g}_{nm} with $(0 \leq m \leq M)$, two orthonormal and complementary (time shift difference of $T/2$) bases on $[-\Omega, \Omega]$ can be introduced

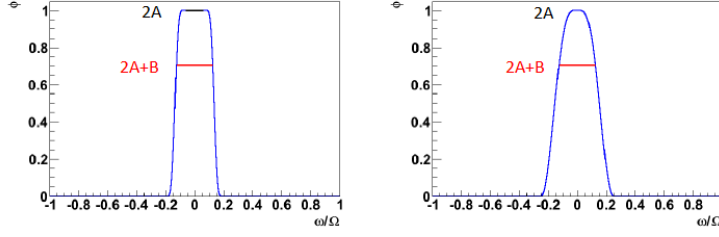


Figure 4.7: The plots show $(\phi(\omega))$ and highlight the defining parameters: the width of the top at region (black) is $2A$, the transition regions (blue) are defined by B , and the red line spans the nominal band width $2A+B$. The shape of the transition region depends on the parameter n in ν_n ; $n = 4$ for the left plot and $n = 2$ for the right plot.

and therefore the WDM expansions become

$$\begin{aligned}
 w_{n0} &= \tau \sum_{k \in \mathbb{Z}} x[2nM + k] \phi[k] \\
 w_{nm} &= \tau \sqrt{2} \operatorname{Re} C_{m+n} \sum_{k \in \mathbb{Z}} e^{i\pi km/M} x[nM + k] \phi[k] \quad , \quad 0 < m < M \quad (4.60) \\
 w_{nM} &= \tau \sum_{k \in \mathbb{Z}} (-1)^k x[2nM + qM + k] \phi[k]
 \end{aligned}$$

and

$$\begin{aligned}
 \hat{w}_{n0} &= \tau \sum_{k \in \mathbb{Z}} x[(2n+1)M + k] \phi[k] \\
 \hat{w}_{nm} &= \tau \sqrt{2} \operatorname{Im} C_{m+n} \sum_{k \in \mathbb{Z}} e^{i\pi km/M} x[nM + k] \phi[k] \quad , \quad 0 < m < M \quad (4.61) \\
 \hat{w}_{nM} &= \tau \sum_{k \in \mathbb{Z}} (-1)^k x[2nM + (1-q)M + k] \phi[k]
 \end{aligned}$$

These transformations are approximately orthonormal, because of the filter $\phi[k]$ needed truncation. Anyway the error introduced by this process is practically insignificant.

Therefore the WDM transform naturally introduces two complete representations of the data in the TF plane, thus ideally they carry redundant information. In reality this double data transformation can be used to have better descriptions of signals whose amplitude, in one of the two representation, is divided in two adjoining pixels, becoming too low to be selected.

The practical advantages of this new representation are:

- the implementation of a faster transformation;
- the introduction of shorter transformation filters, which implies a better time localization of the event;

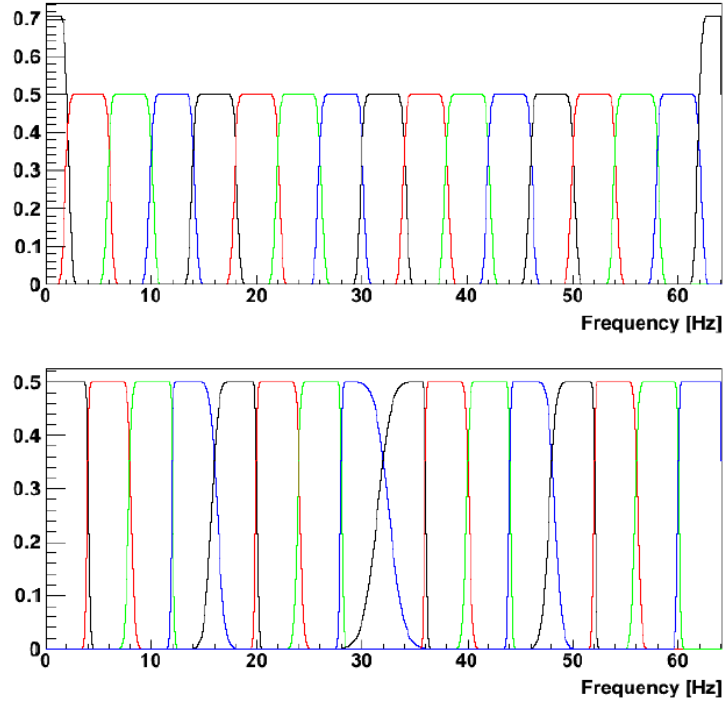


Figure 4.8: Spectral Fourier amplitudes of the basis functions for WDM transform (top) and binary Meyer wavelet (bottom).

- the application of a transform characterized by more limited spectral leakage, which entails a better frequency localization of the GW candidate.

$\Delta F \cdot T = 1$
$\Delta f \cdot T = 1/2$
$T = 2^L / r_s$
$2M = (r_s/2) \cdot 1/\Delta f$
$2M = 2^L$

Table 4.4: Useful relations, for notation see the table 4.3.

Multi-resolution analysis and principal component extraction

The cWB algorithm decomposes the available data streams in different levels to obtain the best representation of the signal. Then in the 1G version, and also for the 2G pipeline when wavelet analysis is selected, the pipeline according to the signal characteristics decides the **optimal level**. Differently

after the data decompositions determined by the WDM transform, a new process is applied: the principal component selection. Instead of selected one levels the algorithm chooses the most energetic pixels which describe the signal. This procedure requires to be very careful to maintain the independence of the collected information. The procedure is conducted following a catalogue which describes how, after the selection of a pixel, remove its relative information from all the remaining levels. Actually the principal component selection does not perform a perfectly complete and independent characterization of the events. The introduced new representation of the GW candidate on the TF plane is very useful to describe compact binary coalescences, which are characterized by shapes better represented by pixels of different levels. The improvements on the event description are very important because they imply the selection of less pixels. This means that the energy is better divided between the pixels so the selection and the consequent event representation are more reliable.

Trigger selection

Any detector data stream are separately converted in the TF plane, where they are represented by pixels whose time-frequency widths are defined by the level (Tab. 4.4). For any analyzed level and for any involved detector the pipeline selects the most energetic pixels, called **black pixels**. The number of these on-pixels depends on their amplitude indeed they correspond to a fixed tail of energy distribution. The remaining pixels are the **white pixels**. After this first process a coincidence study is performed for each level, so that only the pixels appeared on the data stream provided by all the detectors surviving this stage. The procedure is applied considering the possible detection delays. The remaining black pixels determines, in each level, the definition of clusters. They are composed by the selected pixels and the ones around them, which can be both black (**core pixels**) and white (**halo pixels**). Then the information so obtained in the different levels is collected in structures called **super clusters**. In the 2G analysis an updating on the selection procedure is introduced to better identify chirping signals. This consists in labelling as black if it is satisfied a particular condition concerning its time frequency position. This new process is applied only for pixels near original black ones and allows the selection of data standardly rejected (relative low energy excess). Other two additional parameters are also introduced to implement the union of clusters different for default. These two quantities represent the maximum pixel distances, in time and frequency, allowed to consider them belonging from the same event. The final process of the pipeline consists in the individuation of the pixels which better describe the reconstructed event. As shown in the previous paragraph, depending on the chosen analysis and on the target signals two possibility for last pixels

selection are implemented: the optimal level and the principal component extraction. Here the likelihood method are newly applied. The likelihood is calculated at different steps of the analysis: pixel, cluster and multi-cluster, to perform several checks.

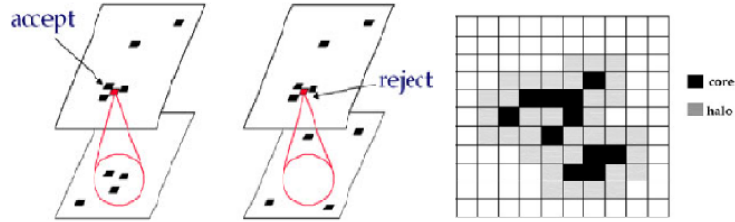


Figure 4.9: On the left: acceptance and rejection of the black TF pixels. In the first column, the black pixel in the above TF layer is accepted if the black pixels identified within a desired TF coincidence window in the lower layer show a combined strength above some threshold. In the second, the black pixel is rejected as no black pixels were identified within the TF coincidence window. On the right: pictorial representation of a TF cluster. Original image in [43].

4.3.3 Enhancement of background statistics

To increase the available data and therefore to analyze the statistical properties of the glitches (background events), a tricky was found: the application of time shifts on data sets. This procedure incredibly increases the available independent triggers without an excessively growing of the computational load required. First we want to assure the noisy origin of the triggered events, for this reason the shift is much greater than the time needed by the a GW to travel the distances between the detectors ($t_{maxH1L1} \sim 10.0$ ms, $t_{maxV1L1} \sim 26.4$ ms, $t_{maxV1H1} \sim 27.3$ ms). Indeed we have to consider also the signal durations. A second limit on the available shift values is that they must be multiple of the maximum time resolution of the analysis in TF in order to avoid strange situations. In the 2G analysis two kind of temporal shifts can be applied:

LAGS (Fig. 4.10): to increase the available background events the pipeline applies to each processed period a serie of shifts which can be represented by vectors

$$v_{shifts} = (0, j_2 T_s, \dots, j_k T_s, \dots, j_N T_s)$$

where each components refers to the segment (relative to the same period) provided by a specific detector, 0 corresponds to the reference

detector, T_s is the value of the minimum temporal shift available for the considerations expressed before (generally $T_s \sim 1 s$) and $j_i \in \mathbb{N}$ with $i=2, \dots, N$ are the lag numbers. Each segment, because of its limited length for any involved detector, has maximum values of possible temporal shifts due to its length. The desire to detect signal with some seconds of livetime causes the use of greater time resolution in the TF plane with respect the 1G version. This will probably provoke an extension of the time T_s , and thus the reduction of the feasible statistics provided by this procedure since the segment maximum duration remains 600 s.

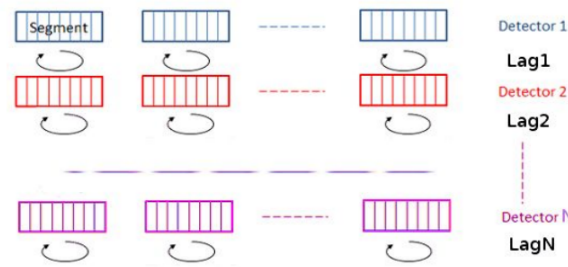


Figure 4.10: LAGS: circular time shifts are performed within the detector segments.

SUPERLAGS (Fig. 4.11): in 2G pipeline another kind of shifts is implemented: the superlags. These involve segments of different periods with the exchanging of their order for data stream collected by $N - 1$ instruments (for the reference detector the segment order is the original). Then the lag-mechanism is newly performed: temporal shifts is applied to the time series provided by interferometers.

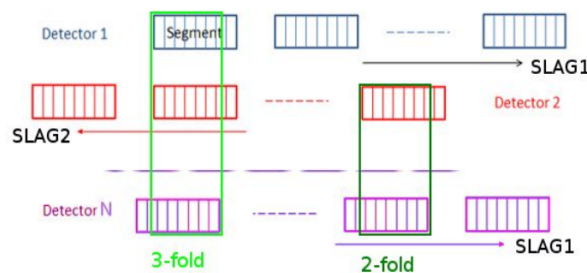


Figure 4.11: SUPER LAGS: time shifts are performed between different segments.

To estimate some of the background properties a very useful quantity is the **live time**. This time, also called the observation time and it is the total analyzed time determined by the coincidence periods between all the instruments of the network. Therefore it increases with the introduction of the time-shifts because with the application of this strategy new data combinations are provided.

4.3.4 Waveform parameter reconstruction

The cWB algorithm has also the purpose to characterized as well as possible the detected events. The main features of a GW candidate which can be estimated by the data are: h_{rss} , SNR, central-time, central-frequency and source coordinates. All of them constitute the *parameter reconstruction* (estimates) provided by cWB analysis. These parameters describe two different source aspects: its location (*Estimate of the source sky location*) and the main properties of the GW emitted (*Waveform reconstruction*).

Waveform reconstruction

Ideally the aim of this study, performed for each cluster, would be the total characterization of the event. A waveform is completely characterized by the time evolution of both its polarizations $h_+(t)$ and $h_\times(t)$. Anyway this is a very ambitious goal because it requires the inverse solution of the likelihood equation. The strategy adopted by cWB is to compute a characterization of the candidate for each the involved detectors. Thus at the end of the analysis N representations for any event are available, each one showing the single detector response. To obtain these features the pipeline collects the TF pixels surviving the several selected and cuts by the likelihood analysis, and then applies to them the inverse transformation. In this manner cWB isolates the part of the collected data which describes the detected excess of energy, and thus the event.

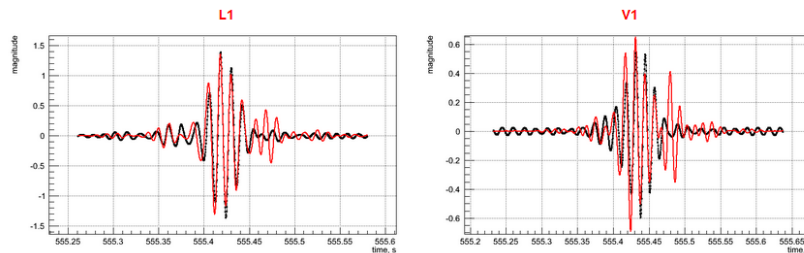


Figure 4.12: Comparison between whitened reconstructed (red) and injected (black) waveforms. The sensitivity curves used are the ones designed for the 2G instruments. The left picture refers to L1, the right one to V1.

Source sky location

To evaluate the most reliable direction for the emission of each the GW candidate, the pipeline calculates the likelihood relative to any sky position. This process is performed taking into account the dependence on the source location of the antenna pattern functions and the time delays on the signal acquisition between the different detectors. Therefore the likelihood calculation implies the necessity of a procedure which applies time shifts on the data. These shifts have to be compatible with the delays induced by different source sky positions.

To simplify the implementation of the combined likelihood method these temporal-offsets are added in the TF plane. A temporal shift of τ applied on data provided by the k -detector and represented in a fixed layer, provokes in a pixel with (i, j) position in the TF plane the transformation:

$$x_k(i, j, \tau) = \sum_{pl} D_{pl}(\tau, j) x_{i+l, j+p} \quad (4.62)$$

where D_{pl} are the delay time filters.

The process allows to evaluate for each sky position the likelihood value. Anyway this parameter is normally considered not sufficient for a correct estimate of the source location. Therefore to better evaluate the most reliable GW direction for each sky position is introduced a new quantity: the **Sky Statistic**. It is defined as follow:

$$S_i = \frac{L_i \cdot E_c}{E(E - L_i + |E_c|)} \quad (4.63)$$

where E is the totally normalized energy of the signal and noise, L_i is the likelihood calculated for the i position and E_c is the coherent energy (Sec 4.4.1), which is expected to better suggest the right coordinates. Concerning the source location an important progress has been achieved with the implementation of the 2G analysis (WDM and Principal component extraction): the direction individuation is improved by a factor 2-3 with respect the results obtained by the 1G pipeline [44].

4.4 Post-Production stage

The maximum likelihood approach well discriminate the glitches from the signal in the assumption of Gaussian and stationary noises. Unfortunately the real data are affected by disturbances which often do not exhibit these qualities. Consequently the effectiveness of the likelihood method in the rejection of background events reduces. The post-production is an additional stage introduced to mitigate this problem and so to enhance the pipeline performances. It consists in a new evaluation of the analyzed data and of

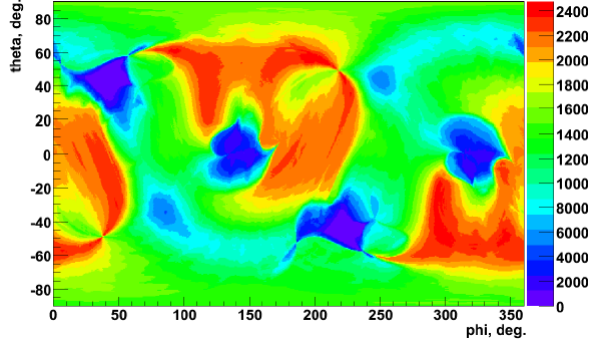


Figure 4.13: Example of the likelihood behaviour as a function of sky coordinates for an event reconstructed from a background analysis.

their statistical properties, indeed all the available information about the events are collected in the output files produced in the production stage. Therefore the application of this further procedure do not need the re-run of the data by the cWB analysis. With this final stage new cuts are introduced to improve the event selections. However the relatives thresholds on the involved quantities depend on the available detector network and on the desired search. For these reasons they are differently chosen according to the specific situation. The main cuts are applied on the **network correlation coefficient** and on the **effective correled SNR**.

4.4.1 Network correlation coefficient

In the DPF the maximum likelihood (4.39) can be written in a $N \times N$ matrix. Indeed

$$\begin{aligned}
 \hat{L} &= (X \cdot e'_+) ^2 + (X \cdot e'_\times) ^2 \\
 &= \sum_{n=1}^N \sum_{m=1}^N (X_m e'_{+m} X_n e'_{+n} + X_m e'_{\times m} X_n e'_{\times n}) \\
 &= \sum_{n,m=1}^N \hat{L}_{mn}
 \end{aligned} \tag{4.64}$$

where e'_+ and e'_\times are the unitary vectors.

This quadratic form includes terms which relate the different detectors, and thus we can define the **coherent energy** E_c as the sum of the off-diagonals matrix elements

$$E_c = \sum_{n \neq m} \hat{L}_{mn} \tag{4.65}$$

We can exploit this quantity to define the **network correlation coefficient**

$$cc = \frac{E_c}{E_c + E_{null}} \quad (4.66)$$

where $E_{null} = |X - \xi_\sigma|^2$ which represent the reconstructed noise energy in terms of its RMS.

This represent one on the most important parameter defined by cWB algorithm and used for the background-signal discrimination. It is a measure of the coherent energy in comparison with the noise one.

4.4.2 Effective Correlated SNR

The coherent energy is also used to define another well discriminant quantity: the **effective correlated SNR**, which represents a sort of coherent SNR [45]

$$\rho = \sqrt{\frac{\langle E_c \cdot cc \rangle}{N - 1}} \quad (4.67)$$

This parameter can help in the signal recognition. This important property can be understood considering a completely coherent signal. These kind of events are characterized by a network correlation coefficient equal to one ($cc = 1$) for each pixels and by a coherent energy equals to the sum of the likelihood diagonal terms. Indeed a coherent energy greater then the uncorrelated one represents an unphysical condition. Therefore for completed correlated signals we find

$$\begin{aligned} \rho &= \sqrt{\frac{\langle E_c \cdot cc \rangle}{N - 1}} \\ &= \sqrt{\frac{\hat{L} \cdot 1}{2(N - 1)}} \\ &= \sqrt{\frac{\sum_{k=1}^N \xi_k^2 / \sigma_k^2}{2(N - 1)}} \\ &= \sqrt{\frac{\sum_{k=1}^N SNR_k^2}{2(N - 1)}} \end{aligned} \quad (4.68)$$

This last equation shows how the effective correlated energy is related to the likelihood and consequently network SNR. In view of the above the discrimination between signal and background events is performed considering that for the formers $\rho \approx \sqrt{\sum_{k=1}^N SNR_k^2 / (2N - 2)}$ while for the latters hold the disugualiance $\rho < \sqrt{\sum_{k=1}^N SNR_k^2 / (2N - 2)}$.

4.4.3 Post Production effects

The introduction of cuts on the key quantities the network correlation coefficient cc and the effective correlated SNR ρ are particularly effective. Indeed they represent two characteristics of the events which differ a lot between background and signal populations. Indeed we expect excesses of noise characterized by low values of cc and thus rejected with a cc cut application. Viceversa for signals the cc value expected is near to one, and therefore they should survive to the cut procedure. Moreover also the ρ helps the signal-background discrimination, indeed in presence of events with a large value of cc , but due to noise fluctuations, excesses of energy are rare. Thus the selection of events with ρ greater then a thershold saves the majority of the signals loosing a lot of glitches.

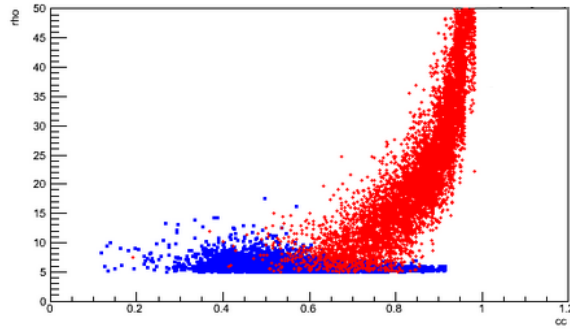


Figure 4.14: ~ 8000 simulated waveforms (red) and ~ 8000 glitches (blue) represented in the cc - ρ plane.

Chapter 5

Artificial Neural Networks for signal recognition

Going into the problem ...

In 2015 the second generation of interferometers will progressively become operative, starting the new data acquisition. The achievement of the design sensitivity curves will incredibly enhance the chances of a GW detection and the introduction on the final instrument configuration of the KAGRA observatory will considerably improve the performances of the analyses.

Unfortunately the measurements will probably begin with the only LIGO observatories, and this will considerably lower the effectiveness of the searches based on a coherent analysis. Particularly problematic can be the detection of unmodelled signals which are in effect based on the correlation analysis.

Also the performances of the Waveburst algorithm will therefore be initially compromised. In the TF plane, the pixels selection will decrease its efficacy, particularly the pixels rejection will become harder. Moreover even the network correlation coefficient, which is one of the most important feature for the signal-background discrimination (see Sec. 4.4.1), will lose effectiveness in comparison with the analyses performed on three detector data streams. The cWB pipeline was therefore improved to perform an analysis competitive also under the expected hard initial conditions. According to this scenario, though remaining robust for unknown waveforms, the algorithm was modified also with the introduction of some tricks aimed at the detection of chirp-like signals. The chirping behaviour is the main feature of the GWs predicted by models for the compact binary coalescences, which represent the most promising GW sources.

In this context, a new idea arises in the cWB group to improve the signals-glitches discrimination. The basic concept is to recognize different signal classes and assign them specific subset of False Alarm Rate instead of ranking any candidate against all the False Alarms. The development of this signal classification starts from the easiest case of waveforms compatible with

compact binary coalescences. According to the models, this kind signals are described by well known signatures which are also really peculiar (see equation 2.11). For these characteristics the expected GWs emitted by coalescences of binary systems are extremely difficult to mimic. Therefore we foresee a final better glitches rejection: the achievement of significant improvements on this discrimination substantially constitutes the main purpose of this project.

The implementation of specific signal searches on an unmodeled pipeline, like cWB, allows a comparison between the two different strategies adopted. Adding astrophysical constraints in Waveburst analysis means the reduction of the parameter space. On the contrary for approaches based on the template matching the introduction of new limits (like spin, eccentricity ecc..) complicate the template construction with an increasing of the parameter space.

Two main different approaches are applied by cWB Burst group to the identify chirp-like signals on the data: a **chirp-mass estimation** and a **TF pattern recognition** performed by artificial neural networks.

In this chapter we will introduce machine learning techniques (Section 5.1) and artificial neural networks (ANNs) (Section 5.2). The we will focus on algorithm of multilayer perceptrons (MLPs) (Section 5.3)

5.1 Machine learning techniques and GW detection

The emissions of GW transients, for the majority of the dragged phenomena, are provoked by poorly understood physical conditions and consequently are characterized by unknown features. For this reason and for the lack of observations the search results will strongly depend on the capability of the analyses to distinguish GW in any form from glitches produced by non stationaty and non Gaussian noise tails.

In the last science run (S6) the expected rate of detectable GWs was extremely low, $\sim 10^{-9}$ Hz, in comparison with the one referred to the glitches, ~ 0.1 Hz [46]. Also in the advanced detector era this difficulty, even if lowered by the several innovations on noise attenuation, will probably persist for burst signals and, as for the previous analyses, it will be particularly marked for poorly modeled searches. It is thus a common goal to reduce the glitch impact on the GW searches.

According to this context several efforts have been made by the GW detection community to individuate the most discriminant characteristics of the signals with respect the glitches. Some of them also concern the applications of Machine Learning techniques. In effect one of the most important purpose of this kind of informatic structures is the discovering of hidden relations between the quantities used as inputs.

5.1.1 Machine Learning

[47] Machine learning is a process through which the implemented system improves the data interpretation. Referring to informatic tools an algorithm is learning whenever a transformation happens on its structure or program in favour of a better representation of the input information. Many of the approaches dragged to this topic are inspired by theories about human and animal capability acquisition. However developments of the machine learning techniques have also helped the psychologists and the zoologists in the comprehension of some mechanisms adopted by living creatures.

The main tasks of machine learning algorithms are associated to “intelligent” decisions, data interpretation and behaviour, as can be: recognition, regression, planning, prediction and classification. Moreover, as announced, the first evaluation step can be oriented in action execution (robot control). One of the most important mechanism at the basis of these informatic structures is the learning by examples. This represents the introduction of algorithms not completely determined and thus opens the possibility of taking into account also relations not yet and not only discovered. Concerning the data-analysis the principal reasons for the introduction of machine learning approaches are:

- the implementation of mechanisms able to analyze a multitude of information, which is difficultly treated by explicit procedures;
- the possibility to extract some non-trivial relations which links the data (*data miming*);
- the possibility to implement algorithms able to represent unknown connections between the data. Specifically the informatic-tool structure changes to accurately interpret also input/output couples of data indescribable by concise relations (*data interpretation*).

These general purposes makes these informatic tools very attractive in several disciplines, which therefore have contributed in their developments and branches. In the following are reported the main fields interested in machine learning.

Statistics In statistics one of the most challenging task is understand the optimal manner to exploit available samples of unknown probability distribution to create algorithms able to decide the distribution from which new samples belong. The same optimization problem can be reported in case of unknown function, only described by some points, which should be used for the interpretation of new data. The methods implemented to treat these issues can be interpreted as machine learning because they are based on a set of examples.

Adaptive Control Theory The adaptive controls are techniques whose aim during their operating period, is to estimate some parameters and so to adjust, according to the environment changes. Thus the robot control present some aspects of the input interpretation problem.

Psychological Models Many psychological studies are performed on human learning processes. On this field particularly interesting searches concern the associative memory, the schematic representation of the information by the human mind and the mechanism activated for decisions. They have respectively stimulated the implementation of associative algorithm, semantic networks and early decision trees.

Evolutionary Models Inspired by animal evolution some researchers have implemented algorithms which mimic this process for computer programs and have proposed these strategies of improvements as learning methods.

Artificial Intelligence Artificial intelligence is interested in machine learning from its first development. Its purpose is to mimic some human behaviours and to achieve this goal two main processes are needed: parameter estimation and learning by examples. Particularly investigations have been made on analogy learning and on rules on the basis of decisions and selections.

Brain Models The topic of brain models have inspired *Artificial Neural Network* implementation. This topic have developed theories about the operations of biological neurons. One simplified representation of the basic mechanism associates the neurons to non linear elements, which are stimulated by the input data.

Many algorithms have been realized to satisfy all these requests. Indeed these kinds of problems have motivated the development of strategies, from which several flexible and powerful devices arise. In the following we focus on three of the most popular machines which apply the learning analysis: decision trees forming a random forest (**RFs**), support vector machines (**SVM**) and artificial neural networks (**ANNs**). All of them have been exploited also in gravity, and specifically all of them have been tested in GW analyses to improve the glitch rejection.

Boosted Decision Trees

[48] A boosted decision tree (**BDT**) is a collection of decision trees developed by the same training set but characterized by different weights, whose final judgment on an event is determined by the kind of output more voted. This approach has the same goal of SVM method: discriminate signal from

background events, but the strategy is however very different. These device are composed by several nodes where a single variable is considered and the best cut on its value is applied. The definition of the decision tree structure starts from the so called root node, which, according to the properties of the full training set, selects the most different feature between the two categories. It is used by the algorithm to perform, with the implementation of a discriminant threshold, the first separation on the considered events. After this training sample split, one discriminant node for each the new subset is defined. Then the process is analogous to those described for the root node: a variable is selected according to the training set characteristics and a cut is applied. The procedure is iterated until one of the following two conditions is satisfied: the achievement of a too small subset for the introduction further nodes or the reaching of maximum/minimum signal purity.

To more effectively separate the events belonging from two the classes several decision trees are constructed starting from the same training set. The two main manners to perform these “forests” are boosting and bagging.

Boosting Bigger weights are applied to wrongly classified training events.

In such manner the multiple applications of this boosting process generate a forest of different tree set and the performances are improved.

Bagging The creation of a decision tree forest happens without taking into account the previous performances. The definition of the set of decision trees is based on a stochastic resampling (bootstrap) of the given training set. Each of the new subsets is used to build a single decision tree.

In light of the previous description the main task provided by this kind of analysis is the event classification.

[49] Recently some algorithm have begin tested BDTs to improve the signals-glitches discrimination. Specifically the analysis performed concerns data provided by Virgo and LIGO observatories triggered by GRBs. The signal events are constructed by the injections of four classes of waveforms: circular sine-gaussian (CSGs), binary neutron star inspirals (BNS), chirplets and white noise bursts (WNBs). Several tests are performed varying the classes included in the training test and checking the variables widest used by nodes. The results are quite interesting: the performances of the basilar analysis, provided by the X-PIPELINE [49], are improved or at least unchanged by the introduction of this further evaluation stage. Even training the BDTs on only CSG and BNS the algorithm is able to recognize some of the waveforms belonging to the other two classes. In this manner the robustness of this method is tested. Moreover the results are compatible and generally more promising then the ones provided by the only X-PIPELINE. The minor changes concern the BNS category, for which no significant improvement on sensitivity has been recorded. On the contrary the CGS class has shown

improvements on the detection of $\sim (35 - 55)\%$. For other two types of waveforms the the performances increase differently from their treatment. More surprising is the result of the studies concerning the quantities most exploited by the decision tree nodes. This analysis shows that the cluster energy of the single detector, the bandwidth and the signal duration play very important roles, that the only X-PIPELINE does not value.

Artificial Neural Networks

The artificial neural networks (ANNs) are algorithms inspired to the operating principle of brains (for more details see Sec. 5.2). // The generalism at the basis of this approach allow the use of these informatic instruments to perform different tasks as regression, classification, pattern recognition and so on. This flexibility attracts several fields, including gravitation. Concerning the GW detection, the most popular applications of this analysis have again the aim to discriminate noisy events from signal. usually the approach to this problem is focusing on the glitch identification, and sometimes on their classification. The motivation of this choice lies in the lack of detected GWs. Different studies, more or less recent, develop the treatment of ANNs to achieve the recognition of events produced by noise (for examples [50] [51] [52]). They show an important improving in the glitch individuation in comparison with the standard deterministic analyses. Moreover these works suggest that the application of this models do not reduce significantly the signal detection and that the glitches can be partially categorize in different classes related to their noise origins.

Support Vector Machines

[53] [48] Support vector machines are algorithms whose aim is to find the best separating hyperplane. They were introduced in 1960s to discriminate linearly separable ensembles however now their developments are generalized to perform non linear separating functions. SVMs are exploited to solve classification and regression problems and thus can be useful in many fields, for example: face detection, character recognition, bioinformatic and text categorization.

The operating idea of SVM algorithms is to define the best hyperplane which separates background and signal events. To perform this task the distance between the separating hyperplanes and the nearest examples *support vectors* is maximized. In presence of non linear separating problems the data are mapped in a higher dimensional space, where the events can be newly distinguished with the implementation of hyperplanes (see Fig. 5.1). To reduce the computational demanding Kernel functions are used. [46] A recent study of the LIGO collaboration has shown the capability of these tree approaches (ANN, RF, SVM) to individuate glitches from the data analysis

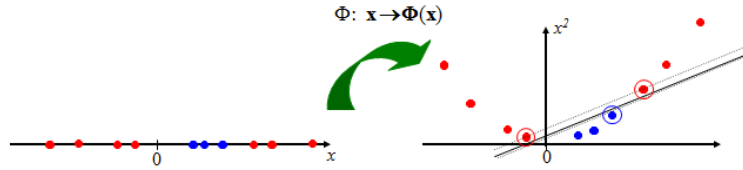


Figure 5.1: SVM operating principle: example of 1D-data non linearly separable mapped in a bidimensional space for the construction of a separating hyperplane.

of some quantities provided by the auxiliary channels. The main idea of this work is to classify differently the time series containing noises detected by the auxiliary channels. All the three structures can be usefully adopted to control the information carried by the several auxiliary channels, even if some of them are redundant or irrelevant. The introduction of such multivariate analysis are particularly interesting also for the form through which the results are provided. Indeed the output of these algorithms is a continuous variable which allow a more reliable approach to its treatment: this further information can be use to “softly” characterize the GW candidates. Moreover these algorithms, thanks to their flexibility, will probably permit to discover unknown relations with the addition of new inputs, as for example an index of the interferometer alignment quality. On the other hand the results obtained by this study shows a quite low efficiencies in glitch recognition of single detectors for a fixed false alarm probability of $\sim 1\%$: from $\sim 30\%$ to $\sim 56\%$. The performances of these multivariate analyses (MVA) are compared to the one of the Ordered Veto List (OVL), an algorithm used for the glitch identification based on comparisons between the gravitational channel and a single auxiliary channel. The results are similar, showing the poor correlation between different auxiliary channels.

5.2 Artificial Neural Network

1cite47 [55] The main functions of human nervous system are primarily realized in three stages:

1. receptors associate to the external stimuli electrical impulses which then are send to the neural network;
2. the neural network elaborates the information and consequently chooses the best decision;
3. actuators convert the electrical impulses belonging to the neural network in actions.

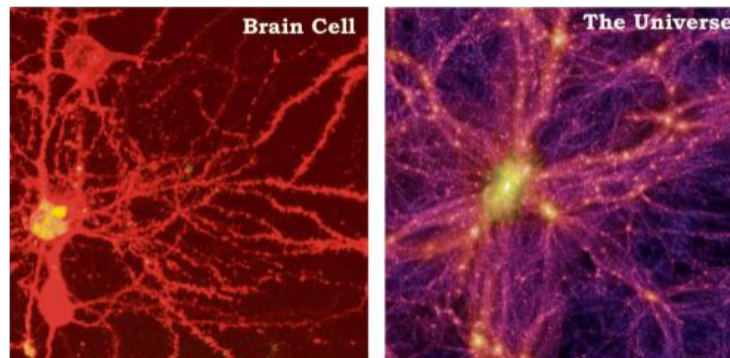


Figure 5.2: The universe structure is incredibly similar to the neural network one.

Therefore the neural network play a fundamental rule in learning processes, elaborating the data provided by the external environment.

5.2.1 Biological neural networks vs artificial neural networks

The biological neural network is composed by a multitude of nervous cells, called **neurons**, all connected to each other with nervous fibers.

The **dendrites** receive the information from other neurons, *inputs*, and drive them to the **soma**, which constitutes the cell nucleus. Here the inputs are evaluated and elaborated: the soma calculates a weighted sum of the electrical impulses coming from the dendrites. Indeed the amount of the carried information depends on several factors: strength of the inputs signals, importance of the dragged connections, *weights*, and above all the activation threshold of the specific neuron. This data analysis made by the soma determines two different behaviours: the passive and the active one. The **passive behaviour** consists on the non-generation of impulses by the soma; instead the **active behaviour** takes place in presence of inputs whose weighted sum reaches a sufficient value for the production of an electric signal, called spike. The result of the calculation unit operation, *output*, is transmitted by the **axon** to the **synapses**, which represent the connectors between different nervous cells. Through the presynaptic process the electrical impulses are associated to the release of a chemical substance (neurotransmitters) which allow the passage of the information from the axon of the pre-synaptic neuron to the dendrites of the post-synaptic neuron. Then the chemical substance is newly related to electrical impulses by the post-synaptic process. The artificial neural networks are informatic algorithms based on the same mechanism. They are composed by calculation units (neurons) which evaluate weighted sum of the inputs applying to it an activation function. The analogy between the biological and the informatic structures of these neural

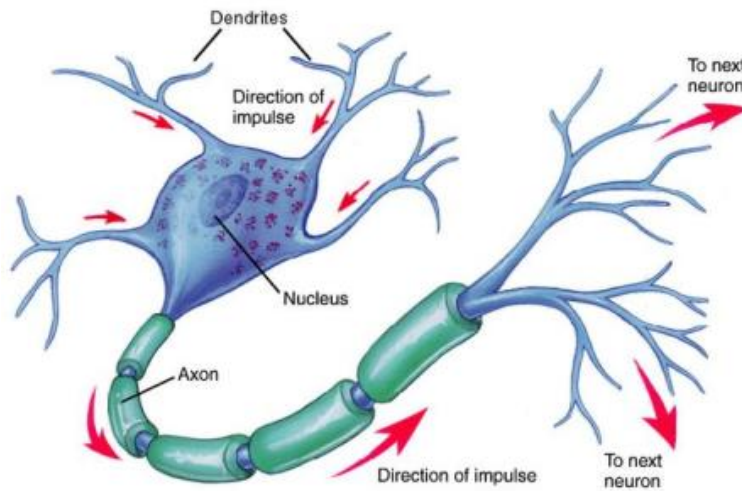


Figure 5.3: Schematic representation of a biological neuron.

networks is illustrated by Fig. 5.4. These systems are particularly interest-

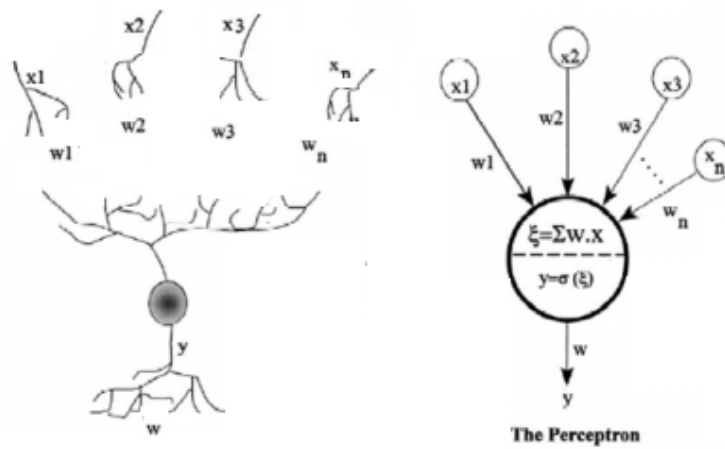


Figure 5.4: Schematic representation of an artificial neuron and a biological one in presence of n inputs x_i , whose corresponding synapses are weighted by w_i . The calculation unit performs the weighted sum ξ and evaluates it with a threshold b and an activation function σ , which gives y as output.

ing because of their capability to learn the “right” behaviour by examples. The learning process is provided by changing the weight values associated to the connections (synapses) according to an optimization procedure. The main properties of an artificial neural network ready for the evalua-

tion of input signals derive from the network structure and from the neuron characterization.

Network structure Chosen the number of the neurons of the network and their organization, the network structure is principally determined by the strenghts of the synapses (weights) and by the type of connections between neurons. Two kinds of networks can be defined distinguishing the directions of the data propagation: the *feedforward* and the *recursive* neural networks. In the first case the structure can be represented by an oriented graph, while in the latter the architecture is characterized by the presence of some feed-back connections between the neurons, which therefore need to be dynamic (see the next step *Neuron*).

Neuron The neuron are characterized by different properties:

- threshold: each neuron applies a different offset (the threshold) on the weighted sum on the inputs;
- activation functions: different functions can be used in the calculation unit to obtain the output. They can be linear or non linear with different complexity. The most popular activation functions are the sign one and the sigmoid;
- consideration/no consideration of the input time evolution: the two possibilities define respectively *dynamic* and *static* networks.

5.2.2 Learning procedures

[56] The main idea on the basis of these algorithms is to define, usins a set of examples called **training set**, an informatic structure ables to exactly interpret the input data. One important characteristic to evaluate in these devices is their ability to generalize the learning to samples excluded by the training set.

The learning procedures train the neural networks modyfing the weights of the connections and thus miming the natural process which changes in time the synapsis thickness, weaking or reinforcing the links between neurons. The learning algorithms can be divided in two categories:

unsupervised learning , where the outputs of the training set are not available or the output neurons are not defined; here the network parameter are defined by clustering techniques applied on the input training sample;

supervised learning , where the weights are calculated taking into account the desired output of the network with the implementation of a process

which minimizes on the training set the **error (or cost) function**. This is usually defined for each ANN output y by two different relations:

$$E(w) = \frac{1}{2} \sum_{p=1}^P (\|y(x^p, w) - t^p\|^2) \quad (5.1)$$

$$E(w) = - \sum_{p=1}^P (t^p \log [y(x^p, w)] + (1 - t^p) \log [1 - y(x^p, w)])$$

where the label p refers to the training set composed by P examples, t is the target vector, i.e. the vector desired at the network output, w and x are respectively the network weight the input vectors. A further distinction in the learning strategies concerns the temporal use or acquisition of the training set.

On line learning : this approach is generally used when the training events are acquired in progression during the learning process. The strategy is to update the network parameters after the evaluation of each single example provided by the training set.

Batch or off-line learning : to implement this kind of algorithms the full training set has to be available before the learning starts. All the events belonging from the training set are considered for each upgrade of the network weights.

5.2.3 Applications

[57] For these characteristics the artificial neural networks are widely used for two main purposes: the association of different information and the interpretation of the inputs by a function.

Concerning the memory association a distinction can be performed between *auto-associators* and *pair associators*. The former class is composed by systems whose aim is reaching the association of patterns. Input configurations of the training sample are stored in the “memory” of the so implemented network. In this manner the response of these algorithms to patterns similar to the train ones (changed for example by noise introduction or by a cut) is their recovery or completion. Instead a pair-associator relates an input configuration (es. A) to another (es. B), so that, after the train, the ANN is able to recognize a pattern ($\sim A$), also slightly different from the training examples, and to return the other which corresponds to (B). Instead we are particularly interesting in solving classification and regression problems, which belong from the class of data interpretation by a function. For these kinds of problems the aim of the ANN is to conform its parameters to mimic such function with an adequate approximation. The performances achieved

depend above all on the choice of the learning variables.

Anyway ANNs are extremely suitable for several applications, including: image compression, stock market prediction, signal filtering, controls and diagnoses.

In the following chapter is instead illustrated a branch of another interesting application: the **character recognition**. Indeed we will use these devices to recognize the time-frequency trace of a GW compatible with the emission of compact binary coalescences and thus to mitigate for them the problem of signal-glitch discrimination.

5.3 Multilayer perceptron

Multilayer perceptrons are particular architectures of neurons which define a subset of ANNs (Sec. 5.3.2). In these devices the neurons are grouped in structures called **layers**. Here we focus on feedforward networks composed by static neurons and trained by supervised learning algorithms.

We are interested in a function approximation; in this field the ANNs performances are ruled by the approximation theory. ANNs are characterized by the consideration of a discrete serie of data in the structure definition and by the choice of the function class exploited for the approximation task, which usually depends on the weights in a non-linear manner. These properties make the application of ANNs very useful, for example for their capability to construct a link between the input-output quantities not yet discovered, but introduce some problems and topics which need to be developed. We can start from the discretization of the data, which causes the existence of an infinite number of functions able to correctly interpret the input-output couples of the training set. Another issue linked to the data is the possible presence of noise, which can affect them and thus the resulting network parameters. Finally other questions arise concerning the characterization of the approximation degree in function of the input number and of the ANN structure and other approximation properties. However a result seems to be clear: the multilayer perceptrons are *universal approximators*, namely any limited function can be approximated with an arbitrary precision by an ANN with a finite number of hidden layers [58] (see 5.3.2).

The learning problem can be summarized in the definition of the best process which describes the training data, building an algorithm able to recognize the general properties of the inputs. A fragile equilibrium is therefore needed between the correct training events interpretation and the capability of generalization: too complex models can be limited at the right evaluation of the only training set, while too simple models define coarse relations between inputs and outputs.

5.3.1 Perceptron

The perceptron is the informatic equivalence of the biological neuron. The main properties of a perceptron are illustrated in the following; in particular we focus on its capability to linearly classify the data by solving, under determined conditions, a system of linear inequalities. Finally the main limits of single perceptrons are shown.

Structure

A neural network is composed by elementary units of calculation called neurons. One of the simplest structure of this algorithm was proposed by McCulloch and Pitts [60] in 1943 and then developed by Rosenblatt [61]. In this model the neuron elaborates a vector of input quantities multiplying them by weights (see Fig. 5.4), computing the weighted sum and finally comparing it to a threshold value in order to return the scalar response. The neuron provides an output equals to 1 if the sum is greater than the threshold, -1 otherwise.

Formally we can define the neuron operation as follows.

Given an input vector $x \in \mathbb{R}^n$, the corresponding weight vector $w \in \mathbb{R}^n$ and a threshold θ the neuron output y is provided by the equation:

$$y(x) = g \left(\sum_{i=1}^N w_i x_i - \theta \right) \equiv g(w^T x - \theta) \quad (5.2)$$

where g represents the activation function of the neuron and in this case it can be described by the *sign-function*:

$$g(t) \equiv \text{sgn}(t) = \begin{cases} 1, & \text{if } t \geq 0 \\ -1, & \text{if } t < 0 \end{cases} \quad (5.3)$$

Other activation functions often used are:

- the *Heaviside function*:

$$g_1(t) = \begin{cases} 1, & t > 0 \\ 1/2, & t = 0 \\ 0, & t < 0 \end{cases} \quad (5.4)$$

- *sigmoidal functions*:

$$\lim_{t \rightarrow -\infty} g(t) = -1 \quad , \quad \lim_{t \rightarrow \infty} g(t) = 1$$

$$g_2(t) = \frac{1}{1 + e^{-t}} \quad g_3(t) \equiv \tanh(t) = \frac{e^t - e^{-t}}{e^t + e^{-t}} \quad (5.5)$$

where the first row expresses the meaning of *sigmoidal function*, and the second describes two important examples: respectively the *logistic function* and the *hyperbolic tangent*.

Considering for simplicity a bidimensional plane, we can easily prove that the algorithm is able to implement elementary logic operations (*and*, *or*, *not*) and thus to realize any logic function through an opportune connection between neurons. Given an activation function

$$f(t) = \begin{cases} 1, & \text{if } t \geq 0 \\ 0, & \text{if } t < 0 \end{cases} \quad (5.6)$$

in the bidimensional space the sign-evaluation of the weighted sum consists on a inequality limited by the implicit equation of a straight line:

$$\sum_{i=0}^n w_i x_i - \theta = w_1 x_1 + w_2 x_2 - \theta > 0 \quad (5.7)$$

This equation shows the opportunity to determine various separation lines by defining different values for the $n + 1$ (in this case: w_1, w_2, θ) parameters dragged. Moreover the formula (5.7) and the picture (Fig. 5.5) illustrate the

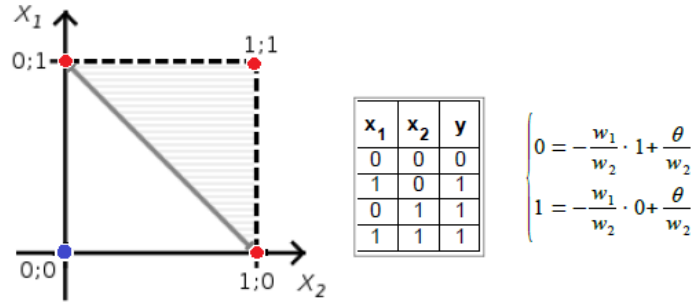


Figure 5.5: Schematic representation of the neuron operation in a bidimensional space (consider $f(t)$ as activation function). The system is imposed to obtain the *or* function but the image shows also the neuron capability of correctly classify the red and blue points as belonging to two different classes.

ability of a neuron to compute classifications of linearly separable examples. For sets of point linearly separable in a n dimensional space the classification can always be performed by the introduction of an $n - 1$ dimensional hyperplane $H = \{x \in \mathbb{R}^n : w^T x = \theta\}$ and thus discriminating the events belonging to the two different categories S and B , evaluating the sign of the *discriminant function*, i.e of $w^T x - \theta$. Formally we have that the elements belonging to the S and B classes are linearly separable and thus can be correctly categorized by the neurons if exists an $n + 1$ vectors of parameters for which is satisfied the system:

$$\begin{aligned} w^T x - \theta > 0 \quad \text{for } x \in S &\quad \mapsto \quad w^T x > 0 \quad \text{for } x \in S \\ w^T x - \theta < 0 \quad \text{for } x \in B &\quad \mapsto \quad w^T x > 0 \quad \text{for } x \in B \end{aligned} \quad (5.8)$$

where to built the relations on the right we have introduced a new dimension in both the input and the weight vectors to take into account the threshold:

$$x = (x_0, x_1, \dots, x_n)^T, \quad w = (\theta, w_1, \dots, w_n)^T, \quad x_0 = -1 \quad (5.9)$$

Therefore now $x \in \mathbb{R}^{n+1}$ and $w \in \mathbb{R}^{n+1}$. As we have announced before, the most characteristic property of the neurons, and more in general of all the ANNs, is the parameter estimation by a learning process based on the consideration of a training set of events. Given again the sign-function to obtain the output value, we can describe the training set as p couples of inputs-output:

$$T = \{(x^p, t^p), \quad x^p \in \mathbb{R}^n, \quad t^p \in \{-1, 1\}, p = 1, \dots, P\} \quad (5.10)$$

where t is the desired output of the neuron (**target**). The trained neuron, i.e. the neuron characterized by precise weights and threshold, is now able to classify also events not included in the training set (if linearly separable). This ability shows the generalization property of this kind of algorithm and defines a new tool for the event classifications called **Perceptron**.

Learning algorithms for perceptrons

For a single perceptron, as for all the ANNs, the learning process consists in updates of the $n + 1$ dimensional weight vector. In 1962 Rosenblatt proposed an algorithm able to infer network parameters which interpret correctly the training data and which are based on their evaluation.

In the following there is described the implementation of this learning method for a perceptron characterized by a sign function (corresponding to its activation function). The main idea is to consider each of the examples included in the training set and to update the weight vector every time an event is wrongly classified. In the picture (Fig. 5.6) is represented the implementation of this algorithm where we have considered, without loss of generalization, $\|x^p\| = 1$. There the counter n_{class} has been introduced to control that all the examples are correctly classified. During the iteration this updating procedure can cause wrong categorization of events previously correctly evaluated. Nevertheless if the subsets $S = \{x^p : (x^p, t^p) \in T, \quad t^p = 1\}$ and $B = \{x^p : (x^p, t^p) \in T, \quad t^p = -1\}$ of T are linearly separable, it can be proven that with a finite number of iteration this algorithm is able to find the hyperplane which divides in an appropriate manner S and B .

The operating principle of this algorithm can be described as a procedure to solve the following system:

$$Aw \geq b \quad (5.11)$$

where the vector $b \in \mathbb{R}^P$, w is always the weight vector with $n + 1$ components and A is a matrix of dimension $P \times (n + 1)$ defined by

$$A^T = (a_1, \dots, a_p) = (t^1 x^1, \dots, t^n x^n) \quad (5.12)$$

```

w(0) = 0, k = 0, nclass = 0
While nclass < P do
  For p = 1, ..., P do
    If sgn(w(k)Txp) = tp then
      nclass = nclass + 1
    else
      w(k + 1) = w(k) + tpxp
      k = k + 1
    end if
    p = p + 1
  End For
  If nclass < P then nclass = 0
end While

```

Figure 5.6: Algorithm proposed by Rosenblatt to train a perceptron.

In 1954 Agmon [62], Motzkin and Shoenberg [63] introduced an iterative method to perform adequate weights w_i for the satisfaction of the equation (5.11), which is analogous to the one proposed by Rosenblatt:

$$w(k+1) = w(k) + \eta \frac{(b_k - a^T w(k))}{\|a_k\|^2} \quad (5.13)$$

where η is a scalar parameter. When the S and B are linearly separable subset of T and $\eta \in (0, 1)$ it is assured the achievement of a weight vector which satisfies the system or the definition of a succession convergent to one of them. To lower the computational time required all the training set can be considered simultaneously, computing a batch learning method.

A generalization and development of these methods is called *delta rule* and, similarly to the previous algorithms, it can be used only for supervised learning. The main idea is to follow the gradient decreasing, searching the minimum of the error function (5.1). For the learning processes it is realized starting from a random point of the space and descending along the opposite direction of the gradient. This approach allow the achievement of the convergence to the nearest local minimum, if the procedure is correctly implemented. The gradient rule for the weight updates can be summarized

as follow:

$$\Delta w_i = -\eta \frac{\partial E(w)}{\partial w_i}, \quad w_i^{k+1} = w_i + \Delta w_i \quad (5.14)$$

where k and $k + 1$ are indexes which describe the iteration step, Δw_i is the applied changing on the weight w_i thus $i = 0, 1, \dots, n$, and finally $0 < \eta < 1$ is the *learning rate* which represents the velocity used to reach the local minimum. The learning rate is a very important parameter to choose; indeed

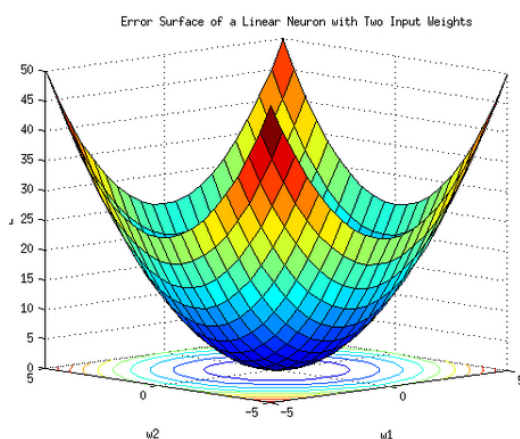


Figure 5.7: Error surface, according to the definition on the first equation of (5.1), for a perceptron characterized by a linear activation function.

with η too large the algorithm can jump from one side to the other of the error function without converging on the local minimum, while with η too small for the neuron can be necessary a long training procedure.

Limits

The perceptron is an effective tool to perform classification of linearly separable subset of events. This condition on the subsets considerably limits the application of the perceptron, indeed for example it is not able to perform the XOR logic function. This problem can be mitigated by the introduction of a set of functions which determines a transformation of the data in a space where they are newly linearly separable. This approach was firstly proposed by Rosenblatt but it presents several limitations due to the restriction on the used functions.

5.3.2 Multilayer perceptron

, structures, hidden input and output The perceptron limits have stimulated the implementation of new informatic instruments, aimed to solve more complicated problems, as the classification of sets non linearly separable. One

successful idea is the building of new devices starting from a set of perceptrons divided in ordered structures, this procedure generates the **Multilayer perceptron**.

For this project we apply the toolkit for multivariate analysis (TMVA) provided by ROOT, a program and library developed by particle physics community of CERN.[59]

Structure

The architecture of multilayer perceptrons is defined by a set of neurons grouped in different classes, called **layers**:

Input layer The input layer is composed by n nodes associated to the n inputs and characterized by a transfer function equal to 1, thus any calculation is performed. The aim of this class is to weight each input quantity differently for the perceptrons of the following layer.

Hidden layers From the hidden layers the data analysis starts. They are composed by calculation units organized in different successive classes. The aim of the neurons dragged is the elaboration of the output-input couples in order to find and test different relations between the inputs and their functions.

Output layer The output layer is the neuron class which return the K outputs $y_i \in \mathbb{R}$ of the network. They perform the final output calculations on the weighted sums of outputs of the last hidden layer.

This kind of neural networks present a particular kind of synapses: the connections are exclusively between neurons of two successive layers. No links are considered between neurons belonging from the same class and the information travels in a single direction (no feedback connections). The connection can be identified determining the calculation-unit j belonging from the layer $l = 1, \dots, L$ and the neuron or node i of the previous layer. To define L we have considered a subclass of $L \geq 2$ layers, which includes only the hidden and the output neuron. These neurons are characterized by an activation function $g_j^{(l)} : \mathbb{R} \mapsto \mathbb{R}$ used to evaluate the weighted sum of its inputs. Therefore the performed calculations become:

$$a_j^{(1)} = \sum_{i=0}^n w_{ji}^{(1)} x_i, \quad z_j^{(1)} = g_j^{(1)} \left(a_j^{(1)} \right), \quad w_{j0} = \theta_j, \quad x_0 = -1, \quad l = 1 \quad (5.15)$$

$$a_j^{(l)} = \sum_{i=0}^{N^{(l-1)}} w_{ji}^{(l)} z_i^{(l-1)}, \quad z_j^{(l)} = g_j^{(l)} \left(a_j^{(l)} \right), \quad w_{j0} = \theta_j, \quad z_0^{(l-1)} = -1, \quad l > 1 \quad (5.16)$$

where we have introduced the number of neurons in the l layer: N^l . Generally this kind of algorithms are characterized by differentiable activation functions with a sinusoidal shape:

- the logistic function which provides for hidden (output) layer a value $z_j(y_j) \in (0, 1)$:

$$g_2(t) = \frac{1}{1 + e^{-ct}}, \quad c > 0 \quad (5.17)$$

- the hyperbolic tangent function which provides for hidden (output) layer a value $z_j(y_j) \in (-1, 1)$:

$$g_3(t) \equiv \tanh(t/2) = \frac{1 - e^{-t}}{1 + e^{-t}} \quad (5.18)$$

Anyway the activation function can vary for different neuron (usually the output layer can have a different activation function with respect the hidden layers).

An example of the resulting architecture for a multilayer perceptron is in the image (Fig. 5.8).

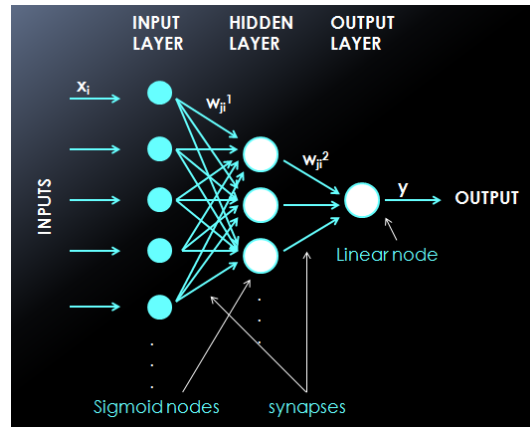


Figure 5.8: Multilayer perceptron characterized by 3 layers ($L = 2$) and by a single output y .

Approximation properties

Several studies have been performed about Multilayer perceptron, specially for ANNs with a single hidden layer and output. In that case we are going to use the following notation:

- number of neurons in the hidden layer: N ;
- threshold of the hidden neuron j : θ_j

- weights between the inputs and the first hidden layer: w_{ij}
- weights between the hidden layer and the output: v_j

Considering an activation function: linear for the output neuron and g for the hidden perceptrons, the output is performed by the equation

$$y(x) = \sum_{j=1}^N v_j g \left(\sum_{i=1}^n w_{ji} x_i - \theta_j \right) = \sum_{j=1}^N v_j g (w_j^T x - \theta_j) \quad (5.19)$$

These studies suggest that a neural network, characterized by a single hidden layer, is a *universal approximator* for continuous functions on compact sets of \mathbb{R}^n for a wide class of activation functions, specifically for non-polynomial continuous functions on \mathbb{R} [64]. Formally this result states that: given a function $f(x) \in \mathcal{C}(\mathbb{R}^n)$, a compact $\Omega \in \mathbb{R}^n$ and a $\varepsilon > 0$ we can build a multilayer perceptron with a single hidden layer, characterized by a continuous non-polynomial activation function, which satisfy:

$$\max_{x \in \Omega} |f(x) - y(x)| < \varepsilon \quad (5.20)$$

More recent studies show improvements on the determination of weights which link the inputs to the first hidden layer, restricting their choice. Another interesting result on the multilayer perceptrons, characterized by a single hidden layer, concerns their capability to correctly interpret the available data. Formalizing this concept [65]:

Theorem (Pinkus 1999): Consider a non polynomial function $g \in \mathcal{C}(\mathbb{R})$. For any k distinct points $\{x^i\}_{i=1}^k \subset \mathbb{R}^n$ and their associated k data $\{\alpha_i\}_{i=1}^k \subset \mathbb{R}$, there exist k vectors $\{w_j\}_{j=1}^k \subset \mathbb{R}^n$ and $2k$ numbers $\{v_j\}_{j=1}^k, \{\theta_j\}_{j=1}^k \subset \mathbb{R}$ such that

$$\sum_{j=1}^k v_j g (w_j^T x^i - \theta_j) = \alpha_i, \quad i = 1, \dots, k \quad (5.21)$$

This theorem explicits the relation found by Hung and Babri (1998) between the k -points available for the interpolation and the number of neurons in the hidden layer. Other results have been performed also concerning the degree of approximation [65].

The theory approximation for MLPs with more than one hidden layer is not well known and thus it is a difficult task to evaluate the advantages and disadvantages which this structure offers in comparison with the MLPs with a single hidden layer. Anyway the majority of the authors seem to support the neural networks characterized by more than one hidden layer. Indeed for structures with a single hidden layer the degree of approximation is limited to a lower bound, which depends on the number of neurons used. This does not hold any more for models of MLPs characterized by 2 hidden layers as

we will see in the following theorem. Consider the output for these kind of algorithms given by:

$$y = \sum_{q=0}^{N_2} u_q g \left(\sum_{j=1}^{N_1} v_{qj} g (w_{qj}^T x - \theta_{qj}) - \gamma_q \right) \quad (5.22)$$

where N_1 and N_2 are respectively the neuron number of the first and the second hidden layers. For MLPs characterized by two hidden layers it is demonstrated the following result:

Theorem (Mayrov and Pincus): There exists an activation function $g \in C^\infty$ sigmoidal and strictly increasing which satisfies the following property. For any function $f \in C([0, 1]^n)$ and any $\varepsilon > 0$, there exist constants u_i , v_{ij} , θ_{ij} , γ_i and vectors $w_{ij} \in \mathbb{R}^n$ which satisfy the inequality:

$$\left| f(x) - \sum_{q=1}^{4n+3} u_q g \left(\sum_{j=1}^{2n+1} v_{qj} g (w_{qj}^T x - \theta_{qj}) - \gamma_q \right) \right| < \varepsilon \quad (5.23)$$

for any $x \in [0, 1]^n$.

The last theorem is based on the *Kolmogorov Superposition Theorem* which states that any continuous function of n variables can be represented (and not only approximated) as a superposition of functions of a single variable. For this topic the most convenient form of this theorem is:

Theorem : There exist n constants $\lambda_j > 0$, $j = 1, \dots, n$ such that $\sum_{j=1}^n \lambda_j \leq 1$ and $2n + 1$ strictly increasing continuous functions $\phi_q : [0, 1] \rightarrow [0, 1]$, $q = 1, \dots, 2n + 1$, such that every continuous function $f \in C([0, 1]^n)$ of n variables can be represented in the form:

$$f(x_1, \dots, x_n) = \sum_{q=0}^{2n+1} g \left(\sum_{j=1}^n \lambda_j \phi_q(x_j) \right) \quad (5.24)$$

for some $g \in C[0, 1]$ depending on f .

This theorem has different interpretation concerning its application for MLPs algorithms. Anyways recent studies suggest its utility for function approximation for models of multilayer network.

Learning approaches

The capability of data interpretation of a MLP characterized by n inputs and K outputs is determined by its *architecture*, i.e. the number of layers $L + 1$ and of calculation units for each layer ($N^{(l)}$, $l = 1, \dots, L$), and by the *learning method*. Both are essential for the correct evaluation of the

weight vectors: specifically the former determines the quantities of these parameters w_{ij}^l , while the latter concerns the ability of the algorithm to reach “optimal” values. To choose these parameters we have also to take into account the dimension of the training set, i.e. the number of the examples in base on which the weights are calculated:

$$T = \{(x^p, t^p), \quad x^p \in \mathbb{R}^n, \quad t^p \in \mathbb{R}^K, p = 1, \dots, P\} \quad (5.25)$$

The weight vectors are obtained by a procedure whose aim is to find the minimum of the *error function*, also called *objective function*. In our case this means solving on optimization problem:

$$\min_{w \in \mathbb{R}^n} E(w) = \sum_{p=1}^P E_p(w) = \sum_{p=1}^P \frac{1}{2} \|y^p - t^p\|^2 \quad (5.26)$$

where y^p is the vector of network outputs $y^p = y(x^p, w)$; anyway different error functions have been implemented (5.1).

Find the minimum of these error fuctions is not an easy task; the most common difficulties are:

- non linearity of the error function which generates depth holes and/or flat zones on the error surface;
- great dimension of the training set and of the total unknown parameters;
- presence of local minima;
- for many algorithms it is not possible to assure the global convergence; however this problem can be solved introducing a regularization term.

We can partially understand some of these points looking at Fig. 5.9. We remember that the major aim of this kind of structures is not to interpret at best the training data, although it is to model the algorithm parameters miming the process which has generated them.

To define the architecture some theories have been developed searching the minimum number of events necessary to the correct definition of the weights. Anyway they are often restricted to particular cases and in practice different techniques are adopted. The main idea at the basis of these approaches is to use different sets of events to evaluate the architecture and then to train the algorithm. To choose the number of neurons for each layer, the process consists on testing stuctures characyterized by an increasing or decreasing number of perceptrons. This procedure is reasonably employed if the tested structures have only one single hidden layer, while for more complex structure follow this strategy seems computationally expensive and time-consuming.

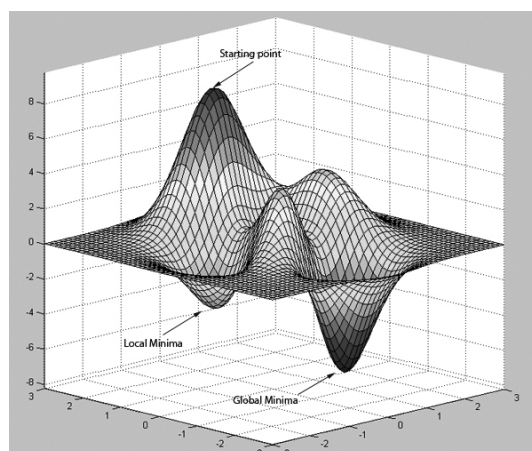


Figure 5.9: Example of error function surface.

Another popular method is performed adding an additional term, which depend on the weight vector norm $\Gamma \|w\|^2$, $\Gamma > 0$ to the error function. This technique is called *regularization technique* and the aim of this procedure is to limit the possible values of the parameters. The results are compatible to processes which impose regularity conditions on the functions approximated by the network.

The learning process ends when the error function on the training set reaches an adequate value or when the error on an independent set of examples starts to increase.

5.3.3 Back propagation

As previously seen to train MLP algorithms a training set of examples is generally used. Giving to the network the couples input-output it can learn the right way to classify the inputs. Initially the synapses are randomly weighted (in TMVA by default though uniform distribution between -0.5 and 0.5) and during the training they are update minimizing the *objective function*. To reach the best configuration different strategies can be adopted. These strategies are called learning methods and generally contain at least the first derivative of the error function with respect to the weights. To calculate the derivatives the back-propagation (BP) algorithm is commonly used. Two different version are available:

BP batch the weights are updated after the consideration of all the training set; in this case the function to minimize is $E(w^k) = \left(\sum_{p=1}^P \|y^p - t^p\|^2 \right) / 2$;

Bp on-line the weights are updated every time an example of the training set is considered and thus the function to minimize is $E_{p(k)}(w^k) = \|y^p - t^p\|^2 / 2$;

We are considering a MLP characterized by L layer, where $x \in \mathbb{R}^n$ is the input vector and $y \in \mathbb{R}^K$ is the output vector. To simplify the notation we define the vectors z

$$z_i^{(0)} = x_i, \quad i = 1, \dots, n \quad z_i^{(L)} = y_i, \quad i = 1, \dots, K \quad (5.27)$$

and in the following we omit the layer label. The back-propagation algorithm consists in the application of the derivative rules for composed functions

$$\frac{\partial E_p}{\partial w_{ij}} = \frac{\partial E_p}{\partial a_j} \frac{\partial a_j}{\partial w_{ji}} \quad (5.28)$$

and therefore in the division of the problem in two parts, as shown in the following.

1. The evaluation of the term $\delta_j = \frac{\partial E_p}{\partial a_j}$. δ_j calculated considering two different cases:

- the j -neuron belongs to the output layer

$$\delta_j \equiv \frac{\partial E_p}{\partial a_j} = g'(a_j) \frac{\partial E_p}{\partial y_j} \quad (5.29)$$

where $y_j = g(a_j)$ (see Fig. 5.10).

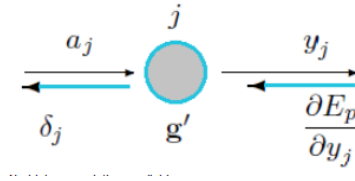


Figure 5.10: The picture shows the propagation of the information when BP is used and the analysed j -neuron belongs to the output layer.

- the j -neuron belongs from one hidden layer

$$\delta_j \equiv \frac{\partial E_p}{\partial a_j} = \sum_k \frac{\partial E_p}{\partial a_k} \frac{\partial a_k}{\partial a_j} \quad (5.30)$$

where $\partial a_k / \partial a_j = g'(a_j) w_{kj}$ (see Fig. 5.11).

Because of the neuron output utility the calculation of this second term is called *back-propagation*.

2. The calculation of the term $\frac{\partial a_j}{\partial w_{ji}} = z_i$, where we have considered $a_j = \sum_h w_{jh} z_h$. The quantity z_i is the i -neuron output, which in case of inactive nodes (input layer) is equivalent to the i -input. The process used to calculate $\partial a_j / \partial w_{ji}$ is called *forward propagation*.

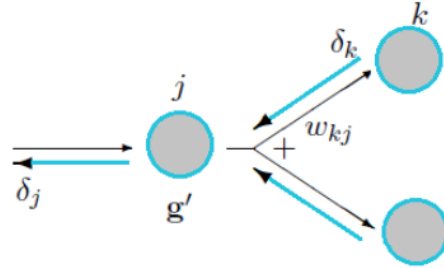


Figure 5.11: The picture shows the propagation of the information when BP is used and the analysed j -neuron belongs to a hidden layer.

Thus we can write

$$\frac{\partial E_p}{\partial w_{ji}} = \delta_j z_i \quad (5.31)$$

Therefore through the BP it is possible to calculate the gradient coming from the sum over the gradients of each example used for the training. Therefore the evaluation of the total gradient computationally costs $O(PxW)$ where P is the total number of the events contained in the training set and W is the number of weights.

The ability of BP method to approximate functions can be described by the *backpropagation theorem*.

Theorem (backpropagation Network Function Approximation) [66]: Given any $\varepsilon > 0$ and any L_2 function $f : [0, 1]^n \rightarrow \mathbb{R}^K$ here exists a three-layer (with two hidden layers) backpropagation network that can approximate f to within ε mean squared error accuracy.

The convergence speed can be improved modifying the searching direction. To reach this purpose a new term proportional to the difference between the weight values of the previous two updates is introduced in the weight iterative formula. This strategy, used to accelerate the achievement of the error function minimum, is called *momentum method*.

5.3.4 Learning methods and conjugate gradients

Different strategies have been adopted to perform the training process. Some of them require a monotonicity on the error function evaluation in correspondence of each weight update. However they often present computational disadvantages and thus a new approach has been recently introduced. It is based on an iterative process which allows momentary increasing of the error function, though assuring the same property of global convergence. Different developments of this method are available and promising.

The center of the issue is how updating the synapses stranghts between neurons of different layers, i.e. in the equation

$$w_{ij}^{k+1} = w_{ij}^k + \Delta w_{ij}^k \quad (5.32)$$

how to determine Δw_{ij}^k . Different learning methods have been developed: the most of them are based on two different approaches: the *gradient methods* and the *conjugate gradients methods*. In this subsection we will mainly consider (if not explicited) the *batch*, also called *off-line*, approach.

Gradient methods

Let start with the first class of learning methods proposed: *the gradient methods* (see also its definition/application for one perceptron: Sec. 5.3.1). One of the easiest version is defined by the following iterative process for the weight update:

$$w^{k+1} = w^k - \eta^k \nabla E(w^k) \quad (5.33)$$

Here each iteration is labelled by the index k and corresponds to an **epoch**. If the learning rate is supposed constant during the iteration $\eta^k = \eta$, $\forall k$, under some conditions on the error function and on the value of η , the convergence is assured. Anyway the process for the determination of the parameters necessary for the η estimation can be complicated and thus a different technique is usually applied. It concern the determination of a learning rate whose value depends on the iteration index k . The different techniques define the values available by η^k to sufficiently move and to reduce adequately the objective function.

The basic idea of this kind of methods is to achieve the minimum of the error function following the direction opposite to the gradient, but, as announced, the final performances depend a lot on the learning rate. Indeed appropriate values of this parameter can help the algorithm to overcome some of its difficulties, for example it can be useful to escape from local minima.

The most trivial learning method implemented on the ROOT toolkit (TMVA) is based on the gradient study and is called the Robbins-Monro stochastic minimization [67]. It is a version of an *on-line* approach and its updating rule is given by:

$$\Delta w_{ij}^k = -\eta \left(\frac{\partial E_p}{\partial w_{ij}} + \delta \right) + \epsilon \Delta w_{ij}^{k-1} \quad (5.34)$$

The search of the error function minimum is therefore along the gradient, but an additional factor δ for the flat-spot elimination is introduced. Moreover the process consider also the first history of the weight evolution by the term Δw_{ij}^{k-1} . We can note that for the application of this algorithm three parameters have to be defined; anyway some reasonable values for these variables are suggested by ROOT.

Conjugate gradients methods

[68] [69] Another approach at the basis of several learning methods (2 in TMVA) is the conjugate gradients methods.

The conjugate gradients is an algorithm aimed to numerically solve sparse systems of linear equations. This is an effective method to treat linear systems of the form:

$$\tilde{A}\tilde{x} = \tilde{b} \quad (5.35)$$

Here \tilde{x} is the unknown vector, while the known \tilde{A} and \tilde{b} are respectively a known symmetric, positive definite ($\tilde{x}^T \tilde{A} \tilde{x} > 0$ for any $\tilde{x} \neq 0$) and real $W \times W$ matrix and another vector. The conjugate gradient method is also useful for solving some optimization problems, this is our case.

Let start with the general idea of this algorithm.

First we define a *quadratic form* as a scalar quadratic function of a vector \tilde{x} :

$$f(\tilde{x}) = \frac{1}{2} \tilde{x}^T \tilde{A} \tilde{x} - \tilde{b}^T \tilde{x} \quad (5.36)$$

It can be proven that, if \tilde{A} is symmetric and positive-definite, this function has a minimum on the solution of the system (5.35) x^* . This can therefore be very interesting for us, indeed it can be use to solve our problem of finding a rule for the weight update which minimize the error function:

$$f(\tilde{x}) = E(w + v) \approx E(w) + E'(w)^T v + \frac{1}{2} v^T E''(w) v \quad (5.37)$$

where we have associated the formalism introduced for the study of the conjugate gradient to the one of the learning process for neural networks. To obtain the relation (5.37) we use the *Taylor expansion*. To find the minimum of the function $f(\tilde{x})$ it is necessary to calculate the gradient of this quadratic form and thus to impose its equality to zero:

$$f'(\tilde{x}) = \frac{1}{2} \tilde{A}^T \tilde{x} + \frac{1}{2} \tilde{A} \tilde{x} - \tilde{b} = \tilde{A} \tilde{x} - \tilde{b} = 0 \quad (5.38)$$

The second equality is valid for symmetric \tilde{A} and shows that find the minimum of $f(\tilde{x})$ is in effect the same of solve the system (5.35). Anyway without imposing any condition on \tilde{A} the critical point x^* can be a minimum, a maximum or a saddle point.

The basic concept of the method illustrated in the following is the generalization of an algorithm able to solve the system (5.35) through updating on orthogonal direction (Fig. 5.12). A brief explanation is reported; we construct the solution:

$$\tilde{x}^{k+1} = \tilde{x}^k + \alpha_k d_k \quad (5.39)$$

where α_k is determined by the orthogonality condition on the new direction of $\tilde{x}(e^{k+1})$:

$$d_k^T e^{k+1} = d_k^T (e^k + \alpha_k d_k) = 0 \quad (5.40)$$

From this equation we obtain

$$\alpha_k = -\frac{d_k^T e^k}{d_k^T d_k} \quad (5.41)$$

Here the problem is that e^k is unknown. The conjugate gradient method

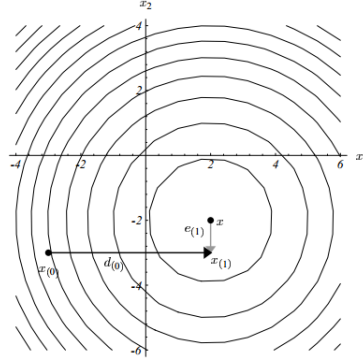


Figure 5.12: The Method of Orthogonal Directions. Unfortunately, this method only works if you already know the answer.

generalizes this idea defining x^* on a basis of *conjugate vectors*, i.e. through a set

$$\tilde{D} = \{d_k : \forall u \neq k \in [1, W] \subset \mathbb{N}, \langle d_u, d_k \rangle_{\tilde{A}=0}\}$$

where we have defined

$$\langle g, h \rangle_{\tilde{A}} := \langle \tilde{A}g, h \rangle = \langle g, \tilde{A}^T h \rangle = \langle g, \tilde{A}h \rangle = g^T \tilde{A}h \quad (5.42)$$

The meaning of the set \tilde{D} is shown in the figure (Fig. 5.13). Therefore we have:

$$\begin{aligned} x^* &= \sum_{i=1}^W \alpha_i d_i \\ \tilde{b} = \tilde{A}x^* &= \sum_{i=1}^W \alpha_i \tilde{A}d_i \end{aligned} \quad (5.43)$$

Thus the coefficients α_i can be found considering the orthogonality of the vectors d_i with respect the product defined by \tilde{A} . For any $k \in \tilde{D}$ we have

$$d_k^T \tilde{b} = d_k^T \tilde{A}x^* = \sum_{i=1}^W \alpha_i d_k^T \tilde{A}d_i = \alpha_k d_k^T \tilde{A}d_k \quad (5.44)$$

and finally

$$\alpha_k = \frac{d_k^T \tilde{b}}{d_k^T \tilde{A}d_k} \quad (5.45)$$

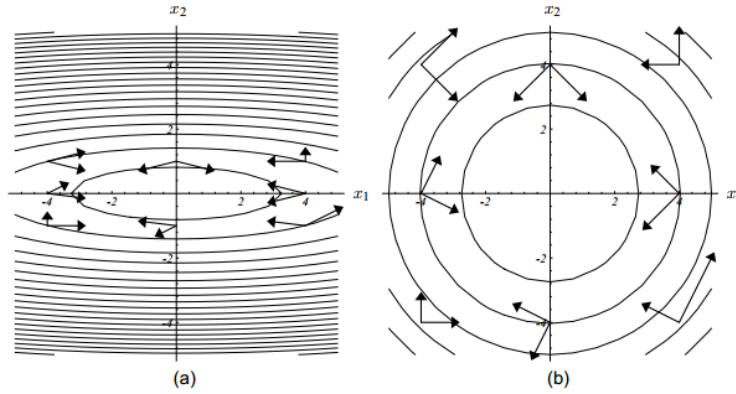


Figure 5.13: In the left picture: pairs of vectors are \tilde{A} -orthogonal. In the right picture: the same pairs of vectors after the ellipses has been “stretched” till appearing circular.

For these approach the problem consists on determining the set \tilde{D} . Therefore to practical implement this algorithm an iterative method was developed. At each iteration a new vector of the set \tilde{D} is defined, indeed this procedure is based on the concept that a good approximation of the solution x^* can be obtained with a subset of the vectors d_i . Starting from a point \tilde{x}_0 the minimization procedure suggests to take $d_0 = \tilde{b} - \tilde{A}x_0$. It is the negative of the gradient calculated in \tilde{x}_0 of the function $f(\tilde{x})$. The name of the algorithm *conjugate gradients method*, arises from the construction of the solution x^* on vectors conjugate to the gradient. At each k iteration step (*epochs*) it is also calculated the distance between the actual representation of the solution and the desired one:

$$r_k = (\tilde{b} - \tilde{A}\tilde{x}_k) - (\tilde{b} - \tilde{A}x^*) = \tilde{b} - \tilde{A}\tilde{x}_k \quad (5.46)$$

where the vectors r_k are called *residuals*. As shown by this definition they also represent the negative gradient of $f(\tilde{x})$ at the k -step ($x = x_k$). Therefore the gradient descent method will follow this direction to search the minimum. To generate the other \tilde{A} -orthonormal and conjugate vectors the *conjugate Gram-Schmidt process* is adopted:

$$d_k = r_k + \sum_{i < k} \beta_{ik} d_i = r_k - \sum_{i < k} \frac{d_i^T \tilde{A} r_k}{d_i^T \tilde{A} d_i} d_i \quad (5.47)$$

where the coefficients β_{ik} are evaluated by the \tilde{A} -orthogonal condition between d_i and d_k with $i \neq k$. Therefore the updating rule becomes:

$$\tilde{x}_{k+1} = \tilde{x}_k + \alpha_k d_k \quad (5.48)$$

The value of α_k can be obtained considering the \tilde{A} -orthogonality of the directions $d_k \in \tilde{D}$ (5.45) in analogy with (5.40):

$$\alpha_k = \frac{d_k^T b}{d_k^T \tilde{A} d_k} = \frac{d_k^T (r_{k-1} + \tilde{A} \tilde{x}_{k-1})}{d_k^T \tilde{A} d_k} = \frac{d_k^T r_{k-1}}{d_k^T \tilde{A} d_k} \quad (5.49)$$

where in the last equality we have exploited the \tilde{A} -orthogonality between d_k and \tilde{x}_{k+1} .

The approach explained before can be summarized (partially elaborated using the relation between the vectors) in the following iterative algorithm:

initialization :

$$\begin{aligned} r_0 &:= \tilde{b} - \tilde{A} \tilde{x}_0 \\ d_0 &:= r_0 \\ k &:= 0 \end{aligned} \quad (5.50)$$

iterative process

$$\begin{aligned} \alpha_k &:= \frac{r_k^T r_k}{d_k^T \tilde{A} d_k} \\ \tilde{x}_{k+1} &= \tilde{x}_k + \alpha_k d_k \\ r_{k+1} &= r_k - \alpha_k \tilde{A} d_k \\ \beta_{k+1} &= \frac{r_{k+1}^T r_{k+1}}{r_k^T r_k} \\ d_{k+1} &= r_{k+1} + \beta_{k+1} d_k \\ k &= k + 1 \end{aligned} \quad (5.51)$$

results : x_{k+1}

This method converges to the optimal solution in a number of iteration $k_{tot} \leq W$. The conjugate gradient algorithm needs less time for the convergence than other approaches, like the gradient methods, and it can be performed also without using the Hessian matrix and the algebra related to it. In the iterating procedure described before the formula used to determine the β_{k+1} coefficients was provided by the Fletcher and Reeves and in the context of the error function minimization it becomes:

$$\beta_{k+1}^{FR} = \frac{\|\nabla E(w^{k+1})\|^2}{\|\nabla E(w^k)\|^2} \quad (5.52)$$

The *conjugate gradient method with the Fletcher-Reeves updating formula* is the learning method used during the development of this project. Another

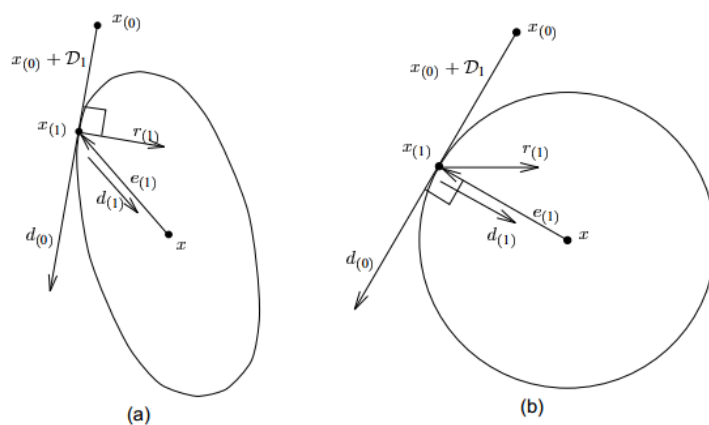


Figure 5.14: Optimality of the Method of Conjugate Directions. (a) A two-dimensional problem. Lines that appear perpendicular are orthogonal. (b) The same problem in a “stretched” space. Lines that appear perpendicular are \tilde{A} orthogonal.

popular strategy used to calculate the β coefficients without the Hessian is known as *Polak-Ribiere (PR)* updating formula:

$$\beta_{k+1}^{PR} = \frac{r_{k+1}^T (r_{k+1} - r_k)}{r_k^T r_k} \quad (5.53)$$

For our minimization problem results:

$$\beta_{k+1}^{PR} = \frac{\nabla E(w^{k+1})^T (\nabla E(w^{k+1}) - \nabla E(w^k))}{\|\nabla E(w^k)\|^2} \quad (5.54)$$

Chapter 6

Implementation and results

Approach: recognition of GWs consistent with compact binary mergers by time-frequency signatures

Noise glitches vs GWs: the main goal of the experimental gravitational astrophysics is a GW detection which implies the implementation of a performant discriminant between the background and the signal events. As shown in the previous chapter, several approaches have been tested to mitigate this problem. In this project we develop a procedure based on the classification of the time-frequency signatures traced by the candidates. To build this tool we start from the cWB analysis and in particular from the reconstruction of the events in the TF plane. Our target signals are GW emitted from compact binary coalescences, which, according to theoretical models, are characterized by the following particular behaviour of the frequency evolution:

$$\omega(t) = \omega(t_0) \left[1 - \frac{256G^{5/3} M_{chirp}^{5/3} t}{5c^5 \omega(t_0)^{-8/3}} \right]^{-3/8} \quad (6.1)$$

Here t_0 represents the time at the measurement start, G the universal gravitational constant, c the speed of light and ω the angular frequency. Since now we will refer to the noisy glitches as *background* and to waveforms radiated by mergers of two compact objects with the word *signals*.

The goal of this project is performing an algorithm able to identify the **shape** signal in the time-frequency (TF) plane. For this reason in this first step we neglect the information about the signature temporal and frequency position, rescaling the interesting part of the TF plane in arbitrary units. The central time and frequency and the candidate widths in these variables will be hopefully used in a next step. We take inspiration from the character recognition procedure, which can be summarized in the following steps:

1. the visual image of a character is converted in an image characterized by on-off pixels;

2. the resulting image is reported in a reduced frame;
3. the analysis of the selected pixels starts; if it is available also a third dimension *-amplitude-* is considered.

The performances reached by the applied method obviously depend on the implemented analysis of the resulting frame. Anyway the first two steps are shared by the majority of the processes.

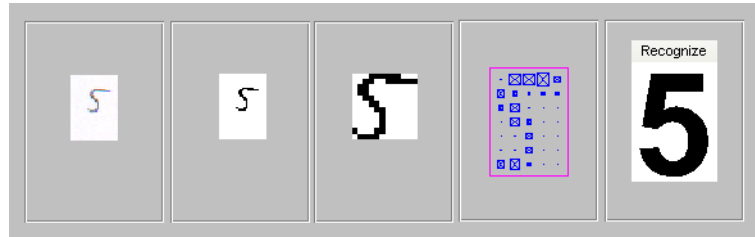


Figure 6.1: Schematic visualization of the procedure for the character recognition.

In this work we adopt this three step procedure in this adapting each step to the TF recognition of cWB events. The first two stages are implemented in a single procedure: we convert the interested image, delimited by the selected WDM-pixels, in a square matrix. In our case also the third dimension are available, it represents the likelihood of the cWB analysis. In our project the resulting matrix is analyzed (third step) by an Artificial Neural Network (see chapter 4.). In this thesis we investigate the performances reached by this analysis applying the TMVA toolkit (MultiVariate Analysis) provided by ROOT program.

Initially in this chapter we will address the process which converts the selected WDM-pixels in a matrix (Section 6.1) and some tests on the ANN parameters aimed to the decision of the its best configuration (Section 6.2). Then we will see some results of the analysis implemented. First we choose as signals chirp-like waveforms injected on gaussian noise and as background respectively some detected glitches and a different kind of simulations (Section 6.4). Then we consider the S6D glitches recolored according to the advanced detector sensitivities and used them as background and as base for injecting waveforms (Section 6.5).

6.1 Matrix implementation

The conversion of the TF traces in a matrix is implemented analyzing the pixels selected by the cwb analysis.

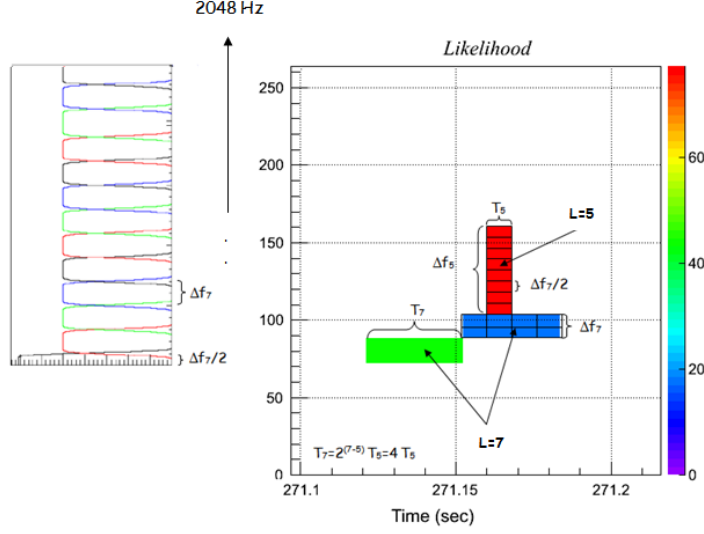


Figure 6.2: Representation of the TF trace compatible with GW emitted by a CBC. The notation is the same used in the Sec. 4.3.2.

The entire process, aimed to the TF plane trasformation in a matrix, is based on shapes and positions of the *core pixels* extracted by the principal component analysis. The conversion procedure begins with the determination of the maximum and the minimum levels used to describe the candidate in the TF plane. Then to compute the frame reduction also the start and stop time of the event and its frequency limits are required and therefore retrieved by the output file produced by cWB pipeline. The matrix is built starting from the construction of a bi-dimensional histogram delimited by the time coordinates previously found and by the frequency range considered in for the analysis. Generally the cWB pipeline provides the possibility to choose three frequency ranges because of the different impact of the noise on the collected data. In this project we focus on the band-width $F_{range} = (64 - 2048) Hz^{-1}$ and thus the ordinate of the initial hystogram varies on the same frequency range. The bin numbers are chosen according to the maximum and minimum levels dragged (notation explained in Sec. 4.3.2). The frequency band is divided in intervals whose width is $\Delta f_{min}/2$ (half the frequency-resolution of the level) according to the natural division provided by the WDM transformation. We can introduce a new variable to describe how many Δf are necessary to built the entire frequency range considered: $layer - 1 = 2M = (r_s/2) \cdot 1/\Delta f$. We remember that the WDM transform provides a division of the frequency range moved on the axis of $\Delta f/2$, thus the number of Δf needed to built the full scale in the number of the divisions (*layer*) less 1. The event duration is instead divided by the minimum time resolution resulted by the multi-resolution analysis on the selected pixels. The hystogram is filled by

the pixel amplitude which is the likelihood calculated taking into account the double representation provided by the WDM transform (see Fig. 6.2), and then for each event the third coordinate is normalized to the sum.

This histogram is then converted to a matrix of $\text{NDIM} \times \text{NDIM}$ dimension. If the number of bins of the histograms is not perfectly a multiple of NDIM , we add white pixels at the edge, taking more white pixels to the right (top) part of the histogram in case of odd pixels to be added. Finally the matrix is constructed filling its elements defined by the last mentioned figurative grid. This means that when more bins of the hystogram are collected in a sigle matrix element their amplitudes are sum up.

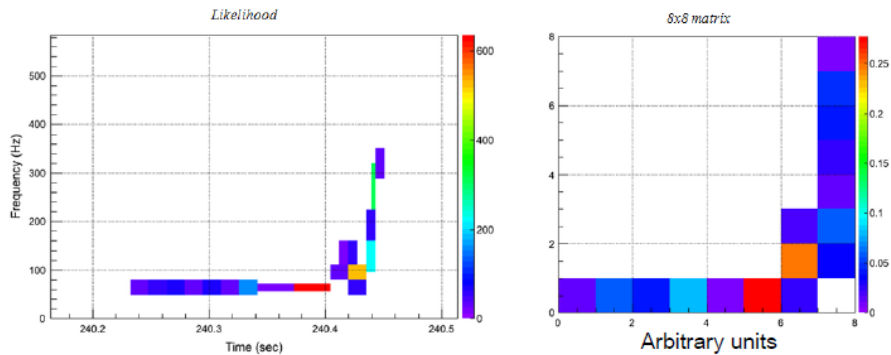


Figure 6.3: Example of TF-trace consistent with GW emitted by CBCs. On the left: signal representation in the TF plane provided by a standard analysis; on the right: correspondent conversion on a 8×8 matrix.

6.2 Train and Test ANNs varying the parameters

In this thesis we test ANN algorithms belonging from the software package TMVA included in ROOT. In particular we focus on the toolkit *TMultiLayerPerceptron* which define a class for the utility of neurons organized multi layers (see Sec. 4.3). The input layer is composed by inactive perceptrons, while the output ones are characterized by an *linear* activation function, which can be switched in a softmax [71] one with an apposite application also associated to the use of the cross entropy error function (5.1). Instead for the hidden neurons the activation function can be chosen by the user; by default the *sigmoidal logistic function* is implemented because of its good characteristics as approximator. This tool proposed by the particle physics community uses one of the most particular intruments included in the ROOT software: the *tree*. These objects are normally used to store different information, grouped in more categories called *branches*, concerning a sample of data. For the application of the multilayer percetpron algorithms proposed by ROOT it is necessary to define a *tree* composed by several branches: the

first and last bins in the two dimensions whose amplitude is different from zero. From the acquisition of these data the construction of the matrix starts. The index intervals found with this procedure are divided by the desired matrix dimensions $NDIM$. The remainder of the division r_d is used to define how many empty pixels are necessary ($NDIM - r_d$, when $r_d \neq 0$) to construct a matrix with the chosen number of elements starting from the natural division allowed by the WDM transformation. The resulting picture is then centered in this new imaginary grid, created by the addition of these “white” squares. If the numbers of columns (rows) are odd, the majority of them are located on the right and on the top.

input branches : it is requested a branch for each input of the desired neural network;

output branches : for any output a branch has to be implemented and filled;

weight branch : it is possible to give different weights to the events, building an associated branch.

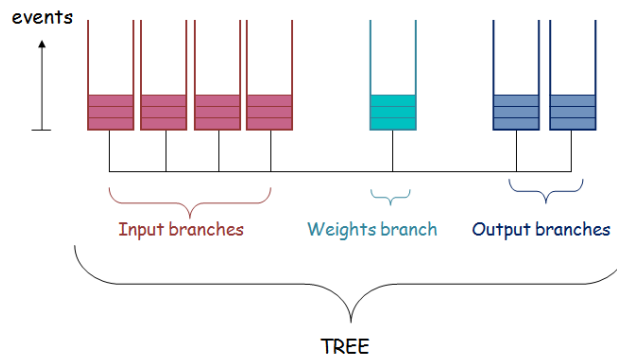


Figure 6.4: Representation of a tree aimed to train and test a multi layer perceptron implemented by ROOT.

To define the networks parameters, i.e. to find the most appropriate weight values, a part of the events stored in the tree-object must be used for the training process. Usually not all the available examples are used to train the network; some of them are required by the implemented ROOT-constructor to test the on-going variables definition. To obtain good performances the *test* and *train* sets are composed by several significant examples; in case of classification problems this means that all the classes are used both for train and test the algorithm.

By default in this toolkit the MSE is adopted as error function, defined as:

$$E(w) = \sum_{p=1}^P \|y_p(w, x) - t_p\|^2 \quad (6.2)$$

where the sum is over the training set, t_p is the desired output of the ANN, let say it *target* and $y_p(w, x)$ is the network output associate to particular event and which depend on the input vector x and on the weight vector w . To calculate the error function in the TMultiLayer Perceptron package the **back propagation** technique is proposed (see Sec. 5.3.3).

6.2.1 Architecture

The aim of the project is the trace identification on the TF plane of compact binary coalescences-like signals. Therefore we want to exploit one of the principal abilities of this kind of informatic instruments: **classification problems** solving.

Output neurons

The number of output neurons in classification issues are generally equal to the number of the considered categories we use to classify events, in this way the ANN outputs suggest the most related class for each candidate. Anyway when we have only two classification categories, we can adopt two main approaches: two neurons (similarly to the case of more classes), or a single output neuron. We adopt the latter, because better performing for the ANN considered [72]. Therefore the network is trained for outputs near to one for chirping-like TF-patterns(*signals*) and near to zero otherwise (*background*).

Inputs neurons

The inputs of ANN are constituted by the amplitude of matrix elements. The number of inactive nodes included in the input layer is equal to the matrix dimension $N_{inputs} = NDIM \cdot NDIM$. The matrix dimension is one of the most important parameter affecting the results of the analysis and of the computational load. We test the following values: 8×8 , 16×16 and 32×32 matrices. Train networks defined by 16×16 or 32×32 inputs increase the number of connections between the inputs in the neural network, so the required computational load is really high, and the training process takes a huge amount of time. Figures (Fig. 6.5 and Fig. 6.6) show results considering a 16×16 matrix.¹ Even if we do not expect important improvements, we decide to focus our first efforts on the development of ANNs characterized

¹The architecture for the shown example of 16×16 inputs was decided according to the best configuration tested on 8×8 matrices: having quadruple the inputs, also the neurons for each hidden layer was quadrupled together with the training sample. The problem is that in this way the number of weights which the algorithm must estimate is multiplied by a factor ~ 16 with respect the corresponded proportional architecture associated with 64 inputs. This consideration explain the result.

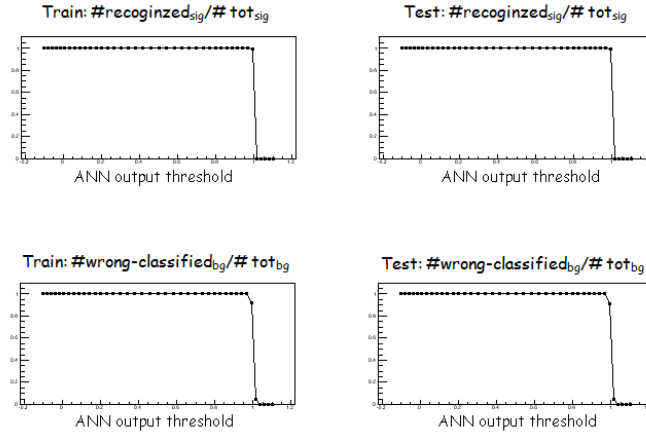


Figure 6.5: Results considering a ANN structure of 256 inputs, 3 hidden layers with 64-128-64 sigmoidal neurons, a single linear output and 1200 epochs. Top (bottom) plots show ratio between rightly (wrongly) identified on total signals, as a function of ANN threshold. Training set is composed of about 65000 events, half background and half signals. Left reports results on the same training set, while right on different events (test set).

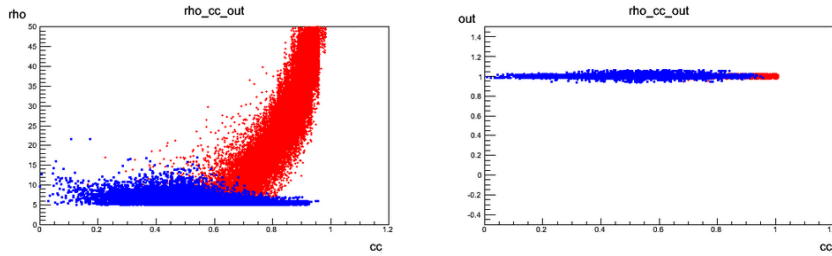


Figure 6.6: Background events (blue) behaviour vs signals one (red) for the standard cWB post-production thresholds (left) and ANN output vs the cc on the right (see Sec. 4.4 for the variable definitions). Same ANN as Fig. 6.5. Note the drawing cut on ρ value on the left picture.

by 64 input nodes (time required for the ANN train $\sim 90min$). The two main reasons of this choice are:

- huge amount of time for the optimization of the ANNs training (more than four days for the results of Fig 6.5 and 6.6);
- training set should be considerably increased.

Another important parameters is the third coordinate parameter, i.e. the pixel likelihood. To understand the importance of this quantity we performed

several tests changing the way of considering this quantity. A first test was to substitute the likelihood values as on-off behaviour. We discover that the implementation of this strategy gives similar results to the standard approach. Other approaches regards the normalization of the likelihood values. One possibility included in the ANN options is to consider separately each input and rescales all the values from each events inside the interval $[-1,1]$. This procedure has the risk to emphasises pixels which have usually small values for all the events. We performed a different algorithm normalizing each amplitude with respect to the maximum of each event, restricting inside the intervals $[0,1]$ or $[-1,1]$. Results wshow negligible differences between the three cases, anyway best performances are given by the normalization proposed by the *TMultiLayerPerceptron* toolkit, probably because it is best adapting to the requirements of the ANN algorithm.

Hidden neurons and layers

We decide to adopt sigmoidal activation function for the hidden layers.

$$g(x) = \frac{1}{1 + e^{-x}} \quad (6.3)$$

which is most approximating the behaviour of biological neurons. The result values distribution from this function is inside the interval $[0,1]$, favouring the extreme with respect to the intermediate values (called uncertained region). Moreover it has a derivative easy to calculate which can simplify and speed the error function estimated by the back-propagation technique.

To define the architecture we start following the previous study we found in literature, in particular we focus on ANN with more hidden layers. We start with the network configuration suggested by the Majorov and Pikus theorem (1999). Matrix elements have been normalized to the maximum. The trained ANN internal organization was therefore composed by the usual input layer (64 inputs), two hidden layers (h.l) with $2(NDIM \cdot NDIM) + 1 = 129$ and $4(NDIM \cdot NDIM) + 3 = 259$ neurons, and a final output perceptron. Results were not satisfactory, we recognize the cause on a poor training sets. Indeed the synapses characterizing this architecture are a huge number ($\sim 4.2 \cdot 10^4$), and so an appropriate training set would have at least the double value, that was not our case (8192 events for signal and for background). So, we performed a new idea: implement an algorithm able to reduce the starting information in a minimum set of parameters [73]. This strategy is normally adopted to find the variables needed for the data representation. They are implemented training the networks with symmetric architecture centered on the layer which contains the minimum number of neurons (training the ANNs using the equagliance $output_i = input_i$). If the number of perceptrons in the central hydden layer is appropriate, they should be related to the unknown parameters. Specifically we test an architecture composed by two or by three hydden layers. They are performed

starting from the 64 inputs and then putting half the neuron number for successive hidden layers, until the output. We will write this ANN architecture in the following simplified notation, which will be adopted also for the future, $64in : 32 : 16 : 1out$ where the number of the hidden layer neurons are between the “:”. The results reached by these ANNs types are rather satisfactory and achieved with a reasonable training time (the weight number are around $2.5 \cdot 10^3$). Anyway other attempts were performed adopting a different strategy. Specifically we test architectures characterized by three hidden layers, composed by same neuron numbers on the extremes and a bigger set of perceptrons in the center. Some examples are: $64in : 10 : 40 : 10 : 1out$ and $64in : 16 : 32 : 16 : 1out$. The main architecture classes tested are reported in the following Fig. 6.7. From this figure we can infer that the

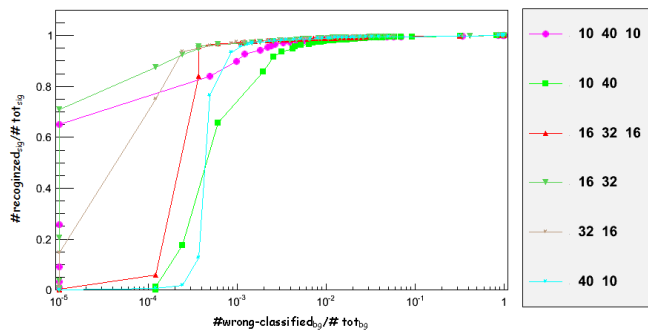


Figure 6.7: The image shows the performances of networks characterized by training processes which differ only by the adopted architectures. The test is performed on a set of 8192 signals and 8192 background events.

best results seem to be achieved by the architectures: $64in : 16 : 32 : 1out$, $64in : 32 : 16 : 1out$ and $64in : 16 : 32 : 16 : 1out$. Indeed the other curves begin the separation to the most performing ones before the “statistically critical zone”. However further tests show that the ANN characterized by $64in : 16 : 32 : 16 : 1out$ is the most performing among the ones studied. Therefore in the following the main results reported are achieved by the application on the data of a network with such architecture.

6.2.2 Learning method

The train process define the synapse strength between the neurons of the implemented ANN-architecture. Evaluating the best values of the weights is the goal of this process and represents the core of the algorithm. The ROOT package provided a default starting configuration of weights randomly generated following a uniform distribution between -0.5 and 0.5 . The power of these informatic instruments is the self-parameter estimation computed with

the only definition of some starting variables. The way in which the synapsis weights are calculated is an important part of all the study because it strongly affects the performances. The toolkit *TMultiLayerPerceptron* allows the application of six different learning methods shown in the successive list.

1. Stochastic minimization The Stochastic minimization is the only *on-line* approach provided by the ROOT package. It is a *gradient method* which updates all the weights after the consideration of each single example provided by the training set. The iterative process which guides the learning at the k step is defined as:

$$w_{ij}^{k+1} = w_{ij}^k + \Delta w_{ij}^k, \quad \Delta w_{ij}^k = -\eta \left(\frac{\partial E_p}{\partial w_{ij}} + \delta \right) + \epsilon \Delta w_{ij}^{k-1} \quad (6.4)$$

In the case of $\epsilon \neq 0$, we take in account the previous steps so to establish the new testing values of the weights. This is a development of the *momentum technique* which adds to the basilar gradient formula only a factor proportional to the difference between the last two values assumed by the analyzed synapsis. The *momentum updating rule* is generally used to make more effective this learning method. As the formula (6.4) shows three parameters are needed to implement a train based on this Stochastic minimization:

- η : the learning rate, which default value is 0.1;
- δ : a constant used to speed the approach to the minimum of the error function. Its value has to be carefully evaluated: an its overestimate can cause the jump from one side to the other on the minimum. The default value is zero;
- ϵ this factor weights the history of the iterative process; its default value is zero.

We note that all the three parameters remain constant during the training (example in Fig. 6.8).

2. Steepest descent with fixed step size (batch learning) The idea applied by this learning method is the same of the *Stochastic minimization*: the difference concerns time of the error function evaluation and, consequently, of the updating rule application. It is an approach based on the *gradient method*, which updates the weights after the consideration of all the training set (*batch learning*). The implementation of this technique requires the definition of the same parameters of the previous case (example in Fig. 6.9).

3. Steepest descent algorithm This algorithm search the minimum along the direction opposite to the gradient. Only a multiplied factor is

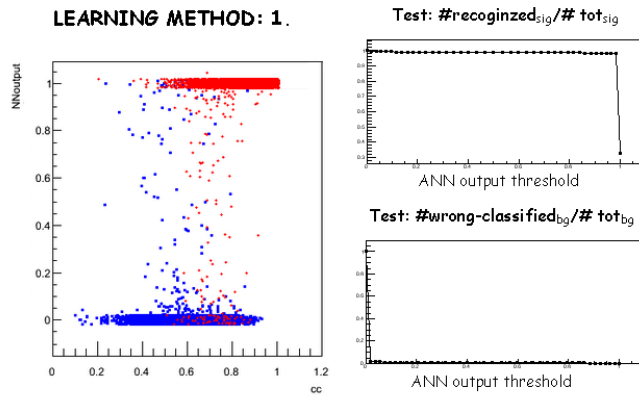


Figure 6.8: Example of results obtained by the application of a network trained with *stochastic minimization*. Note: the on-line methods requires more time than batch (order of magnitude). This and the following figure shows background (blue) and signals (red) events. Left: ANN output vs cc. Top (bottom) right: ratio between recognized (background considered as) signals and the total number as a function of threshold. The ANN characteristics are: train set: 8192 signals plus 8291 background, 600 epochs, 64 input, 3 hidden layers with 32-16-8 sigmoidal neurons and a linear output.

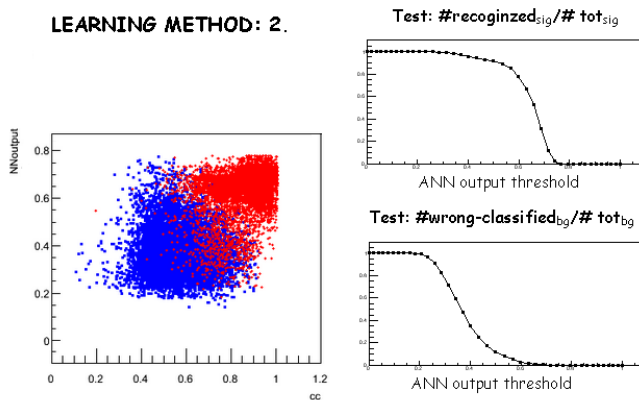


Figure 6.9: Example of results obtained by the application of a network trained with *steepest descent with fixed step size*.

needed for the application of this technique. The Steepest descent algorithm satisfies the conditions of the global convergence theorem and is characterized by a convergence achievement in a linear time (example in Fig. 6.10).

4. Conjugate gradients with the Polak-Ribiere updating formula (GCs)

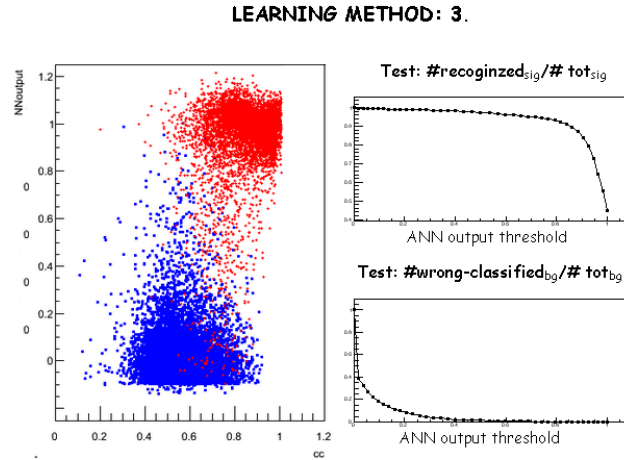


Figure 6.10: Example of results obtained by the application of a network trained with *steepest descent algorithms*.

with P.R.) The algorithm is based on the *Conjugate gradient technique* (for more details see Sec. 5.3.4) and the update of the weights at each iteration is determined by the application of the Polak Rebiere updating formula. The conjugate gradients method can be summarized by the following expressions

$$\begin{aligned}
 w_{ij}^{k+1} &= w_{ij}^k + \alpha_k d_k \\
 \alpha_k &= -\frac{\nabla E(w^k)^T d_k}{d_k^T H d_k} \\
 d_k &= \nabla E(w) + \beta_k d_{k-1}
 \end{aligned} \tag{6.5}$$

where H is the Hessian matrix of the error function and the other quantities are the same explained in the previous chapter. The Polak Rebiere updating formula concerns the iteration on the estimation of β_k :

$$\beta_k = \frac{\nabla E(w^k)^T (\nabla E(w^k) - \nabla E(w^{k-1}))}{\|\nabla E(w^{k-1})\|^2} \tag{6.6}$$

In the previous equations the $E(w^k)$ is the MSE objective function calculated at the k^{th} step.

To apply this learning method two parameters are used:

- τ : a parameter used for the line search and connected to the $\nabla E(w)$, (default value is three);
- *Reset*: it creates a strategy for the conjugate gradient technique stabilization. The set value represents the number of iterations before the algorithm is forced to follow the direction determined

by the gradient and in the case of the `TMultiLayerPerceptron` package it is set to fifty (example in Fig. 6.11).

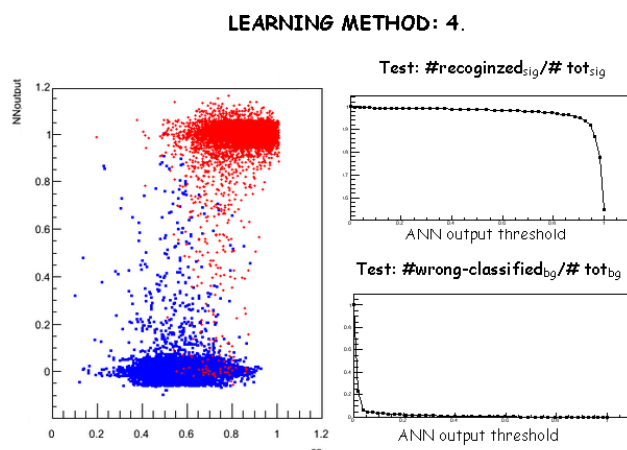


Figure 6.11: Example of results obtained by the application of a network trained with *conjugate gradients with the Polak-Ribiere updating formula*.

5. Conjugate gradients with the Fletcher-Reeves updating formula (CGs with F.R.)

. It is based on the conjugate learning method, summarized in the equation (6.5). Here the update is given by the formula:

$$\beta_k = \frac{\|\nabla E(w^k)\|^2}{\|\nabla E(w^{k-1})\|^2} \quad (6.7)$$

The parameters necessary for the application of this method are the ones defined for the *Conjugate gradients with the Polak-Ribiere updating formula* (example in Fig. 6.12).

6. Broyden, Fletcher, Goldfarb, Shanno (BFGS) method

The *BFGS learning* belong from the *Quasi-Newtonian methods* whose aim is to minimize the error function, requiring the knowledge of the only its first derivatives. The BFGS is one of the most popular algorithm adopted by this Quasi-newtonian class and it is also considered one of the most effective for solving optimization problem of low dimension. This iterative method can be described by the following update:

$$w^{k+1} = w^k - \eta^k B^k \nabla E(w^k) \quad (6.8)$$

where, as usual, w is the weight vector, $E(w)$ is the error function and η^k is the algorithm step. $B \approx H^{-1}$ is instead an approximation of the Hessian matrix inverse, which satisfies the following equation:

$$B^k y^k = s^k, \quad s^k = w^{k+1} - w^k, \quad y^k = \nabla E(w^{k+1}) - \nabla E(w^k) \quad (6.9)$$

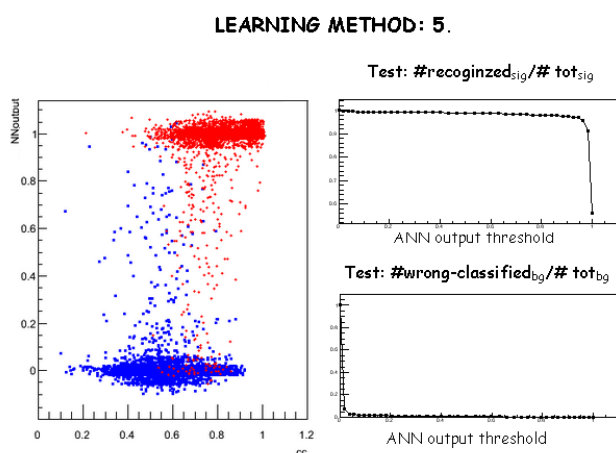


Figure 6.12: Example of results obtained by the application of a network trained with *Conjugate gradients with the Fletcher-Reeves updating formula*.

and the matrix is updated by the formula:

$$B^{k+1} = (V^k)^T B^k V^k + \frac{s^k (s^k)^T}{(y^k)^T s^k}, \quad V^k = I - \frac{y^k (s^k)^T}{(y^k)^T s^k} \quad (6.10)$$

The Quasi-Newtonian methods are implemented because calculating the Hessian matrix requires a great number of operations (example in Fig. 6.13).

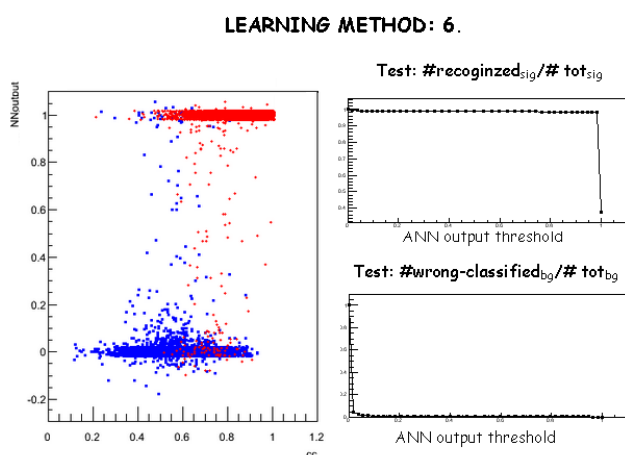


Figure 6.13: Example of results obtained by the application of a network trained with *Broyden, Fletcher, Goldfarb, Shanno (BFGS) method*.

Different learning techniques leads to different results on distinction between signal and noise (Fig. 6.14) and also in the computational load. The *steepest descent batch* methods shows worse performances with respect to the others. Instead the *stochastic minimization approach* needs for the train process huge amount of time (from $\sim 90min$ of the other techniques to some days). In the Fig. 6.14 we compare the six learning techniques on the same set of candidates, which are indipendet on the set used for the training. Given the low statistics (about 8000 events of background and signals) we expect significant fluctuations at the left part of the picture. The picture empha-

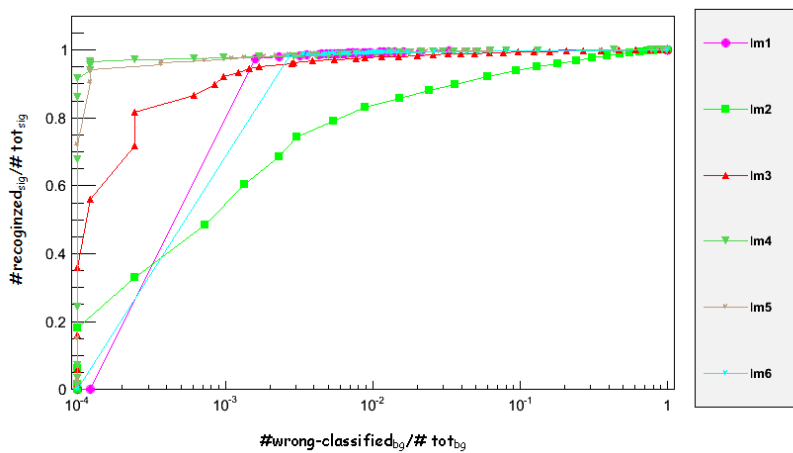


Figure 6.14: Comparison of performances given by ANN trained with different learning techniques (lm on the label, numbers refer to the ones reported in the text) Points concern the thresholds on the ANN output tested. Lower limit on x-axis has been set to 10^{-4} for graphical purpose.

tizes also a common characteristic for the event distributions obtained by the networks trained with the *stochastic minimization* and by the *BFGS* methods. As shown also by the graphs Fig. 6.8 and Fig. 6.13 they performed very restricted bands as output. The problem of this property is that also the events wrongly classified are grouped near these output values and the results is well shown by the image Fig. 6.14. Here these two learning methods are associated to curves that are not able to lower under few tens the background events classified maintaining a good signal recognition. In view of these comments we decide to focus our attention on the *conjugate gradient methods*. The successive picture (Fig. 6.15) shows the similarity of the results reached by the two networks trained with the different updating formulas. According to this result, which shows a similar performances on the event classification and a slightly better background recognition, we choose to develop the version corrispondent to the *Fletcher and Reeves updating formula* and we study the impact of the two parameters necessary for

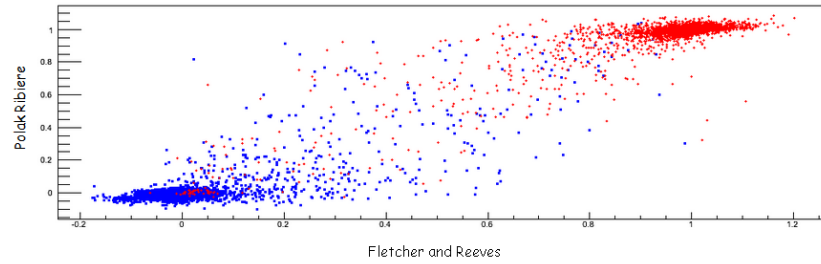


Figure 6.15: We compare two learning methods (reported in the axes) for 10000 background (blue) and 10000 signal events (red). The test is performed on an independent set, while the train is made considering the same events (8192 signals, 8192 glitches) for the two networks as the remaining parameter: 700 epochs and three hidden layers with respectively 16, 32, 16 sigmoidal neurons.

the implementation of the *conjugate gradient methods* on the network performances: the result is summarized in Fig. 6.16. The image highlights that for

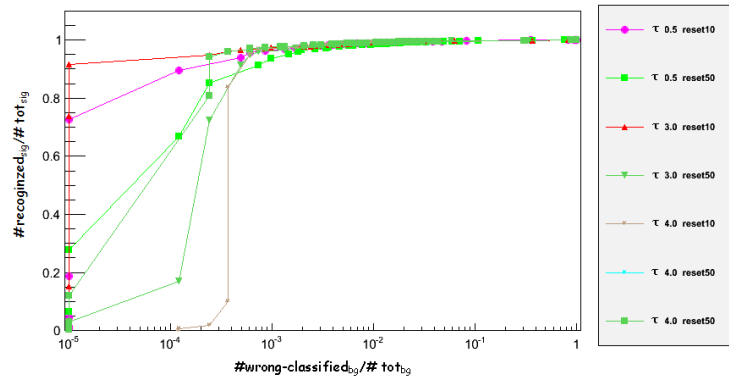


Figure 6.16: The picture shows the performances reached by networks trained using *conjugate gradients* as learning method with Fletcher and Reeves updating formula, with different parameters values. The test set is again composed by 8192 signals and by 8192 background events, and zero glitches exchange is imposed equal to 10^{-4} .

the values tested no significant changes have been provoked by variations of these parameters. Consistently with this result we adopt the default values for the τ and *Reset* variables.

Epochs

The *numbers of epochs* determines how many times the training set is considered in the learning process. For batch-algorithms this number coincides

with the number of the weights iteration, while for the on-line procedures the weight updates are $Epochs \times T$, where T training events number. This is the cause of the huge differences in time for the network training. The major reductions of the error function are performed during the first iterations which generally lower its value by few tenths, as shown in the following picture (Fig. 6.17). Figure 6.18 shows the performances varying

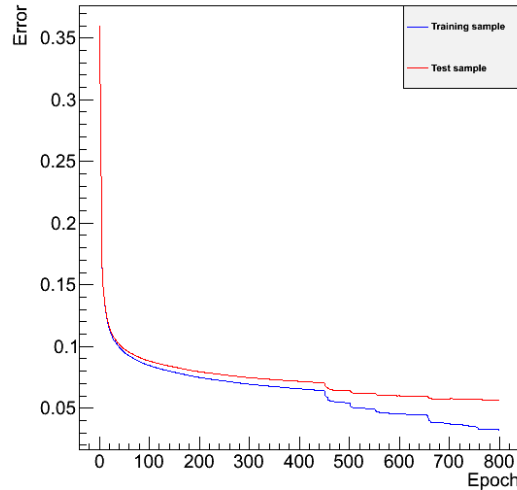


Figure 6.17: Error function behaviour as a function of epoch number, calculated on the train set (blue) and on the test one (red).

the epoch number, there are no clear trends for the value tested. Indeed as

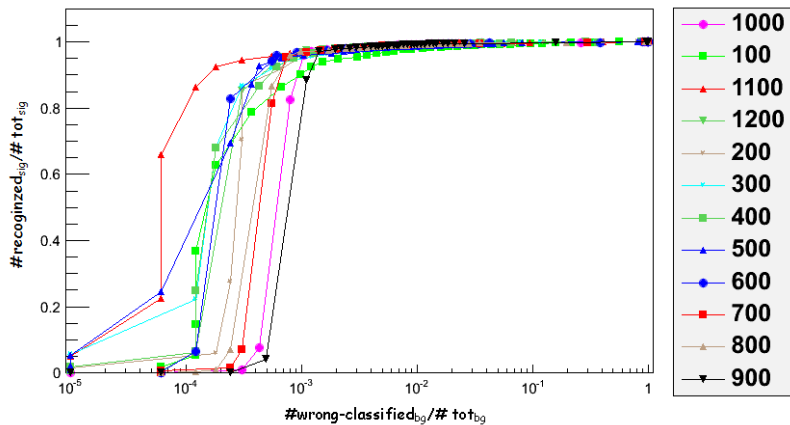


Figure 6.18: This image shows networks with different epochs applied on the same set of events (16384 background and 16384 signal). The lower coordinate on the x-axis is forced to 10^{-5}

we note from the image Fig. 6.17, after a certain iteration the algorithm

continues to lower the error function associated to the train set, without any improvement on the interpretation test events. Moreover, growing too much this parameter can cause an *Overtraining*. Anyway this effect consists on a lost of generalization of the created tool, which exagerately models the weights on the train examples.

Instead concerning our distination goal some cases present an evident improvement when the epochs increase (see Fig. 6.19).

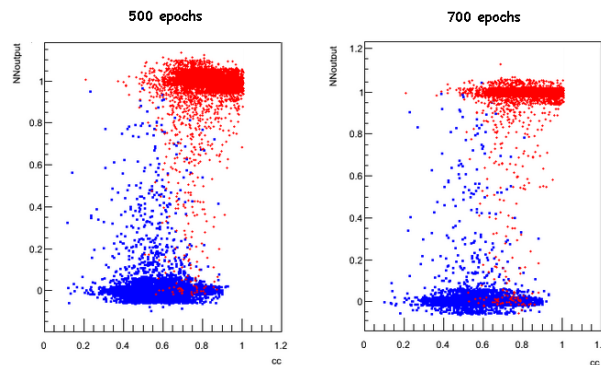


Figure 6.19: Comparison between two networks tested and trained on the same samples and with the same parameters, except for the epoch number: 500 on the left and 700 on the right. The blue points refer to glitches the red ones to signals.

Number of events in the train set

The number of the train set in another key parameter for the determination of the ANN weights. Best performances are reached when the signal events equals the background ones, independently by the real numbers of both sets.

Deciding the absolute number is instead very complicate, indeed all the parameters necessary for the learning process are linked together by a non trivial relation. Anyway, empirically the best results are obtained with a number of events at least of some times the number of the synapses. This explains the result obtained for the 16 inputs: indeed the number of weights for the tested architecture is more or the number of events used for the train.

The image (Fig. 6.20) shows no great changes in varying the number of events in the training sample. Indeed the architecture tested is composed by three hidden layers with respectively 16, 32, 16 neurons. This means that the number of the synapses is 2064 for 64 inputs and 1 output. Therefore it is sufficient to use for each cathegory a number of events more or less double than the number of unknown weights. Therefore to reduce the training time, when we will adopte this architecture to define the network, we will use a

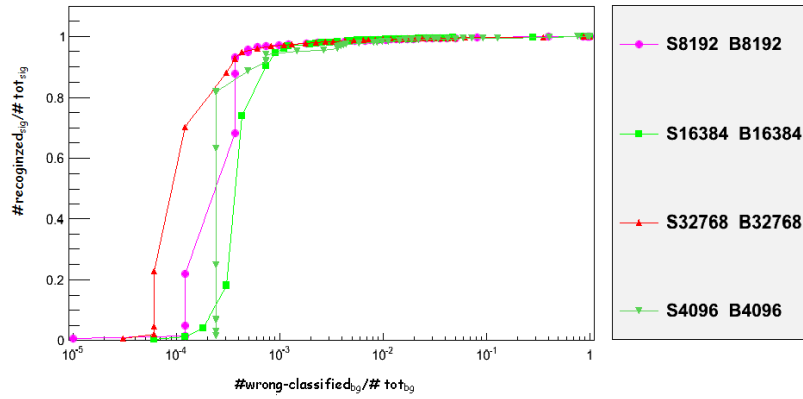


Figure 6.20: Comparison between networks trained with different number of events (“S” for signals and “B” for background) for the training and test. The lower coordinate on the x-axis is set to 10^{-5} .

train sample which contains 8192 signal and 8192 background events.

In conclusion all the dragged parameters must to be chosen consistently between each other to obtain good performances by the implemented algorithm and the decision of all their values is determinant for the time required by the training process.

6.3 Graph explanation

We have studied the impact of the ANN introduction on the standard analysis for different cc (*network correlation coefficient*) and ρ (*effective correlated SNR*) thresholds, which are the standard cWB final discrimination.

The most interesting performances are always analyzed implementing several figures which differently underline the improvement given by the introduction of the new variable: the ANN output.

Scatter Plots In these images the red points are associated to the signal simulations, while the background events are represented by the blue dots. We report four graph types: the top plots show the candidates on the planes $ANNoutput - \rho$ (left) and $ANNoutput - cc$ (right); on the bottom left the plots describes the event distribution of cc and ρ parameters, bottom right graph shows the number of glitches surviving the cc and ANN output cuts varying their thresholds.

Survived events as a function of ANN output The signal and the background events are treated separately by these figures. We consider four graphs, each of them with same axes: the number of events belonging to the considered class versus the applied threshold values. Each graph refers to a particular cut on the cc and contains three curve associated to three different threshold applied on the ρ parameter: 5, 5.33, 5.67.

Survived events as function of ρ Separated signal and background events contained in four graphs associated to different cc threshold value. They report the count of the candidates surviving the rho cuts as a function of rho. Each graph contains several curves related to the ANN threshold applied. The red lines always refer to the results obtained without the introduction of ANN output.

Anyway to reduce the space occupied by these images we have decided to summarized the results focusing on the **Scatter Plots** and a new image **Summarized Results**. In the latter we show the last two graphs previously explained (*Events survive as a function of ANN output* and *Event survived in function of ρ*) for both the *BKG* and the *SIG* classes, focusing on $cc = 0.6$, which is reasonable.

6.4 Results for injections on gaussian noise

6.4.1 Tested events

For the first tests we used the following classes of events analyzed by cWB 2G analysis.

Signals (SIG)

The ANNs should recognize as target features the TF traces produced by waveforms which simulate GWs emitted by compact binary coalescences; specifically we use EOBNR waveforms. In particular we focus our attention on signals with the following characteristics:

- a range for the mass value of a single component from 1.5 to 25 solar masses;
- a mass ration between 1 and 11;
- a uniform distribution in total mass and mass ratio;
- a uniform distance distribution in volume included in three consecutive shells: $(\sim 66.7 - 100)Mpc$, $(100 - 150)Mpc$ and $(150 - 225)Mpc$.

The simulated waveforms are injected on gaussian noise re-coloured to match the advanced detector sensitivity curve.

Two examples of signals with chirp like behaviour are illustrate in the figure (Fig. 6.21) For these chirp-like signals the efficiency of the cWB analysis

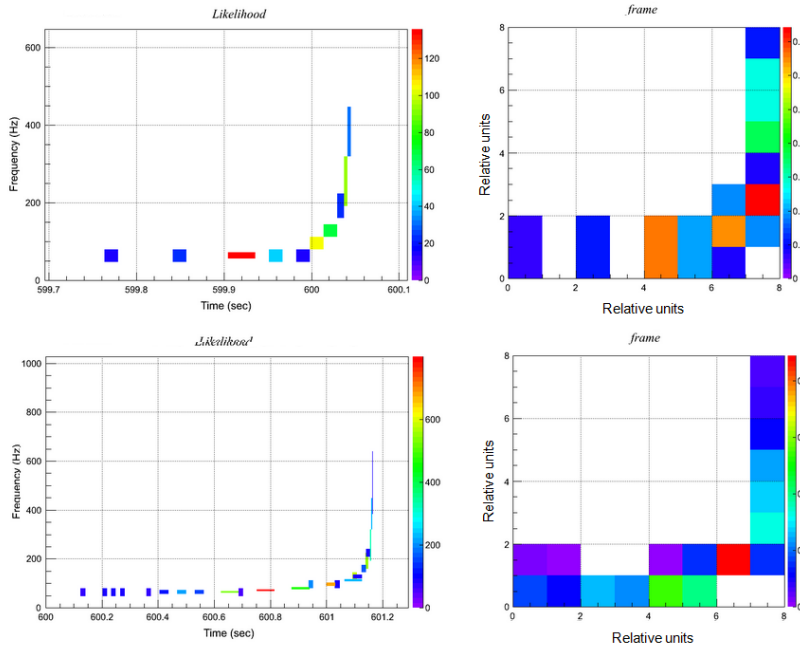


Figure 6.21: In the picture are reported two example of signal events. On the left: representation of the events in the TF plane; on the right: conversion of the candidates in 8×8 matrices.

in the three shells is reported in the following table (Tab. 6.1). The main

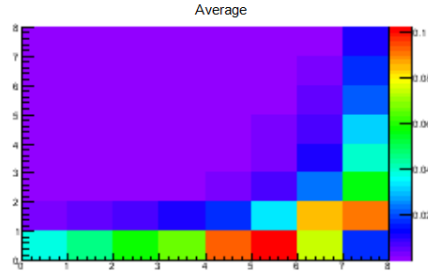


Figure 6.22: SIGNALS: the image shows the average on 32768 events of the input values.

Shell	Estimated efficiency	Error
$(\sim 66.7 - 100)Mpc$	0.915	0.003
$(100 - 150)Mpc$	0.856	0.001
$(150 - 225)Mpc$	0.769	0.002

Table 6.1: cWB-efficiency for the three shells for chirp-like waveforms injected on gaussian noise.

parameters used for the cWB-analysis are written in the successive table (Tab. 6.2).

PARAMETER	VALUE	PARAMETER	VALUE
ρ threshold	5	cc threshold	none
search type	i	detector network	V1H1L1
lower f	64Hz	higher f	2048Hz
Δt_{max}	3s	Δf_{max}	130 Hz
lower level	3	higer level	8

Table 6.2: Main cWB parameters used to search and analyse signal events. Δt_{max} and Δf_{max} refers to the maximum distance between pixels to allow their consideration as a single cluster.

Background (BKGg): glitches

To mark the candidates which the ANNs should categorized as background events we have decided to use the glitches collected during the S6D science run. This sample refer to data acquired during the months July-October 2010. To perform results useful for the second generation of interferometers, the noisy events are recolored according to the advanced detector sensitivity curve. In the Fig 6.23 are reported two examples of glitches in the TF plane and the related matrix and the average behaviour on the matrix representations of these kind of events. The values of the main cWB-analysis

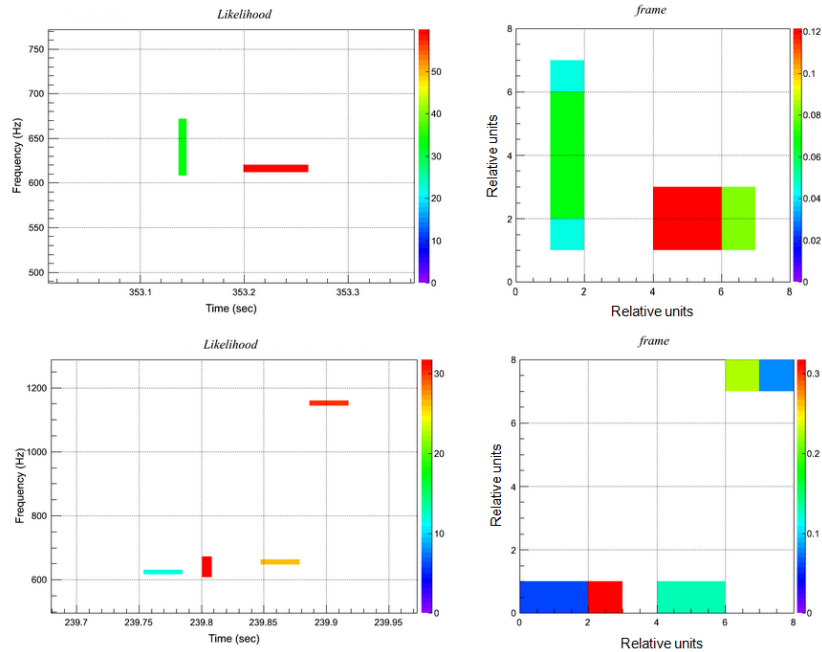


Figure 6.23: In the picture are reported two example of glitches belonging to the 6SD science run. On the left: representation of the events in the TF plane; on the right: conversion of the candidates in 8×8 matrices.

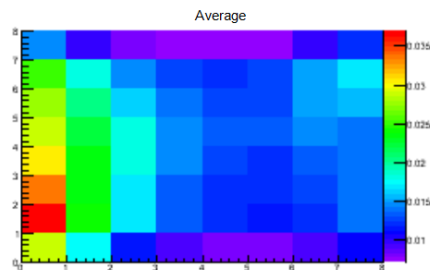


Figure 6.24: BACKGROUND GLITCHES: the image shows the average on 32768 events of the input values.

parameters used for the 6SD-data analysis are reported in the following table (Tab. 6.3).

Background (BKGb): BRST waveforms

To test the classification ability of the ANN algorithms, another kind of background events are considered: the *Standard Simulation Set*. It includes gaussian and sin-gaussian waveforms characterized by different parameters (*duration* for gaussian, *Q* and *frequency* for sin-gaussian) as well as white

PARAMETER	VALUE	PARAMETER	VALUE
ρ threshold	5	cc threshold	none
search type	i	detector network	V1H1L1
lower f	64Hz	higher f	2048Hz
Δt_{max}	3s	Δf_{max}	130 Hz
lower level	3	higer level 8	

Table 6.3: Main cWB paramters used to analyze the S6D data.

noise bursts also in this case tested with different parameters. The simulated GWs are injected on gaussian noise and modulated by ten different multiplied factors.

Therefore this class of events does not include any simaton of astrophysical sources, anyway it contains some standard test waveforms. Two examples of traces on the TF plane and of the corresponding matrices are shown by the following picture (Fig. 6.25), then the average behaviour of the inputs variables is represented in figure (Fig 6.26). For the cWB analysis we have

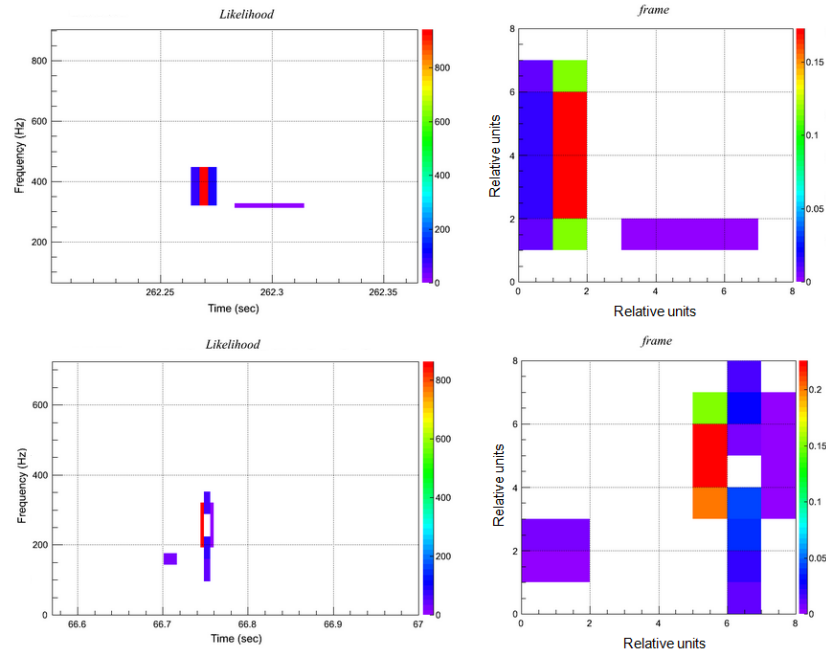


Figure 6.25: In the picture are reported two example of BRST waveforms. On the left: representation of the events in the TF plane; on the right: conversion of the candidates in 8×8 matrices.

used the same parameter values of the signals studies (Tab. 6.2).

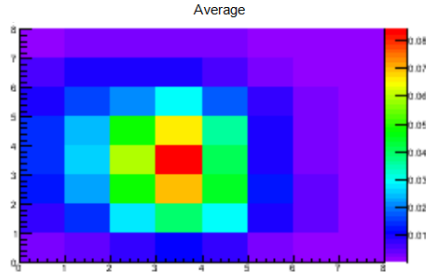


Figure 6.26: BACKGROUND BRST: the image shows the average on 32768 events of the input values.

6.4.2 Results

Signals vs S6D glitches

In this paragraph we report the main results achieved by the analysis computed by cWB and ANNs trained and tested on the events presented in the previous paragraph (Sec. 6.4.1).

The training parameters of the best ANN implemented are summarized in the following table (Tab. 6.4). The preliminary tests associated to this

PARAMETER	VALUE
Number of BKGg events	8192
Number of SIG events	8192
Epochs	650
Learning method	CGs with F.R.
Architecture	64in, 3h.l. (16 : 32 : 16), 1out

Table 6.4: Main parameters used to train the selected network.

ANN are reported in the picture (Fig. 6.27) This network is then used to test the performances of the implemented analysis on a bigger sample of events. Figures 6.28 and 6.29 show that ANN output really well separate the population of the chirp-like events from the background one and that its introduction can significantly improve the analysis performances. Note that the ANN output locates the majority of BKGg events near to zero (Fig. 6.29 bottom right). We can observe a minimal reduction on the signal detection and rightly classification (for a threshold on ANN output of 0.6 we have 1.3% signal lost and 0.5% of survived background). With the introduction of the ANN output the background can be reduced by orders of magnitude, without a significant lost of signal (Fig. 6.29, bottom left). Moreover an analogous improvement can be reached increasing the threshold on the cc parameter (Fig. 6.28 bottom right); anyway, this choice can considerably reduce the recognized fraction of signals (Fig. 6.28 top right). From these

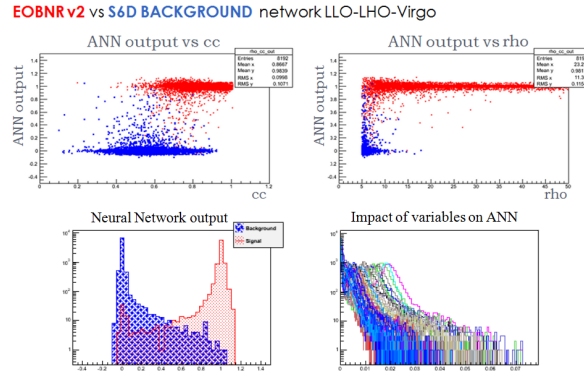


Figure 6.27: SIG(red) vs BKGg (blue) of preliminary test set (8192 chirp-like events, 8192 glitches). Top plots: ANN output versus cc (left) or ρ (right). Bottom graphs: on the left ANN output values for signal and background, on the right variation on each input, belonging from the preliminary test set, modifying the network output.

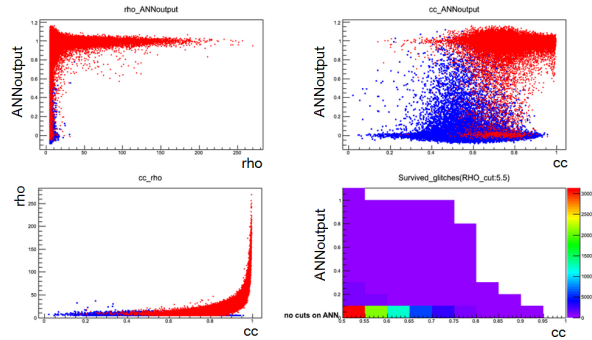


Figure 6.28: Scatter Plots: 10^5 BKGg events (blue), 10^5 SIG simulations (red).

observations we can conclude that the introduction of ANN output can reduce the impact of cc cut on the data, in the case of injections made in gaussian noise. Also the *Big Dog Event*, an hardware injection simulation the coalesce of two compact objects, was analyzed by the neural network, which result is reported in the table 6.5. As the table shown the analysis well

PARAMETER	VALUE
cc	0.70
ρ	8.93
ANN output	1.06

Table 6.5: Main results for the *Big Dog event*.

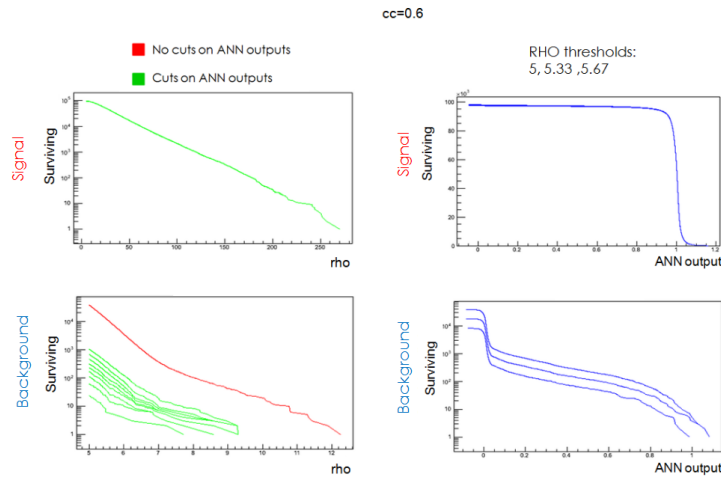


Figure 6.29: **Summarized Results:** 10^5 SIG simulations and 10^5 BKGg events. The ANN thresholds used to perform the several green curves: 0.2, 0.3, 0.4, 0.5, 0.6, 0.7, 0.8, 0.9, 1.

recognize the Big-Dog event as a chirp-like signal. The TF representation has indeed the characteristic shape of a GW consistent with CBC, as shown in the Fig. 6.30.

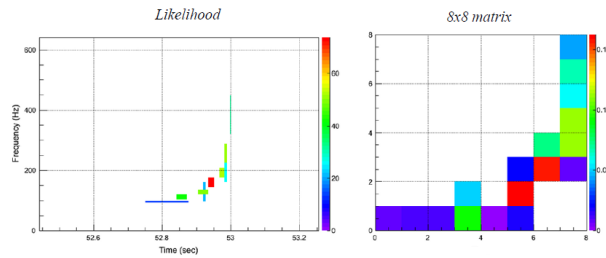


Figure 6.30: Big Dog event representation on the TF plane (left), and on the 8×8 frame.

Signals vs BRST waveforms

In this paragraph we focus on the network capability to separate injected waveforms belonging from different classes. Thus to define the signal category we adopt the usual CBC waveforms, whereas the background events are composed by the Standard Simulation Set (BKGb), which groups some different and general (with any astrophysical association) waveforms.

The training parameters of the best ANN implemented are summarized in the following table (Tab. 6.6). Therefore this network has been adopted to an-

PARAMETER	VALUE
Number of BKGb events	8192
Number of SIG events	8192
Epochs	600
Learning method	CGs with F.R.
Architecture	64in, 3h.l. (16 : 32 : 16), 1out

Table 6.6: Main parameters used to train the selected network.

alyze a bigger sample of events belonging from the same classes. The figures 6.31 and 6.32 illustrate the correspondent results obtained. All the images

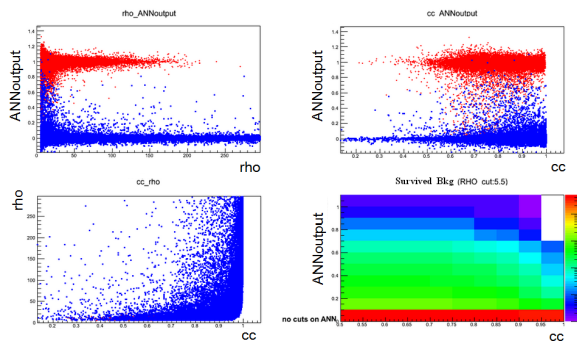


Figure 6.31: **Scatter Plots:** $5 \cdot 10^5$ BKGb events (blue), $5 \cdot 10^5$ SIG simulations (red).

show the good capability of the network implemented in the discrimination of events belonging to the two different classes. Obviously this is the only parameter available for the signal classification, because cWB post-production parameters have similar behavior for the two classes.

Also in this case we applied the analysis on the *Big Dog Event*, the results are shown in table (Tab 6.7). Therefore also against the BRST waveforms the network well identifies this event as associated to a GW emitted by CBC.

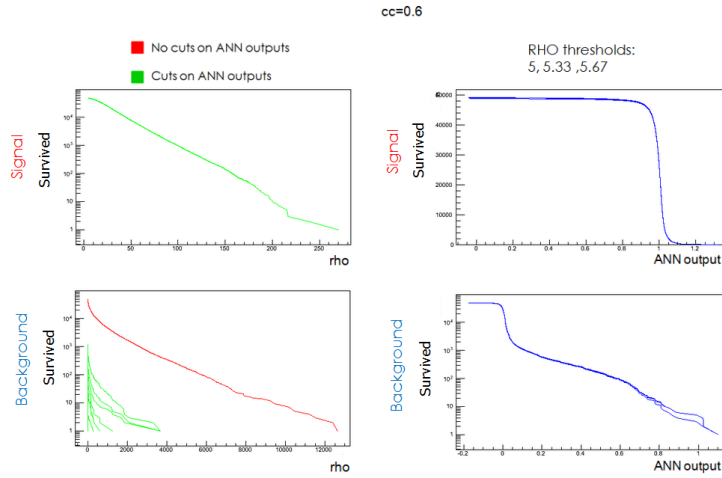


Figure 6.32: **Summarized Results:** $5 \cdot 10^4$ SIG simulations and $5 \cdot 10^4$ BKGg events. The ANN thresholds used to perform the several green curves: 0.2, 0.3, 0.4, 0.5, 0.6, 0.7, 0.8, 0.9, 1.

PARAMETER	VALUE
cc	0.70
ρ	8.93
ANN output	1.04

Table 6.7: Main results for the *Big Dog event*.

Preliminary analysis of on-off pixel amplitude

In this section we will see the comparison between the results obtained using as inputs the continuous values introduced by the matrix conversion and their binary representation (0,1) as on-off pixels. The figures 6.34 and 6.33 show that the networks achieve similar performances. Anyway the distribution obtained by the 0-1 amplitude is more compact near the edges values. Contrary to the expectations, this characteristics lightly worse the signal-background discrimination. Moreover we can note that the network generated with continuous amplitudes is more stable with respect to input variations. This result is therefore consistent with the choice of further develop only algorithms which have been trained with matrices created taking into account the TF pixels amplitudes.

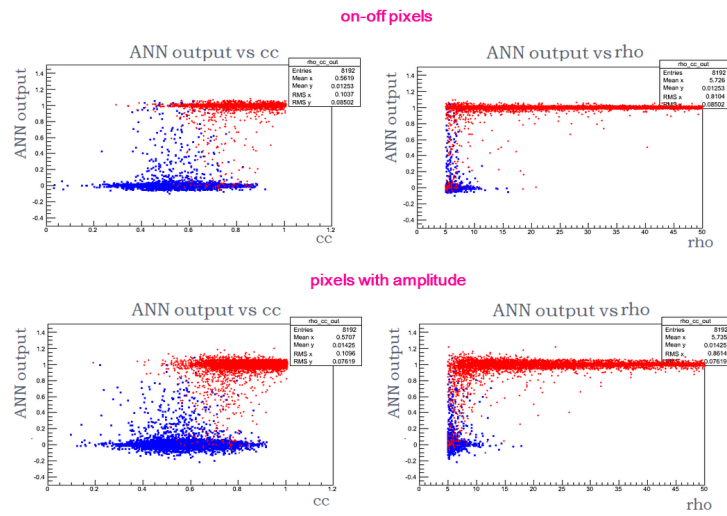


Figure 6.33: 8192 BKGg (blue) and 8192 SIG events (red) for each amplitude representation (independent sets). Top: attempt of on-off pixels, bottom: continuous input values. Left: ANN output vs cc , right: ANN output vs ρ .

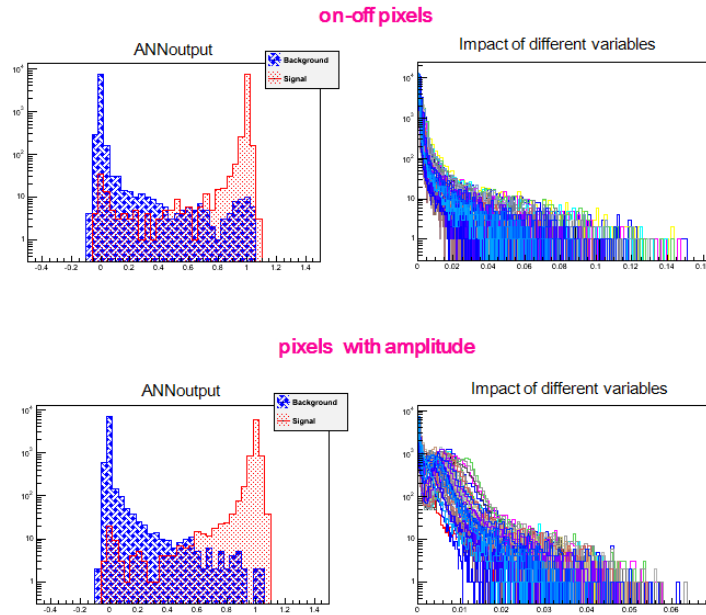


Figure 6.34: Same set of Fig. 6.33. Top: on-off input treatment, bottom: continuous values. Left: ANN output, right: output variations on the test sets due to changes in the inputs.

6.5 Results for recolored data

In the previous cases we have simplified the recognition problem for neural network injecting the waveforms into gaussian noise. To implement realistic tests it is necessary to introduce some real noise features which affect the measurements and the ANN distinction. These features are given by the S6D data detector recolored to match the advanced sensibility curves.

6.5.1 Tested events

Signals (rSIG)

The waveforms associated to CBCs are injected on the S6D recolored background, with the following characteristics:

- A range for the mass value of a single component from 1.5 to 25 solar masses;
- a mass ration between 1 and 11;
- a distribution uniform in total mass and mass ratio;
- a source distribution uniform in the volumes included in five consecutive shells: $(66.7 - 100)Mpc$, $(100 - 150)Mpc$, $(150 - 225)Mpc$, $(225 - 337, 5)Mpc$ and $(337, 5 - 506, 525)Mpc$.

Under this new enviromental conditions the cWB efficiency, calculated on the used samples of events, is reported for each distance-shell in the following table (Tab. 6.8). We can note a considerable decreasing of the efficiencies,

Shell	Estimated efficiency	Error
$(66.7 - 100)Mpc$	0.566	0.004
$(100 - 150)Mpc$	0.390	0.001
$(150 - 225)Mpc$	0.220	0.002
$(225 - 337.5)Mpc$	0.098	0.001
$(337.5 - 506.25)Mpc$	0.035	0.001

Table 6.8: cWB-efficiency for the five shells for chirp-like waveforms injected on recolored S6D glitches.

due to the presence of these non gaussian noise glitches which complicates the correct selection of TF-pixels performed by the cWB analysis (see two examples in Fig. 6.35). An amplitude average of the 8×8 matrix element on 16384 resulted events are illustrate in the successive image (Fig. 6.36). We can see that the TF transform is not well defined as in the previous case (injections on gaussian noise), which surely affects the pattern recognitions

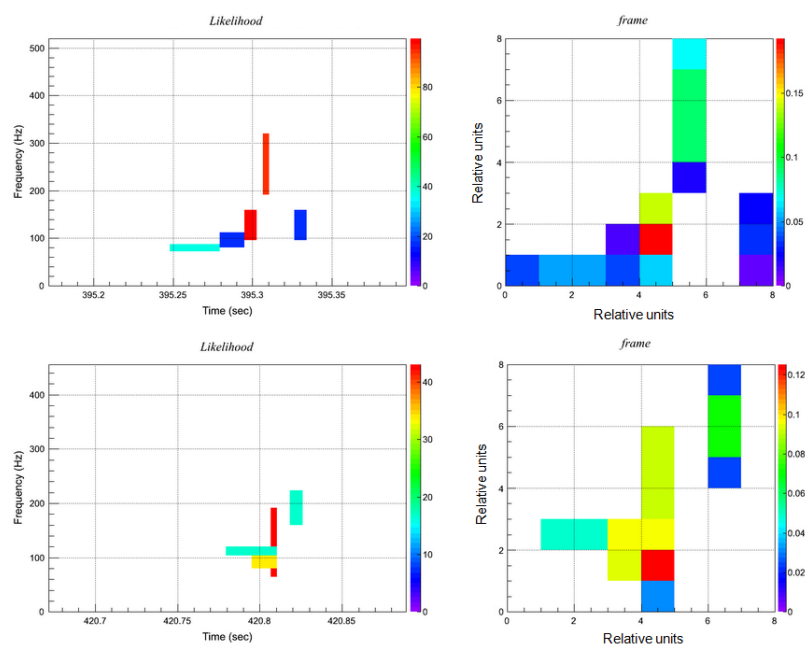


Figure 6.35: Two example of signals injected on recolored data. Left: representation of the events in the TF plane performed by CWB; right: conversion in 8×8 matrices.

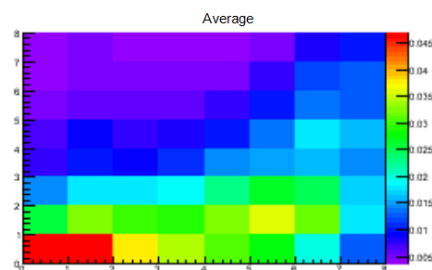


Figure 6.36: SIGNALS: the image shows the average on 16384 events of the input values.

performed by the ANNs, especially for on-pixels on the right bottom part of the frame (Fig. 6.35). Anyway not all the events are corrupted by the noise in a so significant way, as we will see in the following.

The main parameters used to analyze the data through the cWB pipeline are written in the following table (Tab. 6.9).

Background: glitches (rBKGG)

Also the background events have been extracted considering the data collected during the period July-October 2010 (S6D science run) recolored according the Advanced Sensitivity curves.

The analysis was performed with the same parameters used for the signals, reported in the table (Tab. 6.9).

The main characteristic feature of the resulting background on the 8×8 frame is illustrated in the Fig. 6.37.

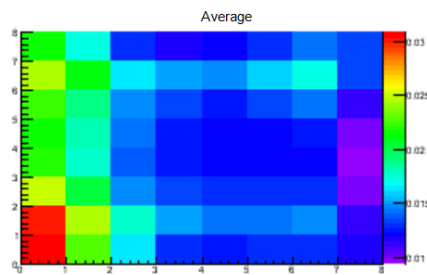


Figure 6.37: RECOLORED BACKGROUND glitches: the image shows the average on 16384 events of the input values.

Background: BRST (rBKGb)

Similarly to the chirp-like signals also the waveforms belonging from the Standard Simulation Set are injected on the real S6D recolored data, with the same cWB parameters (Tab 6.9).

The shape resulting on the 8×8 matrix is reported in the Fig. 6.38.

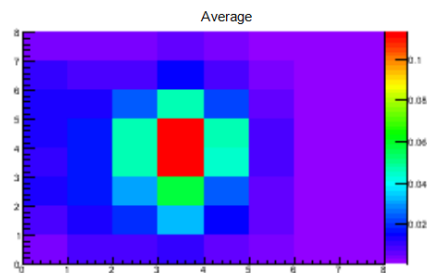


Figure 6.38: RECOLORED BACKGROUND BRST: the image shows the average on 16384 events of the input values.

PARAMETER	VALUE	PARAMETER	VALUE
ρ threshold	5	cc threshold	none
search type	i	detector network	V1H1L1
lower f	64Hz	higher f	2048Hz
Δt_{max}	3s	Δf_{max}	130 Hz
lower level	4	higer level 10	

Table 6.9: Main cWB paramters used to analyze the recolored data.

Main cWB parameters used to analyze the recolored data

6.5.2 ANNs trained with waveforms injected on gaussian noise

In this subsection we will see the effects of performing an analysis on recolored data using a network trained on signal (and BRST) waveforms injected on gaussian noise.

The main results are described by the same pictures introduced in the previous paragraph:

Signals vs S6D recolored glitches Fig. 6.39 and Fig. 6.40;

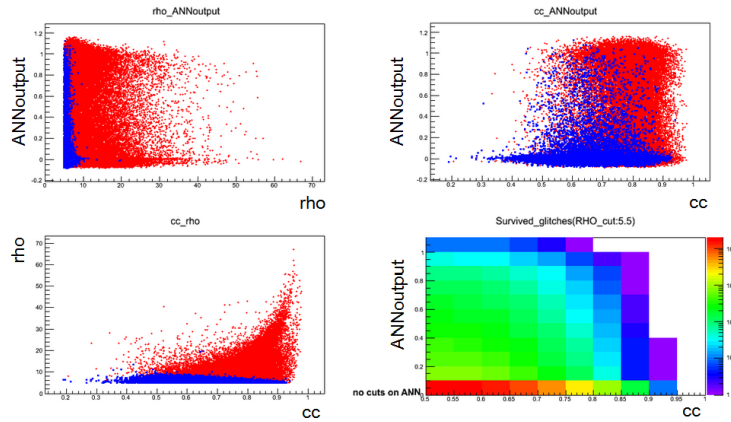


Figure 6.39: **Scatter Plots**: the picture shows $5 \cdot 10^4$ background (blue points) and $5 \cdot 10^4$ signal (red dots) events. The network used for the test these candidates is the same described by the table Tab. 6.4.

Signals vs BRST Fig. 6.41 and 6.42

Considerations

By the previous graphs we can see that the background is rightly classified by the two networks, similarly to what happens for the original S6D glitches and

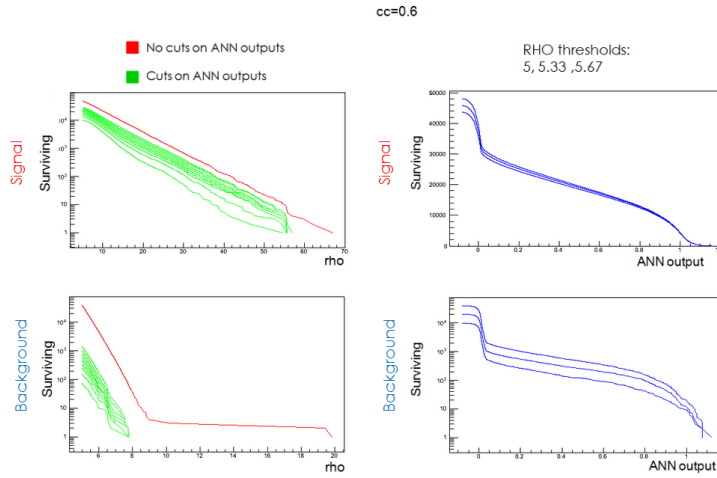


Figure 6.40: **Summarized Results**: the picture shows $5 \cdot 10^4$ background and $5 \cdot 10^4$ signal events. The network used for the test these candidates is the same described by the table Tab. 6.4.

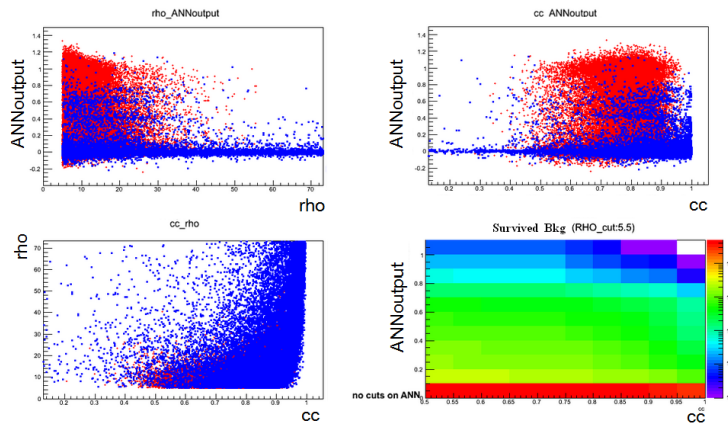


Figure 6.41: **Scatter Plots**: the picture shows $5 \cdot 10^4$ rBKGB and $5 \cdot 10^4$ rSIG events. The network used to the test these candidates is the same described by the table Tab. 6.6.

the waveforms of the Standard Simulation Set tested in the section before. Also the rung-feature is remained to characterize the network behaviours with respect to background events. The main changes concern the signal interpretation. Indeed the selection of noisy pixels near the trace on its right or bottom can cause a considerable deformation in the resulting “input-shape” which the networks are not trained to recognize. This is the main problem obtained by the case of networks which have trained on gaussian data and applied on a set of recolored events, which are generally polluted

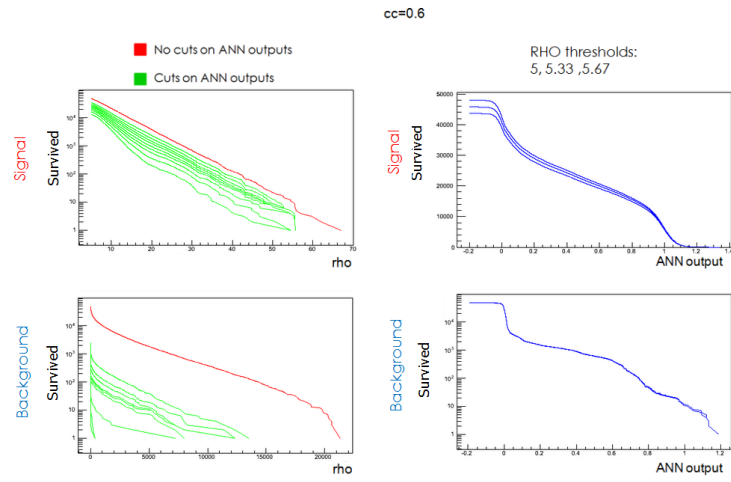


Figure 6.42: **Summarized Results:** the picture shows $5 \cdot 10^4$ rBKGB and $5 \cdot 10^4$ rSIG events. The network used to the test these candidates is the same described by the table Tab. 6.6.

by the detector noise.

6.5.3 ANNs trained with recolored data

A different test was performed training ANNs with the recolored events. For the network learning we decided to apply the best parameters found during the previous training and thus described respectively for the glitches and the Standard Simulation set by the tables 6.4 and 6.6. The main results are reported in the following.

Signals vs S6D recolored glitches Fig. 6.43 and Fig. 6.44;

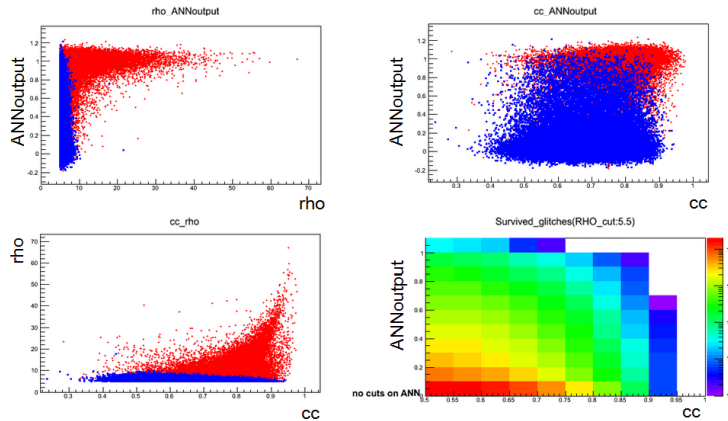


Figure 6.43: **Scatter Plots**: the picture shows $5 \cdot 10^4$ rBKGg (blue) and $5 \cdot 10^4$ rSIG (red) events. The network used to the test these candidates is the same described by the table Tab. 6.4.

Signals vs BRST Fig. 6.45 and Fig. 6.46;

Considerations

Results are very different in comparison to the ones obtained through the use of ANN trained with data from gaussian noise. First of all we can observe that the networks trained on recolored events are not so able to recognize the background features. We have therefore lost the grouping and thus the rung in the background representation (bottom-right) in both the cases. Anyway this non-clear training has the advantage to better classify the signal traces corrupted by the presence of noisy pixels; the most improvement on the signal recognition seems to be shown by the distinction between the two different classes of waveforms. However this increasing of the signal identification probably means that we have trained the networks with more elastic rules, and suggest that this is a more effective approach for the discrimination of the recolored data.

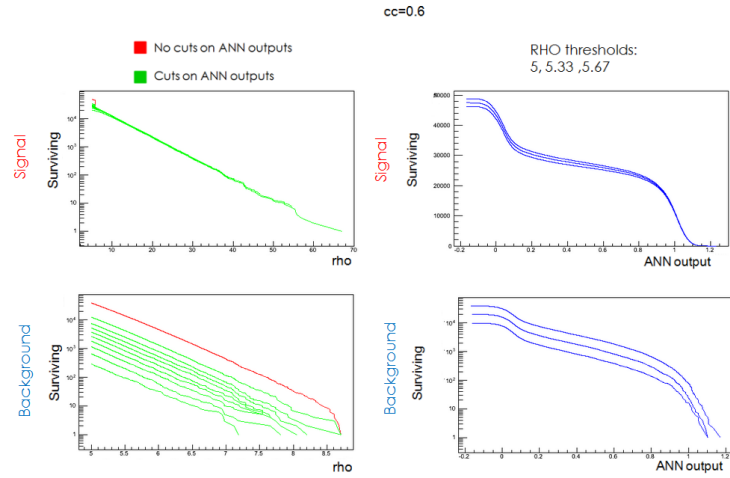


Figure 6.44: **Summarized Results:** the picture shows $5 \cdot 10^4$ rBKGb and $5 \cdot 10^4$ rSIG events. The network used to the test these candidates is the same described by the table Tab. 6.4.

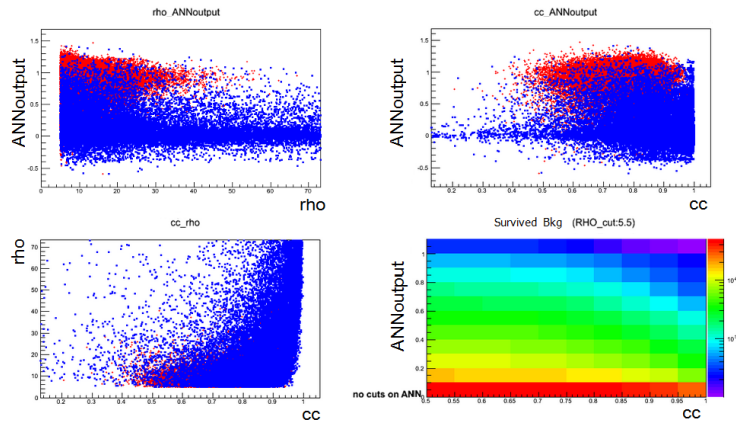


Figure 6.45: **Scatter Plots:** the picture shows $5 \cdot 10^4$ rBKGb (blue) and $5 \cdot 10^4$ rSIG (red) events. The network used to the test these candidates is the same described by the table Tab. 6.6.

ANN colored applied on “cleaned ”data

A final test was performed to evaluate the abilities of the ANNs trained with the recolored data. This consists on apply them to the “cleaned ”data and observe their behaviours. We expect that they are able to recognize the chirp-like signals injected on gaussian noise, but also a dispersion of the background events on the ANN output coordinate, similarly to what happens during the tests on recolored data. These expectations are verified, as shown

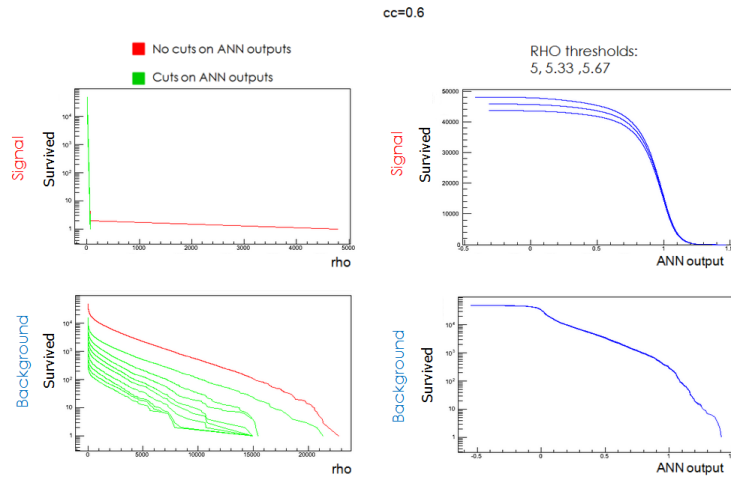


Figure 6.46: **Summarized Results:** the picture shows $5 \cdot 10^4$ rBKGB and $5 \cdot 10^4$ rSIG events. The network used to the test these candidates is the same described by the table Tab. 6.6.

the following two figures (Fig. 6.47 Fig. 6.48). This results are consistent

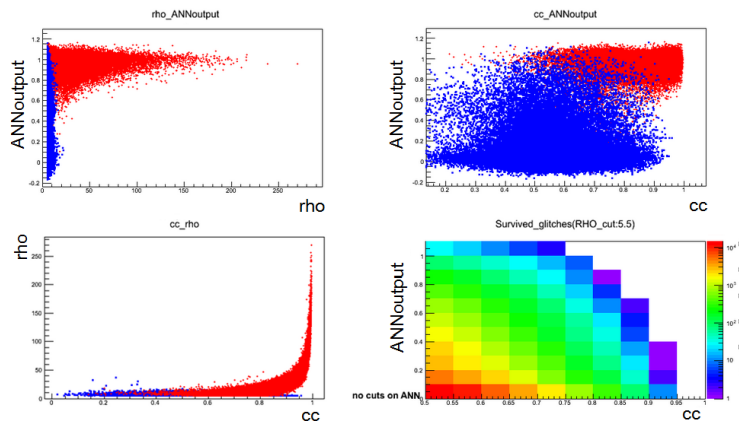


Figure 6.47: **Scatter Plots:** the picture shows $5 \cdot 10^4$ rBKGB (blue) and $5 \cdot 10^4$ rSIG events (red). The network used to the test these candidates is the same described by the table Tab. 6.4.

with the idea of a training less constrained for the signal identifications and thus they shown the disadvantages of a worse background isolation with respect to the performances obtained by networks trained on clearer data. For this reason we do not find the rung feature on the bottom-right of (Fig. 6.48) as for the tests performed n recolored data. Anyway the network remains able to well recognize the chirp-like features, which mean that the

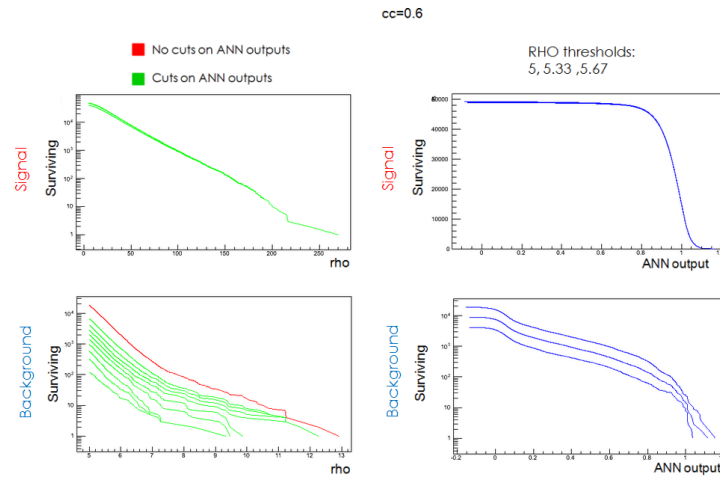


Figure 6.48: **Summarized Results:** the picture shows $5 \cdot 10^4$ rBKGb and $5 \cdot 10^4$ rSIG events. The network used to the test these candidates is the same described by the table Tab. 6.4.

basic idea of learnt by the algorithms is the same and only less restrictive.

Chapter 7

Implemented improvements on ANN analyses and comparison with other methodologies.

In this chapter we will present some improvements, implemented, on the data-treatment for the ANNs analysis and we will briefly discuss also the potentialities of the application of different techniques, both as alternatives and in combination with the proposed pattern recognition computed by machine learning. In all the chapter we will focus on the discrimination between the noisy glitches and the chirp-like signal.

In the following we will focus on developments of the input matrix conversion algorithm (Sec. 7.1), on a comparison between the performances reached by different networks (Sec. 7.2) and on the implementation of an average over the outputs of different networks (Sec. 7.3). A discussion on signal fitting approaches (Sec. 7.4) and a Fisher linear discriminant application to combine results (Sec. 7.5) are then presented.

7.1 Input matrix developments

As we discussed in previous sections (Sec. 6.4 and Sec. 6.5), one of the main issues for the ANN signal classification is that the reconstructed signal cluster sometimes include pixels caused by noise fluctuations. In fact, the cWB clustering algorithm has been set to promote time-frequency pixels in the proximity of the most energetic ones; this feature helps in reconstructing entirely signals of complex time-frequency structure as the chirp-like ones, but sometimes has the drawback of including pixels representing just noise fluctuations. As a consequence, the time-frequency shape of the reconstructed clusters shows a greater variability, as for instance the duration of the event can be overestimated. This in turn is reflected by a larger variability of the

traces in the input matrix representation of the event.

This issue was rare in the test on signals injected on simulated gaussian noise, but becomes important in the actual case of signals injected in real noise. Indeed we have verified that the representations of the signals not correctly classified, are often affected by the presence of pixels following in time the chirp-like trace, thus spoiling the typical final trace of the event.

For this reason, we developed a strategy to remove the most problematic pixels. Starting from the last pixel and going backwards in time, the algorithm cuts pixels from the cWB reconstructed cluster until the cumulative cut overcomes a preset threshold on the relative fraction of the total likelihood of the cluster. In case the last pixel shows a likelihood fraction greater than the preset one, no cut is implemented. Otherwise, the modified cluster is used in place of the original one to create the input matrix.

The tests using different preset thresholds showed that this backward time-clipping procedure works best using a threshold equal to 0.1 times the likelihood of the original cluster. In light of these results, we adopt this rejection procedure as a standard step to build the input matrix for the subsequent pattern recognition. Fig. 7.1 gives a graphical representation of the average effect of this procedure on the input matrix.

Other two changes implemented on the input matrix building process were tested and adopted.

Exploiting the maximum time and frequency resolution (*dt and df min*)

The idea is to improve the T-F resolution used to project events on the input matrix. Previous procedure to build the input matrix considered the minimum ΔT and Δf of the pixels included in the reconstructed cluster of the cWB event (see Sec. 6.1). In many glitch and in some signal cases, where the cluster is made by a just a few pixels, this resolution resulted too coarse and only a fraction of the 8x8 input matrix time and frequency ranges were effectively used by the cluster. Instead, by starting from the minimum ΔT and Δf of the full cWB analysis, the definition of the time-frequency ranges covered by the input matrix can be better fitted to the reconstructed signal.

Clipping time range (*approx*) By looking at mis-classified signals, we found that the choice of the time range of the input matrix should avoid having blank (null) columns corresponding to start and end times. To mitigate this issue, we set up a rounding procedure on the time range of the matrix as follows. We consider the division with remainder between integer numbers, the duration of the cluster expressed as number of minimum ΔT over the input matrix time dimension, equal to 8. If the remainder is > 4 the cluster is centered in time with respect to the input matrix as previously done (see Sec. 6.1). Else, up to 4 of

the starting ΔT of the cluster are clipped out of the input matrix time range; in this case, to avoid losing event amplitude, the amplitude of clipped pixels of the event are summed to the first pixels kept in the input matrix, as if the cluster frame was folded at the clipped time.

The effects of these procedures on the input matrix average for the case of glitches and of signals are reported in Fig. 7.1.

Several tests have been performed to verify if these changes have improve

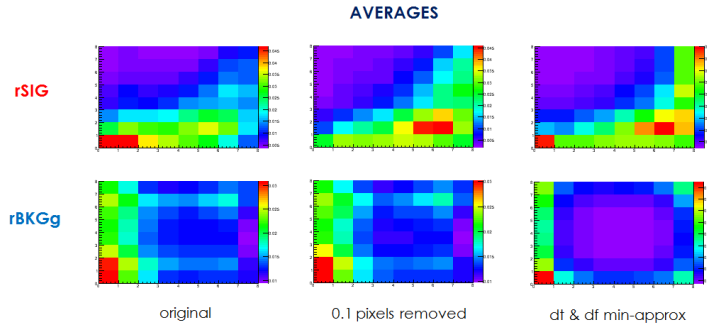


Figure 7.1: Time-frequency input matrices averaged over 16384 signals (top row) and 16384 glitches (bottom row). From left to right: standard procedure of Sec. 6.1, after implementation of the backward time-clipping procedure (0.1 threshold on likelihood fraction cut) and after implementation of *dt* and *df min* and *approx*.

the analysis results. First we apply each of them singularly, and then we combined them. Some results are shown in the following pictures (Fig. 7.2 and Fig. 7.3); These results should be compared with Fig. 6.43 and Fig. 6.44 which were the best results described in the previous section.

The best discrimination is achieved by the matrix conversion which takes into account all these strategies (Fig. 7.3 and Fig. 7.5).

7.2 Comparison between performances of different ANNs

In this section we compare results considering different ANN networks applied to the same set of events, so to have a fair comparison of the performances. The results show generally a consistency between the different ANNs, with light differences. Figure 7.4 shows the impact of different configuration of the starting weight, we can observe that the major part of the events are located on the diagonal, and there is a compact group of signals near to the zero value of output. This shows that the ANN interpretation are

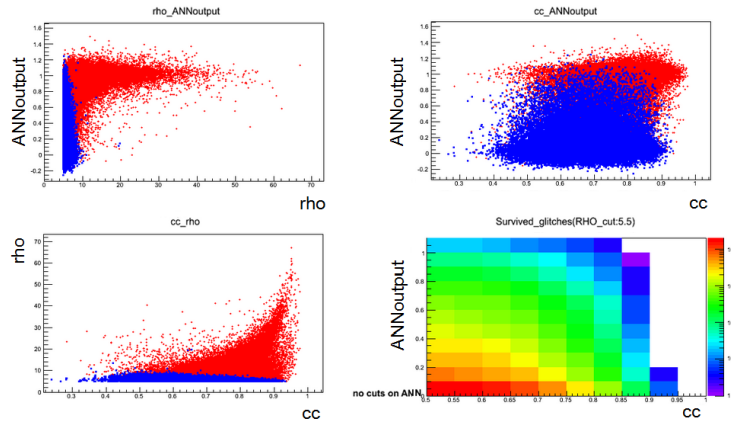


Figure 7.2: **Scatter plots:** the image represents the main results obtained over a sample of $5 \cdot 10^4$ signal (red) and $5 \cdot 10^4$ background (blue) events elaborated through the matrix conversion algorithm resulted by the implementation of the previously described techniques.

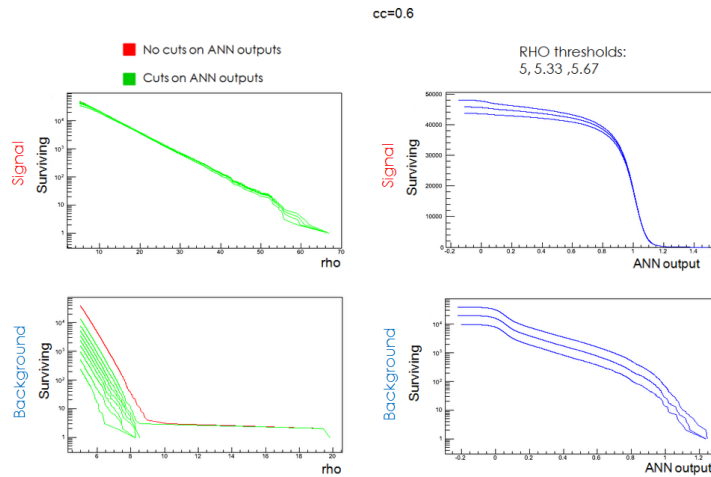


Figure 7.3: **Summarized Results:** the image represents the main results obtained over a sample of $5 \cdot 10^4$ signal and $5 \cdot 10^4$ background events, also in this case they are elaborated by the matrix conversion algorithm obtained by the implementation of the previously described techniques.

consistent between the two networks. In the Figure 7.5 we can analyze the effect of different matrix conversion algorithms. We can observe a considerable improvement on the discrimination due to the changes applied on the conversion technique, in particular on the false dismissal counts, but without a significant increasing on the false alarms.

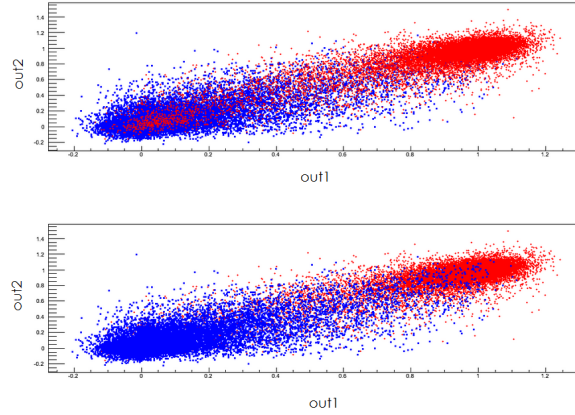


Figure 7.4: Scatter plot of two ANN outputs over 20000 background (blue) and 20000 signal (red) events. The two ANNs are identical apart from the fact that they have been independently trained, i.e. their initial weights were independent and their training sets were disjoint. The best input matrix conversion algorithm is used. In the top plot the signal points are printed on top of the glitch points, vice versa for the bottom plot. The degree of correlation of the two ANN outputs is evident.

Different information can be extracted comparing the networks trained with signals injected on gaussian noise and on recolored data. Indeed, in the two cases network has been trained in a different way, as already explained in the previous chapter. The result of this test can be visualized in the Fig. 7.6. We do not see significant improvements between the two cases, which confirms the consistency between the analyses performed with different networks.

7.3 Averaging over more ANN outputs

Averaging out the outputs of more ANN which have been independently trained is an example of the bootstrapping technique in statistics. We implemented this technique both to estimate the uncertainties related to the results of a single ANN and to check how much the averaging procedure can improve the results. For this test, we used our best input matrix conversion algorithms (0.1 amplitude threshold on the later pixels, the *approximation* and the *minimum dt and df* strategies as described in previous sections).

The entire set of available events has been divided in seven equally numerous and disjoint sets. Seven ANN have been trained independently on each of these sets and provided output results on the remaining events. In this way each event is tested by six independent ANNs while it is used only once to train an ANN. By averaging over the six available outputs per event, we

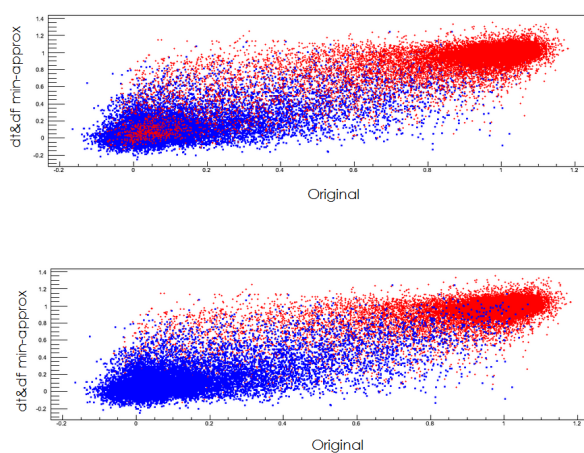


Figure 7.5: Scatter plot of two ANN outputs over 20000 background (blue) and 20000 signal (red) events. The two ANNs have been independently trained and two different input matrix conversion algorithms: the best procedure described in this Chapter (backward time clipping AND *dt and df min* AND *approx*) against the procedure previously used and described in the previous Chapter. This illustrates that the change of input procedures affect the ANN results and that the former procedure discriminates much better the signals from background than the latter.

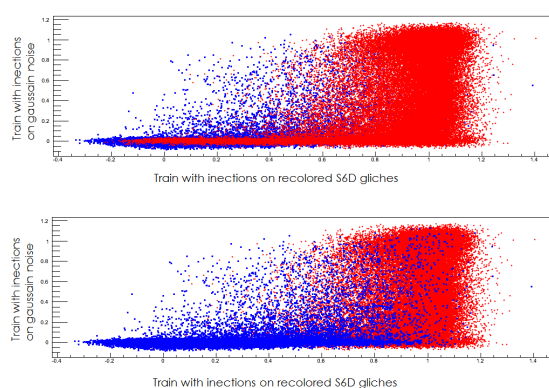


Figure 7.6: Set of $\sim \cdot 10^3$ S6D recolored glitches and signal waveforms injected on recolored data. Ordinate is the output obtained with of network trained on simulation injected on gaussian noise; abscissa refers to output provided by an ANN learned with waveforms injected on recolored S6D glitches.

define an “average ANN output”. The resulting scatter plot of ANN output vs the network correlation coefficient is plotted in Fig. 7.7. Fig. 7.8 shows a

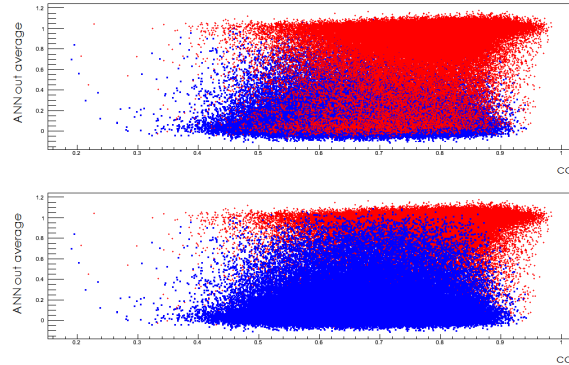


Figure 7.7: Scatter plot of $\sim 11.4 \cdot 10^4$ S6D recolored glitches (blue) and the same number of signal waveforms injected on recolored data (red). The ordinate is the average output of six independent ANNs, the abscissa shows the network correlation coefficient of the event. In the top plot the signal points are printed on top of the glitch points, vice versa for the bottom plot. Our best input matrix algorithm are used as described in the previous subsections (i.e. *approx-dt* and *df min* procedures, 0.1 amplitude cut on the later pixels).

sample comparison of a single ANN output to the ANN output average over 32768 background and 32768 signal events. At a first approximation the overall performances look very similar, the most evident change being a narrowing of the bulk of the signal and glitch distributions of the ANN output average around 1 and 0 respectively. This is again consistent with correlation among different ANNs outputs, i.e. the score of each event is generally not fluctuating much compared to the [0,1] range. To check how much the

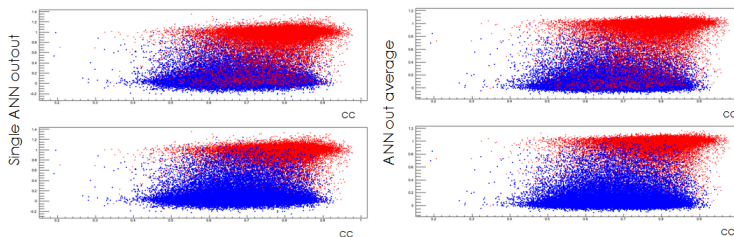


Figure 7.8: Comparison between final values obtained with a single ANN output (left) and with an average over the output of 6 networks (right). On the top the 32768 signals (red) are printed over the 32768 glitches (blue), on the bottom the contrary.

ANN averaging can affect the false alarm and false dismissal for the classification method we considered a threshold value of 0.6 on the ANN output and

computed false alarm counts and false dismissal counts, see Tab.7.1. This implementation of ANN output averaging turns out to improve the average performance of single ANNs, in particular it performs significantly better than any single ANN. The resulting false alarm probability provided by the ANN output averaging and selecting the 0.6 threshold is 0.0403 ± 0.0001 , which is a quite interesting number for astrophysical searches (see Conclusion). The variance of the false alarm counts among ANN 0, 1, ..., 6 is 3061, i.e. significantly larger than what is expected from a Poisson counting uncertainty. On one side we know that independently trained ANNs have positively correlated outputs. Even if this would call for smaller than Poisson fluctuations, we have to mention that the glitches used for testing occur in “families”, i.e. are clustered in the glitch parameter space, a fact that can call for larger than Poisson fluctuations as those observed. Looking closer to the false alarm/false dismissal results of each ANN on single data sets, we observe that performances on disjoint data sets are correlated, e.g. ANN 5 [6] is performing systematically better [worse] than the average for false alarms in all six disjoint data sets. An alternative way to combine responses of more

ANN	False Alarm Counts	False Dismissal Counts
average	~ 520	~ 1820
0	~ 643	~ 1882
1	~ 690	~ 1987
2	~ 666	~ 1939
3	~ 644	~ 2265
4	~ 697	~ 2162
5	~ 564	~ 2330
6	~ 740	~ 2475

Table 7.1: False alarm and false dismissal counts for the seven ANNs independently trained (indexed 0,1,...,6 and for the resulting average over the six ANNs outputs available per each event. All reported counts in are values per data set (16384 background and 16384 signal events each), in particular the reported values are averaged over all the relevant data sets available (seven for the ANN average, six for each single ANN since one is used for training)).

ANNs can be to consider how many ANNs agree on rejecting/accepting an event as signal. In Tab. 7.2 we report the mean false alarm counts per data set when requiring that the majority of the six independently trained ANNs agree to reject the glitch. When requiring a rejection criteria such as that at least 3 ANNs out of 6 should classify the event as glitch (using the same 0.6 threshold on ANN output as before) the achieved false alarm probability is about 6%, a comparable level to the previous strategy.

criterion	mean	standard deviation
FAs by all 6 ANNs	198	8
FAs by 5 ANNs	328	9
FAs by 4 ANNs	462	20
FAs by 3 ANNs	625	28
average of FA	663	23

Table 7.2: Mean false alarm counts per data set requiring a majority criterion among ANNs on the event classification. From top to next to bottom rows: unanimous (6 vs 0) classification as glitch down to parity (3 vs 3) classification. The last row reports the mean false alarm counts for a single ANN (averaged over the ANNs and the data sets).

7.4 Fitting procedure

The well-known behaviour in the Time-Frequency domain of the desired signals suggest the idea to using a fitting procedure for the event classification. In this section we will see two different approaches for this non-trivial issue. The expected trace of the Time-Frequency domain of waveforms compatible with the compact binary coalescences is described by the TF relation $\omega(t) \propto t^{-3/8}$ (see the equation (1.36)). In our case the fit is applied on the TF representation of the signal provided by the cWB analysis with the WDM transformation. The main problems we have encountered on this fit application procedure data are summarized in the following list.

Pixel treatment The uncertainties to be associated to each pixel are not known. We approximated each pixel with its central position and chose to use 1σ error bars assuming a uniform probability distribution inside the pixel resolutions.

Linearization procedure A reasonable procedure is passing from a power law fit to a linear one. This however causes complications related to the error propagation on the frequency. Error bars along the frequencies are no more symmetric. Moreover, data at higher frequencies are characterized by much smaller error bars, and they become predominant in the fitting procedure. In this situation, any selected noisy pixel or non chirp-like signal feature located in the higher frequency band can completely misguide the fit results.

Even if these issues may make the fitting procedure less appealing, it brings also some advantages: fit parameters have a direct astrophysical interpretation, e.g. on the chirp mass of the coalescing binary.

7.4.1 Chirp mass

A fitting approach to select chirp-like events has been developed by another research group within the LIGO Scientific Collaboration (*Mchirp*). It is based on a linearized fit of equation (1.36) and output parameters are chirp occurrence time and chirp mass of the binary. The main idea for this signal classification is that glitches are characterized by lower values of chirp-mass than the astrophysical signals. To calculate this key quantity the algorithm weights each pixel normalizing by its likelihood. In this approach the selected core pixels among all levels of the cWB WDM-analysis are considered together to obtain the results. The goodness of the fitting is not easily to compute: since the considered data are not independent.

The implemented procedure consists in the minimization of the function:

$$\begin{aligned}\tilde{\chi}^2 &:= \sum_i \left(\frac{96\pi^{8/3} G^{5/3} M_{chirp}^{5/3}}{5c^5} t_i + \frac{3}{8} f_i^{8/3} + C \right)^2 \frac{E_i}{E} \\ &\equiv \sum_i (y_i + b(x_i - x_0))^2 \frac{E_i}{E}\end{aligned}\tag{7.1}$$

where C is a constant while x_0 and b are the two unknown parameters. The angular coefficient is related to the chirp mass by the equation:

$$b = M_{chirp}^{5/3}\tag{7.2}$$

Some results on the application of these techniques are reported in the Figures 7.9 and 7.10. These images show that this algorithm reaches good performances: its background reduction in combination with cuts on the network correlation coefficient and on signal strength (ρ) is about the same order of magnitude of the one achievable by the ANN pattern recognition. Also efficiency are similar. The distribution of chirpmass of injected signals is obviously due to chosen distribution of masses of the binary stars.

An interesting comparison is illustrated by the image (Fig. 7.11). It shows the representation of $\sim 50 \cdot 10^3$ signal and $\sim 50 \cdot 10^3$ background events in a plane whose ordinate refers to the average of six ANN outputs and whose abscissa is the M_{chirp} calculated by this procedure. Though both techniques are based on the TF trace interpretation, their results are quite uncorrelated. In particular, they have two different and separate tails of false alarms. Therefore, it will be possible to considerably increase the performances applying elliptical or hyperboloidal joint cuts. As final consideration this first comparison suggest that the results obtained using chirp mass is comparable with that of the ANN method.

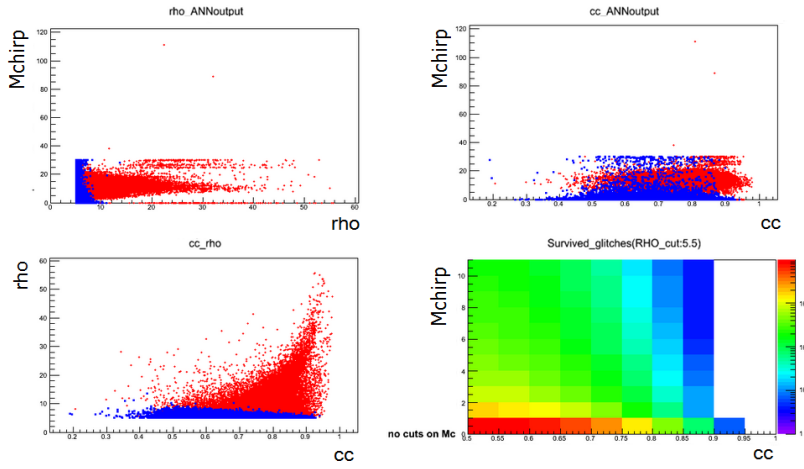


Figure 7.9: **Scatter Plots:** Set of $\sim 25 \cdot 10^3$ S6D recolored glitches (blue) and the same number of signal waveforms injected on recolored data (red). For the graphs explanation we always refers to the apposite paragraph in the previous chapter.

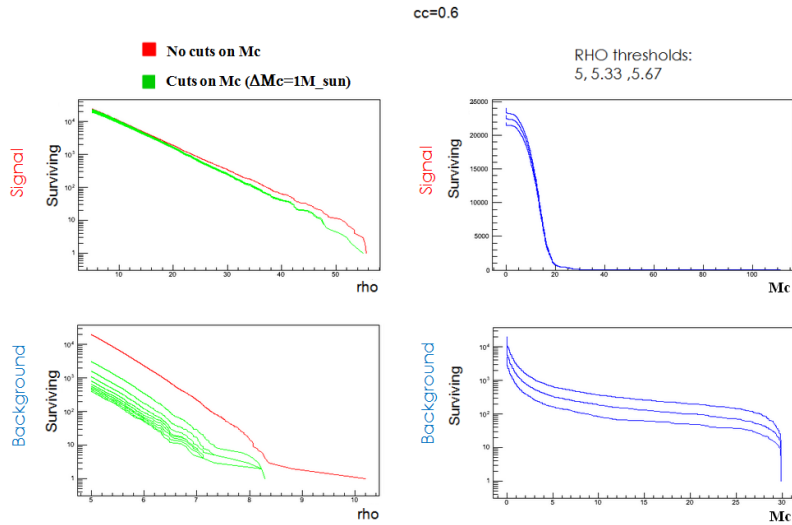


Figure 7.10: **Summarized Results:** Set of $\sim 25 \cdot 10^3$ S6D recolored glitches (blue) and the same number of signal waveforms injected on recolored data (red).

7.4.2 Our implementation of the fitting procedure

Differently from the chirpmass procedure described in the previous section, we implemented a fit considering only the independent pixels selected by the principal component extraction procedure of cWB 2G for the final event rep-

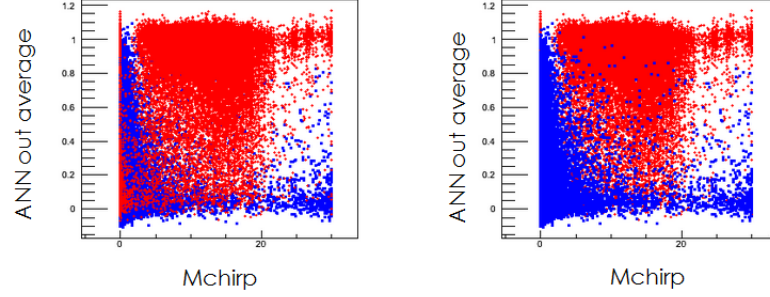


Figure 7.11: Set of $\sim 50 \cdot 10^3$ S6D recolored glitches (blue) and the same number of signal waveforms injected on recolored data (red). On the left the red are printer od the blue points, on the right the contrary. The ordinate is the output average of 6 ANNs as described earlier, the abscissa is the chirpmass parameter estimated from the fitting procedure.

resentation on the TF plane. We consider the pixels as data points centered at pixel's center and define the error bars assuming a uniform distribution, i.e. $1\sigma \sim 0.3 \times$ pixel width. To choose the most adequate technique for the interpretation of our problem we have analyzed different methods to fit the data:

- the **power-law fit** (implemented in ROOT):

$$f(t) = [0]_{pl} ([1]_{pl} - t)^{-3/8}$$

$$[0]_{pl} = \left(\frac{256G^{5/3}M_{chirp}^{5/3}}{5c^5\pi^{-8/3}} \right)^{-3/8}, \quad [1]_{pl} = \frac{5c^5\pi^{-8/3}f(t_0)^{-8/3}}{256G^{5/3}M_{chirp}^{5/3}} \quad (7.3)$$

where $[0]_{pl}$ and $[1]_{pl}$ are the parameter estimated by the fitting procedure;

- the **linear fit** (implemented in ROOT):

$$y(t) = f(t)^{-8/3} = [0]_{lin} ([1]_{lin} - t)$$

$$[0]_{lin} = [0]_{pl}^{-8/3} = \frac{256G^{5/3}M_{chirp}^{5/3}}{5c^5\pi^{-8/3}}, \quad [1]_{lin} = [1]_{pl} \quad (7.4)$$

where $[0]_{lin}$ and $[1]_{lin}$ are the paratemer estimated by the fitting procedure;

- the **linear regression**:

$$y(t) = f(t)^{-8/3} = [0]_{rl}t + [1]_{rl} \quad (7.5)$$

$$[0]_{rl} = -[0]_{lin}, \quad [1] = [0]_{lin} \cdot [1]_{lin}$$

where $[0]_{rl}$ is the angular coefficient of the straight line, and $[1]_{rl}$ its intercept.

Thus we can obtain M_{chirp} from the $[0]$ parameter. The first problem we found was related to the presence of noise pixels, so we implemented procedures to reject them. A first attempt consists on implementing the same procedure used for the input matrix conversion: backward in time clipping up to 0.1 of the total likelihood. Since this was not satisfactory, we add a regression procedure. This algorithm ignores error bars and computes fitting parameters on a cluster of N pixels N times, each time excluding one fitting point. Then we compare the non-normalized-chi-square quantities $\hat{\chi}_k^2 = \sum_{i \neq k} (y_i - g(t_i))^2$ and exclude permanently the $k - th$ pixel associated to the minimum $\hat{\chi}_k^2$ in the set. This step is applied only if the number of surviving pixels is greater than 4. The selected pixels are therefore analyzed by the fit procedure proposed by ROOT. The initialized parameters are set at the values obtained by the previous regression.

The results found are then used to initialize the power law fit implemented on ROOT software. Because this latter was not satisfactory (Fig. 7.12 red-line), we focused on the linear fit.

To have a confirm of the found parameters, another procedure was tested. It consists on a first rough estimates of the parameters from linear fitting applied to independents couples of points and averaging the results. These are also used to set the initial values of the fit parameters obtained by the ROOT analysis, but the results look very similar to the one obtained with feeding this process with the regression parameters. Thus the average parameters are only used to check the results.

In the following we analyze, on a set of seven events contained in a job (i.e. a GW data segment), the performances reached by our fit procedure and compare them also with the results obtained by the other algorithm explained in the paragraph before (M_{chirp}). From the images we note that the fit

Event	$M_{chirp_{lin}}$ (our)	$M_{chirp_{lin}}$ error (our)	$\chi_{lin-norm}^2$ (our)
0	22	1	0.93
1	10.3	0.1	27
2	7.8	0.15	150
3	0.002	0.001	876
4	0.098	0.003	13
5	10.8	0.4	17
6	12.7	0.7	0.4
7	25.7	1.4	0.97

Table 7.3: Main parameters resulted from the fit approach developed by us. The subscript *norm* refers to the reduced (χ^2 normalized by the degrees of freedom).

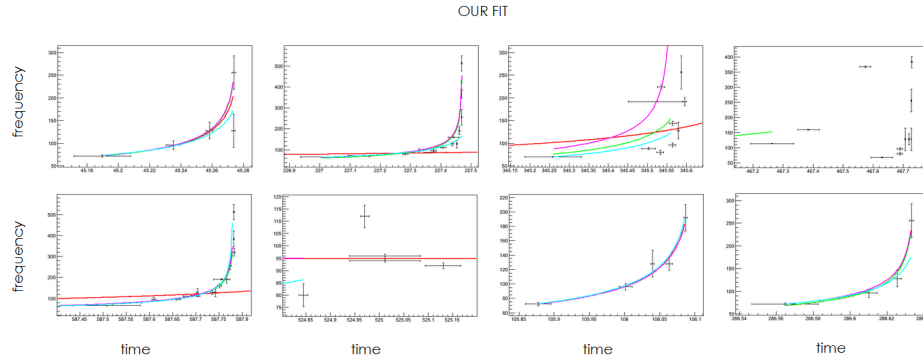


Figure 7.12: In the picture are represented the eight events of the job considered, in order from 0 to 7 from the top-left, along the lines, to the bottom right. The red lines refers to the fit computed by ROOT in the power law; the fuchsia line is associated to the linear fit always obtained by ROOT, while the green and the blue ones represent the linear regression calculated respectively considering and neglecting the error bars.

Event	Mchirp	Mchirp error	$\tilde{\chi}_{norm}^2$
0	11.6	0.004	0.92
1	7.2	0.0002	0.88
2	13.6	0.0004	0.85
3	11	0.0002	0.80
4	7	0.001	0.88
5	6.5	$1 \cdot 10^{-5}$	0.87
6	8	0.002	0.96
7	13.3	0.001	0.95

Table 7.4: Main parameters resulted from the fit approach explained in the previous paragraph (*Mchirp*). The subscript *norm* refers to the reduced χ^2 (normalized by the degrees of freedom).

performed with power law provided the worst results (red lines), on the table we report the results obtained by the fit implemented on ROOT software concerning the linear fit. We can note that the reduced χ_{norm}^2 in our case often acquires strange and big values. This can be due to two causes: in the linear domain the error bars on the points are under estimated or/and a non correct procedure is implemented by ROOT to perform the calculation. Indeed we remember that in the TF plane used for linear fit, the error bars are asymmetric and no more characterized by a uniform probability distribution of the values. Anyway it is clear that, at our starting stage, the *Mchirp* algorithm is more effective.

The procedure is effective when we have few pixels with noise origin. Any-

way the algorithm could be developed introducing an iterating procedure to evaluate if point rejection improves the signal description provided by the fitting. Another improvement can be performed giving a important role to the rough parameters estimation computed by the consideration of independent couples of points. Indeed, when the number of pixels is great enough, this startegy is the most independent from noise contributions with respect to the others (Fig. 7.13). Thus a check on the similarity between the pa-

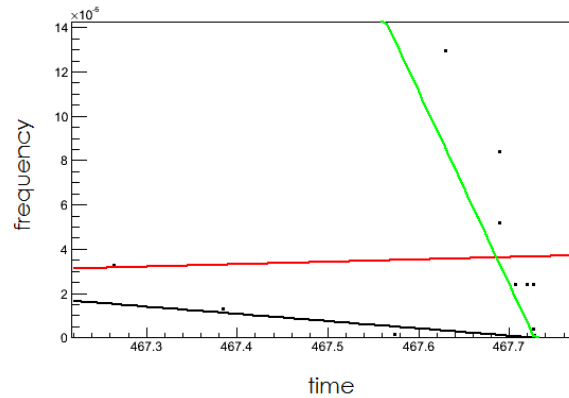


Figure 7.13: Points associated to the pixels in the plane $t, y = f^{-8/3}$. The red line refers to the result obtained by a regression procedure which do not take into account error bars on the data, instead the black one is provided by regression where we take into account also the pixel dimension as error bars. Green line is associated to the rough process of averaging the parameters obtained by independent couples of points.

rameters obtained in this way and the ones found by the other techniques can probably significantly improve the final results.

7.5 Fisher Discriminant

[75] Looking at the plots distribution showing ANN output vs network correlation coefficient (cc), we note that glitches can be separated by simulation using a linear separation in that plane. For this reason we start studying the *Fisher discriminant*.

The main idea of this approach is to separate events belonging from two different classes, finding, in the n dimensional defined by their characterizing n -parameters, the vector which “best” separate the two sets (Fig. 7.14). Thus we start considering events belonging from two different classes, we call them respectively *background* $\vec{x} \in H_0$ and *signal* $\vec{x} \in H_1$. This definition is consistent with our notation associated to the discrimination problem between chirp-like events glitches. In our case the vector dimensions considered are the output of a network (out) and the network correlation coefficient (cc).

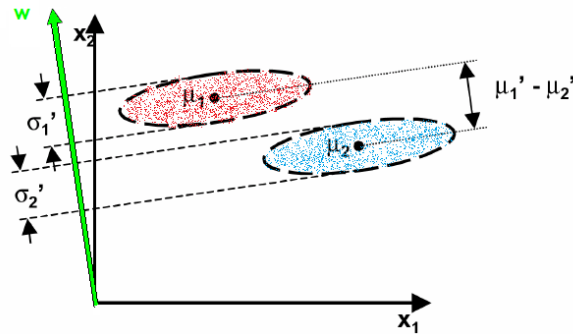


Figure 7.14: The picture represents the main idea of the Fisher discriminant.

Generally we can characterize the two population defining the expectation values and the covariances:

$$\begin{aligned}
 (\mu_k)_i &= \int x_i p(\vec{x}|H_k) d\vec{x} \\
 (V_k)_{ij} &= \int (x - \mu_k)_i (x - \mu_k)_j p(\vec{x}|H_k) d\vec{x}
 \end{aligned}
 \tag{7.6}$$

where the index k refers to the class, and the indices i, j to the vector dimensions; thus in our case $k = 0, 1$ and $i, j = cc, out$.

The main idea of this approach is a change of coordinates representing the projection $t(\vec{x})$ of the points on the vector \vec{w} which “best” separate the events belonging from the two categories. This algorithm is focused on the separation between the means and therefore no good performances are reached when the most discriminating parameter is, for example, the data dispersion (Fig. 7.15). Therefore also for this new variable we can define similarly the

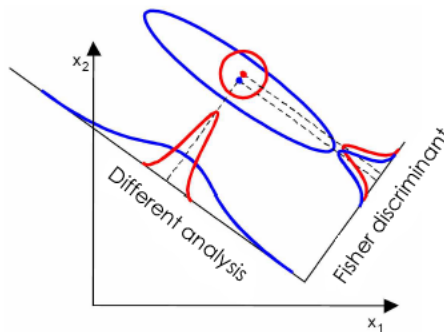


Figure 7.15: The picture represents one limit of the Fisher discriminant method.

mean and the variance:

$$\begin{aligned}\tau_k &= \int t(\vec{x})p(\vec{x}|H_k)d\vec{x} \\ \Sigma_k^2 &= \int (t(\vec{x}) - \tau_k)^2 p(\vec{x}|H_k)d\vec{x}\end{aligned}\quad (7.7)$$

Thus the basic idea of the Fisher discriminant approach is to increase the mean separation of the two classes in the t variable and decreasing in the same domain the data dispersion inside each category; i.e. the “best” separation. The strategy is to maximize the following relation:

$$J(\vec{w}) = \frac{(\tau_0 - \tau_1)^2}{\Sigma_0^2 + \Sigma_1^2} \quad (7.8)$$

We can developpe this expression finding a direct dependence of this function on the vector \vec{w} . For the numerator we find:

$$\begin{aligned}(\tau_0 - \tau_1)^2 &= \sum_{i,j=0,1}^n w_i w_j (\mu_0 - \mu_1)_i (\mu_0 - \mu_1)_j \\ &= \sum_{ij}^n w_i w_j B_{ij} = \vec{w}^T B \vec{w}\end{aligned}\quad (7.9)$$

whereas for the denominator:

$$\begin{aligned}\Sigma_0^2 + \Sigma_1^2 &= \sum_{i,j=0,1}^n w_i w_j (V_0 + V_1)_{ij} \\ &= \vec{w}^T W \vec{w}\end{aligned}\quad (7.10)$$

where we have defined the *within class scatter matrix* W and the *between class scatter matrix* B . In terms of these matrices the function $J(\vec{w})$ can be re-written by

$$J(\vec{w}) = \frac{\vec{w}^T B \vec{w}}{\vec{w}^T W \vec{w}} \quad (7.11)$$

Setting the equation

$$\frac{\partial J(\vec{w})}{\partial w_i} = 0 \quad (7.12)$$

we find that the maximum of the function $J(\vec{x})$ is given performing a projection of the data on a direction given by the vector \vec{w} :

$$\vec{w} \propto W^{-1} (\vec{\mu}_0 - \vec{\mu}_1) \quad (7.13)$$

Some interesting properties of this method can be shown.

Least squares principle Generalizing the coordinate transformation $t(\vec{x})$, defined by the Fisher discriminant, in the following way:

$$t(\vec{x}) = w_0 + \sum_{i=0}^n w_i x_i \quad (7.14)$$

(in our case $i = 0, 1 = cc, out$) i.e. using an offset w_0 and an arbitrary scale to fix the values of τ_0 and τ_1 the analysis performed by Fisher discriminant becomes equivalent to minimizing the denominator of the function $J(\vec{w})$. Thereforore maximize the $J(\vec{w})$ function using a least squares principle.

Gaussian distribution When the data distribution $p(\vec{x}|H_k)$ are multivariate Gaussian with covariant matrices $V_0 = V_1 = V$ we can write the likelihood ratio, a very useful quantity to evaluate two simple hypothesis, as

$$\begin{aligned} \Lambda(\vec{x}) &= \frac{p(\vec{x}|H_1)}{p(\vec{x}|H_0)} \\ &= \exp\left(-\frac{1}{2}(\vec{x} - \vec{\mu}_1)^T V^{-1}(\vec{x} - \vec{\mu}_1) + \frac{1}{2}(\vec{x} - \vec{\mu}_0)^T V^{-1}(\vec{x} - \vec{\mu}_0)\right) \\ &\propto e^{t(\vec{x})} \end{aligned} \quad (7.15)$$

where we have considered $t(\vec{x}) = w_0 + (\vec{\mu}_1 - \vec{\mu}_0)^T V^{-1} \vec{x}$, according to the formula (7.14). This consideration demonstrate that under (and only under) the gaussianity condition the Fisher discriminant is equivalent to the likelihood ratio.

Surely our case does not belong to the Gaussian distribution of the events sets, indeed we have limited domain in cc variable.

The results of the application of this analysis can be summarized in the following picture (Fig. 7.16) As we can see from the picture (Fig. 7.16), the “best” separation, provided by the Fisher discriminant, for the chirp-like signals and the S6D recolored glitches is computed with the application of a line more or less horizontal (orthogonal to the black line, where the points have to be projected). Contrary to the first expectation, based on this appearance of triangular shapes, the vector provided by the Fisher discriminant method has a negative slope. Anyway this can be justified considering the great dispersion on the cc coordinate, rather larger than the one present in the ordinate, which the analysis applied try to minimize. This means that the covariance terms are less important than the variances and thus we can consider the information provided by the ANN outputs more or less independent with respect to the one obtained by network correlation coefficient. Another proof of what we are saying is that increasing the set of the training

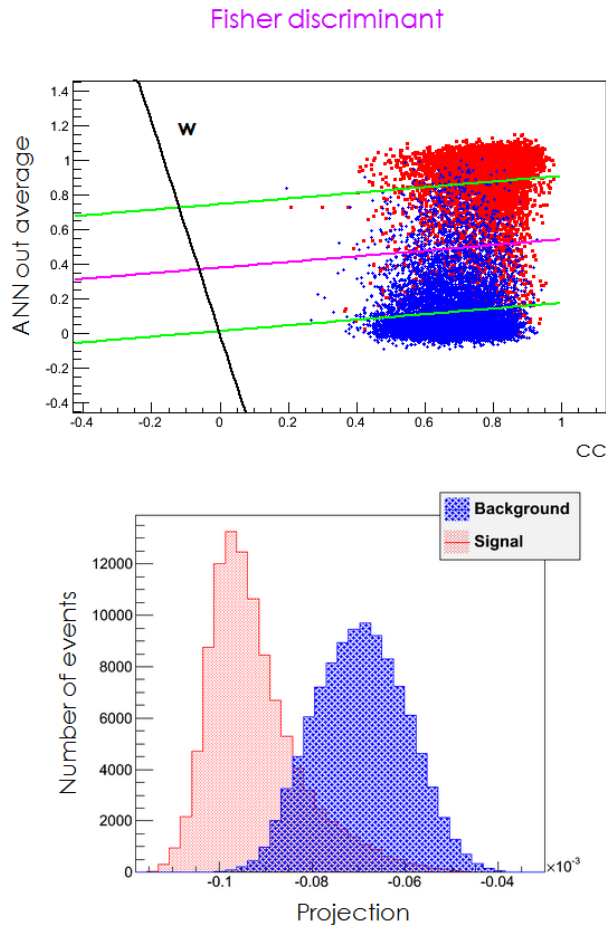


Figure 7.16: Results obtained with Fisher discriminant analysis. On the ordinate is the average of outputs provided by 6 networks trained and here tested on events whose matrix conversion is performed using the final configuration (dt and df min, approx, 0.1 amplitude threshold on the later pixels). The green lines are the projection of the means μ_0 and μ_1 on the black line, which represents the direction provided by the Fisher analysis. The fuchsia line shows one possible threshold for the data discrimination on the projection. The result is obtained using 10^4 background and 10^4 signal events to perform the vector \vec{w} and testing it on a set of 10^5 independent background and 10^5 candidates.

examples the line which describes the direction suggested by \vec{w} converges to vertical (Tab. 7.5).

n. of train ex	10	100	1000	10000	100000
w_{cc}	-0.0917	-0.0102	-0.0103	-0.0050	-0.0008
w_{out}	-0,0198	-0,0016	-0,0008	-0,0003	$-4 \cdot 10^{-5}$
angular coeff.	-4.6	-6.4	-12.6	-17.7	-23.4

Table 7.5: The *n. of train ex* refers the number of events used for both the classes.

Chapter 8

Conclusions and future ideas

In this thesis we addressed one of the main challenges associated to the detection of transient Gravitational Waves: improve the statistical significance of candidates surviving the analysis post-production cuts. To approach this problem several strategies have been tested, this work focuses on signal classification methods implemented for the identification of the GW transient which is most likely to be detected: the one emitted by compact binary coalescences, such as binary Neutro Stars, binary Black Holes of stellar mass and mixed NS-BH systems. Their characteristic morphology in the Time-Frequency plane can be picked-up by any network of GW detectors, even by the next two detectors network which will be composed by two LIGO detectors and will first become operative in late 2015.

In this thesis we developed one possible strategy: the T-F shape recognition by Artificial Neural Networks. The results achieved are at least comparable to the signal selection cut based on fitting procedures developed by a research group of the LIGO Scientific collaboration (yet unpublished). Both methods proved to select the target signal class with a few % loss in efficiency while they are being capable to reject by a factor ~ 20 the background of non gaussian noise transients (“glitches”). This accomplishment, proved that it will be further validated by more simulations, is very crucial for improving the chances of detection of these signals using robust analysis methods (i.e. analysis not based on matched filtering methods and therefore not depending on the accurate model of phase evolution of the signal). In fact, by reducing more than one order of magnitude the rate of louder background glitches, the non-gaussina noise tail of the robust analysis approaches the typical gaussian noise tail achieved by matched filtering methods on the same data. In this way the detection chances of both analysis methods could get comparable, with the advantage of a more robust (and computationally faster) analysis, which remains open to a larger class of possible GW emissions from yet unn-modeled sources.

Improvements with respect to the achieved results are still at hand. We

envisage for instance to address next some of the following ideas:

Increase the matrix dimension : increase the dimension of the T-F pixel matrix used as input of ANNs, currently tested with 8×8 ;

combine ANN method with fitting procedures : first results on fitting algorithm show that is a quite promising technique, so one should to test if a combination of the two techniques brings advantages;

Introducing more inputs on the ANN networks : additional information can be added to better differentiate the events. For instance:

- event duration, central frequency and band;
- distribution of the resolution of the TF pixels making the event cluster (the first results look promising);
- other event parameters as measured by the cWB pipeline. For instance, we found that the network correlation efficient is almost independent from the ANN output and therefore efficient selection cuts can be chosen independently (which is a good news anyway). The situation does not appear as simple looking at additional cWB parameters and has to be investigated.

To address these points we propose a structure composed by more ANNs in hierarchical stages: for instance two parallel ANN for the three items listed above followed by a second stage ANN to synthetize an overall scalar output.

A crucial investigation for the astrophysical interpretation of the results of the technique here developed is still missing, i.e. to test its efficiency versus the the Black Hole mass. In fact we expect that massive stellar BHs binaries will emit in the inspiralling phase outside the detectors frequency band of best sensitivity, therefore loosing the chirp-like T-F characteristic in the detectors responses.

Other tests should be performed to test if multy layer perceptrons are the most appropriate mashine learning to perform the discrimination. As a final remark, we would like to highlight that a long term goal of this research is to find signal classification methods effective for GW emissions from other astrophysical phenomena, such as Neutron Star instabilities and quasi normal modes.

Bibliography

- [1] Michele Maggiore, *Gravitational waves*, vol. 1 (Theory and experiments), p. 576 Oxford University Press (2007)
- [2] Francesco Ravanini, *Appunti di relatività Generale*, Corso di Laurea in Astrofisica e Cosmologia, Università di Bologna (2008)
<http://www.bo.infn.it/~ravanini/relativity/Generale.pdf>
- [3] Guido Cognola, *General Relativity and Cosmology* (Lecture notes); Physical Department, University of Trento, (2014)
- [4] Valeria Ferrari and Leonardo Gualtieri, *General Relativity* (Lecture notes); Department of Physics, University of Rome (A.A. 2011-2012)
<http://www.science.unitn.it/~cognola/DIDATTICA/RGeng2014.pdf>
- [5] Sigg D., LIGO-P980007-00-D; (2009)
- [6] K. S. Thorne, Rev. Mod. Phys.; vol. 52, p. 299, (1980)
- [7] E. Baron and J. Copperstein, Astrophys. J.; vol. 353, p. 597 (1990)
H. A. Bethe, Rev. Mod. Phys.; vol. 62, p. 801 (1990)
- [8] Ott, C.D. Classical Quant. Grav. **26**, 063001 (2009)
- [9] Andrea Vicerè, *The science case for advanced gravitational wave detectors*; Dipartimento di Scienze di Base e Fondamenti, Università di Urbino
- [10] H. A. Bethe, Rev. Mod. Phys.; vol. 62, p. 801 (1990)
H-T Janka et al., Phys Rep; vol. 442, p. 38 (2007)
- [11] J.M LeBlanc and J.R. Wilson, Astrophys J.; vol. 161, p. 541 (1970)
H Swai et al., Astrophys J; vol. 672, p. 465 (2008)
- [12] A. Burrows et al., Phys. Rep.; vol. 442, p. 23 (2007)
- [13] P. C. Peters, Physical Review; vol. 136, p. B1224 (1964)

- [14] M. E. Pati and C. M. Will, Phys. Rev. D; vol. 65, p. 104008 (2002)
C. Konigsdorffer et al., Phys. Rev. D; vol. 68, p. 044004 (2003)
S. Nissanke and L. Blanchet, Class. Quantum Grav.; vol. 22, p. 1007 (2005)
L. Blanchet Living Rev. Rel.; vol. 9, p. 4 (2006)
Class. Quantum Grav.; vol. 15, p. 113 (1998)
M. E. Pati and C. M. Will, Phys. Rev. D; vol. 62, p. 124015
- [15] A. Burrows et al., Phys. Rep.; vol. 442, p. 23 (2007)
S. van den Bergh and G.A. Tammanm, Ann. Rev. Astron. Astroph.; vol. 29, p. 363 (1991)
- [16] M. Campanelli et al., Phys. Rev. Lett.; vol. 96, p. 111101 (2006)
J. G. Baker et al., Phys. Rev. Lett.; vol. 96, p. 111102, (2006)
- [17] E. Berti et al., Class. Quantum Grav. vol. 26, p. 163001 (2009)
- [18] C. W. Misner et al., Gravitation; W. H. Freeman, Ed., 1973.
- [19] T. Damour, Int. J. Mod. Phys; vol. A23, p. 1130 (2008)
- [20] A. Buonanno and T. Damour, Phys. Rev. D; vol. 59, p. 084006 (1999)
- [21] Joel M. Weisberg, David J. Nice, Joseph H. Taylor, Astrophys.J.; vol. 722 p.1030-1034,(2010)
- [22] Matthew Pitkin, Living Rev. Relativity 14; 5 (2011)
- [23] AURIGA Collaboration and Virgo Collaboration, Class.Quant.Grav.; 25:114046 (2008)
- [24] http://www.pd.infn.it/segreterie/segred/trasparenze/2012/preventivi_2013/Gruppo2/AU
- [25] LIGO Scientific Collaboration and Virgo Collaboration, Class.Quant.Grav.; 27:173001(2010)
- [26] Peter R.Sauslon, *Fundamental of interferometric gravitational wave detectors*. World scientific (1994)
- [27] Majorana E., *Acquisizione e controllo del punto di lavoro in un interferometro per la rivelazione delle onde gravitazionali (elementi)*. Corso di Gravitazione Sperimentale, Dipartimento di Fisica Università La Sapienza, Roma, (A.A. 2008-2009)
- [28] <http://www.phys.ufl.edu/~coldwell/ligo/Power.htm>
- [29] http://www.ego-gw.it/virgodescription/pag_5.html
- [30] J. N. Brune and J. Oliver, Bull. Seism. Soc. Am.; vol. 49 (1959)

- [31] www.hts-i.it/documenti/Suprasil-311-312.pdf
- [32] C. Cagnoli, L. Gammaiotni, J. Kovalik, F. Marchesoni and M. Punturo, The Virgo sensitivity curve (virgo note) Perugia; (March 1997)
- [33] Bernard F. Schutz, Submitted to Class. Quantum Grav. (arxiv.org/pdf/1102.5421.pdf); (2011)
- [34] B. J. Meers, Phys. Rev.; vol. D 38, p. 2317 (1988)
- [35] <https://dcc.ligo.org/DocDB/0110/G1301281/002/hannover2013.pdf>
- [36] J. Markowitz et al., Phys. Rev.; vol. D 78, p. 122003 (2008)
F. Cavalier et al., Phys. Rev.; vol. D. 78:082004 (2006)
N. Arnaud et al., Phys. Rev. D; vol. 65, p. 042004 (2002)
L. S. Finn, Phys. Rev. D; vol. 63, p. 102001 (2001)
- [37] S. Klimenko et al, Phys. Rev.; vol. D. 83, 102001 (2011)
- [38] J. Aasi et al., Class. Quantum Grav.; vol. 29, p. 155002 (2012)
J. McIver, Class. Quantum Grav.; vol. 29, p. 124010 (2012)
- [39] J. R. Smith et al., Class. Quantum Grav.; vol. 28, p. 235005, (2011)
- [40] Fulvio De Santis, Luca Tardella e Isabella Verdinelli, *Teoria Dei Test*(appunti); Unisersità di Roma, Corsi di Inferenza Statistica, Roma (A.A. 2010-2011)
- [41] <http://tarot.obs-hp.fr>
- [42] V. Nacula et al., J. Phys.; Conf. Ser. 363 012032 (2012)
- [43] S. Klimenko and G. Mitselmakher, Class. Quantum Grav.; vol. 21, p. S1819 (2004)
- [44] C.Lazzaro, *Coherent Waveburst for burst searches in ADE: comparison with the previous pipeline*; VIR-0018A-14 (<https://tds.ego-gw.it/ql/?c=9995>) (2014)
- [45] <https://wiki.ligo.org/viewfileauth/Bursts/F2FagendaPage/burstOverview.pdf>
- [46] Rahul Biswas, Lindy Blackburn, Junwei Cao, Reed Essick, Kari Alison Hodge, Erotokritos Katsavounidis, Kyungmin Kim, Young-Min Kim, Eric-Olivier Le Bigot, Chang-Hwan Lee, John J. Oh, Sang Hoon Oh, Edwin J. Son, Ruslan Vaulin, Xiaoge Wang, Tao Ye, Phys.Rev.; D.88.062003 (<http://arxiv.org/abs/1303.6984>) (2013)
- [47] <http://robotics.stanford.edu/~nilsson/MLBOOK.pdf>
- [48] http://tmva.sourceforge.net/#mva_bdt

- [49] Thomas S. Adams, Duncan Meacher, James Clark, Patrick J. Sutton, Gareth Jones, Ariana Minot, Submitted to Phys. Rev.; D.88.062006 (<http://arxiv.org/abs/1305.5714>) (2013)
- [50] F Acernese et al, Class. Quantum Grav.; vol. 19 p. 32932002 (2002)
- [51] Salvatore Rampone, Vincenzo Pierro, Luigi Troiano, Innocenzo M. Pinto, International Journal of Modern Physics C; vol. 24, No. 11 (2013)
- [52] F Acernese et al., Class. Quantum Grav.; 22 S1223(2005)
- [53] twiki.di.uniroma1.it/pub/ApprAuto/AnnoAcc0708/9SVM.ppt
- [54] <http://www.dsi.unive.it/~srotabul/files/AppuntiRetiNeurali.pdf>
- [55] Matteo Golfarelli, Elisa Turrlicchia, *Artificial Neural Networks*; Scienze e tecnologie informatiche, Università di Bologna
<http://bias.csr.unibo.it/golfarelli/DataMiningSTI/MaterialeDidattico/Reti20Neurali.pdf>
- [56] L. Grippo and M. Sciandrone, metodi di ottimizzazione per le reti neurali; dipartimento di informatica e sistemistica, Università di Roma
<http://www.dis.uniroma1.it/~lucidi/didattica/Reti-Neurali-1.pdf>
- [57] <http://cs.stanford.edu/people/eroberts/courses/soco/projects/2000-01/neural-networks/Applications/index.htm>
- [58] <http://www2.units.it/mumolo/introNN.pdf>
- [59] <http://root.cern.ch/drupal/>
- [60] McCulloch, W.S., W. Pitts , Bulletin of Mathematical Biophysics; vol. 5, p. 115-133 (1943)
- [61] F. Rosenblatt, Spartan Books; Washington, DC (1962)
- [62] S. Agmon, Canadian Journal of Mathematics; vol. 6, p. 382-392 (1954)
- [63] Motzkin, T.S., I.J. Schoenberg , Canadian Journal of Mathematics; vol. 6 p. 393-404 (1954)
- [64] A. Pinkus, Journal of Approximation Theory; vol. 85, p. 269-287(1996)
- [65] A. Pinkus, Acta Numerica; p. 143-195 (1999)
- [66] <http://www.cs.nott.ac.uk/~qiu/Teaching/G53MLE/ffnets-note.pdf>
- [67] <http://th-www.if.uj.edu.pl/~erichter/dydaktyka/Dydaktyka2008/NeuralNetwork-2008/NN-MLPmethod-delaere.pdf>

- [68] Jonathan Richard Shewchuk, *An Introduction to the Conjugate Gradient Method Without the Agonizing Pain*; School of Computer Science, Carnegie Mellon University Pittsburgh (1994)
<http://www.cs.cmu.edu/~quake-papers/painless-conjugate-gradient.pdf>
- [69] Martin F. Moller A Scaled Conjugate for Fast Supervised Learning; Computer Science Department, University of Aarhus Denmark (1990)
- [70] AURIGA Collaboration and Virgo Collaboration, *Class.Quant.Grav.*; 25:114046 (2008)
- [71] R. A. Dunne and N. A. Campbell, 8th Aust. Conf. on Neural Networks Melb.; p. 181-185 (1997)
- [72] <http://root.cern.ch/root/html/TMultiLayerPerceptron.html>
- [73] P. Graff et al, *Mon. Not. R. Astron. Soc.* 000; p. 1-19 (2013)
- [74] <https://ldas-jobs.ligo.caltech.edu/~stuver/burst/MDC/S6/>
- [75] Cowan *Computing and statistical analysis data*, Lecture Notes; University of London (2012)

Ringraziamenti

In primis un ringraziamento speciale va ai miei fantastici genitori. A mia mamma per l'inifita pazienza con cui mi ha sopportata ogni volta che sono andata in crisi per un esame, per la tolleranza verso il mio ordine in casa a dir poco trascurato e per gli abbracci serali mai mancati. A mio papà per avermi sempre spronata a dare il massimo, per le infinite discussioni, per l'apertura mentale che spero mi abbia trasmesso e le nuove ed interessanti prospettive che spesso mi hanno permesso di vedere il mondo sotto una diversa luce. Li ringrazio infinitamente entrambi per questo sostegno spicologico ed economico con cui mi hanno supportata in questi ultimi 5 anni ed in particolar modo in questi ultimi giorni.

Ringrazio i miei fratelli per il calore che mi hanno sempre trasmesso e che, nei miei momenti peggiori, hanno pazientemente glissato sulle mie escandescenze. In particolare ringrazio mio fratello Giorgio per la sua compagnia in camera, per gli abbracci e per le camomille durante le mie serate di studio e Stefano per il contributo alla correzione di questa tesi e in generale per la disponibilità ad aiutarmi nei momenti di difficoltà. Ringrazio comunque anche Matteo per le divertenti chiacchierate e Luca per il sostegno morale e la gentilezza.

Ringrazio i miei nonni per avermi accolta sempre volentieri in casa loro nei momenti di studio e per avermi, in quelle occasioni, coccolata in tutti i modi possibili.

Un ringraziamento speciale va senza dubbio a Matteo perchè è rimasto al mio fianco in ogni istante sostenendomi anche con estenuanti discussioni e nonostante le difficoltà e il poco tempo che ultimamente gli ho potuto dedicare.

Un grazie di tutto cuore al mio relatore Giovanni Andrea Prodi per tutti il tempo che mi ha dedicato, per le interessanti discussioni intraprese e per le splendide opportunità fornite. Ringrazio infinitamente anche il mio correlatore Marco Drago per l'inifita pazienza e per i preziosi consigli che mi ha fornito in questi ultimi 8 mesi. Molte grazie anche a Gabriele Vedovato che ha proposto questo interessante argomento di tesi e che si è sempre mostrato disponibile ed interessato. Infine ringrazio Claudia Lazzaro, Maria Concetta Tringali e Matteo Leonardi per l'aiuto che mi hanno fornito in questo ultimo periodo e per la gradita compagnia.

A tutti un grazie di cuore.